RENSIT:
RadioElectronics. NanoSystems. Information Technologies

Journal "Radioelectronics. Nanosystems. Information Technologies" (abbr. RENSIT)
publishes original articles, reviews and brief reports, not previously published, on topical problems in **radioelectronics (including biomedical) and fundamentals of information, nano- and biotechnologies and adjacent areas of physics and mathematics.**

Designed for **researchers, graduate students, physics students of senior courses and teachers**.
It turns out **4 times a year** (that includes 4 issues)

Authors of journal are academicians, corresponding members and foreign members of Russian Academy of Natural Sciences (RANS) and their colleagues,
as well as other russian and foreign authors on presentation of their manuscripts by the members of RANS, which can be obtained by authors before sending articles to editors.
And also after its receiving - on recommendation of a member of editorial board of journal, or another member of Academy of Natural Sciences, that gave her opinion on article at request of editor.
The editors will accept articles in both **Russian and English** languages.

Articles are internally peer reviewed (**double-blind peer review**) by members of the Editorial Board.
Some articles undergo external review, if necessary.

Journal RENSIT is included in the **DB SCOPUS, EBSCO Publishing,** in the international abstracts database - **Ulrich's International Periodicals Directory**,(USA, New York, http://www.ulrichsweb.com), in the **AJ and DB VINITI RAS** (http://www.viniti.ru), and DB **Russian Science Citation Index (RSCI** http://elibrary.ru/project_risc.asp). Included in the **List of Higher Attestation Comission** (No. 2204 dated July 17, 2023: K1 in 9 groups of specialties) of Science and Higher Education Ministry of the Russian Federation.

Full-text content is posted in the DB of the **Russian Scientific Electronic Library**
- information resource on the Internet http://elibrary.ru and is available for registered users.
And also - in Open Access **CyberLeninka NEB** of Russian Federation http://cyberleninka.ru.

On journal's website http://www.rensit.ru posted metadata publications
and **RENSIT: Radioelectronics. Nanosystems. Infomation Technologies - english version** (cover-to-cover translation) of journal, which is a party to **CrossRef.**

The founder - the **Russian Academy of Natural Sciences**
Publisher - Publishing Center of the Russian Academy of Natural Sciences
Publisher Address: 29/16, Sivtsev Vrazhek lane, Moscow 119002, Russian Federation

CONTENTS

RUSSIAN ACADEMY OF NATURAL SCIENCES

DEPARTMENT OF RADIOELECTRONICS, NANOPHYSICS AND INFORMATION TECHNOLOGIES PROBLEM

RENSIT:

RADIOELECTRONICS. NANOSYSTEMS. INFORMATION TECHNOLOGIES.

2024, Vol. 16, no. 1

FOUNDED IN 2009
4 ISSUES PER YEAR
MOSCOW

ISSN 2414-1267

The journal on-line is registered by the Ministry of Telecom and Mass Cjmmunications of the Russian Federation. Certificate El. no. FS77-60275 on 19.12.2014

EDITORIAL BOARD ADDRESS
218-219 of., 7 b., 11, Mokhovaya str., 125009 MOSCOW, RUSSIAN FEDERATION,
TEL. +7 495 629 3368
FAX +7 495 629 3678 FOR GRACHEV

DOI: 10.17725/j.rensit.2024.16.003

Physically realizable reconstruction of a continuous signal after sampling

Andrey N. Degtyarev, Igor L. Afonin, Alexander L. Polyakov
Sevastopol State University, http://www.sevsu.ru/
Sevastopol 299053, Russian Federation
E-mail: andegtyarev@mail.sevsu.ru, ilafonin@mail.sevsu.ru, alpolyakov@ mail.sevsu.ru

Received August 23, 2023, peer-reviewed August 30, 2023, accepted September 07, 2023, published March 15, 2024.

Abstract: **It is proposed to describe signals in a physically realizable basis. Correlation functions of impulse characteristics of physically implemented filters are used as basic functions. To obtain analytical expressions of the functions of the proposed physically realizable basis, it is proposed to use inverse Fourier transforms from approximations (Butterworth, Chebyshev, etc.) of the squares of the amplitude-frequency characteristics of normalized low-pass filters. The basis, functions are copies of the indicated correlation functions of the impulse characteristics, shifted relative to each other by the same time interval, which is the sampling interval. It is shown that there is a sampling theorem in the space of the introduced functions. The exact restoration of the signal is possible if the functions of the considered basis have the property of readability. In this case, the considered basic functions are functions of counts and are not physically implemented. To reduce the error of restoring a continuous signal from its readings using the proposed basis, it is necessary to increase the order of the filter, the pulse characteristics of which are used in the formation of the basis. To restore a continuous signal, its samples must be fed to two cascaded filters. The first filter must have an impulse response, the correlation function of which is used to form a physically realizable basis. The second filter must be matched to the impulse response of the first filter.**

Keywords: **sampling, sampling theorem, pulse characteristic of the filter, correlation function**
UDC 621.376.5
For citation: Andrey N. Degtyarev, Igor L. Afonin, Alexander L. Polyakov. Physically realizable reconstruction of a continuous signal after sampling. *RENSIT: Radioelectronics. Nanosystems. Information Technologies,* 2024, 16(1):3-10e. DOI: 10.17725/j.rensit.2024.16.003.

Contents

1. INTRODUCTION

V.A. Kotelnikov's sampling theorem represents band-limited signals in the series form based on sampling functions. The series coefficients are signal samples taken at times that are multiples of the sampling interval $\alpha = 1/(2f_m)$, where f_m – maximum frequency in the signal spectrum. The sampling functions have the property that when one of them reaches its maximum, the other is equal to zero. To restore a continuous signal from its samples, delta pulses weighted by signal samples are applied to an ideal low-pass filter (LPF). However, ideal LPFs are not physically realized, so Butterworth filters are used as such low-pass filters. The impulse response

of Butterworth filters does not have the specified property of sampling functions [1,2,3,13,14,15].

Let's consider the features of discretization and recovery of signals in the basis of physically realizable equidistant functions.

2. MAIN PART

Let the equidistant functions $\varphi_n(t) = \varphi_0(t - n\alpha)$ are orthonormal with weight equal to one. Then some function $f(t)$, which spectral density is equal to

$$F(\mathrm{j}\omega) = F(\omega)\mathrm{e}^{\mathrm{j}\theta_f(\omega)},$$

can be lined up

$$f(t) = \sum_{n=-\infty}^{\infty} y_n \varphi_n(t).$$

Since the basic functions are equidistant $\varphi_n(t)$, then

$$\Phi_n(\mathrm{j}\omega) = \Phi_0(\omega)\mathrm{e}^{\mathrm{j}\theta_\varphi(\omega)}\mathrm{e}^{-\mathrm{j}\omega n\alpha},$$

and the discrete Fourier transform $f(t)$ provides dependence

$$F(\mathrm{j}\omega) = F(\omega)\mathrm{e}^{\mathrm{j}\theta_f(\omega)} = \\ = \Phi_0(\omega)\mathrm{e}^{\mathrm{j}\theta_\varphi(\omega)} \sum_{n=-\infty}^{\infty} y_n \mathrm{e}^{-\mathrm{j}\omega\alpha n}. \quad (1)$$

The mean square of the approximation error $f(t)$ in series is defined as

$$I = \int_{-\infty}^{\infty} [f(t) - \sum_{n=-\infty}^{\infty} y_n \varphi_n(t)]^2 \mathrm{d}t, \quad (2)$$

where

$$y_n = \frac{1}{\|\varphi_n\|^2} \int_{-\infty}^{\infty} f(t)\varphi_n(t)\mathrm{d}t,$$

$$\|\varphi_n\|^2 = E_\phi = \int_{-\infty}^{\infty} \varphi_n^2(t)\mathrm{d}t.$$

Based on the Parseval's identity (2), one can rewrite in the form

$$I = \frac{1}{2\pi} \int_{-\infty}^{\infty} [F(\mathrm{j}\omega) - \sum_{n=-\infty}^{\infty} y_n \Phi_n(\mathrm{j}\omega)] \times$$

$$\times [\overset{*}{F}(\mathrm{j}\omega) - \sum_{n=-\infty}^{\infty} y_n \overset{*}{\Phi}_n(\mathrm{j}\omega)]\mathrm{d}\omega =$$

$$= \frac{1}{2\pi} \int_{-\infty}^{\infty} [F^2(\omega) - F(\mathrm{j}\omega) \sum_{n=-\infty}^{\infty} y_n \overset{*}{\Phi}_n(\mathrm{j}\omega) -$$

$$- \overset{*}{F}(\mathrm{j}\omega) \sum_{n=-\infty}^{\infty} y_n \Phi_n(\mathrm{j}\omega) +$$

$$+ \sum_{n=-\infty}^{\infty} \sum_{k=-\infty}^{\infty} y_n y_k \overset{*}{\Phi}_n(\mathrm{j}\omega)\Phi_k(\mathrm{j}\omega)]\mathrm{d}\omega.$$

One can transform the resulting expression and obtain

$$I = \frac{1}{2\pi} \int_{-\infty}^{\infty} [F^2(\omega) - F(\omega)\mathrm{e}^{\mathrm{j}\theta_f(\omega)}\Phi_0(\omega)\mathrm{e}^{-\mathrm{j}\theta_\varphi(\omega)} \sum_{n=-\infty}^{\infty} y_n \mathrm{e}^{\mathrm{j}\omega n\alpha} -$$

$$- F(\omega)\mathrm{e}^{-\mathrm{j}\theta_f(\omega)}\Phi_0(\omega)\mathrm{e}^{\mathrm{j}\theta_\varphi(\omega)} \sum_{n=-\infty}^{\infty} y_n \mathrm{e}^{-\mathrm{j}\omega n\alpha} +$$

$$+ \Phi_0^2(\omega) \sum_{n=-\infty}^{\infty} \sum_{k=-\infty}^{\infty} y_n y_k \mathrm{e}^{\mathrm{j}\omega k\alpha}\mathrm{e}^{-\mathrm{j}\omega n\alpha}]\mathrm{d}\omega.$$

Let's consider that $F(\omega) = \Phi_0(\omega)$, and obtain where

$$I = \frac{1}{2\pi} \int_{-\infty}^{\infty} [\Phi_0^2(\omega) - \Phi_0^2(\omega)\mathrm{e}^{\mathrm{j}(\theta_f(\omega) - \theta_\varphi(\omega))} \sum_{n=-\infty}^{\infty} y_n \mathrm{e}^{\mathrm{j}\omega n\alpha} -$$

$$- \Phi_0^2(\omega)\mathrm{e}^{-\mathrm{j}(\theta_f(\omega) - \theta_\varphi(\omega))} \sum_{n=-\infty}^{\infty} y_n \mathrm{e}^{-\mathrm{j}\omega n\alpha} + \Phi_0^2(\omega) \sum_{n=-\infty}^{\infty} y_n^2]\mathrm{d}\omega =$$

$$= \frac{1}{2\pi} \int_{-\infty}^{\infty} \Phi_0^2(\omega)[1 - \mathrm{e}^{\mathrm{j}\Delta\theta(\omega)} \sum_{n=-\infty}^{\infty} y_n \mathrm{e}^{\mathrm{j}\omega n\alpha} -$$

$$- \mathrm{e}^{-\mathrm{j}\Delta\theta(\omega)} \sum_{n=-\infty}^{\infty} y_n \mathrm{e}^{-\mathrm{j}\omega n\alpha} + \sum_{n=-\infty}^{\infty} y_n^2]\mathrm{d}\omega,$$

where $\Delta\theta(\omega) = \theta_f(\omega) - \theta_\varphi(\omega)$.

Since the coefficients y_n are delta-correlated with each other, one can have

$$I = \frac{1}{2\pi} \int_{-\infty}^{\infty} \Phi_0^2(\omega)[2 - \mathrm{e}^{\mathrm{j}\Delta\theta(\omega)} \sum_{n=-\infty}^{\infty} y_n \mathrm{e}^{\mathrm{j}\omega n\alpha} -$$

$$- \mathrm{e}^{-\mathrm{j}\Delta\theta(\omega)} \sum_{n=-\infty}^{\infty} y_n \mathrm{e}^{-\mathrm{j}\omega n\alpha}]\mathrm{d}\omega.$$

Taking into account the evenness of the function $\Phi_0^2(\omega)$ and the oddness of the function $\Delta\theta(\omega)$ as well as the fact that the integration is performed over infinite limits, one can get

$$I = \frac{1}{2\pi}\int_{-\infty}^{\infty}\Phi_0^2(\omega)[2-2e^{j\Delta\theta(\omega)}\sum_{n=-\infty}^{\infty}y_n e^{j\omega n\alpha}]d\omega =$$

$$= 2E_\varphi - 2\sum_{n=-\infty}^{\infty}y_n\frac{1}{2\pi}\int_{-\infty}^{\infty}\Phi_0^2(\omega)e^{j\Delta\theta(\omega)}e^{j\omega n\alpha}d\omega =$$

$$= 2E_\varphi\left(1-\frac{1}{E_\varphi}\sum_{n=-\infty}^{\infty}y_n\frac{1}{2\pi}\int_{-\infty}^{\infty}\Phi_0^2(\omega)e^{j\Delta\theta(\omega)}e^{j\omega n\alpha}d\omega\right).$$

The same expression can be obtained when the functions $\varphi_n(t)$ are orthogonal, without considering the coefficients y_n as delta-correlated.

In order for the mean square of the error to be equal to zero, the condition must be satisfied

$$\frac{1}{E_\varphi}\sum_{n=-\infty}^{\infty}y_n\frac{1}{2\pi}\int_{-\infty}^{\infty}\Phi_0^2(\omega)e^{j\Delta\theta(\omega)}e^{j\omega n\alpha}d\omega = 1,$$

which is possible if

$$\frac{1}{2\pi}\int_{-\infty}^{\infty}\Phi_0^2(\omega)e^{j\Delta\theta(\omega)}e^{j\omega n\alpha}d\omega = E_\varphi y_n. \quad (3)$$

Consider the coefficient value y_n

$$y_n = \frac{1}{\|\varphi_n\|^2}\int_{-\infty}^{\infty}f(t)\varphi_n(t)dt = \frac{1}{E_\phi}\int_{-\infty}^{\infty}f(t)\varphi_n(t)dt.$$

Based on the Parseval's identity, one can write down

$$y_n = \frac{1}{E_\varphi}\int_{-\infty}^{\infty}f(t)\varphi_n(t)dt =$$

$$= \frac{1}{2\pi}\frac{1}{E_\varphi}\int_{-\infty}^{\infty}\Phi_0(\omega)e^{j\theta_f(\omega)}\Phi_0(\omega)e^{-j\theta_\varphi(\omega)}e^{j\omega n\alpha}d\omega = \quad (4)$$

$$= \frac{1}{E_\varphi}\frac{1}{2\pi}\int_{-\infty}^{\infty}\Phi_0^2(\omega)e^{j\Delta\theta(\omega)}e^{j\omega n\alpha}d\omega.$$

From comparison (4) and (3) it becomes obvious that equality (3) is an identity. Therefore, the mean square of the signal approximation error (2) equals zero.

Expression (4) can be rewritten as

$$y_n = \frac{1}{2\pi}\frac{1}{E_\varphi}\int_{-\infty}^{\infty}F(j\omega)\Phi_0(-j\omega)e^{j\omega n\alpha}d\omega =$$

$$= \frac{1}{E_\varphi}R_{f\varphi}(n\alpha),$$

where $R_{f\varphi}(n\alpha) = \int_{-\infty}^{\infty}f(t)\varphi_0(t-n\alpha)dt$ – the values of the correlation function of the signal $f(t)$ and the function $\varphi_0(t)$, taken at time points $n\alpha$ (n = 0, 1, 2,...).

In order to determine the value of α, some requirements must be applied to the properties of the signal $f(t)$.

So, if one assumes that the signal $f(t)$ is limited in frequency by the maximum frequency ω_m, then the famous sampling theorem is obtained

Indeed, since the signal is represented as a series

$$f(t) = \sum_{n=-\infty}^{\infty}y_n\varphi_0(t-n\alpha),$$

then its spectral density is equal to (1)

Subsequently, one can write

$$\frac{F(j\omega)}{\Phi_0(j\omega)} = e^{j[\theta_f(\omega)-\theta_\varphi(\omega)]} = \sum_{n=-\infty}^{\infty}y_n e^{-j\omega\alpha n}. \quad (5)$$

The expression $\sum_{n=-\infty}^{\infty}y_n e^{-j\omega\alpha n}$ represents a periodic function with a period $2\pi/\alpha$.

Since the ratio of spectral densities $\frac{F(j\omega)}{\Phi_0(j\omega)}$ is defined for $\omega\in[-\omega_m,\omega_m]$, then (5) is possible only if

$$\frac{2\pi}{\alpha} = 2\omega_m.$$

where one can obtain

$$\alpha = \frac{2\pi}{2\omega_m} = \frac{\pi}{2\pi f_m} = \frac{1}{2f_m}, \quad (6)$$

which corresponds to the sampling interval introduced by the sampling theorem.

In this case, the signal can be represented in series

$$f(t) = \frac{1}{E_\varphi}\sum_{n=-\infty}^{\infty}R_{f\varphi}\left(\frac{n}{2f_m}\right)\varphi_0\left(t-\frac{n}{2f_m}\right). \quad (7)$$

If the sampling functions are used as equidistant functions

$$\varphi_n(t) = \frac{\sin \omega_m \left(t - \frac{n}{2f_m} \right)}{\omega_m \left(t - \frac{n}{2f_m} \right)},$$

then $E_\varphi = \pi/\omega_m$, and according to (5) on the interval $\omega \in [-\omega_m, \omega_m]$, one can have

$$F(\mathrm{j}\omega) = \sum_{n=-\infty}^{\infty} y_n \mathrm{e}^{-\mathrm{j}\omega\alpha n}.$$

The coefficients of the series in this case are defined as

$$\begin{gathered} \int_{-\omega_m}^{\omega_m} F(\mathrm{j}\omega)\mathrm{e}^{\mathrm{j}\omega\alpha n}\mathrm{d}\omega = \sum_{n=-\infty}^{\infty} y_n \int_{-\omega_m}^{\omega_m} \mathrm{e}^{-\mathrm{j}\omega\alpha n}\mathrm{e}^{\mathrm{j}\omega\alpha n}\mathrm{d}\omega, \\ \int_{-\omega_m}^{\omega_m} F(\mathrm{j}\omega)\mathrm{e}^{\mathrm{j}\omega\frac{\pi n}{\omega_m}}\mathrm{d}\omega = y_n \int_{-\omega_m}^{\omega_m} \mathrm{d}\omega. \end{gathered} \quad (8)$$

Since

$$f(t) = \frac{1}{2\pi}\int_{-\omega_m}^{\omega_m} F(\mathrm{j}\omega)\mathrm{e}^{\mathrm{j}\omega t}\mathrm{d}\omega, \quad \int_{-\omega_m}^{\omega_m} \mathrm{d}\omega = 2\omega_m,$$

then equality (8) is rewritten in the form

$$2\pi f\left(\frac{\pi n}{\omega_m}\right) = 2\omega_m y_n.$$

Hence one can get

$$y_n = \frac{\pi}{\omega_m} f\left(\frac{\pi n}{\omega_m}\right).$$

Thus, the band-limited signal is expanded into a series of sample functions as follows

$$f(t) = \sum_{n=-\infty}^{\infty} f\left(\frac{n}{2f_m}\right)\varphi_0\left(t - \frac{n}{2f_m}\right),$$

which corresponds to the sampling theorem.

It is worth noting the sampling theorem is obtained proceeding from the general approximation positions of functions in series in equidistant functions. The assumptions that led directly to the sampling theorem were: firstly, the signal must be limited in frequency and, secondly, the sampling functions are used as equidistant functions [4,5,6,7].

Therefore, the signal expanded in a series of equidistant functions can be written as

$$f(t) = \frac{1}{E_\varphi}\sum_{n=-\infty}^{\infty} R_{f\varphi}(n\alpha)\varphi_0(t - n\alpha).$$

It is rational to determine the dependence of the coefficients in the series on the signal samples.

Let's take the m^{th} sample of this signal

$$\int_{-\infty}^{\infty} f(t)\delta(t - m\alpha)\mathrm{d}t =$$

$$= \frac{1}{E_\varphi}\int_{-\infty}^{\infty}\sum_{n=-\infty}^{\infty} R_{f\varphi}(n\alpha)\varphi_0(t - n\alpha)\delta(t - m\alpha)\mathrm{d}t.$$

Using the filtering property of the delta function, one can get

$$f(m\alpha) = \frac{1}{E_\varphi}\sum_{n=-\infty}^{\infty} R_{f\varphi}(n\alpha)\varphi_0[(m-n)\alpha]. \quad (9)$$

So, the m^{th} sample of the signal $f(t)$ is calculated through the values of the cross-correlation function of the signal $f(t)$ and the function $\varphi_0(t)$ rather complicated (9), using a discrete filter with an impulse response $\varphi_0(m\alpha)$.

Let's consider what requirements can be imposed on the function $\varphi_0(t)$ to simplify the practical definition of the m^{th} sample of the signal $f(t)$.

Since $R_{f\varphi}(n\alpha)$ are readings of the correlation function of the signal $f(t)$ and the function $\varphi_0(t)$ one can write

$$R_{f\varphi}(n\alpha) = \sum_{k=-\infty}^{\infty} f(k\alpha)\varphi_0[(k-n)\alpha].$$

One can get

$$f(m\alpha) =$$

$$= \frac{1}{E_\varphi}\sum_{n=-\infty}^{\infty}\sum_{k=-\infty}^{\infty} f(k\alpha)\varphi_0[(k-n)\alpha]\varphi_0[(m-n)\alpha].$$

Let's introduce the replacement $l = k - n$ ($n = k - l$) and one can obtain

$$f(m\alpha) = \frac{1}{E_\varphi}\sum_{l=-\infty}^{\infty}\sum_{k=-\infty}^{\infty} f(k\alpha)\varphi_0[l\alpha]\varphi_0[(l+m-k)\alpha] =$$

$$= \frac{1}{E_\varphi}\sum_{k=-\infty}^{\infty} f(k\alpha)\sum_{l=-\infty}^{\infty}\varphi_0[l\alpha]\varphi_0[(l+m-k)\alpha].$$

One takes into account that

$$\sum_{l=-\infty}^{\infty} \varphi_0[l\alpha]\varphi_0[(l+m-k)\alpha] = R_\varphi[(m-k)\alpha],$$

where $R_\varphi[(m-k)\alpha]$ – samples of the correlation function of the elementary signal $\varphi_0(t)$, taken at times $(m-k)\alpha$, and one will get

$$f(m\alpha) = \frac{1}{E_\varphi} \sum_{k=-\infty}^{\infty} f(k\alpha) R_\varphi[(m-k)\alpha]. \quad (10)$$

Let's introduce the replacement $n = m - k$ ($k = m - n$) and one can obtain

$$f(m\alpha) = \frac{1}{E_\varphi} \sum_{n=-\infty}^{\infty} f[(m-n)\alpha] R_\varphi(n\alpha). \quad (11)$$

For this equality to be an identity, it is necessary that for all $n \neq 0$ the readings of the correlation function $R_\varphi(n\alpha) = 0$.

Using the formulated requirement for the correlation function $R_\varphi(n\alpha)$, one can transform the right side of equality (11)

$$\frac{1}{E_\varphi} f(m\alpha) R_\varphi(0) = \frac{1}{E_\varphi} f(m\alpha) E_\varphi = f(m\alpha)$$

and conclude that (11) is an identity.

Take a note that from the point of view of linear transformations, equality (11) is a linear discrete transformation with a reproducing kernel. The transformation kernel is the expression $R_\varphi[(m-k)\alpha]$.

Expression (11) gives reason to believe that the series, which coefficients are signal samples, should be built only using functions that have the character of equidistantly biased correlation functions of the impulse responses of linear systems:

$$f(t) = \frac{1}{E_\varphi} \sum_{k=-\infty}^{\infty} f(k\alpha) R_\varphi(t - k\alpha). \quad (12)$$

Take into account that this expression agrees with the sampling theorem. Indeed, the correlation function of the function

$$\varphi_0(t) = \frac{\sin \omega_m t}{\omega_m t}$$

equals

$$R_\varphi(\tau) = \int_{-\infty}^{\infty} \frac{\sin \omega_m t}{\omega_m t} \frac{\sin \omega_m (t-\tau)}{\omega_m (t-\tau)} \mathrm{d}t = \frac{\sin \omega_m \tau}{\omega_m \tau}. \quad (13)$$

Substituting (13) into (12) leads to the eminent sampling theorem.

Let's expand the signal $f(t)$ in a series of orthogonal functions

$\varphi_n(t) = \varphi_0(t - n\alpha) = R_\varphi(t - n\alpha)$

such that $R_\varphi(0) \neq 0$ and $R_\varphi(n\alpha) = 0$, if $n\alpha \neq 0$.

Let's consider that the modulus of the spectral density of the signal $f(t)$ is equal to the modulus of the spectral density of the functions $R_\varphi(t - n\alpha)$.

One can get

$$f(t) = \sum_{n=-\infty}^{\infty} y_n R_\varphi(t - n\alpha). \quad (14)$$

Let us determine the coefficient of the series y_m

$$y_m = \frac{1}{E_R} \int_{-\infty}^{\infty} f(t) R_\varphi(t - m\alpha) \mathrm{d}t = \frac{1}{E_R} R_{fR}(m\alpha), \quad (15)$$

where $E_R = \int_{-\infty}^{\infty} R_\varphi^2(t - n\alpha) \mathrm{d}t$,

$R_{fR}(m\alpha)$ – m^{th} count of the cross-correlation function of the signal and the function $R_\varphi(t)$.

Expression (14) can be written as

$$f(t) = \frac{1}{E_R} \sum_{n=-\infty}^{\infty} R_{fR}(n\alpha) R_\varphi(t - n\alpha).$$

Let us determine the m^{th} sample of the signal $f(t)$

$$f(m\alpha) = \int_{-\infty}^{\infty} f(t) \delta(t - m\alpha) \mathrm{d}t =$$

$$= \frac{1}{E_R} \int_{-\infty}^{\infty} \sum_{n=-\infty}^{\infty} R_{fR}(n\alpha) R_\varphi(t - n\alpha) \delta(t - m\alpha) \mathrm{d}t.$$

Using the filtering property of the delta function, one can get

$$f(m\alpha) = \frac{1}{E_R} \sum_{n=-\infty}^{\infty} R_{fR}(n\alpha) R_\varphi[(m-n)\alpha].$$

Taking into account the specified properties of the function $R_\varphi(t)$, one will obtain

$$f(m\alpha)=\frac{1}{E_R}R_{fR}(m\alpha)R_\varphi(0)=R_{fR}(m\alpha).$$

Thus, the coefficients y_m are signal samples $f(t)$, taken at times multiple of α, and a series (14) can be rewritten as

$$f(t)=\sum_{n=-\infty}^{\infty}f(n\alpha)R_\varphi(t-n\alpha). \quad (16)$$

Let's return to (15). One can rewrite (15) taking into account (14)

$$y_m=\frac{1}{E_R}\int_{-\infty}^{\infty}\sum_{n=-\infty}^{\infty}y_nR_\varphi(t-n\alpha)R_\varphi(t-m\alpha)\mathrm{d}t.$$

Replacing the expression $\tau = t - n\alpha$ and changing the order of summation and integration allows to write down

$$f(m\alpha)=\frac{1}{E_R}\sum_{n=-\infty}^{\infty}y_n\int_{-\infty}^{\infty}R_\varphi(\tau)R_\varphi(\tau+n\alpha-m\alpha)\mathrm{d}\tau.$$

Under the integral sign in this equality there is the value of the correlation function $R_{2\varphi}(t)$ of the function $R_\varphi(t)$, determined at the time $t = n\alpha - m\alpha$. One can write down.

$$f(m\alpha)=\frac{1}{E_R}\sum_{n=-\infty}^{\infty}y_nR_{2\varphi}(n\alpha-m\alpha).$$

In order to $y_m = f(m\alpha)$, it is necessary to impose conditions on the values of the correlation function $R_{2\varphi}(n\alpha)$, similar to the conditions adopted for the values of the correlation function $R_\varphi(n\alpha)$. That is,

$$R_{2\varphi}(0)\neq 0 \text{ and } R_{2\varphi}(n\alpha)=0, \text{ if } n\alpha\neq 0.$$

It should be noted that for functions $R_{2\varphi}(t)$ and $R_\varphi(t)$, that can be secured physically (for example, as correlation functions of the impulse responses of linear physically realizable systems), these requirements are met with a certain error (**Fig. 1**). In addition, the system of functions obtained by biasing the correlation function by time intervals multiple of α is not orthogonal. Therefore, series (16) describes the signal approximately.

Thus, in order to approximately restore the signal from its samples, it is necessary to apply samples to two cascade filters, one of which has

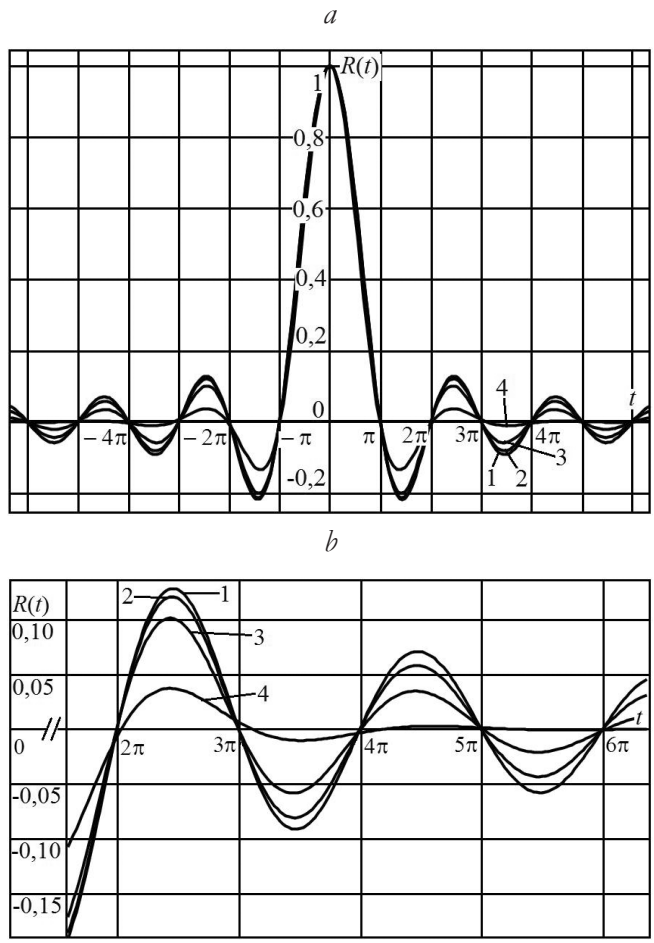

1 – function sin*ct*; normalized correlation functions of impulse characteristics of the normalized low-pass Butterworth filter: 2 – 20th order; 3 – 10th order; 4 – 4th order.

Fig. 1. *The function* sin*ct and normalized correlation functions of impulse characteristics of the normalized low-pass Butterworth filter.*

an impulse response $g(t)$, and the second one is consistent with this impulse response, and the correlation function of the impulse response is equal to $R_\varphi(t)$.

The shift interval of equidistant functions, according to which the signal is decomposed (it is the very discretization interval) is chosen based on the given value of the mean square error (2) of the approximation $f(t)$ in series.

In addition, the shift interval of equidistant functions can be chosen taking into account the periodicity of the discrete signal spectrum. The period of the spectrum is related to the upper

frequency of the signal spectrum taken into account, i.e. with the upper considered cutoff frequency of the filter which impulse responses are considered [10,11,12].

3. CONCLUSION

In order to approximately restore the signal from its samples, it is necessary to apply samples to two cascade filters, one of which has an impulse response $g(t)$, and the second is consistent with this impulse response. The correlation function of the impulse response must have a correlation function $R_{2\varphi}(t)$, the one that $R_{2\varphi}(0) \neq 0$ and $R_{2\varphi}(n\alpha) = 0$, if $n\alpha \neq 0$.

Since in practice it is impossible to implement filters with similar impulse responses, the signal recovery will occur with some error. This error can be reduced by choosing the appropriate reconstruction filter order and sampling interval.

REFERENCES

1. Zyuko AG, Klovski DD, Korjik VI, Nazarov MV. *Teoriya elektricheskoi svyazi* [Theory of electrical communication]. Moscow, Radio i svyaz' Publ., 1999, 432 p.
2. Kusaykin DV. Issledovanie metodov vosstanovleniya diskretnych signalov s neravnomernoy schastotoy discretizazii v sistemah telecommunicaziy [Study of methods for restoring discrete signals with non-uniform sampling rate in telecommunication systems]. *Coll. of abstracts of the VII All-Russian Scientific and Practical Conference "Information technologies in the world of communications*". Moscow, 2014, p. 153-159 (in Russ.).
3. Kusaykin DV. Issledovanie metodov vosstanovleniya schastotno modulirovfnnyh signalov, zadannyh na neravnomernoy vremennoy setke [Investigation of methods for restoring frequency-modulated signals set on an uneven time grid]. *Proc. of the International Scientific and Practical Conference "Society, Science and Innovation",* Ufa, Bashkir State University Publ., 2013, 2:71-75 (in Russ.).
4. El-Chammas M, Murmann B. A 12-GS/s 81-mW 5-bit time-interleaved flash ADC with background timing skew calibration. *Proc. Symposium on VLSI Circuits*, 2010, pp. 157-158. DOI:10.1109/JSSC.2011.2108125.
5. Hormati A, Roy O, Lu YM, Vetterli M. Distributed sampling of correlated signals linked by sparse filtering: Theory and applications. *IEEE Trans. Signal Process*, 2010, 58(3):1095-1109.
6. Karthik M, Prabhu KM. On the Eigenvalues of Matrices for the Reconstruction of Missing Uniform Samples. I*EEE Transactions on signal Processing,* 2010, 58(5):2896-2900.
7. Leming Qu, Routh PS, Anno PD. Wavelet Reconstruction of Nonuniformly Sampled Signals. *IEEE signal processing letters*, 2009, 16(2):73-76.
8. Qu D, Ma B, Zhou J. Optimal Weighted Periodic Nonuniform Sampling Sequences for Digital Alias-free Signal Processing. *Proc. IEEE 10th International Conference "Signal Processing (ICSP)"*, 2010, p. 147-150.
9. Saleem S, Vogel C. Adaptive Blind Background Calibration of PolynomialRepresented Frequency Response Mismatches in a Two-Channel Time-Interleaved ADC. I*EEE Transactions on Circuits and Systems I: Regular Papers.* 2011, 58(6):1300-1310.
10. Senay S. Signal reconstruction from Nonuniform samples using prolate spheroidal wave functions: theory and application. *PhD thesis*. University of Pittsburgh, 2011, p. 117.
11. Senay S, Chaparro LF, Durak F. Reconstruction of nonuniformly sampled timelimited signals using prolate spheroidal wave functions. *Signal Processing,* 2009, 89(12):2585-2595.
12. Singh M, Lu C, Basu A, Mandal M. Choice of low resolution sample sets for efficient super-resolution signal reconstruction. *Journal of*

Visual Communication and Image Representation, 2012, 23(1):194-207.

13. Porschnev SV, Kusaykin DV. Metody povyscheniya totchnosti vosstanovleniya neravnomerno deskritizirovannyh signalov pri neizvestnyh znacheniyah koordinat uzlov vremennoy setki [Methods for improving the accuracy of recovery of unevenly sampled signals with unknown values of the coordinates of the nodes of the time grid]. *Bulletin of Siberian State University of Telecommunications and Informatics*, 2014, 1:24-34 (in Russ.).
14. Porschnev SV, Kusaykin DV. O vosstanjvlenii neravnomerno deskritizirovannyh signalov s neizvestnymi znacheniyami koordinat uzlov vremennoy setki [On the restoration of unevenly sampled signals with unknown values of the coordinates of the nodes of the time grid]. *Uspekhi sovremennoy radioelektroniki* [The successes of modern radio electronics], 2015, 6:3-35 (in Russ.).
15. Porschnev SV, Kusaykin DV. Ozenka totchnosti algoritmov vosstanovleniya diskretnych signalov, zadannyh na neravnomernoy vremennoy setke s totchno neizvestnymi znacheniyami koordinat uzlov [Estimation of the accuracy of algorithms for the recovery of discrete signals given on an uneven time grid with exactly unknown values of node coordinates]. *Bulletin of Siberian State University of Telecommunications and Informatics,* 2015, 1:97-108 (in Russ.).

DOI: 10.17725/j.rensit.2024.16.011

Computational Dielectric Metasurfaces in Photonic Topological Devices for Multidimensional Signal Processing

Alexander A. Potapov
Kotel'nikov Institute of Radioengineering and Electronics of RAS, http://www.cplire.ru/
Moscow 125009, Russian Federation
Jinan University, JNU-IREE RAS Joint Laboratory of Information Technology and Fractal Processing of Signals, https://jnu.edu.cn/
Guangzhou 510632, China
E-mail: potapov@cplire.ru

Received September 29, 2023, peer-reviewed October 02, 2023, accepted October 09, 2023, published March 15, 2024.

Abstract: **A single-layer computational dielectric broadband metasurface (MS) with silicon nanodiscs is proposed to implement spatial differentiation and contour recognition operations. The variety of physical mechanisms of dielectric MSs for performing similar mathematical operations is considered. The necessity of such computational nanostructures for improving the numerous methods of topological texture-fractal processing of signals and fields in modern radio physics and radio electronics is revealed.**

Keywords: **photonics; radio photonics; nanotechnology; radiophysics; radar; radio engineering; texture; fractals; processing of multidimensional signals; frontier optics; computing metasurface; optical transfer function; optical analog computing**
UDC 519.24+ 537.86+621.396.96
Acknowledgments: The research has been performed in the framework of the state task for IRE RAS, theme "Aether-2". The author expresses sincere gratitude to the Chinese scientists with whom articles on photonics were jointly completed and published in leading international scientific journals: Weiping Liu, Tianhua Feng, Lei Wan, Danping Pan, Min Ouyang, Zixian Liang, Zhaohui Li , Shuaifeng Yang, Xia Wu, Yi Xu, Ning Lai, Weilian Chen, Fugen Wang, Wei Zhang.
For citation: Alexander A. Potapov. Computational Dielectric Metasurfaces in Photonic Topological Devices for Multidimensional Signal Processing. *RENSIT: Radioelectronics. Nanosystems. Information Technologies*, 2024, 16(1):11-30e. DOI: 10.17725/j.rensit.2024.16.011.

Contents

1. INTRODUCTION

There are two main types of imaging technologies – digital and optical. Optical image processing is a technology that uses optical means and devices to perform analog computational processing and transmit image information. Optical image processing is characterized by the ability to process in real time up to the speed of light. At the same time, optical analog computing has natural parallel characteristics. Digital imaging actually uses a set of digital matrices to objectively depict objects. Digital image processing is also called computer image processing, but usually must be combined

with software algorithms and hardware co-processing. However, this technology has disadvantages: high hardware requirements and relatively low speed. In addition, the speed and power consumption of standard electronic components are difficult to significantly improve. Thus, research into new photonic devices provides a potential way to overcome these limitations.

The rapid development of nanotechnology has promoted scientific research and industrial applications of micro-nanostructures. The optical properties of micro-nanostructures have become one of the hot spots of research in the field of frontier optics, which has led to the emergence of new disciplines such as nanophotonics, surface plasmon optics, metasurface, metamaterial optics, transformation optics, topological photonics, non-Hermitian optics, etc.

This introduction is necessary in order to show that the continuous improvement of numerous methods of topological texture-fractal processing (TTFP) of signals and fields, first proposed by the author in the IRE AS USSR, starting from the 80s of the 20th century, in modern radiophysics and radio electronics [1-9] implies a natural need to improve the speed of information processing and the search for new physical principles for its implementation. Here, undoubtedly, the future belongs to the most characteristic photonic and radiophotonic technologies discussed below. Compared with traditional bulky optical analog differentiators, spatial differentiators based on metasurfaces (MS) have the advantage of being simpler and more compact. Thus, modern optical analog computing can contribute to the development of image processing technology in conjunction with electronic platforms.

The article also presents selected results in the field of photonics, radio photonics and optical 2D metamaterials (MM), which were obtained by the author with Chinese scientists in the joint laboratory of information technology and fractal signal processing in China [10-17] for the period 2019-2021.

2. SEVERAL DEFINITIONS

Let us recall several definitions necessary in the text. Photonics is a discipline dealing with fundamental and applied aspects of working with optical signals, as well as the creation of various devices based on them; or another way: photonics is a branch of science that studies systems in which photons are information carriers. Nanophotonics is a branch of photonics that examines the complex interactions between light and matter on a subwavelength scale. Photonic systems (compared to "electronic") are not subject to external electromagnetic fields, are more resistant to interference, and also have higher speed and signal bandwidth. Radio photonics (microwave photonics) is a complex of fields of science and technology related to the transmission, reception and conversion of signals using electromagnetic waves in the microwave range and photonic devices and systems. Radio-photonic methods will improve the functional design of new generation equipment, eliminate many problems of electromagnetic compatibility, increase the speed and volume of information transfer by a thousand or more times, and reduce weight, dimensions and energy consumption by an order of magnitude.

Metamaterials (from the Greek μετα - *beyond, outside*) are artificially structured (man-made) materials with unusual properties that are absent in natural materials [18]. Metamaterials (MM) and metasurfaces (MS) or 2D metamaterials have opened up vast opportunities for realizing new electromagnetic properties and functionalities through the creation of subwavelength structures and the integration of functional materials.

All MSs can be divided into two types: a *scattering* type based on metal nanomaterials and a *transmitting* type based on nanostructures of dielectric materials. Let's define *computing metasurfaces* as two-dimensional artificial nanostructures that are capable of performing mathematical operations on the input electromagnetic field, including its amplitude, phase, polarized and frequency distributions [15,19]. Computational MSs have demonstrated remarkable capabilities in optical differential operations and edge-enhanced imaging. The most common are MMs in which the structure of elements (*meta-atom*s several nanometers in size), size and distance between elements are significantly smaller compared to the wavelength of the exciting field. In this case, the result of the interaction of individual elements leads to the fact that the properties of the MM are determined not so much by the properties of its constituent elements, but by the artificially created periodic structure. MSs, as a typical prototype device, consist of artificial subwavelength structures over flat dielectric material surfaces that facilitate flexible control of the amplitude, phase, and polarization of electromagnetic waves. It can be said that MS is the *root of many fascinating topological phenomena in physics and exotic wave manipulations*.

Note [20] that China has a special government program and in 2015 China became the world leader in the production of photonics devices.

3. PHYSICS AND DESIGN OF BASIC COMPUTING MP

MM-inspired structures continue to challenge our imagination and our physics and engineering foundations. They influence the interaction of wave and matter at many frequencies and even in various fields of science and technology.

The concept of computational metamaterials was first introduced in 2014 in [21]: computational metamaterials are metamaterials that can perform desired mathematical operations on arbitrary waveforms as they propagate through it.

Here we will limit ourselves to physics and elementary mathematics exclusively of computational MSs. By designing the geometry of dielectric MSs, optical analog computing devices with various functions, such as spatial differentiators [11,12,15,16,19,21-24], integrators [25] and equation solvers [26,27] can be obtained. The introduction of dielectric MSs simplifies the manufacturing process and increases the design flexibility of optical analog computing devices compared to traditional multilayer film structures [24]. Despite the enormous interest in MS and the presence of a large number of English-language reviews, this issue is practically not covered in the Russian-language literature, with rare exceptions [28,29]. This work, followed by a presentation of our own results, partially fills this gap.

The main parameters of MSs, by which they are compared with each other and with other optical devices, are efficiency and operating wavelength (see, for example, [28]). An electromagnetic wave hitting the MS is partially absorbed and scattered in different directions, and only part of this wave is scattered in the desired direction. The ratio of the intensity of the electromagnetic wave, which propagates in the desired direction after passing through the MS, to the intensity of the incident wave is called the efficiency of the MS. The operating wavelength of MSs is decreasing as technology develops, and currently it is in the visible range. Since the resonances in meta-atoms are quite narrow, MSs operate in a small frequency range, which they try to increase.

Classical processing of optical signals, the so-called Fourier optics (or radio optics) using conventional lenses and spatial filters is

well known [30-32]. This type of processing was widely used by the author back in the 80-90s. XX century together with scientists from Voronezh State University to study all ensembles of textural features of optical and first radar (in the millimeter wave range) images of land covers with objects [33-36].

Typically, a modulated light beam is targeted to an optical lens, which can perform a Fourier transform (FT); thus, the Fourier spectrum can be obtained at the back focal plane. Since edge information is represented by high-order Fourier components that are typically outside the domain of the Fourier pattern, by carefully selecting these high-order components, edge information can be extracted. Finally, real images containing the contour profile can be obtained using the Inverse Fourier Transform (IFT) using a different optical lens. Since all operations are performed as light travels, optical analog computing processes are much faster and consume much less power than the electronic method. Although the above-mentioned optical analog calculations of spatial differentiation and edge detection are simple and straightforward, the large lens size is a critical issue for device integration. In optical lenses, the required wavefront is formed when radiation passes through a substance with a certain refractive index. The passage of rays through the lens leads to a phase shift, and due to the continuous change in the thickness of the lens, the phase acquires a gradient. According to Fermat's principle, the phase gradient leads to a change in the wavefront.

The use of scattering and transmitting MMs for optical analog computing paves the way for the implementation of fully integrated spatial filtering devices. The basic configuration is shown in **Fig. 1** [15,21]. In this process, a two-dimensional gradient index (GRIN) dielectric slab was used to perform FT and output the Fourier spectrum. The required information was selected by an appropriately designed MM as a spatial filter, and IFT was implemented using another MM with a gradient index. As the first block, we consider a dielectric plate GRIN(+) with a two-dimensional gradient index, magnetic permeability $\mu = \mu_0$ and parabolic change in dielectric constant $\varepsilon(y) = \varepsilon_0[1 - (\pi/2L_g)^2 y^2]$, where ε_0 is the dielectric constant in the central plane GRIN, and L_g is the characteristic length.

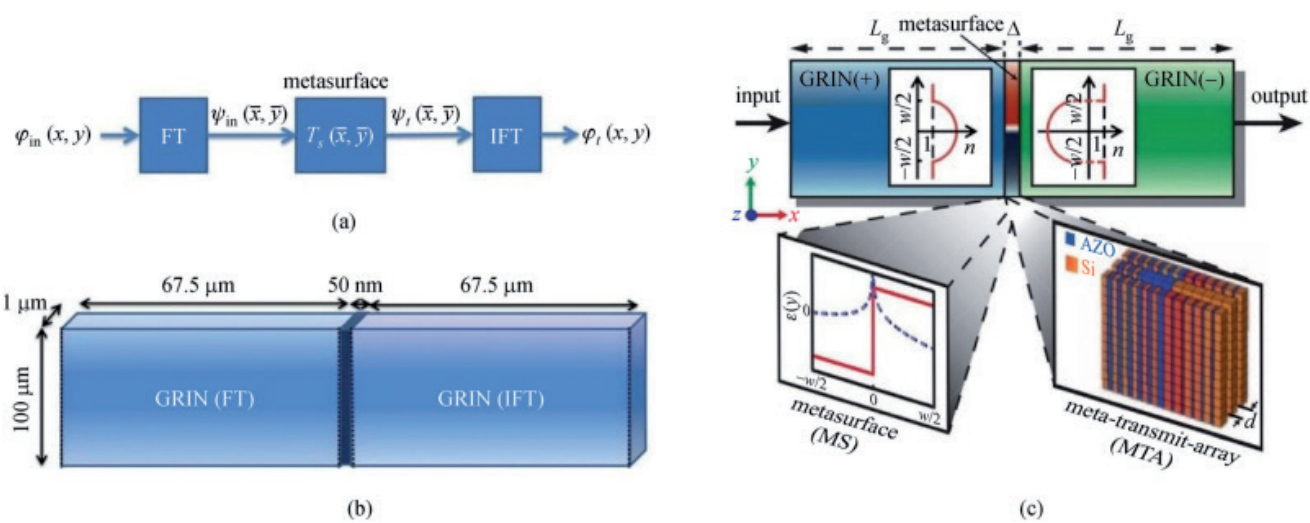

Fig. 1. *The basic principle of spatial differentiation and recognition of MM and MS contours. (a) Information about the Fourier spectrum of the input signal can be obtained by a block with a Fourier transform (FT) function. After passing through the MP, the output signal can be obtained using an inverse Fourier transform (IFT) operation. (b) Gradient index MM (GRIN) can be used to implement FT and IFT* [37]. *(c) Practical implementation of the configuration* [21].

In Fig. 1*c* GRIN(+) denotes normal GRIN, where the (+) sign refers to positive dielectric constant values. In the paraxial approximation, the GREEN(+) plate operates as a Fourier transformer at the "focal" distance Lg along the propagation direction. For the inverse Fourier transform, i.e. GRIN(–) block, the ideal GRIN structure with negative parameters is used: permittivity $\mu = -\mu_0$ and dielectric constant $\varepsilon = -\varepsilon(y)$. Following the concept of complementary materials, GRIN(-) has the opposite functionality compared to GRIN(+); those. it acts as an inverse Fourier transform. A thin, properly designed metastructural screen of thickness $\Delta = \lambda_0/3$ and width $W = 10\lambda_0$, placed between two GRIN structures with positive and negative parameters, can perform mathematical operations in the Fourier domain. GRIN(+) and GRIN(–), each of length $L_g \approx 12\lambda_0$, act as Fourier transforms and inverse Fourier transforms. Two MM designs are proposed: a thin MS formed by a single layer with specified dielectric and magnetic permeabilities [inset on the left, with the real (red) and imaginary (blue) parts of the material parameters] and a realistic metatransmission array (MTA) formed by three layers of two alternating materials (silicon Si and aluminum-doped zinc oxide AlZnO) with a correctly specified non-uniform distribution of their filling volume fractions and with the necessary losses to impart the desired attenuation (right inset). This system forms a computational unit MM that can perform selective mathematical operations on the input function as the wave propagates through the system. In [21], approaches to modeling the operations of differentiation and convolution are considered.

Another method for spatial differentiation and edge detection is the Green's function (GF) method [15,21]. Using this method, no Fourier transforms are required, further minimizing the size of the entire system. The critical point when using the GF method is to achieve a certain optical transfer function (OTF) $T(k_x, k_y)$ with properly designed MSs. Typically, when an incident modulated light field $E_{in}(x, y)$ hits a planar structure, both reflection and transmission exhibit polarization dependence. Therefore, the OTF of an MS can be expressed using a 2×2 matrix that relates the input and output fields as follows:

$$\begin{bmatrix} \tilde{E}^{(s)}(k_x, k_y) \\ \tilde{E}^{(p)}(k_x, k_y) \end{bmatrix} = \begin{bmatrix} T_{ss}(k_x, k_y) & T_{sp}(k_x, k_y) \\ T_{ps}(k_x, k_y) & T_{pp}(k_x, k_y) \end{bmatrix} \begin{bmatrix} \tilde{E}_{in}^{(s)}(k_x, k_y) \\ \tilde{E}_{in}^{(p)}(k_x, k_y) \end{bmatrix} \quad (1)$$

In expression (1) k_x and k_y are components of the wave vector k, two polarizations of *s*- and *p*-waves are considered and the polarization transformation with non-diagonal terms of the OTF matrix is taken into account. Therefore, by intelligently tuning the MS, we can obtain a proper OTF that can realize the desired processing or operation on the input information for specific applications. In fact, the diffraction of light is more significant at the edges of the target, resulting in higher in-plane wavenumbers. This means that if we can achieve the OTF to transmit these higher wavenumber components while blocking the lower wavenumber components, then we can only have edge information at the output, leading to the implementation of spatial differentiation and edge detection. Note that in optics and electrodynamics, an *s*-polarized wave (German senkrecht – perpendicular) has an electric field vector *E* perpendicular to the plane of incidence. The *s*-polarized wave is also called *σ*-polarized, sagittally polarized, *E*-type wave, TE (Transverse Electric) wave. A *p*-polarized wave (lat. parallel – parallel) has an electric field vector *E* parallel to the plane of incidence. A *p*-polarized wave is also called a *π*-polarized, in-plane polarized, *H*-type, or TM (Transverse Magnetic) wave.

The key to the GF method is to design specific MS OTFs so that the input light field can be processed appropriately. For first-order spatial differentiation, we assume that

the incident light field includes a plane wave vector along the *x*-direction. The relationship between output and input fields can be expressed as [38]:

$$\tilde{E}(k_x) = \frac{d}{dx}\tilde{E}_{in}(k_x) = ik_x\tilde{E}_{in}(k_x), \quad (2)$$

where the incident light field is assumed to be $\tilde{E}_{in}(k_x) = E_0 e^{ik_x x}$. Therefore, the OTF must be a linear function of the in-plane wavenumber. For second-order spatial differentiation, the OTF can be obtained in a similar way:

$$\tilde{E}(k_x) = \frac{d^2}{dx^2}\tilde{E}_{in}(k_x) = -k_x^2\tilde{E}_{in}(k_x). \quad (3)$$

This indicates that the OTF should behave like a parabola. Note that in both cases the intensity of the output light field is closely related to the wavenumber. Both OTFs must transmit incident light fields of higher wavenumbers while suppressing fields of lower wavenumbers, thereby enabling detection of image edges.

To develop a proper OTF for spatial differentiation and edge detection of images, adapting the non-local effects of MS is a promising method. In the nonlocal effect, the MS responses to the incident light field are not only related to the normal component of the incident wave, but also depend on the tangential components. This means that the transmission, reflection and SPF of the MS depend on the angle of incidence of the light field. This dependence of the OTF on the angle of incidence is usually created by tuning MT resonances, which typically include guided mode resonance (GMR), Fano resonance, multipole resonance (electric or magnetic dipole), etc. GMR is a unique type of resonance that can be highly limited in structures, but at the same time has a weak connection with external radiation [39]. Compared with the traditional waveguide wave, GMR is usually accompanied by a limited but high quality factor. Moreover, its resonant frequency and quality factor significantly depend on the in-plane wave vector. As another important type of resonance, Fano resonances have been demonstrated on various platforms [40]. Fano resonances arise from the interference of two wave channels, which typically have a narrow and a wide bandwidth. In particular, the narrow-bandwidth resonance that is determined by the structures provides a universal degree of tuning freedom for Fano resonances.

In addition to the two kinds of resonances described above, multipole resonances of dielectric nanoparticles also provide a promising route for tuning the oscillation properties of MSs [11,41]. Compared with plasmonic structures, dielectric nanostructures can not only solve the loss problem and improve the operating efficiency of MSs, but also facilitate the control of light scattering and propagation (**Fig. 2**). The electric and

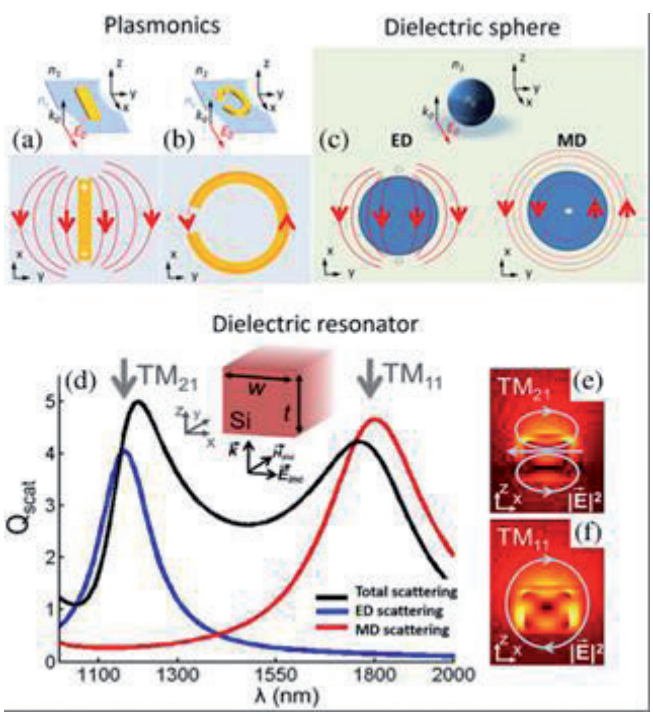

Fig. 2. *Schematic representations of electric fields in (a, b) plasmonic resonators and in (c) dielectric sphere. Plasmonic rod antennas support only electrical resonances with negligible magnetic contribution. Strong magnetic dipole resonance can be achieved in plasmonic particles by forming a metal rod in the form of a split ring resonator* [42,44]. *d) rectangular dielectric nanoparticles also have electrical and magnetic polarizability. Shown are the electric dipole (ED), magnetic dipole (MD) and total scattering cross sections (arbitrary units) associated with the corresponding modes given in (e) and (f)* [43,44].

magnetic dipole resonances of nanostructures offer multiple degrees of freedom for tuning the MS oscillation properties. These types of dielectric MSs are characterized by large spatial bandwidth, and 2D edge detection of images for arbitrary polarization has been successfully demonstrated. Given these advantages, it is believed that dielectric MSs can play an important role in other mathematical operations and optical analog computing. Apart from resonant circuits to realize spatial differentiation and image edge detection, non-resonant schemes such as spin-orbit coupling in Pancharatnam-Berry phase MSs have also been explored to achieve image edge detection [45,46].

The use of dielectric MMs instead of classical plasmonic structures reduces ohmic (thermal) losses and makes it possible to control not only the electrical, but also the magnetic component of the light wave. In other words, due to the free penetration of the electromagnetic field inside the dielectrics, such nanostructures have both electric and magnetic Mie resonance.

4. EXPERIMENTAL RESULTS OF THE MAIN CLASSES OF COMPUTING MS

In this section, we mainly focus on the characteristic analysis and comparison of the built-in spatial differentiators implemented using GMR, Fano resonance and multipole resonance [15]. To begin with, with a two-dimensional array of holes in a dielectric slab, *photonic crystals* can provide almost isotropic second-order differentiation or a mathematical Laplace operation [15,47,48]. In **Fig. 3***a* shows the structure of an optical spatial differentiator device based on a photonic crystal, consisting of a photonic crystal plate and a separate dielectric plate. The Fano resonance can be constructed by interfering with the GMR of the structured plate with the incident wave, allowing the correct OTF to be established for the transfer mode Laplace calculation. In fact, the reflection and transmission properties of MSs depend on polarization. Therefore, it is necessary to consider the influence of polarization on optical analog computing. For a linearly polarized wave, the OTF of a spatial differentiator based on dielectric MSs usually differs between *s*- and *p*-waves. As shown in Fig. 3*b* and 3*c*, the *p*-wave transmission is much lower than the *s*-wave transmission. Depending on the frequency of the light and the choice of transmission or reflection mode, the device implements isotropic filtering of high-pass, low-pass and bandpass frequencies in wavevector space. These filter functions are important for a variety of image

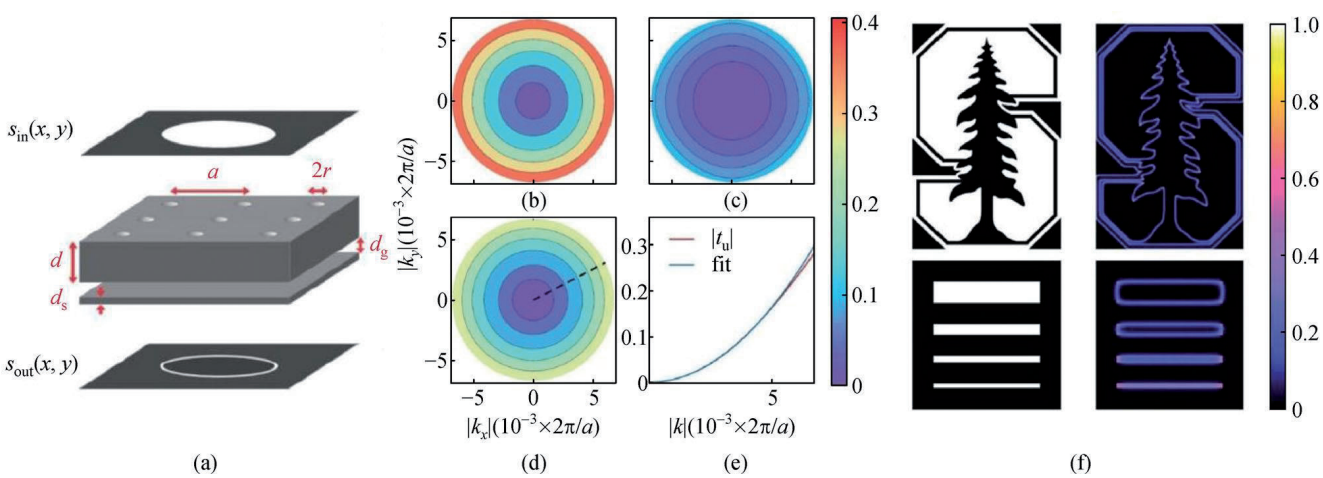

Fig. 3. *Scheme of a second-order isotropic spatial differentiator, implemented in the form of a photonic crystal plate and a separate dielectric plate. (b) SPF of the device for s-wave, (c) p-wave, and (d) unpolarized light. (e) One-dimensional OTF as a function of the wave vector and the corresponding quadratic approximation. (f) Morphology of the Stanford logo and slot patterns (left column) and corresponding edge images (right column)* [47].

processing tasks, including edge detection, anti-aliasing, white noise reduction, and periodic noise reduction or extraction.

However, a spatial differentiator based on a photonic crystal has a small spatial bandwidth (less than 1°) due to its high quality factor. In contrast to the above-mentioned two-layer structure, a single-layer dielectric MS with Fano resonances for first- and second-order spatial differentiators made it possible to expand the range to 17° [49].

The spatial bandwidth can be expanded by developing a non-local MS response. A second-order differentiator with a band of about 40° based on a nonlocal MS with split rings is presented in [25] – **Fig. 4**.

The transmittance properties of the MS were influenced by scattering between unit cells, leading to different transmission curves at different angles of incidence – see Fig. 4*b*. The implementation of the second-order differentiation operation was facilitated by the Fano resonance of the MS. However, the missing edge information along some directions further illustrates the anisotropic optical transmission properties of the spatial differentiator. In terms of device morphology, three-dimensional symmetric or antisymmetric split-ring resonator arrays have increased the complexity of fabrication. Although the proposed nonlocal MSs based on a split-ring resonator array have significantly improved the performance of the spatial differentiator, the implementation of the device configuration must be carefully considered in practical applications.

In addition to the transmission mode, a spatial differentiator based on a dielectric MS can also operate in a reflection mode. In 2020, [50] proposed a first-order spatial differentiator using a dielectric MS, which consisted of an array of silicon square fragments on a gold wafer, as shown in **Fig. 5.**

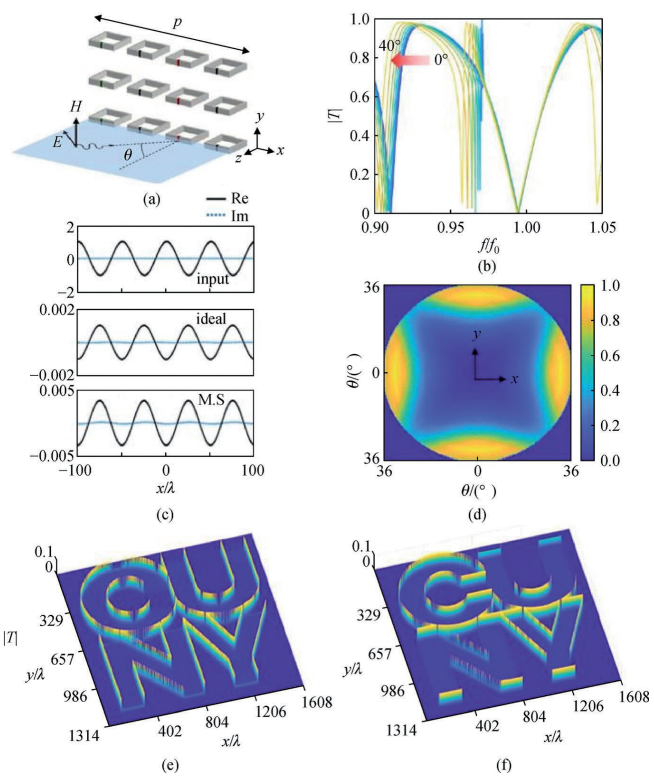

Fig. 4. *(a) Scheme of a second-order spatial differentiator based on nonlocal MSs consisting of open ring resonators. (b) Evolution of the transmittance curves of the MS-based spatial differentiator as the incidence angle increases from 0° to 45°. (c) Results of the ideal d^2/dr^2 operation for a sine wave. (d) 2D OTF of the differentiator as a function of incidence angle. (e) Contour detection results for x-polarized wave and (f) y-polarized wave* [25].

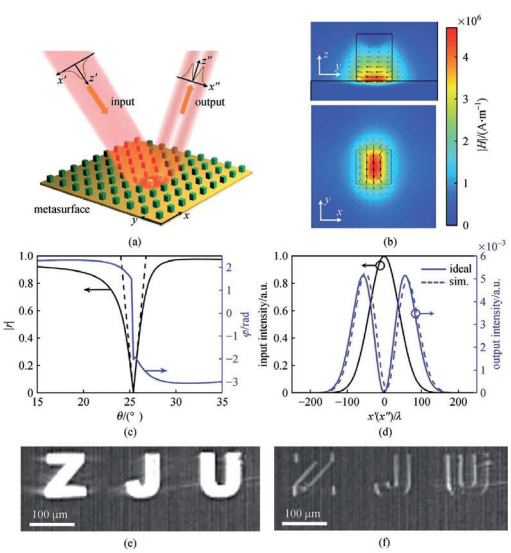

Fig. 5. *Scheme of a first-order spatial differentiator based on a reflective dielectric MS. (b) Magnetic field profiles in the x-z and x-y planes. (c) 1D OTF spatial differentiator corresponding to changes in reflection amplitude and phase upon incident transversely magnetic (TM) polarized light. (d) Output MS intensity curve and theoretically calculated results for the input Gaussoid. (e) Input image – letters "ZJU". (f) Output image of the reflected wave* [50].

An abrupt change in reflectance accompanied by a phase change of π near an incident angle of 25.4° at 1565 nm was achieved, resulting in an OTF for first-order spatial differentiation. In principle, the implementation of the first-order differentiation operation benefits from the hybridization of a localized magnetic resonance mode with a classical modulated grating limited to a surface mode. However, loss of information in the horizontal direction affected edge detection due to polarization dependence.

To reduce the limitations of polarization dependence, a model of polarization-independent MSs based on Fano resonances is presented in [51] (**Fig. 6**).

As shown in Fig. 6, the MS is formed by a single-layer triangular array of holes in the silicon membrane, which induces a strong non-local response in the transverse spatial frequency spectrum. The generation of Fano resonance arose from the coupling between the leaky wave and the longitudinal Fabry-Perot resonance in the lossless MS structure. By optimizing the geometry of the unit cell in dielectric MSs, 2D OTFs were achieved, approaching isotropic transmission for *s*- and *p*-polarized beams within an angle of 8° – Fig. 6*c* and 6*d*. In addition to implementing even-order differentiation, an odd-order isotropic response was also obtained by modifying the MS unit cell to break both transverse and longitudinal mirror symmetry.

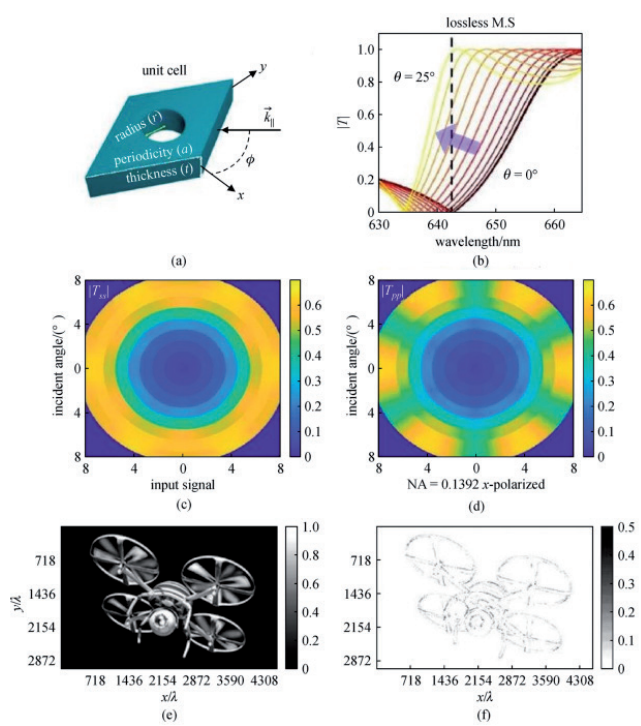

Fig. 6. *(a) Elementary cell of a second-order spatial differentiator based on a hole dielectric MF. (b) Transmission curves of the Fano differentiator as a function of incidence angle from 0° to 25°. 2D OPF devices corresponding to the incidence of an s-polarized wave (c) and a p-polarized wave (d). (f) Output of edge detection (e) of a complex input 2D image under x-polarized light illumination* [51].

As mentioned earlier, spatial differentiation and edge recognition can operate in both transmission and reflection modes. In fact, the transmission mode is preferred in traditional optical systems because the installation is usually more convenient than the reflection mode. Therefore, it is desirable to migrate traditional optical configurations to MM and MT platforms operating in transmit mode. In addition, the transfer type module is more convenient to integrate with other modules, especially in optical imaging systems.

The applicability of spatial differentiators based on dielectric MSs in a real optical imaging system was demonstrated in [52]. To implement the required transfer function, a two-dimensional photonic crystal consisting of cylindrical silicon nanorods embedded in polymethyl methacrylate (PMMA) on a silicon dioxide (SiO_2) substrate was used (**Fig. 7***a,b*). There is also a diagram of a two-dimensional MS and its corresponding image obtained using a scanning electron microscope (SEM). Silicon nanorods have a height of 440 nm, a diameter of 280 nm, and a period of 600 nm. In this structure, the transmittance amplitude was theoretically calculated as a function of frequency and incidence angle along the *G–X* direction ($\varphi = 0$, where φ is the azimuthal angle in the horizontal plane) for s- and p-polarization. It should be noted that for transmitted light there is no polarization conversion. At normal incidence, two broad transmission dips are observed at 244 and 268

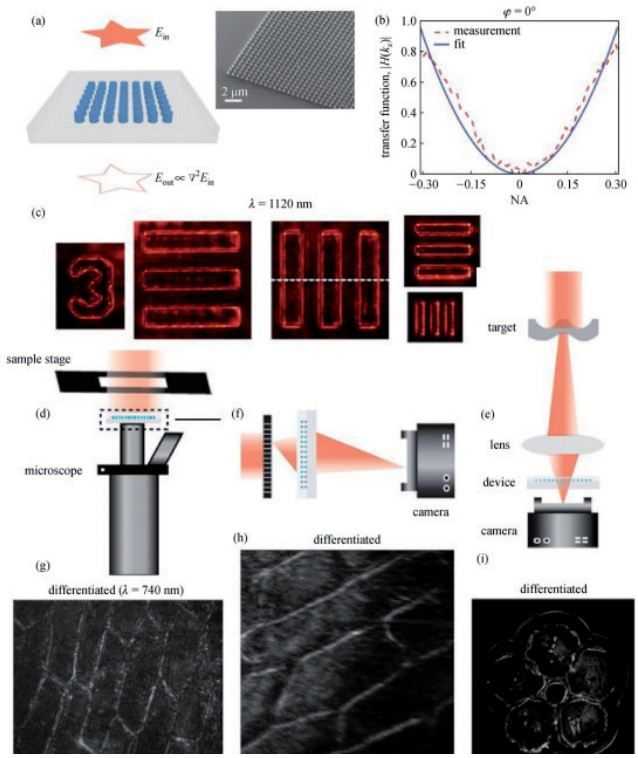

Fig. 7. *(a) Schematic of a second-order spatial differentiator consisting of an array of silicon nanorods and the corresponding SEM image. (b) Measurement results and fitted parabolic 1D ODF curve as a function of numerical aperture (NA). (c) Images of edge recognition using the differentiator test pattern under 1120 nm unpolarized light illumination. Optical path configurations corresponding to differentiators integrated at the front (d) of the objective lens, at the front (e) of a commercial charge-coupled device camera, and at the rear (f) of the metal lens. Target edge images of (g), (h) biological cell and (i) plastic flower shape with 2D spatial differentiator corresponding to three types of optical path configurations* [52].

THz, indicating the presence of two low-Q Mie resonances. Considering the mirror symmetry and reciprocity of the 2D photonic crystal slab in the direction perpendicular to the MP, there was no output signal for *s*-polarized illumination. However, the Fano resonance produced by the quasi-driven mode resulted in a dramatic change in transmittance with increasing angle of incidence for illumination with *p*-polarized light. The one-dimensional OTF $H(k_x)$ was measured along the azimuthal plane $\varphi = 0$ and fitted using a parabolic curve in the numerical aperture (NA) range $nk_x = 0.3$, as shown in Fig. 7*b*. Here n means the refractive index of the dielectric. The MS was experimentally verified using a resolution test chart under illumination with unpolarized and collimated light at a wavelength of 1120 nm ($f = 268$ THz).

The results shown in Fig. 7*c* shows the edge detection result when modulated light passed through the silicon nanorod MS, which illustrates that the spatial detection resolution was less than 4 μm.

Combined with an MS-based spatial differentiator and a practical optical imaging system, three types of optical path configurations based on a commercial microscope and charge-coupled device (CCD) elements were created to obtain the shapes and boundaries of various biological cells and plastic flower shapes, as shown in Fig. 7*d*, 7*e* and 7*f*. By integrating a differentiator on the surface of the objective lens and CCD camera, images of the target edges were clearly visible to demonstrate the feasibility of a compact optical imaging system based on all-dielectric MSs – Fig. 7*g*, Fig. 7*h* and 7*i*. The implementation of a monolithic optical spatial differentiator based on 2D silicon MSs and its integrative applications for imaging systems may pave the way for the development of embedded optical analog computing devices in the field of biological imaging. Additionally, [52] demonstrated how a complete imaging system can be implemented using monolithic planar optics.

5. DEVELOPMENT OF A NEW COMPUTING DIELECTRIC METASURFACE IN THE CHINESE-RUSSIAN LABORATORY OF INFORMATION TECHNOLOGY AND FRACTAL SIGNAL PROCESSING

Optical analog computing using metasurfaces has been the subject of much research aimed at realizing highly efficient and ultra-fast image processing in a compact device. The approaches proposed to date have shown limitations in terms of spatial resolution, overall efficiency, polarization and azimuthal angular dependence. Here we present the design of a

polarization-insensitive metasurface. Our works present a path to realizing high-performance optical MSs that perform isotropic and polarization-insensitive edge detection on an arbitrary 2D image [11,12,15,16].

The basic configuration for optical analog spatial differentiation computations with dielectric MS is shown schematically in **Fig. 8**. Information about the boundary between homogeneous regions of high contrast will be taken into account by wave vector components deviating from the normal z direction due to diffraction. If the spatial dispersion of the MS is properly designed, such wave vector components can pass through the MS with high efficiency, while at low angles of incidence, considering homogeneous regions of modulated light, the MS will be blocked, leading to the implementation of spatial differentiation and then edge detection object.

As an example, consider an MS consisting of silicon nanodisks with a radius and height of 92 nm and 150 nm, respectively. Such nanodisks are located in a square lattice with a period of 350 nm and are embedded in a homogeneous medium with a refractive index of 1.45. The transmission spectrum of a normally incident plane wave is calculated by the finite element method (COMSOL Multiphysics 5.3*a*) and is shown in **Fig. 9***a*. Two resonances are visible, corresponding to two transmission dips around $\lambda = 630$ nm and $\lambda = 710$ nm, respectively.

To find out the nature of resonances, we use multipole decomposition technology for analysis. The results are presented in Fig. 9*b* and show that the two resonances are an electric dipole resonance at a shorter wavelength and a magnetic dipole resonance at a longer wavelength, respectively. To investigate the spatial dispersion of the two resonances, we calculated the *s*-wave transmission spectra at different incident angles along the *x*-direction, which are also shown in Fig. 9*a*. As the angle of incidence increases, the dip at $\lambda = 630$ nm shifts toward a longer wavelength, and at $\lambda = 710$ nm it remains virtually unchanged. Such properties

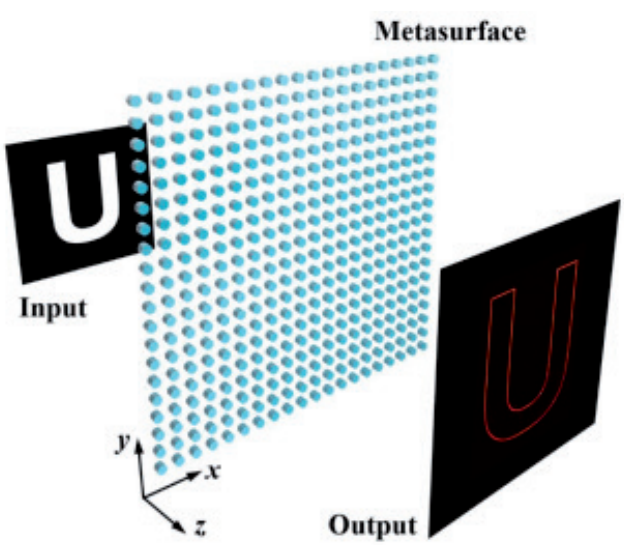

Fig. 8. *Optical analog computing scheme for 2D spatial differentiation and edge detection using MS. The 2D image of the symbol U is the input, and the incident light along the z direction will be modulated so that it passes through the white region while it is blocked by the black region. When a modulated light field passes through the MS, the U symbol outline profile will be shown in the output image* [11].

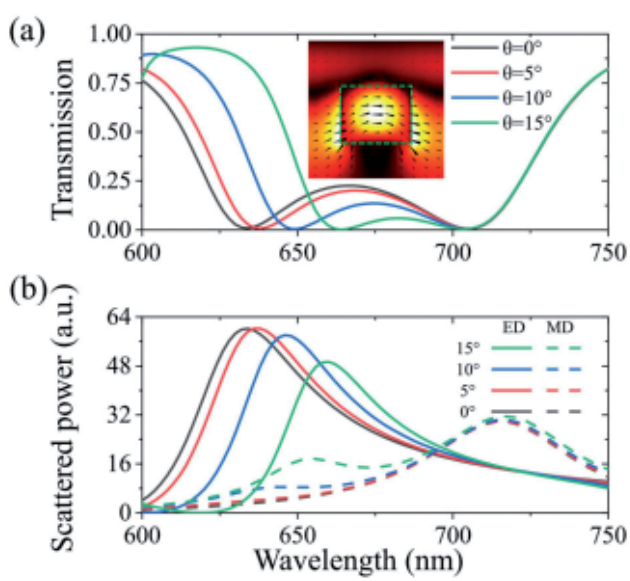

Fig. 9. *(a) MS transmission spectrum for the s-wave and different angles of incidence θ. Inset: electric field magnitude at 630 nm for normal incidence. Arrows indicate the direction of the field. (b) Multipole decomposition results showing that resonances at shorter wavelengths correspond to electric dipole (ED) resonances (solid lines), while longer wavelengths correspond to magnetic dipole (MD) resonances (dashed lines). Y axis – dissipated power* [11].

can also be determined using the results of multipole analysis – Fig. 9*b*.

In fact, the shift of the electric dipole resonance with increasing incidence angle θ provides the main mechanism for spatial differentiation and edge detection. For example, assuming that the wavelength of the modulated light field is 630 nm, higher throughput can be obtained for a larger incident angle, which contains spatial variation information that can be collected after light passes through the MS. To explicitly represent the properties, we show in **Fig. 10***a* transmission as a function of the angle of incidence, namely the OTF $H(k_x)$ at a wavelength of 630 nm. You can see that this looks like a parabolic line shape. It should be noted that the incidence angle can be up to 15°, and the corresponding numerical aperture is about 0.37, indicating a larger spatial bandwidth compared to most previous works. This bandwidth can provide a spatial resolution of 1.93λ. Meanwhile, the maximum transmittance is about 90% at $\theta = 15°$, which can ensure good output signal-to-noise ratio.

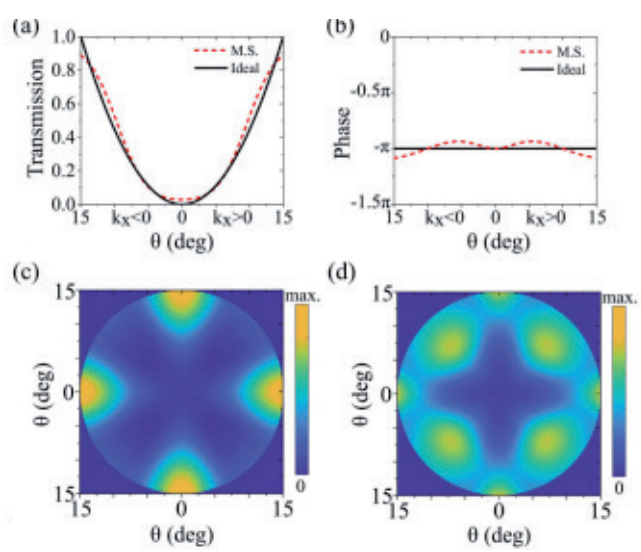

Fig. 10. *(a) RFT along the x-direction for both the MS (red dotted line, M.S.) and the ideal (black solid line) case at 630 nm. (b) Corresponding phases of the OTF. The reference plane is deliberately chosen so that the transmission phase is –π at normal incidence. (c) and (d) 2D OTF for s and p waves, respectively* [11].

For ease of comparison, we have also presented results for an ideal second-order differentiation transfer function (3) $H_0(k_x) = -\alpha k_x^2 / 2$, where α is a constant ensuring that the transfer is equal to unity at $\theta = 15°$. It can be found that both results are in good agreement with each other. In addition, we have shown the corresponding transmission phases in Fig. 10*b*, and there are only small deviations between them. Therefore, such an MS can provide optical analog computations for second-order derivative and edge detection. Since the lattice has fourth-order rotation symmetry, the OTF along the *y* direction is the same. This means that taking the second-order derivative in two dimensions is possible. We calculated the two-dimensional OTF $H(k_x, k_y)$ of the MS for the *s* and *p* waves, which are shown in Fig. 10*c* and 10*d*. It can be found that the transmissions for smaller incidence angles are close to zero, and for larger incidence angles they approach unity for most wave vectors. Although the MS OTF is not perfectly isotropic in the xy plane, which would ensure the existence of a differential Laplace operator, it can still practically perform edge detection for 2D images. In addition, since the OTFs for *s*- and *p*-waves have the same parabolic shape along high symmetry directions, spatial differentiation can be performed for both polarized and unpolarized light fields, indicating great potential in practice.

To clearly demonstrate the functionality of spatial differentiation using the developed MS, we first explore the application of the simulations in Fig. 10*a* and 10*b* results for one-dimensional spatial functions. Two cases typical of the logic function and the sine wave, shown in the top row of **Fig. 11***a* and 11*b* were studied, respectively. We first calculated the frequency spectra $\tilde{S}(k_x)$ of spatial functions using FT. We then multiplied it by the OTF $H(k_x)$ and the results were returned to the spatial domain by the inverse FT.

As standard output, we presented the results processed using the ideal second-order derivative

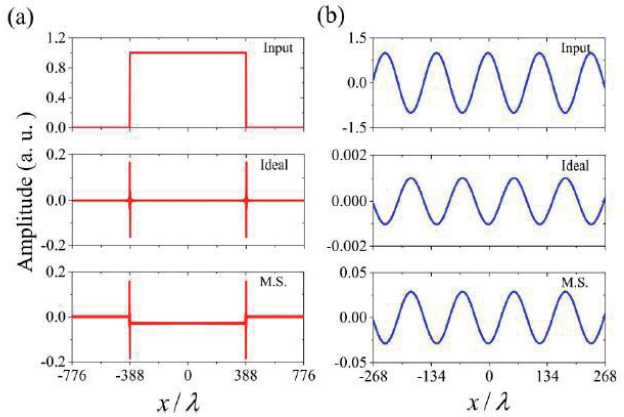

Fig. 11. *(a) Results of finding the second-order derivative of a 1D spatial logical function. The input and output data for the ideal case and the proposed MS are shown in the top, middle and bottom rows, respectively. (b) Corresponding results for a one-dimensional sinusoidal spatial function. In both cases, the input pixel size is 1.94λ* [11].

– the middle row of Fig. 11*a* and 11*b*. There is no doubt that clear output appears only in places with rapid changes in the logical function. For a sine function, the output signal is also a sine wave, but with the opposite sign. For the case of our proposed MS, we show the results in the bottom rows of Fig. 11*a* and 11*b*. In the case of the logic function, the output from the MS also shows obvious signals at the change positions, although there is a very weak signal around the central region due to non-vanishing transmission for low incidence angles, which must be optimized to get closer to ideal results and increase throughput. For the sine function, the MS output provides excellent profile matching to the ideal case. Therefore, MS can indeed perform second-order derivative functionality for one-dimensional spatial functions.

As mentioned above, our proposed MS can perform spatial differentiation and edge detection for 2*D* images. Next, we will examine it using an input image consisting of the Jinan University boat logo, which is shown in **Fig. 12***a*. This image should be a good test sample because it contains the edges of lines, arcs, and circles.

To obtain the output, we project the linearly polarized input fields onto the *s*- and *p*-polarizations and then apply the corresponding

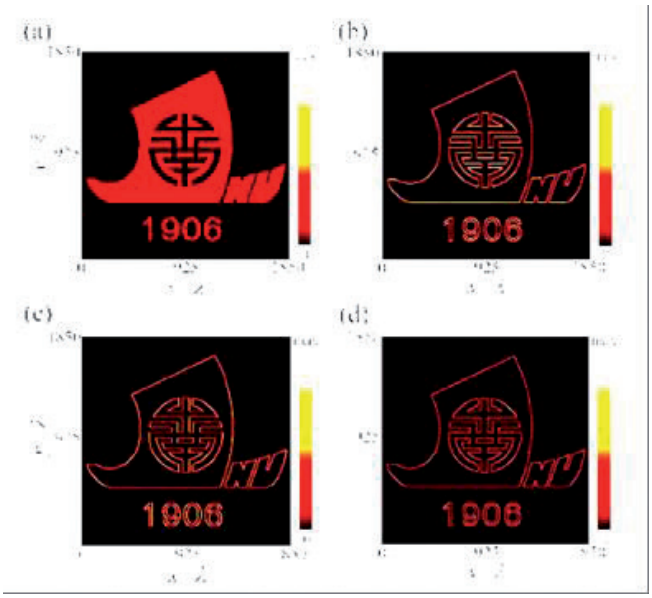

Fig. 12. *(a) 2D image of Jinan University boat logo. The pixel sizes in the x and y directions are set to 1.94 λ. (b) MS output image for modulated light field with x polarization. (c) Output image for the case of y polarization. (d) Output image for the case of unpolarized light* [11].

OTFs. By averaging the individual outputs of *s*- and *p*-polarizations, we obtain results for the unpolarized case. First, we will assume that the image is modulated by an *x*-polarized plane wave. In this case, the output image after the light passes through the MS is shown in Fig. 12*b*. It can be seen that the edges of all elements were successfully extracted, and such effects are not limited to specific directions. This is due to the fact that the OTF of the proposed MS has a parabolic shape along most directions in the xy plane. In addition, the OTFs for *s*- and *p*-waves complement each other in different in-plane directions - see Fig. 10*c* and 10*d*. Next, we studied the case for a light field with polarization along the *y* direction – Fig. 12*c*. In this case, the output image also shows a well-defined edge profile that is very similar to the *x*-polarization case.

Finally, the result for unpolarized light is shown in Fig. 12*d*. Since the edges of all elements in the image can be well detected for both linearly polarized light fields, they can also be detected for the case of unpolarized light. As discussed above, the OTF of the

proposed MS cannot be considered as an ideal Laplace operator. However, this MS can still offer acceptable results for edge detection, although the output values are not exactly the same for different polarizations. In addition, such an MS includes only a single layer of silicon nanodisk resonators, which can greatly simplify parameter tuning and fabrication for practical applications.

The implementation of the Laplace operation in the form of optical analog computing has recently attracted attention, and a compact device with high spatial resolution has yet to be invented. In [16], we proposed a Laplace metasurface that can perform the Laplace operation almost perfectly for different configurations of the incident light field. Most importantly, the maximum incidence angle θ has been greatly expanded and the numerical aperture can approach 0.14, which improves the practical setup and results in a spatial resolution of approximately 4 times the operating wavelength. The proposed Laplace MS is based on the excitation of a bound state in the continuum, which has demonstrated exotic optical properties. The highly symmetric mode profile provides a nearly isotropic OTF of the Laplace operation. We have demonstrated that such an OTF can not only perform second-order differentiation for a one-dimensional spatial Gaussian function, but also produces correct results for a two-dimensional Bessel function. In addition, we also showed that Laplace MS can be used to implement edge detection of objects of interest in an image. The proposed Laplace MS can be configured to operate at different wavelengths in the transmission mode, which provides benefits for applications in optical computing, medical diagnostics, machine vision, etc.

To meet the requirements of OTF and transmission properties, we have developed a new Laplace MS, which is shown in **Fig. 13***a*. When passing through the Laplace MS, the input light field will be automatically processed, and the

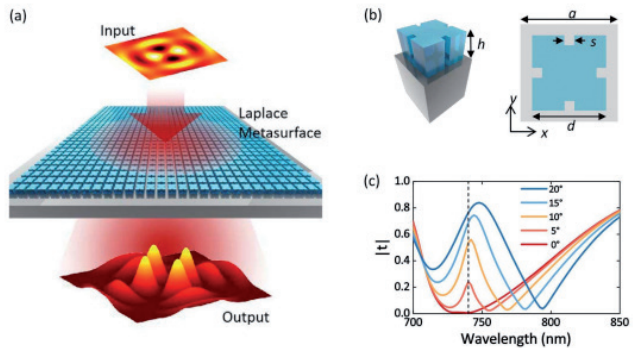

Fig. 13. *(a) Dielectric MS transforming the input two-dimensional spatial function into another function as the Laplace operator; (b) Unit cell of a dielectric MS. Left, 3D view of the unit cell. It consists of a silicon brick (blue color) with a thickness of h = 163 nm and a glass substrate (gray color). Right, top view of the unit cell. The period is a = 331 nm, and the width of the silicon brick is d = 251 nm. At the center of all edges are four square voids with a width of 33 nm. (c) Spectra of the transmittance of the Laplace MS at different angles of incidence along the x direction for a p-wave* [16].

results of the Laplace operation can be obtained simply by simply and instantly recording the output light field.

The Laplace MS consists of a square lattice of modified silicon brick on a glass substrate, which is shown in Fig. 13*b*. The high symmetry of the square lattice and the defects on the four sides of the silicon brick provide isotropic OTF for in-plane directions. We calculated the transmission spectra of the Laplace MS at various angles of incidence and presented them in Fig. 13*c*. It can be found that resonance occurs at wavelength $\lambda \approx 740$ nm when the light field is incident at an angle. The transmittance increases with increasing angle of incidence θ. As a result, the necessary conditions are provided for the implementation of the Laplace operation. To explain the dependence of the transmittance on the angle θ for the Laplace MS, we calculated the dispersion bands around 740 nm of the proposed dielectric MS (lossless silicon with a refractive index of 3.73). All calculations are given in detail in [16].

To check the correctness of the Laplace operation, a one-dimensional spatial function

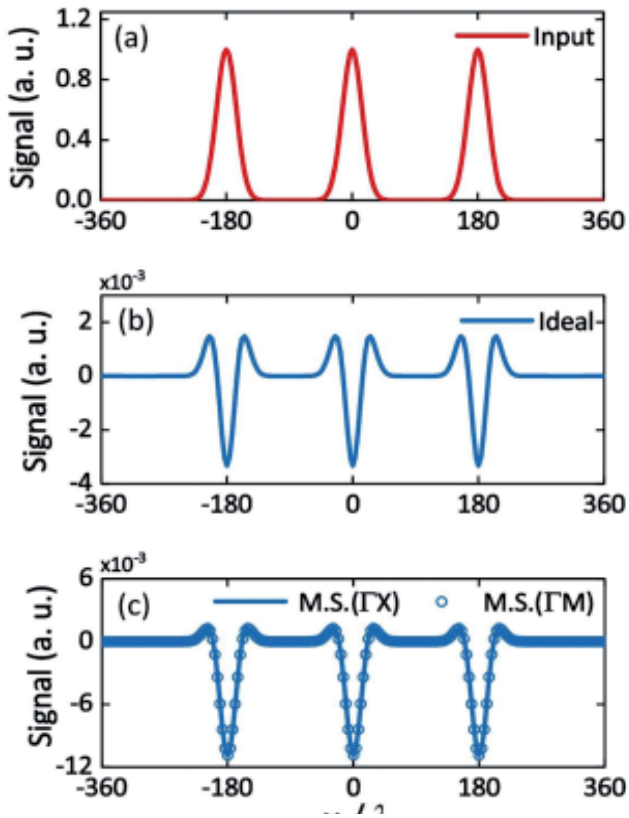

Fig. 14. *One-dimensional spatial function with three Gaussian envelopes as the input light field; (b) Result after second order ideal differentiation operation; (c) Result from Laplace MS. Both the OTF in the ΓX (solid line) and ΓM (symbols) directions are considered. The input pixel size is 3.6λ* [16].

was first used – **Fig. 14***a*. This function consists of three Gaussian envelopes and can be thought of as the electric field profile of the incoming light beam. The output signals are shown in Fig. 14*b* and 14*c*. The tiny difference between the results of the ideal case and the MS can be explained by the slight deviation of the OTF of the Laplace MS from the ideal one. We set the spatial resolution to 3.6λ for the input function, which is close to the maximum spatial resolution of this MS.

One application of the Laplace operation is to detect the edges of problematic targets in an image. We also demonstrated that the proposed Laplace MS can be used for traffic sign recognition, which is critical for automated driving. A road sign was chosen, which is shown in **Fig. 15***a*.

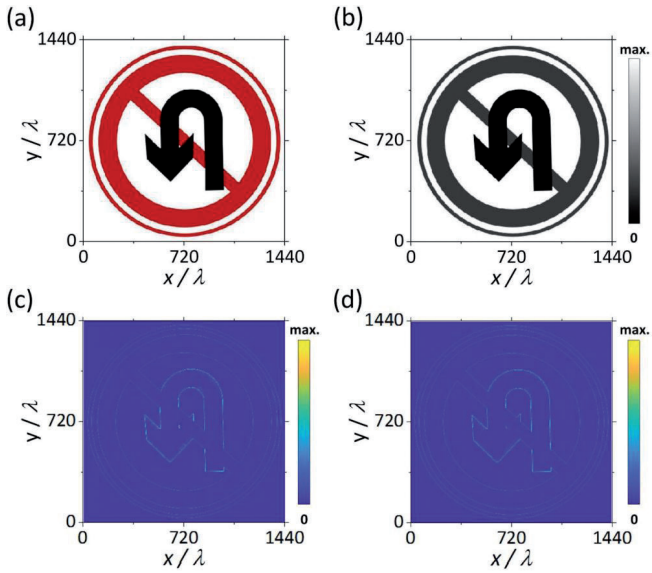

Fig. 15. *(a) Color image of a road sign. (b) Corresponding grayscale image as input. (c) and (d) Output image from ideal Laplace operator and Laplace MS for (b), respectively* [16].

Halftone image in Fig. 15*b* can be considered as an unpolarized light field with intensity modulation, which is incident on the Laplace MS. From the results after the ideal Laplace operation, which are shown in Fig. 15*c*, it can be seen that the edges of both the outer circles and the arrow can be clearly identified. Consequently, necessary information can be safely stored while redundant information is discarded, speeding up information processing in the first stage. We have shown the output results of Laplace MS in Fig. 15*d*, where it can be found that such edge detection can also be successfully implemented.

The Laplace MS can be converted to operate at other wavelengths by adjusting the size of the structure. To demonstrate this, another Laplace MS operating at a wavelength of 1550 nm (the transparency window of the optical fiber) was developed in a similar manner. The shape of the structure is the same as in Fig. 13*b*, but with different parameters: a = 743 nm, d = 560 nm, s = 69 nm and h = 360 nm, respectively. In this case, the transmittance could reach 0.9, and the angle of incidence could be 10°.

We used a typical *QR* code as the input 2*D* image because *QR* codes are now important in

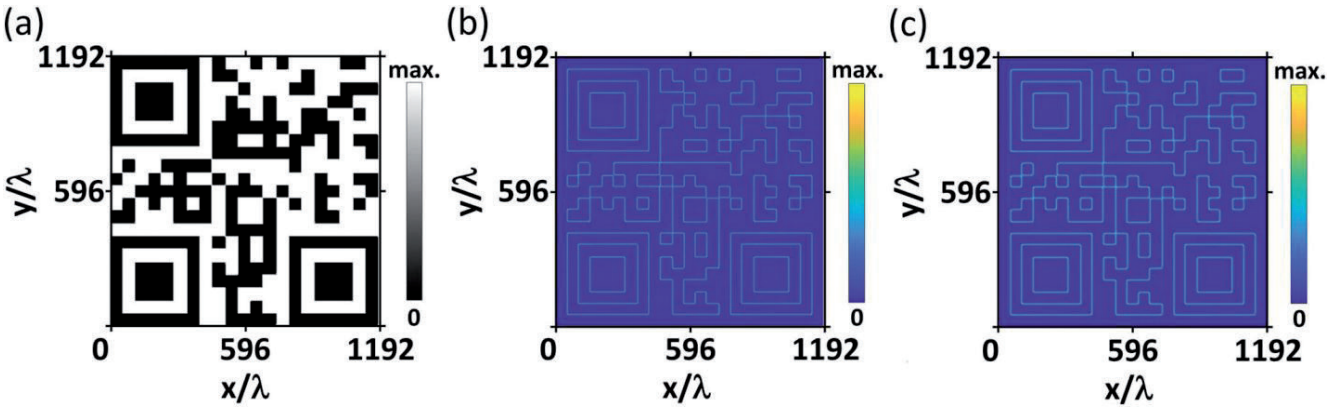

Fig. 16. *(a) Input image consisting of a QR code; (b) output image of the ideal Laplace operation; (c) exit from the Laplace MS. All images are light intensity profiles; pixel sizes are set to 2.88* [16].

our daily life and edge detection for them plays a crucial role in detecting the *QR* code area. The *QR* code we chose is shown in **Fig. 16***a*, which carries information about the Chinese character meaning "Light". Through the processing procedure discussed in this context, we can obtain the results from the ideal Laplace operation and from the Laplace MS, which are shown in Fig. 16*b* and 16*c*.

From the data in Fig. 16 shows that the edges of all elements were successfully detected. In addition, the light intensity at the output of the MS is very similar to the ideal one, which implies high edge detection quality for Laplace MS images.

Due to the limited scope of the article, the author will only briefly list other areas of photonics, which are also studied in our works [10-17] and presented in detail there. These are: control of light scattering by nanoparticles using magneto-electric coupling and zero backscattering (theory of light scattering by nanoparticles and electromagnetic multipoles, numerical modeling, testing experiments in the frequency range from 4 to 7.5 GHz) [10,13,14]; strong optomechanical coupling in chain waveguides made of silicon nanoparticles with quasi-bound states in the continuum (photon–phonon interaction with microstructures) [17], etc. These areas, undoubtedly, can become topics of future reports at the conferences "Radar, navigation, communications - RLNC" at VSU.

6. CONCLUSION

Metasurfaces are a very broad area of research in photonics, its development is just beginning, and the study of dielectric magnetic fields is of great interest. MSs have the advantage of occupying less physical space than 3*D* MMs; therefore, MSs offer the possibility of designing structures with lower losses. In particular, we note that the use of dielectric MSs instead of plasmonic structures, along with a decrease in ohmic losses, helps to realize control of not only the electrical, but also the magnetic component of the light wave, which increases the efficiency of light control in nanoscale structures. To date, embedded optical spatial differentiators have been demonstrated using various artificial MSs [15,18,19]. Compared with metal MS-based spatial differentiator configurations, all-dielectric MS-based operational devices have recently become a popular research topic due to their excellent compatibility and integration with real imaging systems. To further meet the edge detection requirements in practical applications, high-performance spatial differentiators with high efficiency and resolution will be preferred. Construction of spatial differentiators with high energy transfer, large spatial bandwidth and polarization independence is currently the dominant task. Combined with a commercial silicon photonics platform and advanced nanofabrication technologies, experimental demonstrations of mathematical operations and

edge detection will be conducted in numerous image processing scenes to unlock much greater application potential. Moreover, on-chip integration of operational devices with other planar optical elements based on dielectric metasurface platforms such as metalens will also be a valuable direction in the future.

So, the article examined in some detail computational dielectric MSs that implement mathematical operations of spatial differentiation and contour recognition in photonic topological signal and field processing devices. Such MSs have a wide range of potential applications in electromagnetism.

Their use in general brings to a new level all the functional characteristics of the topological texture-fractal processing of signals and fields proposed by the author at the end of the 20th century when solving classical problems of detection, measurement, recognition and classification by intelligent radio systems and devices. Such a task has not yet been posed in the scientific world. The author is motivated by the belief that our current and future research will be extremely useful for future information flow processing devices, and not only in radar.

REFERENCES

1. Potapov AA. *Fractals in radiophysics and radar*. Moscow, Logos Publ., 2002, 664 pp.; Potapov AA. *Fractals in radiophysics and radar: Sampling topology*. Ed. 2nd, revised and additional Moscow, University Book Publ., 2005, 848 p.
2. Gulyaev YuV (ed.). *Professor Alexander Alekseevich Potapov. Fractals in action: Biobibliographic index*. Moscow, CPU "Rainbow" Publ., 2019, 256 p.
3. Potapov Alexander A, Wu Hao, Xiong Shan. *Fractality of Wave Fields and Processes in Radar and Control*. Guangzhou, South China University of Technology Press, 2020, 280 pp.
4. Kuznetsov VA, Potapov AA, Alikulov EA. *Patent RU 2746038 C1 G06T 5/50* (2020.09). A method for fractal integration of multi-frequency radar images. Invention priority 09/05/2020, state registration date 04/06/2021 Bull. No. 10.
5. Potapov AA, Kuznetsov VA, Alikulov EA. Analysis of methods for integrating images generated by multi-band synthetic aperture radar stations. *Izv. universities in Russia. Radioelectronics*, 2021, 24(3):6-21.
6. Potapov AA, Kuznetsov VA, Pototsky AN. A new class of topological texture-multifractal features and their application for processing radar and optical low-contrast images. *Radiotekhnika i elektronika*, 2021, 66(5):457-467 (in Russ.).
7. Potapov AA. Mathematical foundations of the fractal scaling method in statistical radiophysics and applications. *RENSIT: Radioelectronics. Nanosystems. Information Technologies,* 2021, 13(3):245-296. DOI: 10.17725/rensit.2021.13.245.
8. Beliaeva VS, Klyuev DS, Neshcheret A M, Potapov AA, Sokolova YV. Fractal Antenna Systems with Chiral Metamaterials Substrates for MIMO Systems. In: Hu Z, Petoukhov S, He M (eds). *Advances in Artificial Systems for Medicine and Education V*. (Lecture Notes on Data Engineering and Communications Technologies, v. 107). Cham, Springer, 2022, pp. 329-345.
9. Potapov AA, Kuznetsov VA, Alikulov EA. Structural-parametric synthesis of systems for optimal texture-fractal processing of multidimensional radar images. *Radiotekhnika i elektronika*, 2022, 67(1):51-67 (in Russ.).
10. Danping Pan, Tianhua Feng, Wei Zhang, and Alexander A. Potapov. Unidirectional light scattering by electric dipoles induced in plasmonic nanoparticles. *Optics Letters,* 2019, 44(11):2943-2946.
11. Wan Lei, Pan Danping, Yang Shuaifeng, Zhang Wei, Potapov Alexander A, Wu Xia, Liu Weiping, Feng Tianhua, and Li Zhaohui. Optical analog computing of spatial

differentiation and edge detection with dielectric metasurfaces. *Optics Letters,* 2020, 45(7):2070-2073.

12. Pan Danping, Wan Lei, Potapov Alexander A, Feng Tianhua. Performing Spatial Differentiation and Edge Detection with Dielectric metasurfaces. QELS_ Fundamental Science "*OSA Technical Digest Conf. on Lasers and Electro-Optics* (*CLEO*) (San Jose, California, USA, May 10-15, 2020)." – Washington, Optical Society of America, 2020. Paper FW4B.2.pdf. 2 pp. (From the session "Inverse Design and Computation (FW4B)").
13. Feng Tianhua, Potapov Alexander A., Liang Zixian, Xu Yi. Huygens Metasurfaces Based on Congener Dipole Excitations. *Physical Review Applied*., 2020, 13, Article No. 021002, 6 pp.
14. Feng Tianhua, Yang Shuaifeng, Lai Ning, Chen Weilian, Pan Danping, Zhang Wei, Potapov Alexander A, Liang Zixian, Xu Yi. Manipulating light scattering by nanoparticles with magnetoelectric coupling. *Physical Review B,* 2020, V 102, Article No. 205428, 7 pp.
15. Wan Lei, Pan Danping, Feng Tianhua, Liu Weiping, Potapov AA. A review of dielectric optical metasurfaces for spatial differentiation and edge detection. *Frontiers of Optoelectronics,* 2021, 14(2):187-200.
16. Wan Lei, Pan Danping, Ouyang Min, Zhang Wei, Potapov Alexander A, Liu Weiping, Liang Zixian, Feng Tianhua, Li Zhaohui. Laplace metasurfaces for optical analog computing based on quasi-bound states in the continuum. *Photonics Research*, 2021, 9(9):1758-1766.
17. Yang Shuaifeng, Wan Lei, Wang Fugen, Potapov Alexander A, Feng Tianhua. Strong optomechanical coupling in chain-like waveguides of silicon nanoparticles with quasi-bound states in the continuum. *Optics Letters*, 2021, 46(18):4466-4469.
18. Ziolkowski RW, Engheta N. Metamaterials: Two Decades Past and Into Their Electromagnetics Future and Beyond. *IEEE Trans. Antennas and Propagation,* 2020, AP-68(3):1232-1237; doi: 10.1109/TAP.2019.2938674.
19. He Shanshan, Wang Ruisi, Luo Hailu. Computing metasurfaces for all-optical image processing: a brief review. *Nanophotonics,* 2022, 26 p.; doi: 10.1515/nanoph-2021-0823.
20. Gulyaev YuV. Interview. Intellekt i tekhnologii, 2017, 4(19):6-11 (in Russ.).
21. Silva A, Monticone F, Castaldi G, Galdi V, Alù A, Engheta N. Performing mathematical operations with metamaterials. *Science*, 2014, 343(6167):160-163.
22. Pors A, Nielsen MG, Bozhevolnyi SI. Analog computing using reflective plasmonic metasurfaces. *Nano Letters,* 2015, 15(1):791-797.
23. Chen H, An D, Li Z, Zhao X. Performing differential operation with a silver dendritic metasurface at visible wavelengths. *Optics Express,* 2017, 25(22):26417-26426.
24. Wu W, Jiang W, Yang J, Gong S, Ma Y. Multilayered analog optical differentiating device: performance analysis on structural parameters. *Optics Letters,* 2017, 42(24):5270-5273.
25. Kwon H, Sounas D, Cordaro A, Polman A, Alù A. Nonlocal metasurfaces for optical signal processing. *Physical Review Letters,* 2018, 121(17). Article No. 173004.
26. Zhang W, Qu C, Zhang X. Solving constant-coefficient differential equations with dielectric metamaterials. *Journal of Optics,* 2016, 18(7). Article No. 075102.
27. Abdollahramezani S, Chizari A, Dorche AE, Jamali MV, Salehi JA. Dielectric metasurfaces solve differential and integro-differential equations. Optics Letters, 2017, 42(7):1197-1200.

28. Remnev MA, Klimov VV. Metasurfaces: a new look at Maxwell's equations and new methods for controlling light. *Phys. Usp.*, 2018, 61:157-190. DOI: 10.3367/UFNe.2017.08.038192.
29. Rybin MV, Limonov MF. Resonance effects in photonic crystals and metamaterials. *Phys. Usp., 2019,* 62:823-838. DOI: 10.3367/UFNe.2019.03.038543.
30. Goodman J. *Introduction to Fourier optics*. Moscow, Mir Publ., 1970, 364 p.
31. Papulis A. *Theory of systems and transformations in optics*. Moscow, Mir Publ., 1971, 495 p.
32. Zverev VA. *Radio optics*. Moscow, Sovetskoe radio Publ., 1975, 304 p.
33. Potapov AA. A statistical approach to describing images of the earth's surface textures in the optical and radio range. *Abstract report All-Union conf. "Mathematical methods of pattern recognition - MMRO-IV"*, Riga, Publishing house MIPCRRiS at the Council of Ministers of Latvia SSR, 1989, Part 4, p. 3-5.
34. Potapov AA, Kolesnikov AI. Correlation characteristics of images of the earth's surface. *Radiotekhnika i elektronika*, 1993, 38(7):1270-1279 (in Russ.).
35. Potapov AA, Kolesnikov AI. Spectral characteristics of images of the earth's surface. *Radiotekhnika i elektronika*, 1993, 38(10):1851-1862 (in Russ).
36. Potapov AA. Synthesis of images of land covers in the optical and millimeter wave ranges. *Abstract of thesis*. ... Doctor of Physics and Mathematics. Sciences, Moscow, IRE RAS Publ., 1994, 44 p.
37. Farmahini-Farahani M, Cheng J, Mosallaei H. Metasurfaces nanoantennas for light processing. *Journal of the Optical Society of America B*, 2013, 30(9):2365-2370.
38. Zhu T, Zhou Y, Lou Y, Ye H, Qiu M, Ruan Z, Fan S. Plasmonic computing of spatial differentiation. *Nature Communications,* 2017, 8(1). Article No. 15391.
39. Fan S, Joannopoulos JD. Analysis of guided resonances in photonic crystal slabs. *Physical Review B.*, 2002, 65(3). Article No. 235112.
40. Limonov MF, Rybin MV, Poddubny AN, Kivshar YS. Fano resonances in photonics. *Nature Photonics,* 2017, 11(9):543-554.
41. Kuznetsov AI, Miroshnichenko AE, Brongersma ML, Kivshar YS, Luk'yanchuk B. Optically resonant dielectric nanostructures. *Science*, 2016, 354(6314). Article No. aag2472.
42. Whitehead LA, Hardy WN. Split-ring resonator for use in magnetic resonance from 200-2000 MHz. *Rev. Sci. Instrum.*, 1981, 52:213-216.
43. Aieta F, Kats MA, Genevet P, Capasso F. Multiwavelength achromatic metasurfaces by dispersive phase compensation. *Science,* 2015, 347:1342-1345.
44. Genevet Patrice, Capasso Federico, Aieta Francesco, Khorasaninejad Mohammadreza, Devlin Robert. Recent advances in planar optics: from plasmonic to dielectric metasurfaces. *Optica,* 2017, 4(1):139-152.
45. Zhou J, Qian H, Chen CF, Zhao J, Li G, Wu Q, Luo H, Wen S, Liu Z. Optical edge detection based on high-efficiency dielectric metasurface. *Proc. National Academy of Sciences of the United States of America,* 2019, 116(23):11137-11140.
46. He S, Zhou J, Chen S, Shu W, Luo H, Wen S. Wavelength-independent optical fully differential operation based on the spin-orbit interaction of light. *APL Photonics,* 2020, 5(3). Article No. 036105.
47. Guo C, Xiao M, Minkov M, Shi Y, Fan S. Photonic crystal slab Laplace operator for image differentiation. *Optica,* 2018, 5(3):251-256.
48. Guo C, Xiao M, Minkov M, Shi Y, Fan S. Isotropic wavevector domain image filters by a photonic crystal slab device.

Journal of the Optical Society of America, 2018, A35(10):1685-1691.

49. Cordaro A, Kwon H, Sounas D, Koenderink AF, Alù A, Polman A. High-index dielectric matesurfaces performing mathematical operations. *Nano Letters*, 2019, 19(12):8418-8423.
50. Zhou Y, Wu W, Chen R, Chen W, Chen R, Ma Y. Analog optical spatial differentiators based on dielectric metasurfaces. *Advanced Optical Materials,* 2020, 8(4). Article No. 1901523.
51. Kwon H, Cordaro A, Sounas D, Polman A, Alù A. Dual-polarization analog 2D image processing with nonlocal metasurfaces. *ACS Photonics,* 2020, 7(7):1799-1805.
52. Zhou Y, Zheng H, Kravchenko II, Valentine J. Flat optics for image differentiation. *Nature Photonics*, 2020, 14(5):316-323.

DOI: 10.17725/j.rensit.2024.16.031

Practical aspects of design of the wireless underwater optical communication system for telecommunication applications

Igor B. Shirokov, Vladislav V. Golovin, Elena A. Redkina, Igor V. Serdyuk, Pavel P. Ovcharov

Sevastopol State University, http://www.sevsu.ru/
Sevastopol 299053, Russian Federation
E-mail: shirokov@ieee.org, vvgolovin@mail.sevsu.ru, earedkina@mail.sevsu.ru, ivserdyuk@mail.sevsu.ru, ppovcharov@mail.sevsu.ru

Received September 18, 2023, peer-reviewed September 25, 2023, accepted October 02, 2023, published March 15, 2024.

Abstract: **The overview of the principles of organizing underwater wireless optical communication is presented in the paper. The basic features of the optical communication system design with the usage of laser and LED emitters working in the visible range, as well as using various types of modulation, are considered. A comparative review of the developments of underwater wireless optical communication systems, operating at distances up to one hundred meters and with data transfer rates up to tens of Gbit/s, is presented. In addition, a comparative review of design of underwater optical modems is considered. It is shown, that the further prospect of their development is the combination of various methods of underwater wireless communication, including the use of MIMO technology.**

Keywords: **underwater optical communication, optical communication in the visible range, optical modem for underwater communication, underwater communication system**

UDC 654.026

For citation: Igor B. Shirokov, Vladislav V. Golovin, Elena A. Redkina, Igor V. Serdyuk, Pavel P. Ovcharov. Practical aspects of design of the wireless underwater optical communication system for telecommunication applications. *RENSIT: Radioelectronics. Nanosystems. Information Technologies,* 2024, 16(1):31-42e. DOI: 10.17725/j.rensit.2024.16.031.

Contents

1. INTRODUCTION

In modern telecommunication systems, the several approaches are used to organize wireless underwater communication.

Acoustic underwater communication (UAWC) is considered as the most popular method of underwater wireless communication because of the low values of the attenuation of acoustic waves under water (about 0.1-4 dB/km). Disadvantages of UAWC are the low acoustic wave propagation speed (1500 m/s) and limited UAWC bandwidth (kHz), which leads to the multipath phenomenon, large time delay, and bulky acoustic antennas [1]. For example, in [2], a UAC system with a data transfer rate of 60 Kbit/s with 32 QAM is considered This UAC system can communicate at a depth of 100 m and at a distance of 3 km horizontally. In order to achieve high data transfer rates without

the need for complex calculations, many researchers have widely used orthogonal frequency division multiplexing (OFDM) in underwater acoustic communication [3].

Underwater radio communication (URWC) is used to organize high-speed data transmission over short distances. Electromagnetic waves are affected by temperature, salinity and depth, which leads to a strong weakening of electromagnetic waves and limits the range of signal propagation in water. Due to the high electrical conductivity of water in microwave range, it is difficult to implement URWC on communication lines with a length of more than 10 m [4] in the ranges of meter and shorter waves (in the 2.4 GHz range, the attenuation of radio waves in salt water is about 169 dB/m). For such communication lines, a large power of transmitters (more than 100 watts) is required [5]. In the DV (30-300 kHz) and SDV (3-30 kHz) bands, the attenuation of the electromagnetic wave can be considered low enough to provide reliable communication at a distance of many kilometers. URWC systems in the DV range are used in underwater military systems or when creating communication lines between ground and underwater objects [6]. The main disadvantages of such systems include complex design requirements for very large antennas and low data transfer rates.

*Underwater communication using magnetic inductio*n (UWMIC), as a promising replacement of traditional acoustic systems and radio communications, has attracted considerable attention [7], due to its inherent qualitative amplitude-frequency response of the channel, low propagation delay and relatively low energy consumption [8]. UWMIC involves the transition from traditional unidirectional antennas to multidirectional MI-antennas. There is also a great research interest in the currently available approaches to expanding or reusing the available frequency bands to increase the capacity of the underwater MI channel [7].

Underwater optical communication (UOWC) is based on the use of a visible part of the optical spectrum. UOWC is characterized by a large available bandwidth, which can help to realize high data transfer rates, and has the advantages of low power consumption, low cost and compact size. The complex underwater environment has a serious impact on the propagation of light under the water. Absorption, scattering and turbulence are the dominant harmful effects that degrade the optical transmission characteristics at low temperatures. Underwater transmission of optical waves in the 450-500 nm band (blue and green) has the least attenuation for pure seawater or transparent ocean (0.4 dB/m) compared to other bands. In this band the attenuation effect caused by the interaction of photons with water molecules and other particles is limited. The 520-570 nm band (yellow-green) is suitable for coastal ocean or turbid waters in ports (11 dB/m).

In the underwater environment, a chlorophyll substance absorb blue and red light. These and other colored dissolved organic substances (CDOMS) increase the turbidity of water and reduce the distance of light propagation. The concentration of CDOM varies depending on the depth of the water medium, thereby changing the corresponding light attenuation coefficients. The total absorption in seawater can be determined taking into account a complex of factors according to the formula [9]

$$a(\lambda) = a_w(\lambda) + a_f c_f exp(-k_f \lambda) + \\ + a_h c_h exp(-k_h \lambda) + a_c (c_c)^{0,622},$$

where $a_w(\lambda)$ – an absorption coefficient in pure water; a_f – a partial absorption coefficients of fulvic acids; c_f – a fulvic acid concentration; k_f

– an exponential coefficient of fulvic acids; a_h – a humic acid absorption coefficient; c_h – a humic acid concentration; k_h – an exponential coefficient of humic acid; a_c – a chlorophyll absorption coefficient; c_c – a chlorophyll concentration.

Due to the complexity of the water environment, the implementation of UOWC systems requires reliable underwater devices. The performance and service life of UMPC devices are largely influenced by the current, temperature pressure and salinity of seawater. The power consumption of the system's transmitter, taking into account the capacity of the batteries, determines the battery life.

The main disadvantage of optical communication is that the range is limited to a distance of about 1-100 meters, because of the water parameters and suspended particles in the water, where the light is either attenuated or scattered. Another disadvantage is that optical communication usually requires a line of sight from the transmitter to the receiver.

Fig. 1 shows a generalized comparison of available wireless underwater communication technologies [10].

Therefore, the generalization of the results of UOWC developments for communication and information transmission systems has a great practical interest.

2. APPROACHES TO THE CONSTRUCTION OF UNDERWATER WIRELESS OPTICAL SYSTEMS

In practice, the technology of "optical communication in the visible range" (VLC) is widely used for the organization of wireless underwater optical communication, as the most promising. Due to the rapid development of LED lighting, the cost of the component is decreasing. However, some of the problems that need to be solved are listed below:

– an integration of the VLC system with existing communication standards;

– a problem with interference from the ambient light source;

– a VLC must correctly support handover in coverage areas;

– an application of error correction methods to improve the performance of the communication system.

As the number of VLC devices increases, there will be interference between different VLC devices. The Electronic Information Technology Industry Association has developed the 802.15.7 standard, which is the standard established by the IEEE for the physical layer and the MAC layer [11]. The objectives of this standard are:

– providing access to hundreds of terahertz frequency bands;

– providing protection against electromagnetic interference;

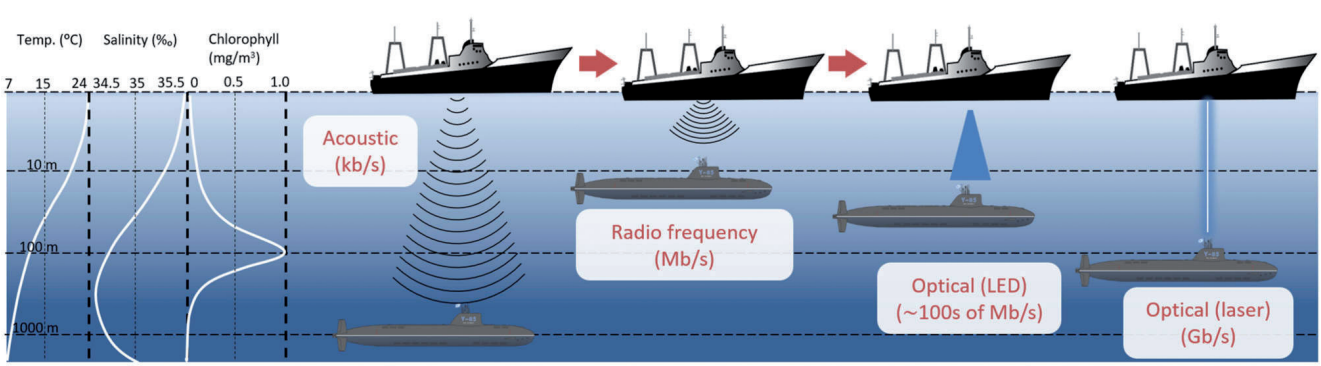

Fig. 1. *Comparison of available wireless underwater communication technologies.*

– provision of additional services that complement the existing visible light equipment;

– the VLC-connection that prescribes a forward error correction (FEC) scheme, a form of modulation and a data transfer rate;

– a channel access mechanism, since visibility range support also describes channel access, as well as the time period when contention for the network environment (contention access period, CAP) and the competition-free time period (CFP);

– the physical layer specifications: the optical projection, TX-RX, RX-TX cycle time, flicker and dimming.

The three different types of devices used by VLC are: mobile objects, a mobile equipment, and the infrastructure [12]. VLCs can be used indoors [13,14], in identification and location systems [15], in communication systems in transport [16], and are used for the organization of wireless underwater communication channels [17].

The VLC system mainly consists of two components: an optical transmitter (Tx) and an optical receiver (Rx). After preprocessing and encoding, the binary bit stream directly simulates the emission of the light source. To increase the transmission rate and the efficiency of the spectrum, high-order coding modulation methods are used.

The implementation of extended and high-speed underwater communication lines using laser diodes (LD) as a source of optical radiation has been considered in a number of papers [18, 19]. However, due to the narrow directional pattern of LD in the underwater environment, problems arise with the positioning of the receiving and transmitting paths. At the same time, the additional beam expansion or other solutions are used to achieve the required technical characteristics of the UOWC.

Therefore, the most common type of radiation sources in the UOC structure are light-emitting diodes (LEDs) [20], which provide many advantages: a safety for the eyes, the long service life, a low power consumption, the possibility of simultaneous lighting and communication. Since LEDs are characterized by a wide directional pattern, they solve the problem of positioning, which allows the use of simpler and more compact UOWC systems. Large divergence angles and a relatively small frequency band of LED modulation limit their use in terms of data transmission range and speed: for example, for communication between underwater vehicles and nodes of underwater wireless sensor networks, etc.

A comparison of the characteristics of LD and LED used in VLC is presented in **Table 1**.

To increase the efficiency of using the LED modulation range, it is customary to investigate methods of digital compression of the signal spectrum, for example, due to quadrature amplitude modulation (QAM) and multiplexing with orthogonal frequency division (OFDM) [21]. The following types of modulation are also used:

– the multilevel pulse-amplitude modulation (PAM), which is characterized by a simpler structure, more flexible implementation and less computational complexity [22];

– the amplitude manipulation without returning to zero (NRZ-OOK) as is the

Table 1

Comparison of LD and LED characteristics used in VLC.

Light source	Transverse dimensions, mm^2	Modulation bandи	Power, Watt
LED	0.1-1	~ 10 МГц	> 1
LD	< 0.2	10-20 ГГц	> 1

most intuitive and simple modulation scheme suitable for light communication;

– the phase-pulse modulation (PPM);

– the frequency manipulation (FSK);

– the digital pulse interval modulation (DPIM) is a method of isochronous pulse-time modulation, in which data is encoded as a series of discrete time intervals, or time intervals between adjacent pulses. The length of the symbol is variable and is determined by the information content of the symbol. To avoid symbols in which the time between adjacent pulses is zero, an additional guard interval can be added to each symbol immediately following the pulse.

When modulations are modified, a discrete multi-tone transmission is used (DMT) [23].

The key element of the VLC receiving path of the system is a photodetector that converts the energy of the received optical radiation into a photocurrent. VLC receivers use different types of photodiodes, such as:

– the semiconductor pin photodiode (PIN PD): high-speed contact photodiodes have a fast reaction time, low cost, single gain and high resistance to ambient light; the main type of noise is thermal;

– the avalanche photodiode (APD): APD has a high intrinsic current gain and high quantum efficiency (70-90%). The main type of noise is shot noise. APD requires high bias voltage and complex control circuits; the quantum efficiency of APD depends on the thickness of the material, for example, in the range of 400-500 nm, silicon has very low sensitivity. Therefore, the contact photodiode seems to be a more promising technology at shorter wavelengths than APD for the UOWC system [12];

– the photomultiplier (PMT), which is the type of vacuum lamp that is very sensitive to light, has a large photocurrent gain, low noise, high frequency response and large overall dimensions compared to photodiodes; PMT requires a high supply voltage (about 100 V) and have a high cost, also have a fragile design.

The main requirements for photodetectors in the VLC system are:

– the high quantum efficiency; the output photocurrent can be as large as possible to create a certain incident optical power;

– the sufficiently high response rate for use in a high-speed broadband system;

– the noise level should be as low as possible;

– a low level of nonlinear distortion;

– small size and long service life.

3. OVERVIEW OF THE DEVELOPMENT OF UNDERWATER VLC SYSTEMS

A comparative analysis of the characteristics of various options for building VLC systems designed for the organization of UOWC is considered below.

A comparison of the characteristics of VLC systems, the transmission path of which is implemented on the basis of laser diodes, is shown in **Table 2**.

Table 2

Comparison of the characteristics of VLC systems with laser diodes

Source	Photo-detector	Modulation	Dis-tance, m	Data transfer rate, Gbit/s	Refe-rence
Laser diode (LD)	Avalan-che photo-diode	NRZ-OOK	7	2.3	[24]
		PSK/QAM	64	5	[25]
			8	1	
		QAM-OFDM	5.4	4.8	[26]
		OAM-OOK	2.96	3	[27]
		OOK	20	1.5	[28]
		OFDM	1.7	14.8	[29]
		NRZ-OOK	34.5	2.7	[30]
		OFDM	21	5.5	[31]
		NRZ-OOK	34.5	2.7	[32]
	PIN-photo-diode	16-QAM	3	0.05	[33]
		OOK	1.6	0.1	[34]

A comparison of the characteristics of VLC systems, the transmission path of which is implemented on the basis of light-emitting diodes, is shown in **Table 3.**

Analysis of recent publications shows that today LED arrays are increasingly popular in the design of UOWC transmission modules [50]. LED arrays with increased optical power can provide a sufficiently long data transmission distance under the water. In addition, LED arrays with a relatively large light spot in the receiving plane can reduce the influence of turbulence and inhomogeneities in the UOWC channel.

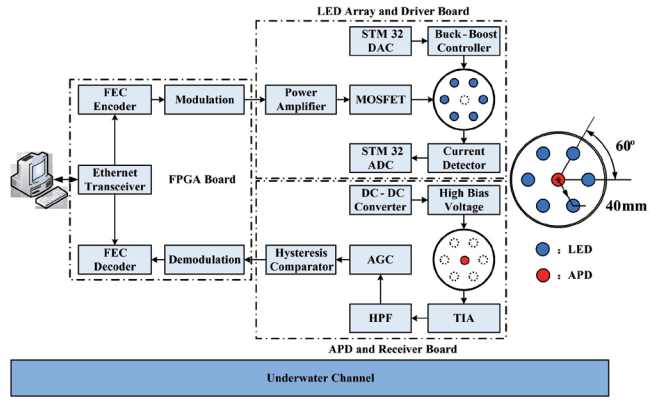

Fig. 2. *Block diagram of the VLC receiving and transmitting module of the UOWC system.*

Table 3

Comparison of the characteristics of VLC systems with light-emitting diodes

Type of transmitter	Receiver Type	Modulation	Distance, м	Data transfer rate	Reference
521 нм LED	2 PIN PD	64-QAM-DMT	1.2	2,175 Gbit/s	[35]
470 нм LED array	PMT	OOK	8	19 Gbit/s	[36]
RGBYC LED	PIN PD	64QAM-DMT bit-loading-DMT	1.2	14.81-15.17 Gbit/s	[37]
Blue LED	PIN PD	64 QAM DMT	1.2	3.075 Gbit/s	[38]
Blue LED	MPPC	PPM	46	~ MHz	[39]
458 нм LED	PIN PD array (2×2)	32 QAM DMT	1.2	20.09 Gbit/s	[40]
LED (4×4) array	PIN PD	PS-bit loading DMT	1.2	20.09 Gbit/s	[41]
450 нм LED	PIN PD	16QAM OFDM	3	50 Mbit/s	[42]
450 нм LED array	APD	video broad-cast	10	1 Mbit/s	[43]
450 нм LED	APD	PAM4	5	1.25 Gbit/s	[44]
450 нм LED	APD	GS-8QAM OFDM	3.6	2,2 Gbit/s	[45]
448 нм LED	APD	OOK	118	25 Mbit/s	[46]
480 нм LED	APD	DPIM	30	1,2 Mbit/s	[47]
470 нм LED	APD	DPIM	50	2,28 Mbit/s	[48]
Blue LED	APD	NRZ-OOK	11.5	235 Mbit/s	[49]
445 нм LED	APD	2FSK	14.5	1 Mbit/s	[50]

A typical example of the block diagram of the VLC receiving and transmitting module of the UOWC system [50] is shown in **Fig. 2**.

Depending on the number of LEDs in the grid, LEDs can be connected in series, in parallel, or in a combined way. In a serial line, usually no more than 10 LEDs are included.

The modern way to improve the reliability of UOWC systems is to use the multiple-input multiple-output (MIMO) technology [51]. The system characteristics of MIMO wireless optical communication using spatial modulation (SM-OMIMO) in the OWC of free space [52] and wireless indoor environment [53] have already been studied. It has been shown that the SM can help to achieve improved spectral efficiency and is more resistant to high channel correlation compared to conventional MIMO using a code with repetitions [51]. In addition, SM has the advantage of implementation, since it requires only a low complexity detection algorithm [54]. However, for realization of UOWC, it is still not clear to what extent the SM-OMIMO methods can provide a gain, because the channel attenuation will be more severe in an underwater environment.

Using a typical equal power absorption algorithm (PAA) [55], receivers can only determine the intensity of signals, but cannot determine the position of the activated transmitter. To negate the limitations associated with high channel correlations, power imbalance (PI) technology on transmitters has recently been introduced. In [56], an optimal power distribution was proposed for a spatially modulated VLC system with OFDM for the case of a simple MIMO structure with two transmitters. Expressions for the power distribution coefficient for four transmitters are obtained in [57]. In most recent reference sources related to the SM system, a simple pulse-amplitude modulation scheme is used, including OOK [55] and the pulse-amplitude modulation (PAM) [57]. In [58], UOC MIMO using spatial modulation (SM-UOMIMO) and the flag two-amplitude pulse positional modulation (FDAPPM) is considered [59].

4. OVERVIEW OF THE DESIGN OF UNDERWATER OPTICAL MODEMS

The practical implementation of various approaches to the design of UOWC receiving and transmitting equipment, taking into account existing data transmission protocols, is presented on the market of underwater optical modems. Comparative characteristics of the developments of underwater optical modems are presented in **Table 4**.

Table 4

Comparative characteristics of the development of underwater optical modems

Organization	Light source	Data transfer rate	Distance, м	Reference
WHOI (2005)	LEDs	10 Mbit/s	100	[60]
Laurentian Univ. (2009)	LED	1 Gbit/s	20	[61]
MIT (2010)	LEDs	2.28 Gbit/s	50	[62]
Maritime Technology and Research (2017)	LD	100 Mbit/s	2	[63]
Dalian Univ. Of Technology (2018)	LD	100 Mbit/s	4.8	[64]
Tsinghua Univ. (2018)	LED	235 Mbit/s	11.5	[49]
MIT Lincoln Lab. (2019)	LED	1 Gbit/s	20	[65]
Sonardyne (2019)	LEDs	10 Mbit/s	150	[66]
Nanjing Univ. of Posts and Telecommunications (2020)	LEDs	1 Mbit/s	10	[67]
KAUST (2020)	LD	1.2 Mbit/s	2	[68]
KAUST (2021)	LED	1.5 Mbit/s	0.6	[69]
KAUST (2022)	LED	2.5 Mbit/s	5	[70]

The prospect of the development of underwater communication modems is associated with the combination of two or more different methods of underwater communication. This approach is often used for ocean mooring with sensors on an anchor cable and wireless mobile communication. Hybrid systems can take advantage of each method and therefore increase the reliability of the system. Today, one of the most important tasks of hybrid systems is an adaptive and smooth transition from one communication environment to another, which makes the system more complex and requires protocols and algorithms to understand the environment in a hybrid system [71]. Many underwater vehicles used hybrid communication systems, which included both acoustic and optical systems [72]. Choosing the appropriate communication channels in response to changing traffic load and weather conditions, presented in [73], the hybrid optical-acoustic underwater wireless communication system that minimizes network power consumption and provides high data transfer rates in underwater applications. Compared with conventional optical-acoustic methods, the proposed approach allows saving up to 35% of electricity.

5. CONCLUSION

VLC optical technologies are widely used for the organization of underwater wireless telecommunication systems, which provide unique opportunities for high-speed communication, including the organization of promising underwater networks of the

Internet of Things. The developed component optical base (lasers, LEDs and various types of photodiodes) is well adapted to solve the problems of UOWC design using VLC technologies and make it possible to find the most effective combinations to implement the various technical tasks. Various types of digital modulation, noise-proof coding and MIMO technologies can significantly increase the efficiency of using the frequency band of communication channels, the reliability of data transmission over long distances at different states of the communication channel in terms of transparency, heterogeneity, the content of various organic substances, etc. Modern UOWCS make it possible to get data transfer rates from Mbit/s up to tens of Gbit/s for distances from several to hundreds of meters. Numerous studies in the field of VLC design for various UOWCS have determined the production and active improvement of underwater optical modems with data transfer rates from 1 Mbit/s to 2 Gbit/s at distances up to 150 m. Further development of underwater modems is associated with the combined use of various methods of underwater communication.

REFERENCES

1. Zeng Z, Fu S, Zhang H, Dong Y, Cheng J. A survey of underwater optical wireless communications. I*EEE Commun. Surv. and Tutorials*, 2017, 19(1):204-238.
2. Song HC, Hodgkiss WS. Efficient use of bandwidth for underwater acoustic communication. *Acoust. Soc. Am.*, 2013, 134: 905-908. DOI: 10.1121/1.4812762.
3. Frassati F, Lafon C, Laurent P-A, Passerieux J-M. Experimental assessment of OFDM and DSSS modulations for use in littoral waters underwater acoustic communications. *Proc. Europe Oceans Conference,* 2005: 826-831. DOI: 10.1109/OCEANSE.2005.1513163.
4. Gussen CM, Diniz PSR, Campos MLR, Martins WA, Costa FM, Gois JN, Commun J. A Survey of Underwater Wireless Communication Technologies. *Inf. Sys.*, 2016, 31:242-255. DOI: 10.14209/jcis.2016.22.
5. Al-Shamma'a AI, Shaw A, Saman S. Propagation of electromagnetic waves at MHz frequencies through seawater. *IEEE T. Antennas Propag.,* 2004, 52:2843-2849. DOI: 10.1109/TAP.2004.834449.
6. Clam L. Extremely Low Frequency Transmitter Site Clam Lake. The United State Navy. *Navy fact file. Tech. Rep.,* Wisconsin, 2001. [Online] Available: https://nuke.fas.org/guide/usa/c3i/fs_clam_lake_elf2003.pdf, access data 09.08.2023.
7. Li Y, Wang S, Jin C, Zhang Y, Jiang T. A Survey of Underwater Magnetic Induction Communications: Fundamental Issues, Recent Advances, and Challenges. *IEEE Commun. Surv. Tutor.*, 2019, 21:2466-2487. DOI: 10.1109/COMST.2019.2897610.
8. Arunkumar K, Murthy CR. Soft Symbol Decoding in Sweep-Spread-Carrier Underwater Acoustic Communications: A Novel Variational Bayesian Algorithm and Its Analysis. *IEEE Trans. Signal Process.,* 2020, 68:2435-2448. DOI: 10.1109/TSP.2020.2983830.
9. Shherbakov AV, Petruhin GD, Miroshnikova NE, Titovets PA. Estimation of underwater optical communication link operating distance. *Communications,* 2020, 14(3):53-60. DOI: 10.36724/2072-8735-2020-14-3-54-60.
10. Guo Y, Kong M, Alkhazragi O, Sait MA, Kang CH, Ashry I, Yang Q, Ng TK, Ooi BS. Current Trend in Optical Internet of Underwater Things. *IEEE Photonics*

J., 2022, 14(5):1-14. DOI: 10.1109/JPHOT.2022.3195700.
11. IEEE Approved Draft Standard for Short-Range Wireless Optical Communication Using Visible Light. [Online]. Available: https://ieeexplore.ieee.org/servlet/opac?punumber=6016193, access data 09.08.2023.
12. Dimitrakopoulos G, Demestichas P. Intelligent transportation systems. *IEEE Veh. Technol. Mag.*, 2010, 5:77-84.
13. Vucˇic´ J, Kottke C, Nerreter S, Langer K-D, Walewski JW. 513 Mbit/s Visible Light Communications Link Based on DMT-Modulation of a White LED. *J. Lightwave Technol,* 2010, 28:3512-3518.
14. Chang C-H, Li C-Y, Lu H-H, Lin C-Y, Chen J-H, Wan Z-W, Cheng C-J. A 100-Gb/s Multiple-Input Multiple-Output Visible Laser Light Communication System. *J. Lightwave Technol,* 2014, 32:4121-4127.
15. Do T-H, Yoo M. An in-Depth Survey of Visible Light Communication Based Positioning Systems. *Sensors,* 2016, 16(5):40. DOI: 10.3390/s16050678.
16. Căilean A, Dimian M. Current Challenges for Visible Light Communications Usage in Vehicle Applications: A Survey. *IEEE Commun. Surv. Tutor.,* 2017, 19:2681-2703.
17. Kaushal H, Kaddoum G. Underwater Optical Wireless Communication. *IEEE Access,* 2016, 4:1518-1547.
18. Al-Halafi A, Oubei HM, Ooi BS, Shihada B. Real-time video transmission over different underwater wireless optical channels using a directly modulated 520 nm laser diode. *J. Opt. Commun. Netw.*, 2017, 9(10):826-832.
19. Liu X, Yi S, Zhou X, Fang Z, Qiu ZJ, Hu L, Cong C, Zheng L, Liu R, Tian P. 34.5 m underwater optical wireless communication with 2.70 Gbps data rate based on a green laser diode with NRZ-OOK modulation. *Opt. Express,* 2017, 25(22):27937-27947.
20. Xu J, Kong M, Lin A, Song Y, Yu X, Qu F, Han J, Deng N. OFDM-based broadband underwater wireless optical communication system using a compact blue LED. *Opt. Commun.,* 2016, 369:100-105.
21. Xu J, Song Y, Yu X, Lin A, Kong M, Han J, Deng N. Underwater wireless transmission of high-speed QAM-OFDM signals using a compact red-light laser. *Opt. Exp.*, 2016, 24(8):8097-8109.
22. Szczerba K, Westbergh P, Karout J, Gustavsson J, Haglund Å, Karlsson M, Andrekson P, Agrell E, Larsson A. 30 Gbps 4-PAM transmission over 200 m of MMF using an 850 nm VCSEL. *Opt. Exp.*, 2011, 19(26):B203-B208.
23. Hoeher PA. *Visible Light Communications. Theoretical and Practical Foundations*. Munich, Hanser Publishers, 2019: 95-100.
24. Oubei HM, Li C, Park KH, Ng TK, Alouini MS, Ooi BS. 2.3 Gbit/s underwater wireless optical communications using directly modulated 520 nm laser diode. *Opt. Exp.,* 2015, 23(16):20743-20748.
25. Nakamura K, Mizukoshi I, Hanawa M. Optical wireless transmission of 405 nm, 1.45 Gbit/s optical IM/DD-OFDM signals through a 4.8 m underwater channel. *Opt. Exp.*, 2015, 23(2):1558-1566.
26. Oubeietal HM. 4.8Gbit/s 16-QAM-OFDM transmission based on compact 450-nm laser for underwater wireless optical communication. *Opt. Exp.,* 2015, 23(18):23302-23309.
27. Baghdady J, Miller K, Morgan K, Byrd M, Osler S, Ragusa R, Li W, Cochenour BM, Johnson EG. Multi-gigabit/s underwater optical communication link using orbital angular momentum multiplexing. *Opt. Exp.*, 2016, 24(9):9794.
28. Shen C, Guo Y, Oubei HM, Ng TK, Liu G, Park K-H, Ho K-T, Alouini M-S, Ooi BS. 20-meter underwater wireless optical

communication link with 1.5 Gbps data rate. *Opt. Exp.*, 2016, 24(22):25502.

29. Huang Y-F, Tsai C-T, Chi Y-C, Huang D-W, Lin G-R. Filtered Multicarrier OFDM Encoding on Blue Laser Diode for 14.8-Gbps Seawater Transmission. *Journal of Lightwave Technology,* 2018, 36(9):1739-1745.
30. Liu X, Yi S, Zhou X, Fang Z, Qiu Z-J, Hu L, Cong C, Zheng L, Liu R, Tian P. 34.5 m underwater optical wireless communication with 2.70 Gbps data rate based on a green laser diode with NRZ-OOK modulation. *Opt. Exp.*, 2017, 25:27937-27947.
31. Chen Y, Kong M, Ali T, Wang J, Sarwar R, Han J, Guo C, Sun B, Deng N, Xu J. 26 m/5.5 Gbps air-water optical wireless communication based on an OFDM-modulated 520-nm laser diode. *Opt. Exp.*, 2017, 25:14760-14765.
32. Liu X, Yi S, Zhou X, Fang Z, Qiu ZJ, Hu L, Cong C, Zheng L, Liu R, Tian P. 34.5 m under-water optical wireless communication with 2.70 Gbps data rate based on a green laser diode with NRZ-OOK modulation. *Opt. Exp.*, 2017, 25(22):27937-27947.
33. Wang J, Tian C, Yang X, Shi W, Niu Q, Gulliver TA. Underwater wireless optical communication system using a 16-QAM modulated 450-nm laser diode based on an FPGA. *Applied Opt.*, 2019, 58(16):4553-4559.
34. Li Y, Yin H, Ji X., Wu B. Design and implementation of underwater wireless optical communication system with high-speed and full-duplex using blue/green light. *Proc. Int. Conf. Commun. Softw. Netw.*, 2018, Chengdu, China: 99-103.
35. Wang F, Liu Y, Jiang F, Chi N. High speed underwater visible light communication system based on LED employing maximum ratio combination with multi-PIN reception. *Opt. Commun.,* 2018, 425:106-112. DOI: 10.1016/j.optcom.2018.04.073.
36. Han B, Zhao W, Zheng Y, Meng J, Wang T, Han Y, Wang W, Su Y, Duan T, Xie X. Experimental demonstration of quasi-omni-directional transmitter for underwater wireless optical communication based on blue LED array and freeform lens. *Opt. Commun.,* 2019, 434:184-190.
37. Zhou Y, Zhu X, Hu F, Shi J, Wang F, Zou P, Liu J, Jiang F, Chi N. Common-anode LED on a Si substrate for beyond 15 Gbit/s underwater visible light communication. *Photon. Res.*, 2019, 7(9):1019-1029. DOI: 10.1364/PRJ.7.001019.
38. Wang F, Liu Y, Shi M, Chen H, Chi N. 3.075 Gb/s underwater visible light communication utilizing hardware pre-equalizer with multiple feature points. *Opt. Eng.,* 2019, 58:056117. DOI: 10.1117/1.OE.58.5.056117.
39. Shen J, Wang J, Yu C, Chen X, Wu J, Zhao M, Qu F, Xu Z, Han J, Xu J. Single LED-based 46-m underwater wireless optical communication enabled by a multi-pixel photon counter with digital output. *Opt. Commun.,* 2019, 438:78-82. DOI: 10.1016/j.optcom.2019.01.031.
40. Li J, Wang F, Zhao M, Jiang F, Chi N. Large-coverage underwater visible light communication system based on blue LED employing equal gain combining with integrated PIN array reception. *Appl. Opt.,* 2019, 58:383-388. DOI: 10.1364/AO.58.000383.
41. Hu F, Li G, Zou P, Hu J, Chen S, Liu Q, Zhang J, Jiang F, Wang S, Chi N. 20.09-Gbit/s Underwater WDM-VLC Transmission based on a single Si/GaAs-substrate Multichromatic LED array chip. *Proc. Optical Fiber Communication Conference* (*OFC*), 2020, San Diego, California.
42. Wang J, Tian C, Yang X, Shi W, Niu Q, Gulliver AT. Underwater wireless optical communication system using a 16-QAM

modulated 450-nm laser diode based on an FPGA. *Appl. Opt.,* 2019, 58(16):4553-4559. DOI: 10.1364/AO.58.004553.
43. Sait M, Guo Y, Alkhazragi O, Kong M, Ng TK, Ooi BS. The impact of vertical salinity gradient on non-line-of-sight underwater optical wireless communication. *IEEE Photon. J.,* 2021, 13(6), Art. no. 7300609. DOI: 10.1109/JPHOT.2021.3121169.
44. Di Y, Shao Y, Chen L-K. Real-time wave mitigation for water-air OWC systems via beam tracking. *IEEE Photon. Technol. Lett.*, 2022, 34(1):47-50.
45. Shao Y, Deng R, He J, Wu K, Chen L-K. Real-time 2.2-Gb/s water-air OFDM-OWC system with low-complexity transmitter-side DSP. *J. Lightw. Technol.,* 2020, 38(20):5668-5675.
46. Wang P, Li C, Xu Z. A cost-efficient real-time 25Mb/s system for LED-UOWC: Design, Channel Coding, FPGA implementation, and Characterization. *J. Lightw. Technol.*, 2018, 36(13):2627-26378.
47. Doniec M, Detweiler C, Vasilescu I, Chitre M, Hoffmann-Kuhnt M, Rus D. AquaOptical: a lightweight device for high-rate long-range under-water point-to-point communication. *Proc. OCEANS*, 2009, USA, Biloxi, MS:1-6.
48. Doniec MW, Rus D. Bidirectional optical communication with AquaOptical II. *Proc. IEEE Int. Conf. Commun. Syst.* (*ICCS*), 2010, Singapore, pp. 390-394.
49. Wei Z, Mu X, Fu H. Wearable full-duplex digital transceiver for underwater optical wireless communications. *Proc. Conf. on Lasers and Electro-Optics/Pacific Rim,* 2018, China, Hong Kong, 2018. DOI: 10.1364/CLEOPR.2018.W3A.153.
50. Li J, Yang B, Ye D, Wang L, Fu K, Piao J, Wang Y. A Real-time, Full-duplex System for Underwater Wireless Optical Communication: Hardware Structure and Optical Link Model. *IEEE Access,* 2017, 8:17.
51. Song Y, Lu W, Sun B, Hong Y, Qu F, Han J, Zhang W, Xu J. Experimental demonstration of MIMO-OFDM underwater wireless optical communication. *Opt. Commun.,* 2017, 403:205-210.
52. Renzo MD, Haas H, Ghrayeb A, Sugiura S, Hanzo L. Spatial modulation for generalized MIMO: Challenges, opportunities and implementation. *Proc. IEEE,* 2013, 102(1):56-103.
53. Popoola WO, Poves E, Haas H. Error performance of generalized space shift keying for indoor visible light communications. *Trans. Commun.,* 2013, 61(5):1968-1976.
54. Popoola WO. Merits and limitations of spatial modulation for optical wireless communications. *Proc. 2nd Int. Workshop Opt. Wireless Commun.,* 2014, pp. 152-156.
55. Dong Y, Liu J. On BER performance of underwater wireless optical MISO links under weak turbulence. *Proc. Oceans 2016-Shanghai*, 2016, pp. 1-4.
56. Zhang X, Dimitrov S, Sinanovic S, Haas H. Optimal power allocation in spatial modulation OFDM for visible light communications. *Proc. IEEE 75th Veh. Technol. Conf.*, 2012, pp. 1-5.
57. Fath T, Haas H. Performance comparison of MIMO techniques for optical wireless communications in indoor environments. *IEEE Trans. Commun.*, 2013, 61(2):733-742.
58. Huang A, Tao L, Niu Y. Underwater wireless optical MIMO system with spatial modulation and adaptive power allocation. *Opt. Commun.,* 2018, 412:21-27.
59. Huang A, Fan Y. Flag dual amplitude pulse position modulation for atmospheric FSO communication. *Proc. ICSPCS*, 2013, pp. 1-5.
60. Farr N, Chave AD, Freitag L, Preisig J, White SN, Yoerger D, Sonnichsen F.

Optical modem technology for seafloor observatories. *Proc. OCEANS MTS/ IEEE,* 2005, pp. 928-934.
61. Baiden G, Bissiri Y, Masoti A. Paving the way for a future underwater omni-directional wireless optical communication systems. *Ocean Eng.,* 2009, 36(9):633-640.
62. Doniec M, Rus D. BiDirectional optical communication with AquaOptical II. *Proc. IEEE Int. Conf. Commun. Syst.*, 2010, pp. 390-394. DOI: 10.1109/ICCS.2010.5686513.
63. Scholz T. Laser based underwater communication experiments in the baltic sea. *Proc. 4th Underwater Commun. Netw. Conf.*, 2018, pp. 1-3. DOI: 10.1109/ UComms.2018.8493174.
64. Li Y, Yin H, Ji X, Wu B. Design and implementation of underwater wireless optical communication system with high-speed and full-duplex using blue/green light. *Proc. 10th Int. Conf. Commun. Softw. Netw.*, 2018, pp. 99-103. DOI: 10.1109/ ICCSN.2018.8488232.
65. Hardy ND, Rao HG, Conrad SD, Howe TR, Scheinbart MS, Kaminsky RD, Hamilton SA. Demonstration of vehicle-to-vehicle optical pointing, acquisition, and tracking for undersea laser communications. *Proc. Free-Space Laser Communications XXXI* (*SPIE*), 2019, v. 10910: 205-214. DOI: 10.1117/12.2511178.
66. BlueComm 200. *Underwater optical communications and data transfer modem* [Online]. Available: https://www.sonardyne.com/products/bluecomm-200-wireless-underwater-link/, access data 09.08.2023.
67. Li J, Yang B, Ye D, Wang L, Fu K, Piao J, Wang Y. Real-time, full-duplex system for underwater wireless optical communication: hardware structure and optical link model. I*EEE Access,* 2020, 8:109372–109387. DOI: 10.1109/ACCESS.2020.3001213.
68. Kong M, Lin J, Guo Y, Sun X, Sait M, Alkhazragi O, Kang CH, Holguin-Lerma JA, Kheireddine M, Ouhssain M, Jones BH, Ng TK, Ooi BS. AquaE-lite hybrid-solar-cell receiver-modality for energy-autonomous terrestrial and underwater internet-of-things. *IEEE Photon. J.,* 2020, 12(4), Art. no. 7904713. DOI: 10.1109/ JPHOT.2020.3013995.
69. Kong M, Guo Y, Sait M, Alkhazragi O, Kang CH, Ng TK, Ooi BS. Toward automatic subsea operations using real-time underwater optical wireless sensor networks. *IEEE Photon. J.,* 2021, 14(1), Art. no. 7308408. DOI: 10.1109/ JPHOT.2021.3136922.
70. Kong M, Guo Y, Alkhazragi O, Sait M, Kang CH, Ng TK, Ooi BS. Real-time optical-wireless video surveillance system for high visual-fidelity underwater monitoring. *IEEE Photon. J.,* 2022, 14(2), Art. no. 7315609. DOI: 10.1109/ JPHOT.2022.3147844.
71. Chowdhury MZ, Hasan MK, Shahjalal M, Hossan MT, Jang YM. Optical wireless hybrid networks: trends, opportunities, challenges, and research directions. *IEEE Commun. Surv. Tutor.,* 2020, 22:930-966. DOI: 10.1109/COMST.2020.2966855.
72. Dunbabin M, Corke P, Vasilescu I, Rus D. Data muling over underwater wireless sensor networks using an autonomous underwater vehicle. Proc. *IEEE International Conference on Robotics and Automation* (*ICRA*), 2006, pp, 2091-2098. DOI: 10.1109/ ROBOT.2006.1642013.
73. Islam KY, Ahmad I, Habibi D, Zahed MIA, Kamruzzaman J. Green Underwater Wireless Communications Using Hybrid Optical-Acoustic Technologies. *IEEE Access,* 2021, 9:85109-85123. DOI: 10.1109/ ACCESS.2021.3088467.

DOI: 10.17725/j.rensit.2024.16.043

Investigation a method for measuring blood pressure with a capacitive integrated sensor

Andrey K. Movchan, Eugeniy V. Lomakov, Eugeniy V. Rogozhnikov, Kirill V. Savenko
Tomsk State University of Control Systems and Radioelectronics, https://tusur.ru/
Tomsk 634050, Russian Federation
E-mail: ltaak@tu.tusur.ru, evgenii.v.lomakov@tusur.ru, evgenii.v.rogozhnikov@tusur.ru, kirill.savenko@tusur.ru

Received October 19, 2023, peer-reviewed October 26, 2023, accepted November 02, 2023, published March 15, 2024.

Abstract: **A method of wireless measurement of blood flow parameters is investigated using an implantable passive capacitive sensor and an external reader. This device is designed to measure the parameters of blood flow in the human body, through the installation of a passive capacitive sensor and inductive coupling with an external reader device. The method of wireless measurement is based on the connection of resonant circuits at an operating frequency of 10 MHz. The mathematical calculation of the device circuit is presented. The result of the calculation was the dependence of the output voltage of the external reader on the change of capacitance in the implanted passive sensor. The values of the potential sensitivity of the device are obtained. The manufactured layout of the device and its parameters are presented. The mock-up allowed to investigate the dependences of the coupling factor of the circuits when using coils of an external reader of different sizes. Also the measurement of the output voltage of the external reader from the value of the passive sensor capacitance was made. The value of real sensitivity of the device layout was measured.**

Keywords: **resonant circuit, passive sensor, blood flow, coupling factor, stent, capacitive sensor**

UDC 621.31

For citation: Andrey K. Movchan, Eugeniy V. Lomakov, Eugeniy V. Rogozhnikov, Kirill V. Savenko. Investigation a method for measuring blood pressure with a capacitive integrated sensor. *RENSIT: Radioelectronics. Nanosystems. Information Technologies,* 2024, 16(1):43-52e. DOI: 10.17725/j.rensit.2024.16.043.

Contents

1. INTRODUCTION

Cardiovascular diseases (CVD) remain the leading form of mortality worldwide, which may affect one in three of us. Atherosclerosis is a progressive form of CVD that is characterised by the imperceptible development of fatty plaques that are caused by proliferation of vascular smooth muscle cells and influx of inflammatory cells and proteins [1]. This leads to narrowing of blood vessels and restricted blood flow, which is responsible for most heart attacks and strokes. The problem remains unresolved despite intensive research and numerous drug trials. The consequences of vasoconstriction often require surgical intervention, one of which is the endoprosthesis of arterial aneurysms with a stent graft. Stent restenosis

may occur despite the successful opening of blood vessels and restoration of blood flow. Stents are developed with the integration of devices that include various sensors, as well as a wireless communication system. This is necessary for early diagnosis of restenosis and monitoring of blood flow in real time. Integrated devices can be categorized into active and passive devices. The advantage of active devices is a high level of functionality, since electronic circuits and power supply devices are integrated together. However, such devices have a disadvantage in the built-in power supply device, which has a limited service life. Consequently, such devices are unsuitable for implantation into the human body or into a blood vessel. Also, active devices can have wireless communication, as described in the article [2]. But in this paper, the simulation is carried out using an optimal current source and complex circuits, which increases the cost of such a sensor. Passive devices do not need a constant power source, but have lower efficiency compared to active ones. Also, passive devices have a lower manufacturing cost. As a rule, an integrated passive device includes a capacitor and an inductor, which can be a conventional inductor or an arterial stent [3].

The integrated passive devices can be designed in a variety of ways. One of the articles under consideration describes an implementation where an external signal source creates a radio frequency field that affects the resonant circuit of a passive device. The passive device has a resonant frequency due to inductance and capacitance. The oscillations at the frequency of the external source are generated during the operation of the passive device in the resonant circuit. Then the external device receives the parameter due to inductive coupling with a passive sensor. The parameter is related to the oscillations that are necessary to evaluate the characteristics of the fluid flow through the stent. Despite the scope of this study, the working distance of the sensor is several millimeters, which is not enough for the sensor to work in the human body [4].

Also, articles [5,6] consider variants of embedded antennas in passive sensors that allow improving the efficiency of wireless transmission of energy and data.

We can conclude that the area of implantable sensors is being actively explored for monitoring blood flow parameters. We have established that methods of early detection of restenosis need further research and development, including integrated sensors and external reader devices.

This work considers the possibility of implementing remote measurement of blood flow parameters due to an integrated passive capacitive sensor that is inductively connected to an external reader device.

2. MEASURING PRINCIPLE

The measurement principle is implemented as follows: the external reader device and the passive sensor are the primary and secondary resonant circuits, which are schematically shown in **Fig. 1.** The primary circuit consists of an inductance L_1 and a capacitor C_1, which form an LC oscillating circuit. The circuit also has a signal generator for generating oscillations with a certain frequency. The secondary circuit includes an inductance L_2 and a variable capacitor C_2, which mimics a capacitive sensor to form an LC-oscillating circuit.

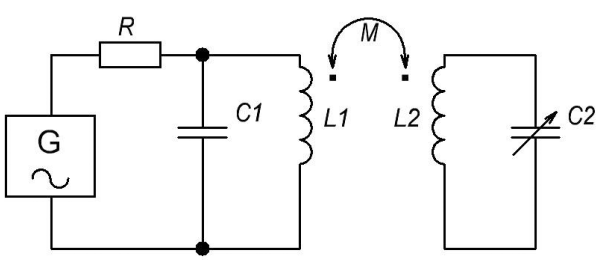

Fig. 1. *Simplified electrical diagram.*

The secondary circuit receives energy from the primary circuit due to their inductive coupling. In this case, the blood flow affects the capacitive sensor, thereby affecting the parameters of the primary circuit due to inductive coupling.

The resonant frequency of a passive device can be expressed as its function of inductance L and capacitance C, as shown in equation (1)

$$\omega_0 = \frac{1}{\sqrt{LC}}. \quad (1)$$

The value of the inductance of the passive device remains constant after manufacture, and the capacitance of the capacitor changes when the parameters of the blood flow change. Accordingly, the resonant frequency of the passive device will also depend on the parameters of the blood flow according to expression (1). Remote determination of the parameters of the internal passive device is realized due to the inductive coupling of the external and internal devices. As a result, the parameters of the integrated sensor affect the parameters of the reader device. This allows to be determined the blood flow parameters on the external device side.

Energy losses during the propagation of radio frequency signals can depend on many parameters, including the resonant frequencies of the two coils and their orientation. If the thickness of the tissue between the external and internal devices is less than one tenth of the wavelength, then the energy absorption is proportional to the square of the signal frequency. Therefore, the operating frequency of the signal cannot be too high. In other words, a system with a high resonant frequency is capable of transmitting a large amount of energy, but this frequency must be reduced due to the increase in energy absorbed by human tissues. On the other hand, high Q-factor are difficult to obtain at low resonant frequencies. Therefore, the resonant frequency should be chosen according to the factors of the device application. In this study, the operating frequency was chosen to be 10 MHz.

High energy transfer efficiency is important in wireless systems where energy is transferred from one coil to another. The high Q-factor allows the oscillating circuit to save energy for a long time. Also, the high Q-factor allows to reduce energy losses and improve transmission efficiency.

The Q-factor of the circuit is determined by the ratio of the characteristic impedance ρ of the oscillating circuit to the internal resistance r of this circuit:

$$Q = \frac{\rho}{r}. \quad (2)$$

The characteristic impedance of the circuit is defined by the formula:

$$\rho = \sqrt{\frac{L}{C}}. \quad (3)$$

The internal resistance of the external circuit is selected 0.1 Ohm, and the required Q-factor is at least 500. The parameters of the oscillatory circuit are obtained equal to L = 800 nH and C = 320 pF based on the condition of the oscillation frequency of the circuit equal to 10 MHz and formula (4):

$$f = \frac{1}{2\pi\sqrt{LC}}. \quad (4)$$

3. MATHEMATICAL MODELING

The idea of a non-contact passive sensor of blood flow parameters investigated in this work is based on inductively coupled resonant circuits, as shown in **Fig. 2**.

The resonant circuit of the integrated part of the sensor is formed by elements L_2, r_2 and the capacitive sensor C_2, and the external circuit of the reader part is formed by elements L_1, r_1, C_1. The equivalent sources e_{21} and e_{12} reflect the mutual electromotive force (EMF) that is induced in each of the circuits due to the action of the inductive coupling. The source E_0 is the energy

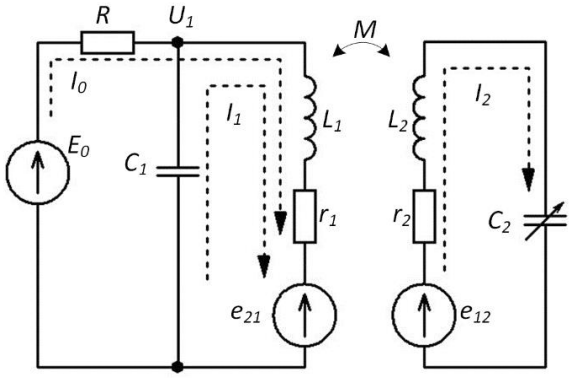

Fig. 2. *Electrical diagram of the sensor.*

source in this circuit and forms a harmonic EMF with a circular frequency ω.

The output parameter of the reader part of the sensor is the voltage U_1 of the external reader circuit. In this case, U_1 is determined by the circuit parameters and, in particular, by the capacitance of the capacitive sensor C_2, which is used in the device for measuring blood flow parameters. The change in the output parameter U_1 can be determined using a linear amplitude detector. The estimate of the potential sensitivity of the sensor is determined from the dependence $U_1(C_2)$, where U_1 is the output voltage of the reader part, C_2 is the capacitance of the capacitive sensor of the integrated part of the device.

$U_1(C_2)$ is determined using the mesh current method [7]. The system of equations of mesh current for the circuit shown in Fig. 2 has the following form:

$$\begin{cases} (R + r_1 + j\omega L_1)I_0 + (r_1 + j\omega L_1)I_1 - e_{21} = E_0, \\ (r_1 + j\omega L_1)I_0 + (r_1 + j\omega L_1 + \dfrac{1}{j\omega C_1})I_1 - e_{21} = 0, \\ (r_2 + j\omega L_2 + \dfrac{1}{j\omega C_2})I_2 - e_{12} = 0. \end{cases} \quad (5)$$

The mutual induction EMFs e_{21} and e_{12} are determined as follows in the respective circuits:

$$e_{21} = j\omega M I_2, \quad (6)$$

$$e_{12} = j\omega M (I_0 + I_1), \quad (7)$$

where M is the mutual inductance of the connected circuits, defined as:

$$M = k\sqrt{L_1 L_2}, \quad (8)$$

where k is the coupling factor of the coupled circuits determined by the mutual configuration of the windings of inductances L_1 and L_2 and the distance between them.

The following substitutions are used to simplify the presentation of the results of solving contour equations (5):

interaction impedance

$$X_M = \omega M, \quad (9)$$

serial impedance of the reader circuit Z_1

$$Z_1 = r_1 + j\omega L_1 + \frac{1}{j\omega C_1}, \quad (10)$$

impedance $L_1 r_1$ of the reader circuit branch Z_{11}

$$Z_{11} = r_1 + j\omega L_1, \quad (11)$$

serial impedance of the integrated circuit Z_2

$$Z_2 = r_2 + j\omega L_2 + \frac{1}{j\omega C_2}. \quad (12)$$

Taking into account the above mentioned substitutions, the system of equations of mesh current for the circuit shown in Fig. 2 will have the following form:

$$\begin{cases} (R + Z_{11})I_0 + Z_{11}I_1 - jX_M I = E_0, \\ Z_{11}I_0 + Z_1 I_1 - jX_M I_2 = 0, \\ Z_2 I_2 - jX_M (I_0 + I_1) = 0. \end{cases} \quad (13)$$

The solution of the system of equations (5) will be expressions for the currents corresponding to the branches of the circuit shown in Fig. 2. In particular, the expression for the current I_0 feeding the reader circuit has the following form:

$$I_0 = \frac{E_0}{R + Z_{11} + \dfrac{X_M^2}{Z_2} - \dfrac{\left(Z_{11} + \dfrac{X_M^2}{Z_2}\right)^2}{Z_1 + \dfrac{X_M^2}{Z_2}}}. \quad (14)$$

In expression (14), the summand $X_M^2 / Z_2 = Z_{ins}$ is the amount of insertion

resistance from the integrated circuit to the readout circuit.

The introduced resistance Z_{ins} is a consequence of the inductive coupling of the circuits and is determined by the magnitude of the coupling factor k and, importantly, the parameters of the integrated circuit.

The expression for the current I_0 will take the following form taking into account the introduced notation Z_{ins}

$$I_0 = \frac{E_0}{R + Z_{11} + Z_{ins} - \frac{(Z_{11} + Z_{ins})^2}{Z_1 + Z_{ins}}}. \quad (15)$$

From equations (13) it is also possible to determine the values of the remaining currents using the current I_0. Thus, the expression for the current I_1 of the read circuit is as follows:

$$I_1 = \frac{Z_{11} + Z_{ins}}{Z_1 + Z_{ins}} I_0. \quad (16)$$

Expression for the current I_2 of the integrated circuit

$$I_2 = \frac{jX_M}{Z_2}(I_0 + I_1). \quad (17)$$

The voltage U_1 on the reader circuit can be obtained as follows:

$$U_1 = E_0 - RI_0. \quad (18)$$

Expression (18) leads to the following result for U_1 taking into account (15):

$$U_1 = E_0 \left[1 - \frac{R}{R + Z_{11} + Z_{ins} - \frac{(Z_{11} + Z_{ins})^2}{Z_1 + Z_{ins}}} \right]. \quad (19)$$

Fig. 3 shows the dependence of the absolute value of the voltage on the reader circuit on the frequency $U_1(f)$. Dependences are plotted for three values of coupling factor k_1 = 0.05, k_2 = 0.01, k_3 = 0.005 and frequency range f from 9.5 MHz to 10.5 MHz. The values of the parameters of the circuit elements (Fig. 2) are as follows: E_0 = 10 *V*, R = 1 kOhm, $L_1 = L_2$ = 800 nH, $C_1 = C_2$ = 320 pF, r_1 = 0.1 Ohm, r_2 = 1 Ohm.

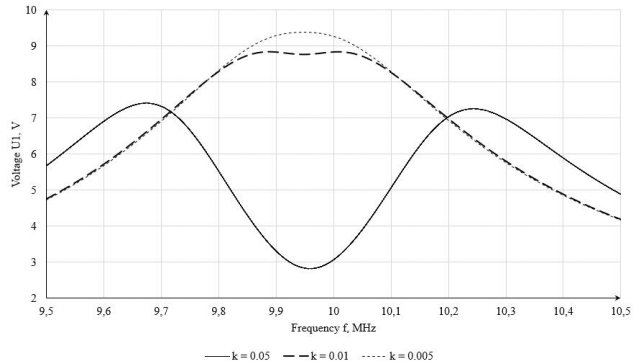

Fig. 3. *The dependence of the absolute value of the voltage on the reading circuit on the frequency.*

The voltage U_1 on the reader circuit and its dependence on the capacitance of the capacitive sensor of the integrated circuit must be determined to assess the potential sensitivity of the sensor.

Fig. 4 shows the dependence of the absolute value of the voltage on the reader circuit on the capacitance value of the sensor of the integrated circuit $U_1(C_2)$.

The dependences are constructed for three values of the coupling factor k_1 = 0.05, k_2 = 0.01, k_3 = 0.005 and the range of variation C_2 from 260 pF to 380 pF. The values of the parameters of the circuit elements (Fig. 2) are as follows: R = 1 kOhm, $L_1 = L_2$ =800 nH, C_1 = 320 pF, r_1 = 0.1 Ohm, r_2 = 1 Ohm, f = 10 MHz.

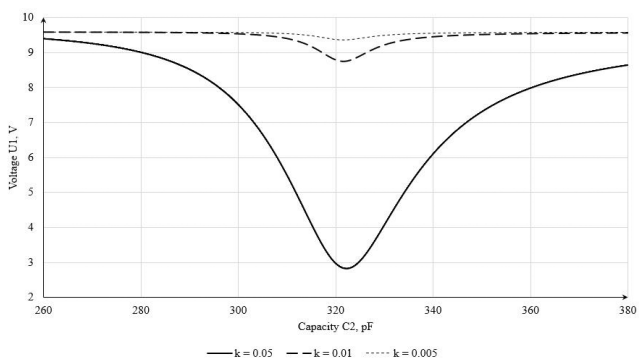

Fig. 4. *Dependences of the absolute value of the voltage on the reading circuit on the capacitance C_2.*

In this case, the potential sensitivity of the sensor is determined by the dependence of the voltage change ΔU_1 on the reader circuit when the capacitance C_2 in the integrated circuit changes by the value ΔC. That is, it is necessary to find the differential of the dependence $U_1(C_2)$:

$$\Delta U_1(C_2) = \frac{\partial}{\partial C_2} U_1(C_2) \cdot \Delta C. \quad (20)$$

Expressions (5) are calculated and dependences $\Delta U_1(C_2)$ are constructed for three values of the coupling factor $k_1 = 0.05$, $k_2 = 0.01$, $k_3 = 0.005$, frequency $f = 10$ MHz, the range of capacitance C_2 from 260 pF to 380 pF and $\Delta C = 1$pF. The remaining parameters of the circuit elements (Fig. 2) are as follows: $R = 1$ kOhm, $L_1 = L_2 = 800$ nH, $C_1 = 320$ pF, $r_1 = 0.1$ Ohm, $r_2 = 1$ Ohm.

Based on the graphs shown in **Fig. 5**, the maximum sensitivity values $\Delta U_1(C_2)$ at $\Delta C = 1$ pF for each of the values of the coupling factor have the following values: for $k_1 = 0.05$, the maximum sensitivity is achieved when the capacitance of the capacitive sensor $C_2 = 310$ pF and is $\Delta U_1(C_2) = -0.237$ V/pF, for $k_2 = 0.01$, when $C_2 = 317$ pF, $\Delta U_1(C_2) = -0.085$ V/pF, and for $k_3 = 0.005$, when $C_2 = 318$ pF, $\Delta U_1(C_2) = -0.024$ V/pF. The minus sign in $\Delta U_1(C_2)$ indicates that as the capacitance of C_2 increases, the voltage U_1 decreases.

The results obtained show that the sensitivity of this meter depends on the coupling factor of the circuits k, i.e. on the mutual configuration

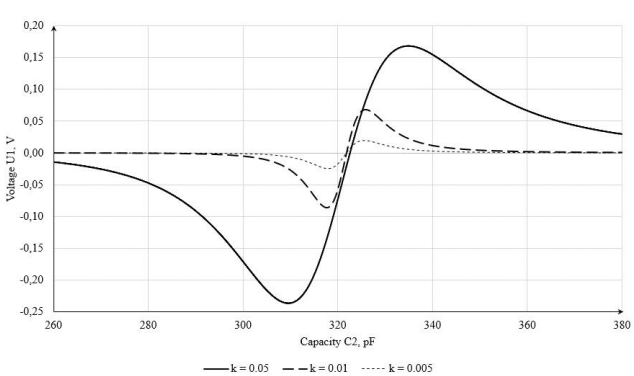

Fig. 5. *Dependences of sensor sensitivity on C_2 capacity.*

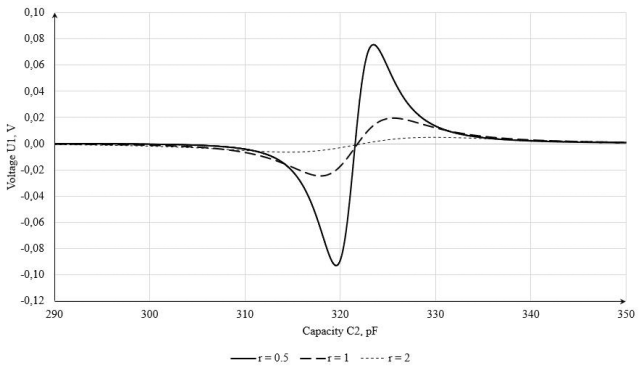

Fig. 6. *Dependences of sensor sensitivity on C_2 capacity.*

of the inductance windings L_1 and L_2 and the distance between them.

Since r_2 to make a small value is a very labour-intensive task in view of the small overall size of the coil L_2, it is of interest to obtain the dependence of the sensor sensitivity on the active loss resistance r_2 in the integrated circuit.

Fig. 6 shows the dependences of the sensor sensitivity $\Delta U_1(C_2)$ for a fixed value of the coupling factor $k = 0.005$ and three values of the loss resistance r_2 in the integrated circuit: $r_2 = 0.5$ Ohm, $r_2 = 0.5$ Ohm and $r_2 = 2$ Ohm. Frequency is $f = 10$ MHz, the range of capacitance C_2 is from 290 pF to 350 pF and $\Delta C = 1$ pF. The remaining parameters of the circuit elements (Fig. 2) are as follows: $R = 1$ kOhm, $L_1 = L_2 = 800$ nH, $C_1 = 320$ pF, $r_1 = 0.1$ Ohm.

Based on the graphs shown in Fig. 6, the maximum sensitivity values $\Delta U_1(C_2)$ at $\Delta C = 1$ pF for each of the loss resistance values r_2 have the following values: for $r_2 = 0.5$ Ohms, the maximum sensitivity is achieved at the capacitance of the capacitive sensor $C_2 = 319$ pF and is $\Delta U_1(C_2) = -0.092$ V/pF, for $r_2 = 1$ Ohm, at $C_2 = 318$ pF, $\Delta U_1(C_2) = -0.02$ V/pF, and for $r_2 = 2$ Ohms, at $C_2 = 314$ pF, $\Delta U_1(C_2) = -0.006$ V/pF.

The results obtained show that the sensitivity of this meter also significantly depends on the loss resistance r_2. At the same time, the active resistance of losses in the L_2 coil of the integrated circuit must be reduced to increase the sensitivity of the device.

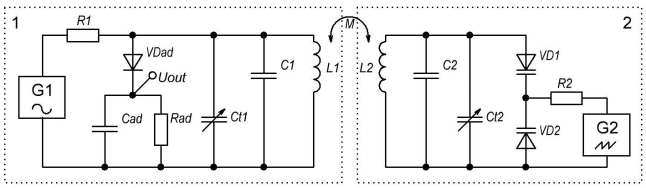

Fig. 7. *Electrical schematic diagram of the layout.*

4. EXPERIMENTAL RESEARCH

The experimental layout was designed and assembled to study the practical implementation of the described method based on the above. **Fig. 7** shows the electrical circuit of the layout, which contains the following components: inductance $L_1 = L_2 =$ 800 nH, constant capacitance $C_1 = C_2 = 300$ pF, variable capacitance $C_{t1} = C_{t2} = 2$-30 pF, resistor $R_1 =$ kOhm, generator of a sinusoidal signal with a frequency $G_1 = 10$ MHz, varicap $VD_1 = VD_2 =$ KB121A, limiting resistor $R_2 = 152$ kOhm, generator of linearly increasing voltage with frequency $G_2 = 2$ Hz, diode $VD_{ad} = 1N4148$, constant capacitance $C_{ad} = 12$ nF, resistor $R_{ad} = 100$ kOhm.

Components L_1, C_1, C_{t1} form the primary oscillating circuit (reader circuit), L_2, C_2, C_{t2} form the secondary oscillating circuit (integrated circuit), VD_{ad}, C_{ad}, R_{ad} form the amplitude detector of the primary circuit, VD_1, VD_2 form the voltage controlled variable capacitance to simulate the operation of the capacitive sensor of the integrated circuit.

Fig. 8 shows the voltage dependence of the capacitance, which is the main characteristic of the voltage-controlled variable capacitance for this device.

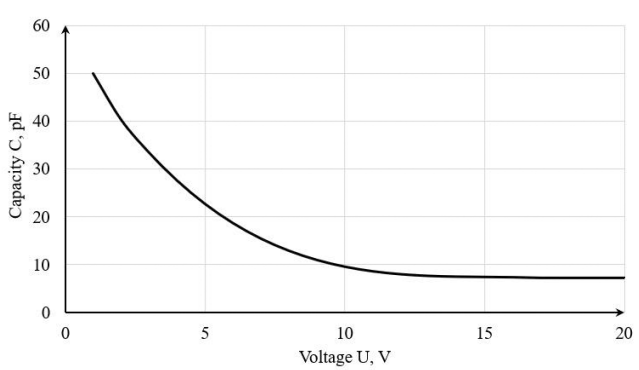

Fig. 8. *Capacitance-voltage curve of the KV121A varicap.*

The pressure-simulating signal can be isolated using an amplitude detector. The amplitude detector is used to isolate the amplitude envelope of a high-frequency radio signal. The calculation of the parameters of the amplitude detector was based on the condition of formula (17) and the parameters of the experimental layout.

$$Xc = \frac{1}{2\pi f \cdot C}. \quad (17)$$

The layout consists of two universal printed circuit boards with a soldered circuit, according to Fig. 7. One of the printed circuit boards is fixed and represents the primary circuit. The secondary circuit is located on a movable printed circuit board, which has the ability to move in the longitudinal axis, thereby making it possible to change the distance between the coils of the primary and secondary circuits. **Fig. 9** shows the assembled layout.

The first stage of the work is to study the dependence of the coupling factor on the form factor of the coils. The coupling factor of inductance determines the degree of mutual inductive coupling between two coils in an electrical circuit. It shows how a change in the current I_1 in one coil affects the induction of voltage U_2 in another coil. The coupling factor depends on the geometry of the coils, the distance between them and other factors. It is assumed that the inductance coil included in the passive device has small overall dimensions due to the limitation that this coil is integrated into a human artery.

It is assumed that the inductance included in the passive device has small overall

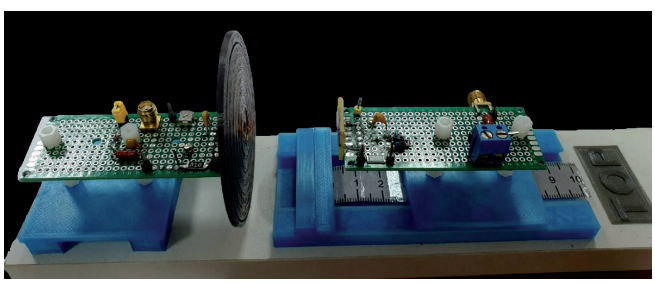

Fig. 9. *Experimental layout.*

dimensions due to the limitation that this coil is integrated into a human artery. Therefore, the form factor of the external reader coil must be changed to achieve a high coupling factor. A flat spiral coil on a printed circuit board was used as an inductance oMf a passive device with the following characteristics: outer diameter D = 15 mm, inner diameter d = 2 mm, printed track width W = 0.035 mm, winding pitch s = 0.6 mm, printed conductor thickness h = 0.035 mm, number of coils turns N = 11, inductance L = 800 nH.

Table 1 shows the parameters of the coils that were used as the inductance of the external device. Coils 1-3 have the shape of a ring, wound turn to turn, coil 4 has the shape of a flat spiral.

Table 1

Parameters of external coils

Coil	D, mm	d, mm	N	L, nH
1	22	10	6.3	760
2	28	20	4.25	720
3	64	60	2.25	760
4	54	10	5	850

All the capacitive elements, as well as the elements of the amplitude detector, were switched off when measuring the coupling factor from the circuit shown in Fig. 7. **Fig. 10** shows the graphs that were obtained as a result of the study of the dependence of the coupling factor on the distance for various external inductance.

The formula for calculating the coupling factor is (18).

$$k = \frac{U_2}{2\pi f I_1 \sqrt{L_1 L_2}}. \quad (18)$$

We can conclude from the data on the graph shown in Fig. 10 that the form factor of the coils affects the coupling factor. Coil 4 is used for further research in the external reader circuit, due to the greater coupling factor at the interval from 10 mm to 40 mm.

The next stage of the work is the measurement of the volt-farad characteristics of the sensor, in accordance with the scheme shown in Fig. 7. A linearly increasing voltage was applied from the generator to the varicap to simulate pressure changes. The magnitude of the amplitude varied in the range according to the volt-farad characteristic of the varicap shown in **Fig. 11**.

The range of capacitance variation is limited by the volt-farad characteristic of the varicap, in this regard, only part of the dependence of the output voltage of the primary circuit on the capacitance value of the capacitive sensor is shown. The curve of the volt-farad characteristic has an asymmetric character based on the graph shown in Fig. 11. This is caused by the difference in the parameters of the primary and secondary circuits, as well as the nonlinear dependence of the varicap capacitance on the applied voltage. The

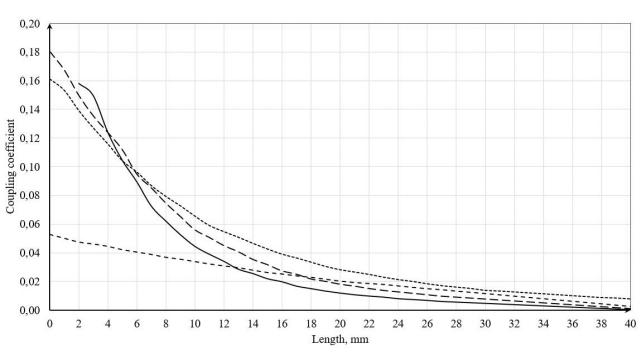

Fig. 10. *Experimental dependences of the coupling factor on the distance.*

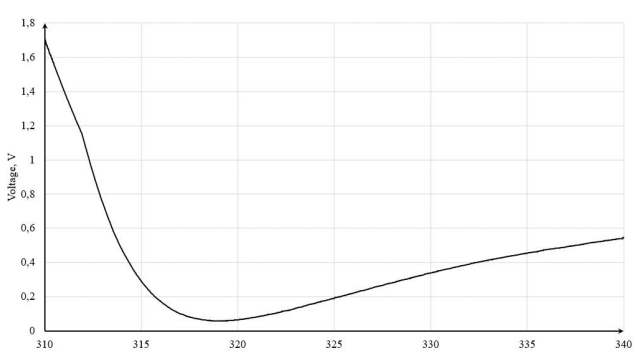

Fig. 11. *Experimental capacitance-voltage curve of the sensor.*

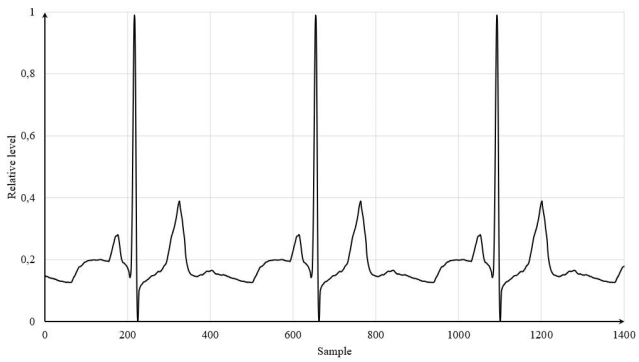

Fig. 12. *Cardioimpulse.*

maximum value of the real sensitivity $\Delta U_1(C_2)$ was 30 mV/pF.

Further simulations of blood pressure changes were performed using a G_2 generator connected to the secondary circuit. **Fig. 12** shows samples of the cardiac pulse signal that was generated by the G_2 generator. This signal, having 438 samples per pulse, with a frequency of 2 Hz was applied to the varicaps (Fig. 7), thereby changing the total capacity of the secondary circuit. **Fig. 13** shows factorgram at the output of the linear amplitude detector of the reader device.

The graph of the output signal of the reader circuit has some differences from the signal loaded into the generator G_2, due to the nonlinearity of varicaps, the difference of parameters of both circuits, and the small number of samples per pulse. The nonlinearity of the sensor can be compensated by calibrating the device.

Fig. 13. *The output signal of the reader circuit.*

5. CONCLUSION

This work deals with a method of wirelessly measuring blood flow parameters using an implantable passive sensor and reader device. This study performs a mathematical calculation of the electrical circuit of the measuring device, which resulted in the dependence of the output voltage of the reader device on the change of capacitance in the implanted sensor. The potential sensitivity of the measuring device is calculated based on the obtained dependencies for the specified parameters. The potential sensitivity was $\Delta U_1(C_2)$ = –0.085 V/pF with a contour coupling factor k = 0.01.

Next, the manufactured layout was presented and its parameters were given. The dependence of the coupling factor of the circuits was studied for different dimensions of the primary circuit coils on this layout. The coupling factor was k = 0.008 when using a spiral coil with a diameter of 54 mm of the primary circuit and a coil of a secondary circuit with a diameter of 15 mm at a distance of 40 mm based on the results obtained. Next, the dependence of the output voltage of the reader device on the change in the capacitance of the secondary circuit was measured. The capacitance of the secondary circuit was changed by a linear change in the voltage on the varicap. The real sensitivity of the measurement device layout was estimated and amounted to 0.03 V/pF at a distance between the coils of 35 mm, which corresponds to the coupling factor $k \approx 0.011$. The difference between the potential and real sensitivity of the measuring device is caused by the difference in the parameters of the primary and secondary circuits, as well as the nonlinear dependence of the varicap capacitance on voltage.

An experiment was also performed in which a voltage was applied to the varicaps in the form of a cardioimpulse. As a result, the amplitude detector of the external reader device showed a distorted cardio pulse signal, reflecting the nonlinearity of the measurement device. The

study showed a strong dependence of the output parameter of the device on the distance between the external reader and the implantable sensor and the size of the coils of the contours, as well as on the losses in the contour of the implantable sensor.

The study showed a strong dependence of the output parameter of the device on the distance between the external reader and the implanted sensor and the size of the coils of the circuits, as well as on the losses in the circuit of the implanted sensor. Despite this, the method of measuring blood flow parameters presented in this paper can be used in practice with appropriate calibration.

REFERENCES

1. World Health Organization: Cardiovascular Diseases (CVDs), June 11 2021, accessed: Oct. 1 2023, available: https://www.who.int/news-room/fact-sheets/detail/cardiovascular-diseases-(cvds)
2. Yakovlev A, Kim S, Poon A. Implantable biomedical devices: Wireless powering and communication. *IEEE Communications Magazine,* 2012, 50(4):152-159.
3. Bussooa A, Neale S, Mercer JR. Future of smart cardiovascular implants. *Sensors,* 2018, 18(7):2008.
4. Park J, Kim JK, Patil SJ, Park JK, Park S, Lee DW. A Wireless Pressure Sensor Integrated with a Biodegradable Polymer Stent for Biomedical Applications. *Sensors*, 2016, 16:809.
5. Zhang J, Das R, Abbasi QN, Mirzai N, Mercer J, Heidari H. Dual-band Microstrip Patch Antenna for Fully-Wireless Smart Stent. *IEEE: International Symposium on Antennas and Propagation and USNC-URSI Radio Science Meeting* (*APS/URSI*), 2021, p. 1035-1036.
6. Chen SC, Zhang ZY, Liu CH. Stent-Based Antennas for Smart Stent Applications. *IEEE: International Symposium on Antennas and Propagation* (*ISAP*), 2018, p. 1-2.
7. Yorke R. *Electric Circuit Theory: Applied Electricity and Electronics.* Oxford, Pergamon Press, 1981, 350 p.

DOI: 10.17725/j.rensit.2024.16.053

A Robust and Efficient Scheme for ECG Signal Classification Based on Digital Signal Processing, Feature Engineering Selection, and Random Forest Classifier

Anas Fouad Ahmed, Baraa M. Albaker

Al-Iraqia University, College of Engineering, Electrical Engineering Department, http://www.aliraqia.edu.iq/
Al Adhmia-Haiba Khaton, 6029, Baghdad, Iraq
E-mail: anas.ahmed@aliraqia.edu.iq, baraamalbaker@aliraqia.edu.iq

Hadeel N. Abdullah

University of Technology, Electrical Engineering Department, http://www.uotechnology.edu.iq/
Al wehada-Neighborhood, 19006, Baghdad, Iraq
E-mail: 30002@uotechnology.edu.iq

Received September 11, 2023, peer-reviewed September 18, 2023, accepted September 25, 2023, published March 15, 2024.

Abstract: **Determining the optimal integration between features and classifiers has a significant effect on the performance of automatic heartbeat diagnostic systems. This importance stands out when dealing with critical applications that contain limited resources devices and require accurate and fast heartbeat classifiers to help the doctor make an accurate and quick diagnosis of heart diseases. Aiming at this task, this paper introduces a novel approach for choosing the optimal features of the ECG signal to be used with the Random Forest (RF) classifier following the inter-patient method for ECG signals division and obeying the instructions of the "Association for the Advancement of Medical Instrumentation (AAMI)." The features were chosen based on the concept of "Mutual Information Ranking (MIR)." The presented framework is comprehensive in terms of performing all the necessary processes efficiently, starting from ECG digital signal processing, segmentation, feature extraction, feature selection, and ending with ECG classification. The results of the experiments demonstrate that features corresponding to the normalized QRS width and the normalized RR intervals are the most influential features in the heartbeat classification. All tests were conducted using real ECG signals taken from the "MIT-BIH" Arrhythmia Database (MIT-BIH-ARR-DB). The suggested scheme attained the following F1-scores: 91.02%, 73.17%, and 98.04% in the classification of the Ventricular Ectopic Beats (V or VEB), Supraventricular Ectopic Beats (S or SVEB), and Normal Beats (N or NB), respectively. The overall accuracy was 96.26%. Despite its relative simplicity and reliance on few features, the proposed approach outperforms most of the reported state-of-the-art.**

Keywords: **Mutual Information; Feature Selection; Cardiac Arrhythmia; Discrete Wavelet Transform (DWT); ECG classification; Random Forest (RF)**

UDC 53.047:57(075.8)

For citation: Anas Fouad Ahmed, Hadeel N. Abdullah, Baraa M. Albaker. A Robust and Efficient Scheme for ECG Signal Classification Based on Digital Signal Processing, Feature Engineering Selection, and Random Forest Classifier. *RENSIT: Radioelectronics. Nanosystems. Information Technologies*, 2024, 16(1):53-66e. DOI: 10.17725/j.rensit.2024.16.053.

Contents

1. INTRODUCTION

Cardiovascular ailments are the main reason for killing millions of people around the world, and the electrocardiogram (ECG) signal is a magnificent and effective means in their diagnosis [1,2]. The ECG is a low-cost and non-invasive means frequently used by cardiologists to record electrical activity and to detect abnormalities in the heart [3-5]. The ECG instrument senses this electrical activity using electrodes placed on the body and shows it on the screen [6-9]. An ECG signal is composed of a collection of periodical heartbeats, which are examined by a doctor to make a diagnosis and treatment [10]. This procedure relatively requires a lot of time and intensive efforts, in addition to human errors that may occur due to workload [11]. Nowadays, it has become easier to acquire the ECG signal due to the availability of portable and wearable devices and the possibility of using them in ambulatory healthcare applications [12]. Employing these devices requires evolution not only in accuracy and reliability but also simple and computationally efficient methods for intelligent automatic heartbeat detection and classification to limit the amount of information or data required to be sent to the doctor to evaluate the case and give counsel [13].

By referring to the AAMI, the approaches that classify the heartbeats must at most discriminate the following categories: Fusion Beats (F or FB), Unclassifiable or paced Beats (Q or QB), (VEB), (SVEB), and (NB). It is necessary to detect and count the number of period ectopic beats to avoid dangerous heart disease. For instance, the repetition of SVEB is related to dangerous illness, "Atrial Fibrillation," also the recurrence of VEB is exceptionally indicator because it can be utilized as a predictor of the most dangerous disease, "Heart Failure," which often leads to death [14,15].

Many efforts have been made by researchers in recent years to solve the problem of automatic diagnosing or classifying heartbeats by proposing various techniques to fulfill this task. Generally, these techniques can be classified into two approaches: the first one is based on a deep-learning strategy, while the other is based on a feature-engineering. Some researchers have applied Deep Neural Networks (DNNs) for classifying ECG signals [16-18], but the DNN experiences redundancy of parameters and complexity of calculations. It is significant to mention here that the analytical classification based on features engineering can assist cardiologists in accurately diagnosing and precisely drawing up suitable therapy schedules by taking advantage of the understandable extracted features.

Deep learning algorithms, on the other hand, are unable to provide cardiologists with interpretable features and cannot analyze the effects of feature selection on ECG classification efficiency because the features are tacitly captured by deep layers in the network.One of the most important surveys of heartbeat classification schemes was introduced by Luz et al. [19]. Machine learning (ML) techniques have enticed great interest nowadays, and perhaps the most famous of these is the RF technique, in which a set of classifiers is produced as an "ensemble" of Decision Trees (DTs) [20]. The input is classified by the ensemble (forest) based on the majority principle [21]. Therefore, the RF classifier is considered extremely effective and has been recommended for resource-restricted devices that are intended to work in real-time [22-25]. Emanit [26] applied the DWT to the ECG signals and used the resultant coefficients as features to train the RF classifier. Llamedo et al. [27] presented a simple ECG classifier that classifies the SVEB and VEB based on coefficients of the DWT and RR intervals. Alickovic and Subasi [28] suggested utilizing the distribution of DWT coefficients to extract various features that feed into RF for heartbeats classification purposes. Gutierrez et al. [29] classified ECG signals using Quadratic Wavelet Transform (QWT) and neural networks. Ganesh and Kumaraswamy [30] proposed a method for ECG signals classification based on RR intervals and features extracted by taking the Discrete Cosine Transform (DCT) for ECG signals to train the RF classifier. Park et al. [31] used collections of different time-domain features with an RF classifier for heartbeat classification. Aravind et al. [32] offered an algorithm for heartbeat classification using the Convolutional Neural Network (CNN) and Continuous Wavelet

Transform (CWT). Yuanlu et al. [33] classified the ECG signal based on deep residual CNN.

The aforementioned studies achieved excellent accuracy (ACCo); however, some limitations exist, such as few of them: obeyed the AAMI guidelines regarding the type of heartbeat to be detected and classified, offered a robust model that can be applied to imbalanced data or signals directly, and employed the other metrics to evaluate the classification quality, such as F1-Score, besides the Positive Predictivity (PPr), and Sensitivity (Sen), that may be degraded because of the majority class domination. Most importantly of all, there are no previous studies (as far as the authors know) that deal with the use of the RF classifier obeying the inter-patient mode. In this mode, the signals are separated into two groups: the first is used in the training phase and the second is used in the test phase, and there is no intersection between the two groups (there are no signals taken from the same patient in both groups) this leads to a more reliable assessment of the performance of the classifier. In this research, we used an efficient RF classifier for classifying the ECG signals according to the AAMI recommendations and the inter-patient mode. The following are the contributions of this work:

- We introduce a comprehensive, robust, and efficient framework for ECG signals classification based on an improved RF classifier, taking into consideration all the required digital signal processing and analysis for the collected signals and adhering to the instructions of the AAMI and the inter-patient mode.
- A simple and efficient mechanism for detecting R-peaks based on trigonometry is proposed.
- New considerations for evaluating the normalized features are presented.
- Optimizing the performance of the RF classifier without requiring complex computations by using the MIR to obtain an optimal and reduced group of features from a large feature set that contains the most important features suggested in previous studies.
- Successful dealing with the problem of imbalanced data of ECG signals where the abnormal signals are much less than normal signals; this attained by using the RF classifier, which is actually composed of an ensemble of several DTs that are sensitive to imbalanced classes and it takes a Uniform Random Sample (URS) from the data of ECG signal with replacement strategy.
- An understandable analysis for ECG signal is attained by providing feature sets from various ECG signals, which are indispensable for medical purposes.

2. PROPOSED FRAMEWORK

The complete block diagram of the suggested framework is illustrated in **Fig. 1**. It consists of the following stages: collecting ECG signals, digital signal preprocessing, preparing heartbeats, features extraction, features selection, heartbeats classification, and classifier evaluation. Each one of these stages is further detailed in the subsequent sections.

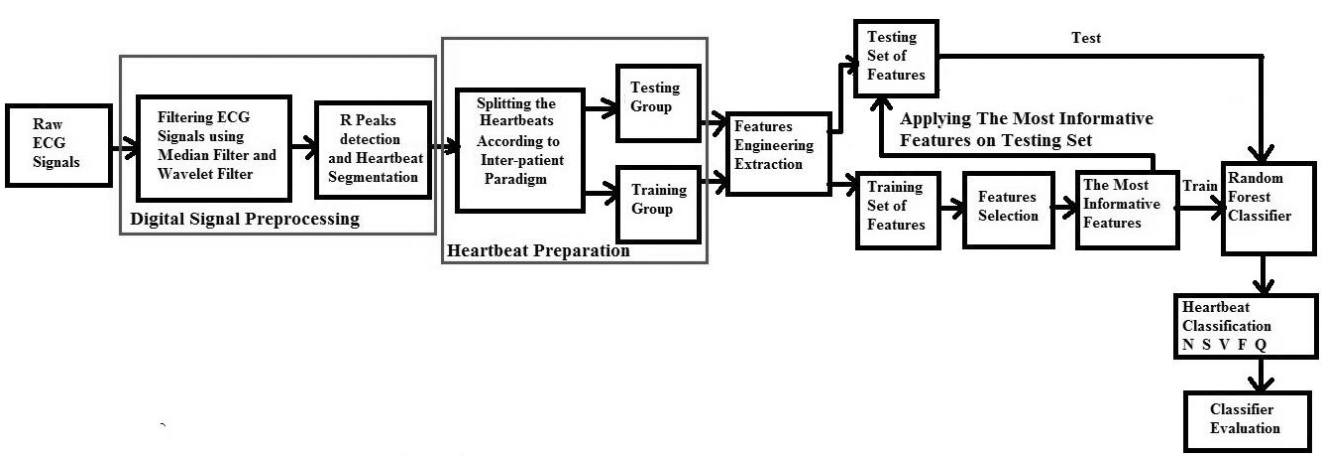

Fig. 1. *Block diagram of suggested framework.*

2.1. Collecting ECG signals

The ECG signals were collected from MIT-BIH-ARR-DB, which is available in [34]. It is well-known and used by many researchers, and this facilitates the process of comparing the suggested scheme with previous works. **Table 1** describes these signals briefly.

Table 1

Description of the collected ECG signals

Parameter	Value
No. Records	48
Duration (Minutes)	30
Sampling Frequency (Hz)	360
Leads	Single (MLII)
No. Heartbeats	109,494
No. Heartbeats types	15
Gender of the Participants (%)	53% males, 47% females
Age Range (Years)	23-89

The relabeling process for the collected signals was conducted to obtain five heartbeats classes according to the AAMI instructions, as shown in **Table 2.**

Table 2

Relabeling the MIT-BIH-ARR-DB according to the AAMI instructions

AAMI Classes with Explaination	MIT-BIH Beats with Labels	
Normal beats (**N**)	N	Normal beat
	L	Left bundle branch block beat
	R	Right bundle branch block beat
	e	Atrial escape beat
	j	Nodal (junctional) escape beat
Supraventricular ectopic beats (**S**VEB)	A	Atrial premature beat
	a	Aberrated atrial premature beat
	J	Nodal (junctional) premature beat
	S	Supraventricular premature beat
Ventricular ectopic beats (**V**EB)	V	Premature Ventricular contraction
	E	Ventricular escape beat
Fusion beats (**F**)	F	Fusion of ventricular and normal beat
Unknown beats (**Q**)	/	Paced beat
	f	Fusion of paced and normal beat
	Q	Unclassified beat

2.2. Digital Signal Preprocessing

In practice, the ECG signals during their acquiring or transmitting are usually corrupted with two main types of noises: Baseline Wanders (BW) and White Gaussian Noise (WGN) [35]. These noises must be reduced as possible to avoid their negative impact on the quality of the signals and the classification performance. **Fig. 2** demonstrates an example of an ECG signal contaminated with BW and WGN.

To obtain baseline-corrected ECG signals, each signal passed through two Median Filters (the width of the first is 200 ms, while the width of the second is 600 ms). Next, it is subtracted from the raw ECG signal. After that, to eliminate the WGN, the DWT is

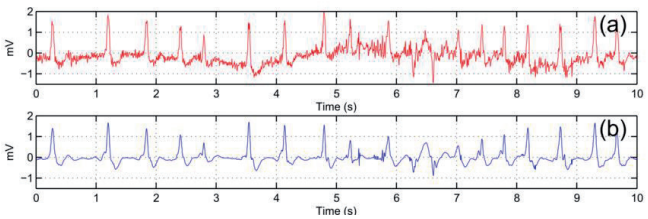

Fig. 2. *An example of ECG signal corrupted with BW and WGN.*

taken for the baseline-corrected signal to decompose it into various frequency bands. The Daubechies-6 (DB6) wavelet filter, four levels of decomposition, soft thresholding scheme (defined in Eq. (1)), and universal threshold determination strategy (given in Eq. (2)) are optimal for removing the WGN from the ECG signal.

$$S_{thresholding}\left(De\right)=\text{sign}\left(De\right)\left(\left|De\right|-t_{hr}\right) \quad \text{for}\left|De\right|>t_{hr},\ \text{and}\,0\ \text{for}\left|De\right|\le t_{hr}, \tag{1}$$

where De are the detail coefficients; t_{hr} is the threshold value.

$$t_{hr}=\text{SDN}.\sqrt{2\log\left(\text{No.Samples}\right)}, \quad \text{SDN}=\text{Median}\left(D\right)/0.6745 \tag{2}$$

where SDN – is the Standard Deviation of Noise.

The DB6 is characterized by the following features [35]:

- It has a very close shape to the ECG signal, which is essential for the ideal reconstruction.
- It is suitable for non-stationary signals due to its short vanishing moments.
- It has relatively low-cost computations due to its orthogonality.

Fig. 3 illustrates the shape of the DB6 wavelet filter.

Fig. 3. *The shape of the DB6 wavelet filter.*

2.3. R Peak Detection

This research suggests a simple and efficient strategy for R peak detection by evaluating the angles in degrees between sequential samples of the amplitude of the signal followed by applying a dynamic threshold to these angles and a time window as described in equations (3), (4), (5), (6), and (7), respectively:

$$\theta(k) = \tan^{-1}\left(\frac{V}{W}\right) = \tan^{-1}\left[\frac{\beta \times \left|\delta(k) - \delta(k-1)\right|}{\dfrac{360}{\text{Sampling frequency}}}\right] \quad (3)$$

$$\beta = \begin{cases} 500, & \textit{initial value} \\ 1000, & \left(\frac{V}{W}\right) < 57.5 \ \textit{or} \ \theta(k) < 89^{\circ} \ \textit{during} \ 2s \ \text{interval} \\ 500, & \left(\frac{V}{W}\right) < 117 \ \textit{or} \ \theta(k) > 89.5^{\circ}, \end{cases} \quad (4)$$

where β is the magnification factor, δ(*k*) is the k^{th} sample of the amplitude.

Note that β in Eq. (4); is adjusted in a way that ensures detection of low-amplitude beats. **Fig. 4** illustrates this concept; when sampling frequency = 360 Hz, it is clear that the range of angles is maintained between 80° and 90°. The dynamic threshold value in degrees *D*(*k*) is varied according to Eq. (5) to tackle the variations of the heartbeats due to different patient cases and recording circumstances. The values of *θ*(*k*) and *D*(*k*) are compared, then the time window *G*(*k*) is used for *R* peak detection.

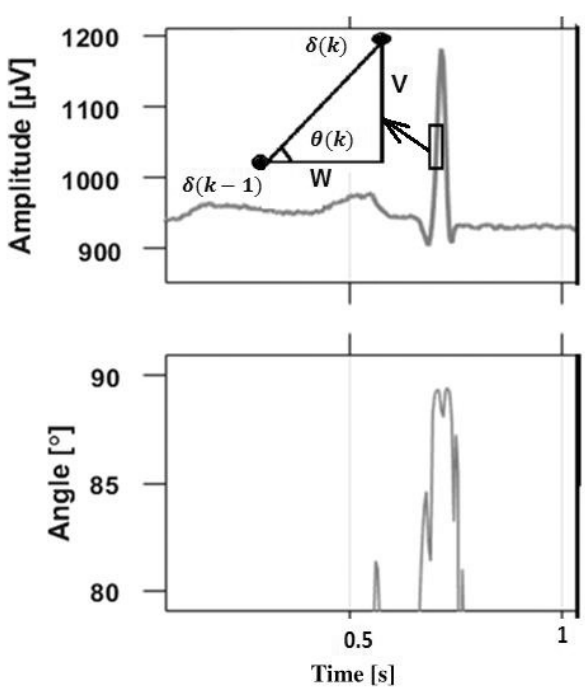

Fig. 4. *Evaluating the angles of the heartbeat based on trigonometry.*

$$D(k+1) = \begin{cases} 0, & \textit{initial value} \\ \theta(k) - Y_1, & \|I\| \theta(k) > D(k) + Y_1 \\ D(k), & \|I\| D(k) > \theta(k) \le D(k) + Y_1, \beta t = 0, \\ D(k) - (Y_2 \times \beta t), & \|\theta(k) \le D(k), \beta t = \beta t + 1 \\ 80, & |D(k) \le 80, \end{cases} \quad (5)$$

where Y_1 and Y_2 are empirically set to 0.4° and 0.00012°, sequentially to get the smallest detection error as illustrated in **Appendix A.**

$$G(k) = \begin{cases} \textit{Signal amplitude}, & 0 \le \beta t \le Y_2 \\ 0, & \textit{otherwise} \end{cases} \quad (6)$$

$$Y_2 = \begin{cases} 0.25s, & \textit{initial value} \\ 0.450s \times F_s, & \textit{Mean of last 8 RR intervals} \ge 0.68s \\ 0.25s \times F_s, & \textit{otherwise.} \end{cases} \quad (7)$$

After the time interval of *G*(*k*) is evaluated, a comparison between the |local maximum| and |local minimum| amplitude of the signal within *G*(*k*) is conducted; the highest one is specified as the *R* peak point, as illustrated in **Fig. 5.** The strengths of the proposed strategy can be summarized as follows: Eq. (1) guarantees that the relationship between *θ*(*k*) and |δ(*k*) – δ(*k* – 1)| is nonlinear, and *θ*(*k*) is restricted for a fixed range (0° and 90°). In other words, *θ*(*k*) is immune to the different changes of the QRS complex. Moreover, the $\tan^{-1}$ term makes the computation of *θ*(*k*) easy and fast.

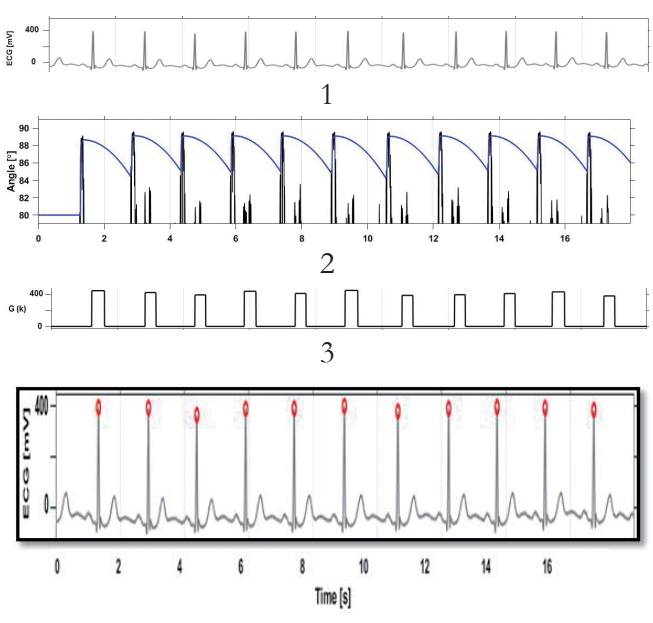

Fig. 5. *A demonstrative example of the suggested approach for detecting the R peaks. (1). Denoised signal, (2). Angles (black) and dynamic thresholding (blue), (3). Time window G (k), (4). Locating and tagging the R peaks.*

After performing the filtering process, and *R* peak detection, the segmentation process is carried out. Each ECG signal is segmented into several heartbeats based on *R* peaks locations. The heartbeat is defined by specifying 92 sampling points before the *R* peak and 146 sampling points after the *R* peak (i.e., the length of each heartbeat is 238 samples).

2.4. Preparing Heartbeats

The segmented heartbeats are divided (according to the inter-patient scheme [36]) into two groups: the training group, which results from filtering and segmenting the signals of set 1, and the testing group, which results from filtering; and segmenting the signals of set 2. There is no intersection between the two sets (they come from different patients). The recordings for set 1 and set 2 are shown in **Table 3.** According to AAMI standards [37], the four recordings that contain pace beats are eliminated.

Table 3

Signals of set 1 and set 2 with their associated recordings.

Signals	Recordings from MIT-BIH-ARR-DB
signals of set1	101, 106, 108, 109, 112, 114, 115, 116, 118, 119, 122, 124, 201, 203, 205, 207, 208, 209, 215, 220, 223, 230
signals of set2	100, 103, 105, 111, 113, 117, 121, 123, 200, 202, 210, 212, 213, 214, 219, 221, 222, 228, 231, 232, 233, 234

2.5. Features Extraction

A large number of features were examined in this paper, and they represent the most notable eighty-five features, most of which were addressed in previous works [31,37-41], and they are as follows:

- **The Coefficients of DWT:** The DWT has the ability to extract detailed information from both the frequency and temporal domains, making it ideal for ECG representation. In this study, the first-order Daubechies mother wavelet (DB1) with three decomposition levels was used to introduce twenty-three features.
- **The Coefficients of Hermite Basis Functions (HBF):** The coefficients of HBF were utilized as the features describing the pattern of the ECG signal. The sample points situated 250 ms before and following each R peak represent the beat segment. The parameters for evaluating the coefficients of HBF were described in [38]. The order of HBF was fixed to twenty, and the width variable was estimated to reduce the reconstruction error (as possible) for each beat [37]. Three, four, and five HBFs were used to get fifteen features.
- **Higher-Order Statistics (HOS)**: They are functional in capturing the slight variations in ECG signals [39]. Each heartbeat was segmented into 5 intervals over each one; the third and fourth-order statistics (skewness and kurtosis) were determined to generate ten features. The range of delay variables, which are centered on the R peak, is (–250 to 250) ms as described in [39].
- **QRS Complex Durations and Their Normalizations:** They include the following five durations and their normalizations (ten features): overall QRS duration (QRSo), the QRS duration at the middle value of the R peak (QRSm), the QRS duration at the quarter value of the R peak (QRSq), the duration between Q and S waves (dQS), the duration between P wave and the starting point of the QRS complex (dPQRS). These features are demonstrated in **Fig. 6**. The normalization for the above features can be obtained by dividing the feature value by the mean of its value in the last thirty-two heartbeats. A comprehensive explanation for extraction mechanism is demonstrated in **Appendix B.**
- **Euclidean Distances:** These four features depend on Euclidean distances between the R peak and four points of the beat that represent the amplitude values through several samples (as proposed in [37]): maximum amplitude (Beat [0, 40]), minimum amplitude (Beat [75, 85]), minimum amplitude (Beat [95, 105]), and maximum amplitude (Beat [150, 180]).

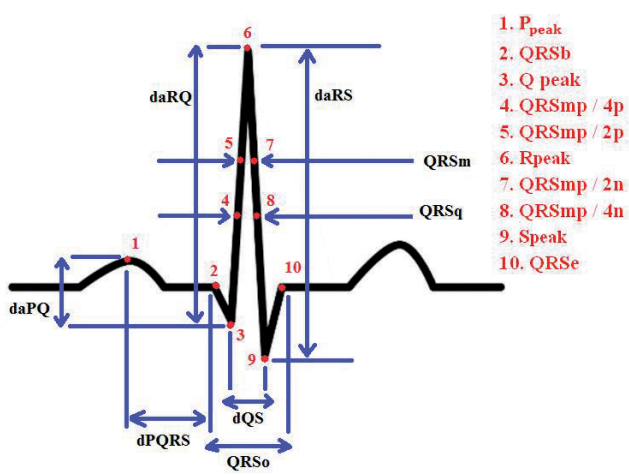

Fig. 6. *Demonstration of features of the QRS complex durations and amplitude differences.*

- **Amplitude Differences and Their Normalizations**: They consist of the following seven amplitudes and their normalizations (fourteen features): the difference in amplitude between R and Q waves (daRQ), the difference in amplitude between P and Q waves (daPQ), the differences in amplitude between R and S waves (daRS), and the peak values of (S, R, P, and Q) waves. All these features are illustrated in Fig. 6. The normalization for the above features can be determined by dividing the feature value by the mean of its value in the latter thirty-two heartbeats. A comprehensive explanation for the extraction mechanism is demonstrated in **Appendix B.**
- **RR Intervals and Their Normalizations**: They are the most utilized features for classification purposes. These features can be calculated from the time distance between consequent beats. If we denote RRp for the present RR interval, then RRp – 1 and RRp + 1 represent the pre RR and post RR intervals, respectively. The number of RR intervals considered in this paper is three. The following six features are the normalized RR intervals:

  Normalized RRp = (RRp)/mean of the latter thirty-two RR intervals

  Normalized RRp – 1 = (RRp – 1)/mean of the latter thirty-two RR intervals

  Normalized RRp + 1 = (RRp + 1)/mean of the latter thirty-two RR intervals

  Normalized RRr1 = (RRp – 1)/RRp

  Normalized RRr2 = (RRp + 1)/RRp

  Normalized RRpt = [RRp – mean of the latter thirty-two RR intervals]/ standard deviation of the latter thirty-two RR intervals.

2.6. Feature Selection

To minimize the computational cost of the introduced framework without sacrificing the performance of the classifier, the number of features for the training stage was adjusted to ten; this is consistent with the conclusions of the specialists and previous work [27,41]. The MIR principle is used to select just the most significant features according to the class of the heartbeats. From the perspective of selection features, MIR has been recognized to be an impressive strategy as it can identify non-linear relevance between features of a given features-vector or features-matrix. The scores of MIR (or MI values) evaluated between the labels of the classes and features indicate the discrimination ability of these features.

$$MI(\text{feature}, \text{class label}) = E(\text{feature}) - E(\text{class label} \mid \text{feature}) \quad (8)$$

where E (feature): is the entropy of a feature; E (class label | feature): is the conditional entropy of the class label given feature evaluating the uncertainty about the class label whenever the feature is known. In this research, the MI values are estimated based on work in [42] and [43] and using a python function called "mutual_info_classif.".

2.7. The Classification of Heartbeats

In this study, the RF classifier is utilized for the heartbeats classification task. It is an ensemble of Z trees R1(I), R2(I), …, RZ(I), where I = i_1, i_2, …, i_j is a *j*-dimension vector of inputs and the obtained group generates Z outputs O1= R1(I), O2= R2(I), …, Oz = Rz(I). Oz is the value of the prediction taken by tree number z. The final prediction O is determined by aggregating the output of all random trees (majority voting). The RF produces Z number of DTs from L-trained samples. The new training group is produced by conducting bootstrap sampling for all trees in the forest individually. This group is utilized to develop DT without trimming. In each division of a DT node, just little numbers of *j* features are chosen randomly rather than all of them. In order to construct a randomly produced forest, this procedure iterated to generate *J* of the DTs.

The following is a brief description of the training process for a randomly created forest:

Stage One: From the training group, choose an arbitrary sample.

Stage Two: For every arbitrary sample, create a tree with the following alteration: at every node, choose the optimal division among an arbitrary chosen subgroup of input parameters, which is the RF's tuning parameter. The tree is completely created until no more divisions are potential and not trimmed.

Stage Three: Reiterate stages one and two until Z such trees are created.

The RF classifier was constructed by utilizing the Scikit-learn library of Python [44]. All the variables remained at their default configuration, except the number of trees. To discover the best number of trees, the training was performed with an increased

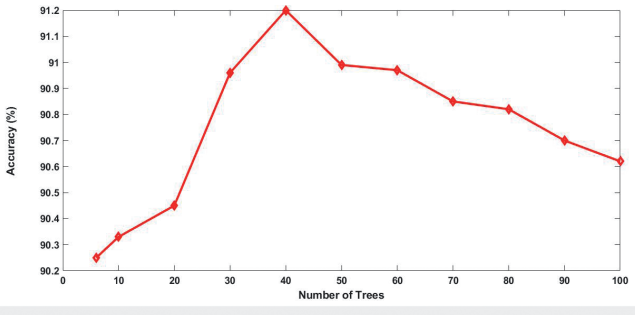

Fig. 7. *Accuracy vs. the number of trees attained from LOOCV on the training set for the RF classifiers.*

number of trees by utilizing the optimal ten features, and the ACC achievement was examined. **Fig. 7** depicts the results of applying the LOOCV on the training set. It is clear that when the number of trees exceeds forty, the accuracy of the classifiers does not improve and may even deteriorate.

2.8. Classification Assessment Metrics

The measurement for the classification performance and comparison with state of the art was conducted by determining the following metrics: Overall Accuracy (ACCo), F1-score, Positive Predictivity (PPr), and Sensitivity (Sen).

$$\mathrm{F1-Score} = \frac{2 \cdot \mathrm{PPr} \cdot \mathrm{Sen}}{\mathrm{PPr} + \mathrm{Sen}} \tag{8}$$

$$\mathrm{PPr} = \frac{\mathrm{TP}}{\mathrm{TP} + \mathrm{FP}} \tag{9}$$

$$\mathrm{Sen} = \frac{\mathrm{TP}}{\mathrm{TP} + \mathrm{FN}} \tag{10}$$

$$\mathrm{ACCo} = \frac{\mathrm{TP} + \mathrm{TN}}{\mathrm{TP} + \mathrm{TN} + \mathrm{FP} + \mathrm{FN}} \tag{11}$$

where TP – True Positive, TN – True Negative, FP – False Positive, and FN – False Negative.

3. RESULTS AND DISCUSSION

This paper performs an investigation into the exploitation of the RF classifier for ECG signal classification by employing the optimal choice for the extracted Time-Domain (TD) features and obeying the AAMI standards and the inter-patient approach. Various eighty-five features were examined in this research. All the features suggested in [37], which are considered important research work in this direction, were implemented. Furthermore, most of the features offered or based on [41] and [38] were used. In this study, normalization was accomplished by dividing the features by the mean of the most recent heartbeats. This process can be conducted more practically in real-time medical wearable and portable monitoring devices. Further normalizations for the RRp – 1 and RRp + 1 were performed by dividing them by the RRp interval; this was presented as an effort to comprise the timing relevance between the sequential R peaks, which is also addressed in [45]. The normalized RRpt was calculated to implicate a quantitative measure of the standard deviations for a specific interval from the mean. **Table 4** illustrates the most significant ten features evaluated by the MIR principle. Because the high proportion of the above normalizations is presented in the table of the most significant features (as indicated in Table 4), our findings reveal that the normalized RR intervals provide further information and are more effective for classifying ECG signals than other classical RR intervals. Just the best ten with the highest significant features were utilized in the tests. The results exhibit that only six features are adequate to attain the optimum outcomes (ACCo = 96.26%), as illustrated in **Fig. 8**, this is consistent with the obtained results

Table 4
The most significant ten features resulting from MIR with their MI values

Position According to MIR	Feature Name	MI Value
1	Normalized QRSm	0.19037819
2	Normalized QRSq	0.17508354
3	Normalized RRp	0.16311836
4	Normalized RRr2	0.14615831
5	QRSm	0.14439339
6	First fitting coefficient of the fourth degree of HBF (HBFC1D4)	0.14157413
7	HBFC2D4	0.14001679
8	QRSq	0.13641600
9	HBFC0D4	0.13299729
10	Normalized RRr1	0.13147040

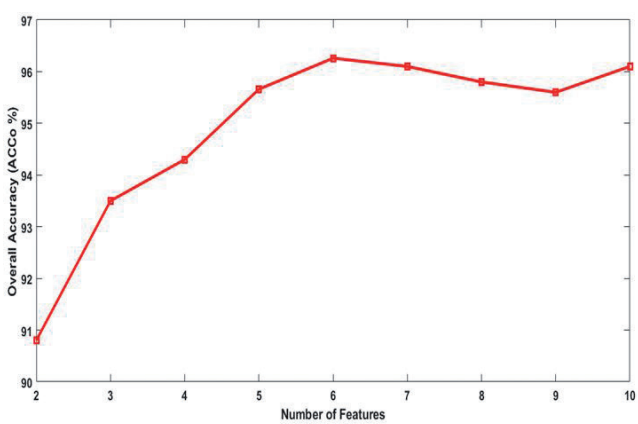

Fig. 8. *Overall accuracy (ACCo%) vs. the number of features for the RF classifier.*

Table 5

Performance of the proposed method in terms of the confusion matrix using testing set

			Prediction	
		NB	SVEB	VEB
	NB	43494	653	69
	SVEB	367	1447	23
True	VEB	377	15	2818
	FB	269	2	67
	QB	3	1	5

Table 6

Performance of the suggested approach in terms of Sen, PPr, F1-Score, and ACCo using the testing set

	Sen	PPr	F1-Score	ACCo
NB	98.04%	97.71%	98.04%	
SVEB	78.77%	68.32%	73.17%	**98.26%**
VEB	87.78%	94.50%	91.02%	

in [38], which show the number of most distinctive features in a subset is typically few and eliminating the less significant ones can effectively boost the classifier's performance.

Besides the normalized RR intervals features, the largest number of the ten most significant features is concerned with the duration of the QRS complex computed at specific magnitudes. This indicates that those particular features are more robust identifiers of the QRS shape than fiducial points that are characterized by small-amplitude variations, which are often disturbed by baseline noise. **Tables 5** and **6** demonstrate the performance of the proposed framework in terms of the confusion matrix and various assessment metrics, respectively. Since the wrong classification of QB and FB is not taken into consideration, according to the AAMI guidelines, therefore, they are not regarded in this study (as the most prior works), but they are still involved in the assessment. It is noteworthy that the F1-Score gives a more reliable indication for the performance of the classifiers, especially when the data are unbalanced. In the context of a comparison with previous works, the proposed framework is distinguished from approaches in previous researches by being comprehensive and fully automated. In contrast to the previous methods, which did not automatically detect the locations of the R peaks (they work only if these locations are pre-defined in the database), the proposed framework presented a new, simple, and efficient method to detect these locations based on trigonometry. **Table 7** compares the results achieved with the testing set of this paper with

Table 7

A comparison of the performance of the suggested framework with state-of-the-art methods

Referer	Extracted Features	Size of used Features	Classifier	F1 Class of NB	F1 Class of SVEB	F1 Class of VEB	ACCo
[48]	RR intervals, time morphology, and WT	101	Ensemble of SVM	97.59%	57.68%	92.37%	93.8%
[37]	RR intervals, time morphology, HOS, and WT	45	Ensemble of SVM	97.04%	60.74%	94.29%	94.5%
[46]	GM, HOS, and RR intervals	33	Ensemble of BDT	97.89%	**88.64%**	85.82%	96.15%
[49]	DCT Random Projections, RR intervals	33	SVM	96.88%	33.37%	77.29%	93.1%
[27]	RR intervals, time domain morphology, and WT	8	Linear Dis-criminant	96.48%	17.16%	83.89%	93%
[50]	HOS	4	Naive Bayes	65.6%	0.4%	84.7%	94.0%
	RR intervals, HOS, WT and time domain morphology	45	SVM and DNN	91.50%	54.45%	**94.47%**	88.69%
[33]	–	–	RCNN	93.93%	45.9%	83.89%	88.99%
Presented Paper	**RR intervals, time domain morphology, and HBF**	**6**	RF	**98.04%**	73.17%	91.02%	**96.26%**

WT: Wavelet Transform, SVM: Support Vector Machine,
BDT: Bootstrap aggregated Decision Trees.

several methodologies presented in the literature that attained a very good ECG signal classification performance and used the AAMI advice and the inter-patient concept. It has been shown that the overall accuracy obtained in this paper is one of the best achieved using the same assessment indicators (ACC = 96.26%), outperforms the performance accomplished in [46] (ACCo = 96.15%), which is, according to our research, the highest in the previous works. The researchers in [46] utilized the Gaussian Mixture (GM) approach (which is computationally expensive) to obtain various features, and they used the Bagging Tree technique for classification purposes. The RF classification scheme can give better results than Bagging Tree because RF provides a minimum correlation between trees; this was also highlighted in [47]. The suggested method in [46] used one hundred trees to obtain their results, while the results introduced in this paper use forty trees only. Moreover, the proposed method is more general and practical in the real world because it deals with the problem of WGN that can negatively affect the classification results. This problem is neglected in [46] and in most previous methods. The best detection results for SVEB were achieved in [46]; however, the suggested framework outperformed in terms of detection of VEB. The presented framework ranked second in the detection of VEB (F1-score = 91.02%) after the first rank which, was achieved in [51] (F1-score = 94.47%). Nevertheless, our model is more efficient in terms of complexity, simplicity, and fit for wearable and portable devices than the one offered in [51], which is based on DNN. The detection of VEB is especially important because its recurrence can be utilized as a predictor of the most dangerous disease, "Heart Failure," which often leads to death [14,15].

4. CONCLUSION

In this research, a comprehensive, robust, efficient, and fully automated framework for ECG signal classification based on digital signal processing, feature engineering selection, and RF classifier was suggested. Optimal incorporation between features engineering and the RF classifier was introduced to meet the heartbeat classification task for devices with limited resources. The ECG signal classification performance was reasonably calculated by obeying the AAMI advice and the inter-patient approach. The most significant features for the ECG classification problem were the normalized features associated with the RR intervals and durations of the QRS complex computed at specific magnitudes. The optimal outcomes were attained with the best six most significant features and forty decision trees of the RF classifier. The assessment was based on MIT-BIH-ARR-DB. By comparing the proposed scheme in this paper with the reported literature, it can be noted that our findings are one of the best performances achieved to present. The outcomes not only asserted that the RF classifier is a superior approach for classifying the ECG signals, but also, comparatively, few numbers of features and trees are adequate to achieve or outperform literature performance.

Appendix A

Tuning Y_1 and Y_2 to obtain the smallest detection error

			Y_2		
Y_1	0.00006	0.00008	0.00018	0.00012	0.00014
0.2	0.350	0.281	0.262	0.251	0.624
0.3	0.235	0.218	0.216	0.207	0.218
0.4	0.198	0.191	0.190	0.185	0.193
0.5	0.198	0.196	0.195	0.193	0.200
0.6	0.200	0.195	0.208	0.203	0.220

Appendix B

Extracting the key points of ECG signal

The highest absolute amplitude of the signal in the period 100 ms prior to and following the R peak is assigned as a reference base point. The following procedures have been conducted for obtaining the ECG key points: (note the R peaks are detected and extracted as explained in section 2.3)

1 Initially, suppose that the peaks of P, Q, and S = 0 (no associated waves exist).

2. Go back before QRSmp and determine the transition points as follows:

i. Set [QRSmp/2p] = the first position at which the signal value is under QRSmp/2.

ii. Set [QRSmp/4p] = the first position at which the signal value is under QRSmp/4.

iii. Set Qpeak = amplitude of the first negative transition point.

iv. If the first transition point $t_{rp} \geq 0$, then specify this point as QRSb, set Speak = QRSmp, and Qpeak = 0.

v. If QRSmp > 0, and the second $t_{rp} < 0$, and Qpeak = 0, then specify the amplitude of this point as Qpeak.

vi. If Qpeak ≠ 0, and the signal passes through 0, then set QRSb = the first point that is ≥ 0.

vii. If the second $t_{rp} \geq 0$, and QRSb has still not been determined, then specify this point as QRSb.

3. Go ahead after QRSmp and determine the transition points as follows:

i. Set [QRSmp/2n] = the first position at which the signal value is under QRSmp/2.

ii. Set [QRSmp/4n] = the first position at which the signal value is under QRSmp/4.

iii. Set Speak = amplitude of the first t_{rp}, that is < 0.

iv. If Speak ≠ 0, and the signal passes through 0, then set QRSe = the first point that is ≥ 0.

v. If the second $t_{rp} \geq 0$ and QRSe has still not been determined, then specify this point as QRSe.

4. Evaluate the maximum amplitude of the signal in the period between 236 ms and 70 ms prior to QRSb (MApriQRSb[236,70]). If this amplitude is > 3·STD of the signal through the period of 70 ms before the period under consideration and its location matches the trp of the signal, then set Ppeak = MApriQRSb[236,70].

Note: QRSb: beginning of the QRS, QRSe: ending of the QRS, STD: Standard Deviation.

REFERENCES

1. Xu J, Xiao W, Liang X, Shi L, Zhang P, Wang Y, Wang Y, Yang H. A meta-analysis on the risk factors adjusted association between cardiovascular disease and COVID-19 severity. *BMC Public Health*, 2021, 21(1):1533; doi: 10.1186/s12889-021-11051-w.
2. Tyagi A, Mehra R. 2021. Intellectual heartbeats classification model for diagnosis of heart disease from ECG signal using hybrid convolutional neural network with GOA. *SN Applied Sciences*, 2021, 3(2):1-14.
3. Pal HS, Kumar A, Vishwakarma A, Singh GK, Lee HN. An effective ECG signal compression algorithm with self-controlled reconstruction quality. *Computer Methods in Biomechanics and Biomedical Engineering*, 2023, pp. 1-11. DOI: 10.1080/10255842.2023.2206933.
4. Ali AM, Ahmed AF, Najim AH. 2020, November. Efficient and Effective Scheme for ECG Compression. Proc. *2nd Annual International Conference on Information and Sciences (AiCIS)*, 2020, pp. 91-94. DOI: 10.1109/AiCIS51645.2020.00024.
5. Martínez JP, Almeida R, Olmos S, Rocha AP, Laguna P. A wavelet-based ECG delineator: evaluation on standard databases. *IEEE Transactions on biomedical engineering,* 2004, 51(4):570-581.
6. Sharma M, Dhiman HS, Acharya UR. 2021. Automatic identification of insomnia using optimal antisymmetric biorthogonal wavelet filter bank with ECG signals. *Computers in Biology and Medicine*, 2021, 131:104246.
7. Hussain I, Park SJ. Big-Ecg: Cardiographic Predictive Cyber-Physical System for Stroke Management. *IEEE Access*, 2021, 9:123146-123164.
8. Chandra S, Sharma A, Singh GK. A comparative analysis of performance of several wavelet based ECG data compression methodologies. *IRBM*, 2021, 42(4):227-244. DOI: 10.1016/j.irbm.2020.05.004.
9. Yan Z, Zhou J, Wong WF. 2021. Energy efficient ECG classification with spiking neural network. *Biomedical Signal Processing and Control*, 2021, 63:102170.
10. Saini I, Singh D, Khosla A. 2013. QRS detection using K-Nearest Neighbor algorithm (KNN) and evaluation on standard ECG databases. *Journal of advanced research*, 2013, 4(4):331-344.
11. Martis RJ, Acharya UR, Mandana KM, Ray AK, Chakraborty C. Cardiac decision making using higher order spectra. *Biomedical Signal Processing and Control*, 2013, 8(2):193-203.
12. Kim H, Kim S, Van Helleputte N, Artes A, Konijnenburg M, Huisken J, Van Hoof C, Yazicioglu RF. A configurable and low-power mixed signal SoC for portable ECG

monitoring applications. IEEE transactions on biomedical circuits and systems, 2013, 8(2):257-267.

13. Scirè A, Tropeano F, Anagnostopoulos A, Chatzigiannakis I. Fog-computing-based heartbeat detection and arrhythmia classification using machine learning. *Algorithms*, 2019, 12(2):32.
14. Acharya T, Tringali S, Bhullar M, Nalbandyan M, Ilineni VK, Carbajal E, Deedwania P. Frequent atrial premature complexes and their association with risk of atrial fibrillation. *The American journal of cardiology*, 2015, 116(12):1852-1857.
15. Liaqat S, Dashtipour K, Zahid A, Assaleh K, Arshad K, Ramzan N. Detection of atrial fibrillation using a machine learning approach. *Information,* 2020, 11(12):549. DOI:10.3390/info11120549.
16. Pyakillya B, Kazachenko N, Mikhailovsky N. Deep learning for ECG classification. *Journal of Physics Conference Series,* 2013, 913(1):012004. DOI: 10.1088/1742-6596/913/1/012004.
17. Hannun AY, Rajpurkar P, Haghpanahi M, Tison GH, Bourn C, Turakhia MP, Ng AY. Cardiologist-level arrhythmia detection and classification in ambulatory electrocardiograms using a deep neural network. *Nature medicine*, 2019, 25(1):65-69.
18. Murat F, Yildirim O, Talo M, Baloglu UB, Demir Y, Acharya UR. Application of deep learning techniques for heartbeats detection using ECG signals-analysis and review. *Computers in biology and medicine*, 2020, 120:103726.
19. Luz EJDS, Schwartz WR, Cámara-Chávez G, Menotti D. 2016. ECG-based heartbeat classification for arrhythmia detection: A survey. *Computer methods and programs in biomedicine*, 2016, 127:144-164.
20. Ani R, Krishna S, Anju N, Aslam MS, Deepa OS. Iot based patient monitoring and diagnostic prediction tool using ensemble classifier. *Proc. International Conference on Advances in Computing, Communications and Informatics (ICACCI)*, 2017, pp. 1588-1593.
21. Saffari A, Leistner C, Santner J, Godec M. Bischof H. On-line random forests. *Proc. IEEE 12th international conference on computer vision workshops*, 2009, pp. 1393-1400.
22. Lempitsky V, Verhoek M, Noble JA, Blake A. Random forest classification for automatic delineation of myocardium in real-time 3D echocardiography. *Proc. International Conference on Functional Imaging and Modeling of the Heart,* 2009, pp. 447-456. Springer, Berlin, Heidelberg.
23. Vamsi IV, Abhinav N, Verma AK, Radhika S. Random forest based real time fault monitoring system for industries. *Proc. 4th International Conference on Computing Communication and Automation (ICCCA),* 2018, pp. 1-6.
24. Zhao X, Song Z, Guo J, Zhao Y, Zheng F. Real-time hand gesture detection and recognition by random forest. *Proc. Int. Conf. "Communications in computer and information processing" (ICCIP)*, 2012, 289:747-755. Springer, Berlin, Heidelberg.
25. Li J, Zhong PA, Yang M, Zhu F, Chen J, Liu W. Xu S. Intelligent identification of effective reservoirs based on the random forest classification model. *Journal of Hydrology,* 2020, 591:125324.
26. Emanet N. ECG beat classification by using discrete wavelet transform and Random Forest algorithm. *Proc. Fifth International Conference on Soft Computing, Computing with Words and Perceptions in System Analysis, Decision and Control,* 2009, pp. 1-4.
27. Llamedo M, Martínez JP. 2010. Heartbeat classification using feature selection driven by database generalization criteria. *IEEE Transactions on Biomedical Engineering,* 2010, 58(3):616-625.
28. Alickovic E, Subasi A. Medical decision support system for diagnosis of heart arrhythmia using DWT and random forests classifier. *Journal of medical systems*, 2016, 40(4):108.
29. Gutierrez-Gnecchi JA, Morfin-Magaña R, del Carmen A, Tellez-Anguiano DLE, Reyes-Archundia E, Díaz OH. Cardiac Arrhythmia Classification Using a Combination of

Quadratic Spline-Based Wavelet Transform and Artificial Neural Classification Network. *Proceedings 2nd International Work-Conference on Bioinformatics and Biomedical Engineering (IWBBIO)*, 2014, Vols 1, pp.1743-1754.

30. Kumar RG, Kumaraswamy YS. Investigating cardiac arrhythmia in ECG using random forest classification. *Int. J. Comput. Appl,* 2012, 37(4):31-34.
31. Park J, Lee S, Kang K. Arrhythmia detection using amplitude difference features based on random forest. *Proc. 37th Annual International Conference of the IEEE Engineering in Medicine and Biology Society (EMBC)*, 2015, pp. 5191-5194.
32. Aravind S, Sanjay M. ECG Classification and Arrhythmia Detection Using Wavelet Transform and Convolutional Neural Network. *Proc. International Conference on Communication, Control and Information Sciences (ICCISc)*, 2021, Vol. 1, pp. 1-5.
33. Li Y, Qian R, Li K. Inter-patient arrhythmia classification with improved deep residual convolutional neural network. *Computer Methods and Programs in Biomedicine*, 2022, 214:106582.
34. https://physionet.org/content/mitdb/1.0.0/.
35. Wang T, Lu C, Sun Y, Yang M, Liu C, Ou C. 2021. Automatic ECG Classification Using Continuous Wavelet Transform and Convolutional Neural Network. *Entropy,* 2021, 23(1):119.
36. De Chazal P, O'Dwyer M, Reilly RB. Automatic classification of heartbeats using ECG morphology and heartbeat interval features. *IEEE transactions on biomedical engineering,* 2004, 51(7):1196-1206.
37. Mondéjar-Guerra V, Novo J, Rouco J. Penedo MG, Ortega M. Heartbeat classification fusing temporal and morphological information of ECGs via ensemble of classifiers. *Biomedical Signal Processing and Control*, 2019, 47:41-48.
38. De Lannoy G, François D, Delbeke J, Verleysen M. Weighted SVMs and feature relevance assessment in supervised heart beat classification. *Proc. International Joint Conference on Biomedical Engineering Systems and Technologies*, 2010, pp. 212-223. Springer, Berlin, Heidelberg.
39. Osowski S, Linh TH. ECG beat recognition using fuzzy hybrid neural network. *IEEE Transactions on Biomedical Engineering,* 2001, 48(11):1265-1271.
40. Ince T, Kiranyaz S, Gabbouj M. A generic and robust system for automated patient-specific classification of ECG signals. *IEEE Transactions on Biomedical Engineering*, 2009, 56(5):1415-1426.
41. Mar T, Zaunseder S, Martínez JP, Llamedo M, Poll R. Optimization of ECG classification by means of feature selection. *IEEE transactions on Biomedical Engineering,* 2011, 58(8):2168-2177.
42. Kraskov A, Stögbauer H, Grassberger P. Estimating mutual information. *Physical review E,* 2004, 69(6):066138.
43. Ross BC. Mutual information between discrete and continuous data sets. *PloS one*, 2014, 9(2):e87357.
44. Pedregosa F, Varoquaux G, Gramfort A, Michel V, Thirion B, Grisel O, Blondel M, Prettenhofer P, Weiss R, Dubourg V, Vanderplas J. Scikit-learn: Machine learning in Python. *The Journal of machine Learning research,* 2011, 12:2825-2830.
45. Tsipouras MG, Fotiadis DI, Sideris D. An arrhythmia classification system based on the RR-interval signal. *Artificial intelligence in medicine,* 2005, 33(3):237-250.
46. Afkhami RG, Azarnia G, Tinati MA. Cardiac arrhythmia classification using statistical and mixture modeling features of ECG signals. *Pattern Recognition Letters*, 2016, 70:45-51.
47. Banfield RE, Hall LO, Bowyer KW, Kegelmeyer WP. A comparison of decision tree ensemble creation techniques. *IEEE transactions on pattern analysis and machine intelligence*, 2006, 29(1):173-180.
48. Huang H, Liu J, Zhu Q, Wang R, Hu G. A new hierarchical method for inter-patient heartbeat classification using random projections and RR intervals. *Biomedical engineering online*, 2014, 13(1):1-26.
49. Chen S, Hua W, Li Z, Li J, Gao X. Heartbeat classification using projected and dynamic

features of ECG signal. *Biomedical Signal Processing and Control*, 2017, 31:165-173.

50. Marinho LB, de MM Nascimento N, Souza JWM, Gurgel MV, Reboucas Filho PP, de Albuquerque VHC. A novel electrocardiogram feature extraction approach for cardiac arrhythmia classification. *Future Generation Computer Systems*, 2019, 97:564-577.
51. Li Y, He Z, Wang H, Li B, Li F, Gao Y, Ye X. CraftNet: a deep learning ensemble to diagnose cardiovascular diseases. *Biomedical Signal Processing and Control,* 2021, 62:102091.

DOI: 10.17725/j.rensit.2024.16.067

Investigation and development of methods for automatic search for AUC-diagram-based features of Parkinson's disease and essential tremor

Olga S. Sushkova, Alexei A. Morozov, Margarita N. Khokhlova, Ivan A. Kershner
Kotel'nikov Institute of Radioengineering and Electronics of RAS, http://www/cplire.ru/
Moscow 125009, Russian Federation
E-mail: o.sushkova@mail.ru, morozov@cplire.ru, margokhokhlova@gmail.com, ivan.kershner@gmail.com

Alexandra V. Gabova
Institute of Higher Nervous Activity and Neurophysiology of RAS, http://ihna.ru/
Moscow 117485, Russian Federation
E-mail: agabova@yandex.ru

Larisa A. Chigaleychik, Alexei V. Karabanov
Research Center of Neurology, https://www.neurology.ru/
Moscow 125367, Russian Federation
E-mail: chigalei4ick.lar@yandex.ru, doctor.karabanov@mail.ru

Received March 08, 2024, peer-reviewed March 11, 2024, accepted March 13, 2024, published March 15, 2024.

Abstract: **Methods and optimization algorithms for automatic search for AUC-diagram-based features of Parkinson's disease and essential tremor were studied and developed. AUC diagrams are a new method for statistical analysis of biomedical signals, based on visualizing the parameters of wave train electrical activity in the brain and muscles. The effectiveness of this method has been demonstrated in solving problems of early and differential diagnosis of Parkinson's disease and essential tremor. The disadvantage of this method is the need to construct and analyze a large number of graphic diagrams. In this regard, automation of the analysis of AUC diagrams is an urgent task. The mathematical problem of finding features based on the analysis of AUC diagrams is reduced to an optimization problem in a multidimensional feature space. A distinctive feature of the space constructed using AUC diagrams is the presence of relatively large compact areas containing local maxima and minima. This property of the feature space facilitates the search for solutions to the optimization problem, but at the same time requires the selection of optimization algorithms and fitness functions that increase the likelihood of detecting global extrema. In this work, methods for automatically searching for global extrema in the multidimensional space of features of wave train electrical activity are investigated and developed.**

Keywords: **optimization methods, robustness, AUC diagrams, ROC analysis, wave train, electromyogram, Parkinson's disease, essential tremor, differential diagnosis, neurodegenerative disease features**

UDC 519.67, 612.8, 53.083, 519.24, 004.93

Acknowledgements: The authors are grateful to Dr. Yu.V. Obukhov, who proposed the idea of analyzing local maxima on wavelet spectrograms, as well as Academician of the Russian Academy of Sciences S.N. Illarioshkin for help with the research. The research was supported by the Russian Science Foundation grant No. 22-75-10079, https://rscf.ru/en/project/22-75-10079/.

For citation: Olga S. Sushkova, Alexei A. Morozov, Margarita N. Khokhlova, Ivan A. Kershner, Alexandra V. Gabova, Larisa A. Chigaleychik, Alexei V. Karabanov. Investigation and development of methods for automatic search for AUC-diagram-based features of Parkinson's disease and essential tremor. *RENSIT: Radioelectronics. Nanosystems. Information Technologies*, 2024, 16(1):67-78e. DOI: 10.17725/j.rensit.2024.16.067.

Contents

1. INTRODUCTION

The goal of this work is to further develop the wave train electrical activity analysis method [1-18], designed by the authors for identifying regularities in biomedical signals. The concept behind the analysis of wave train electrical activity is to merge the advantages of conventional spectra and wavelet spectrograms. This involves identifying wave trains (local maxima) on wavelet spectrograms of signals, calculating these wave train characteristics – namely, the central frequency of the wave train, maximum power spectral density (PSD) of the wave train, duration of the wave train in seconds, duration of the wave train in periods at the central frequency, bandwidth of the wave train normalized to the central frequency of the wave train, and instantaneous phase of the wave train. Subsequently, mathematical statistics methods are employed to uncover generalized properties of wave trains (for example, ranges of listed wave train parameters) that are characteristic of the analyzed signal sample or differentiate one signal sample from another. The effectiveness of the proposed method was demonstrated in the early (preclinical) and differential diagnosis of neurodegenerative diseases Parkinson's Disease (PD) and Essential Tremor (ET) [1-3,16,17], as well as in the recognition of so-called immature epileptic discharges in laboratory animals [15,18]. All examples discussed in this paper are based on the analysis of a special type of wave train electrical activity – the so-called cross-wave trains [3], which are local maxima on cross-spectra of electromyographic (EMG) signals of paired antagonist muscles in patients with ET and patients with the first stage of PD.

The primary tool of the wave train electrical activity analysis method is AUC diagrams [1-3]. An AUC diagram is a way to visualize statistical regularities that distinguish two signal samples. Different types of AUC diagrams [2,3] are used to analyze various wave train parameters, but the principle of using any AUC diagram boils down to creating a two-dimensional diagram, with the abscissa axis representing the value of the lower boundary of the investigated wave train parameter, and the ordinate axis representing the upper boundary of this parameter (see example in **Fig. 1**). For each possible combination of lower and upper wave train parameter boundaries, an AUC diagram uses a color scale to show the degree of difference between one signal sample and another. The degree of difference is characterized by the area under the ROC curve (AUC), constructed to compare the average number of wave trains (per second of time) found in the analyzed signal samples, such that the value of the considered wave train parameter falls within the range between the considered

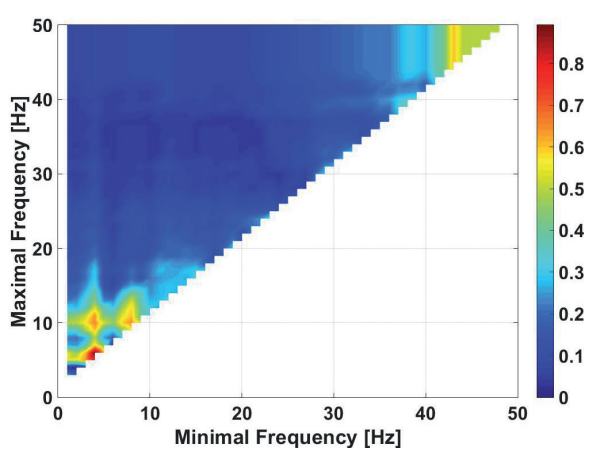

Fig. 1. *An example of a frequency AUC diagram. The comparison involves the EMG signal envelopes in paired antagonist muscles in the left hands in two patient groups. The first group consists of patients with the first stage of PD with onset in the left hand (10 individuals), and the second group consists of patients with ET (13 individuals).*

lower and upper parameter boundaries (indicated on the abscissas and ordinates of the diagram). Historically, a blue-red color scale is used for AUC diagrams, so values of AUC close to 0 correspond to blue areas on the diagram, while values close to 1 correspond to red areas. For researchers, both blue and red areas on the AUC diagram are of interest. Blue areas correspond to wave train parameter ranges in which the number of wave trains in the first sample is less than in the second, while red areas correspond to ranges in which the number of wave trains in the first sample is more than in the second. In this paper, we will adhere to the same terminology. In particular, when automatically searching for features distinguishing signal samples, we will talk about "blue" and "red" solutions to the optimization problem corresponding to blue and red areas discovered on AUC diagrams.

Searching for regularities in signal samples using AUC diagrams manually is a rather laborious process. During data analysis, the researcher creates AUC diagrams of various types. Upon detecting a blue or red area with a good AUC value on one of the diagrams, the researcher decides to further investigate the found area. A constraint corresponding to the selected area on the AUC diagram is imposed on the investigated range of the parameter, after which AUC diagrams of all other types need to be rebuilt and reanalyzed. This described sequence of actions is repeated iteratively until the observed AUC values cease to improve [2]. From the standpoint of mathematical analysis, the mentioned algorithm for finding regularities represents solving an optimization problem in a twelve-dimensional space (six parameters of wave trains, each with a lower and upper bound) by iteratively moving two-dimensional slices of this space (i.e., AUC diagrams). In practice, it may take a week or even a month of manual work to search for signs of neurodegenerative disease in a sample of electroencephalographic (EEG) or electromyographic signals.

Of course, the idea of automatic analysis of AUC diagrams arose from the very beginning of the development of the method for analyzing wave train electrical activity. Analyzing the twelve-dimensional parameter space is not a difficult task for modern optimization algorithms, so we hoped to automate the search for regularities in biomedical signals using standard optimization algorithms [19], such as simulated annealing [20], pattern search [21], and genetic algorithms [22]. However, our experiments quickly showed that this idea was very naive.

The first problem we encountered in the automatic search for blue and red areas on AUC diagrams was that some automatically found wave train parameter ranges that differentiate signal samples with very good AUC values (close to 0 or 1) ceased to "operate" after we rounded the values of these ranges to one or two decimal digits after dot. We termed this issue the "fragile solutions" problem. A careful examination of the fragile solutions problem revealed that in the twelve-dimensional wave train parameter space, indeed, there are very narrow areas with AUC values close to 0 or 1, around which AUC sharply worsens and approaches 0.5 (indicating an inability to distinguish the analyzed signal samples). During manual analysis of AUC diagrams, a person naturally avoids entering such areas of parameter space, focusing mainly on blue and red areas of relatively large sizes. Standard optimization algorithms lack criteria for assessing the robustness (resistance to small parameter changes) of the solutions found and therefore identify formally very good but impractical solutions.

The second problem encountered in the automatic analysis of AUC diagrams was the large number of solutions computed. From the perspective of practical use of wave train parameters for the recognition and differential diagnosis of neurodegenerative diseases, one could simply select several good (in some sense) solutions and disregard the rest. However, if AUC diagrams are used as a research tool, it is

necessary to somehow compare and interpret the entire set of found solutions as a whole. For example, when analyzing tremor signals in patients with the first stage of PD, we found that the AUC diagram comparing the group of patients with tremor in the right hand with the group of patients with ET (**Fig. 2**) substantially differs from the AUC diagram comparing the group of patients with PD with tremor in the left hand (Fig. 1) with ET. This raised the question of whether the observed differences are manifestations of fundamentally different neurophysiological mechanisms in the right and left hands of patients, or whether similar regularities are observed in both hands of patients but in a different ratio. The automatic search identified hundreds of solutions on the AUC diagrams, which did not simplify answering the posed question.

Fortunately, automatic methods allow for the implementation of more complex schemes for analyzing the parameter space of wave trains than simply searching for global extrema, and we can take advantage of them for a detailed study

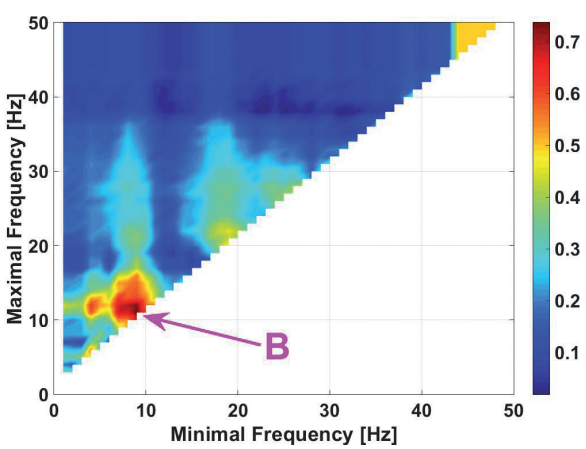

Fig. 2. *An example of a frequency AUC diagram. The diagram compares the envelopes of electromyographic (EMG) signals in paired antagonist muscles in the right hands in two patient groups. The first group consists of patients with the first stage of PD with onset on the right hand (12 individuals), and the second group comprises patients with ET (13 individuals). The arrow points to a large red area absent in Fig. 1.*

of the structure and properties of this space. The second part of the paper discusses the method of so-called "multidimensional drilling of the wave train parameter space", developed by the authors for the search and analysis of local extrema in the wave train parameter space. The third part of the paper considers the problem of assessing the robustness of optimization problem solutions and proposes a criterion for assessing robustness, based on the physical meaning of the wave trains parameter space. The fourth part of the paper discusses the application of developed statistical tools for researching clinical data of patients and developing diagnostic procedures.

2. MULTIDIMENSIONAL DRILLING METHOD OF THE WAVE TRAIN PARAMETER SPACE

The idea of multidimensional drilling of the wave train parameter space aims to enhance the expressive capabilities of conventional AUC diagrams through the application of optimization algorithms. The improved AUC diagrams (referred to as AUC-Drilling diagrams) differ from the standard ones in that, within each cell of the diagram, not just the AUC value is calculated, but the global extremum of the AUC function within the wave train parameter space. In the search for the global extremum, the optimization algorithm is allowed to vary all the boundaries of the wave train parameters, except for the two that correspond to the abscissa and ordinate of the diagram under consideration. These two parameter boundaries must remain within the confines of the considered cell on the diagram.

Fig. 3 illustrates the idea of multidimensional drilling of the wave train parameter space using an analogy with drilling oil wells. The figure shows a three-dimensional cube (a particular case of a twelve-dimensional cube). Each face of this cube can correspond to a certain AUC-Drilling diagram; the top face is chosen for the illustration. The perpendicular edges of the top face correspond to the axes of the abscissa and

Fig. 3. *The concept of multidimensional drilling of the wave train parameter space.*

ordinate of the AUC-Drilling diagram. In each cell of the top face of the cube, a well is drilled through the remaining ten dimensions of the space, to find areas of the space where AUC values are close to 0 or 1. Depending on which specific optimization problem solutions we are looking for, blue or red, two different AUC-Drilling diagrams can be constructed – blue or red.

The initial experiments with multidimensional drilling revealed that the results of EMG signal analysis of patients with PD and ET differ substantially from those shown by conventional AUC diagrams. Continuing the analogy with mineral extraction, the difference between the types of AUC diagrams is akin to that between surface geological surveys and exploratory drilling. Primarily, we observed that in some frequency ranges, both blue and red solutions with AUC close to 0 and 1 exist simultaneously. On conventional AUC diagrams, these solutions may overlap each other, preventing a complete view of the regularities within the wave train parameter space. AUC-Drilling diagrams separate blue and red solutions into different diagrams, allowing us to study them independently.

For example, on the red AUC-Drilling diagram for the left hands of patients, a red

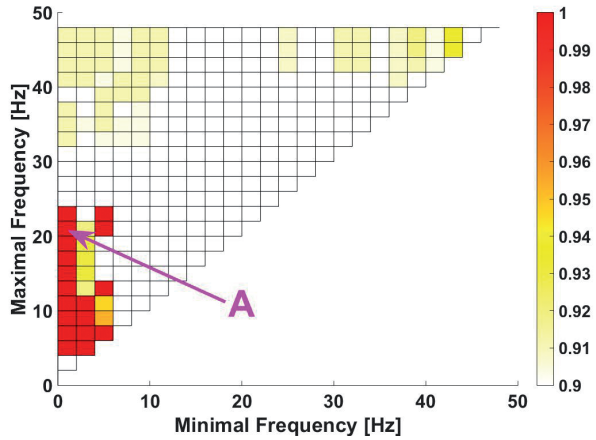

Fig. 4. *An example of a red frequency AUC-Drilling diagram. The envelopes of EMG signals in paired antagonist muscles in the left hands in two patient groups are compared. The patient groups are the same as in Fig. 1. A red area, invisible on the corresponding AUC diagram in Fig. 1 due to its overlap with a certain blue area, is indicated by an arrow. To solve the optimization problem here and in subsequent considerations, a pattern search algorithm is applied* [21].

area was discovered (see **Fig. 4**, area A) that is invisible on the corresponding AUC diagram (Fig. 1) because it is covered by a certain blue area (see **Fig. 5**).

At the same time, it was found that the red areas on the AUC-Drilling diagrams for the right

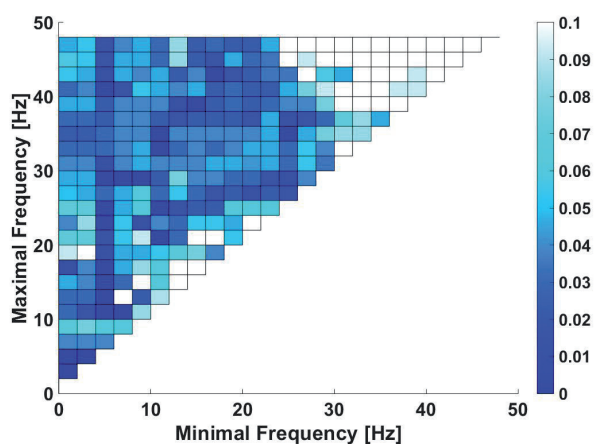

Fig. 5. *An example of a blue frequency AUC-Drilling diagram. The envelopes of EMG signals in paired antagonist muscles in the left hands in two patient groups are compared. The patient groups are the same as in Figs. 1 and 4.*

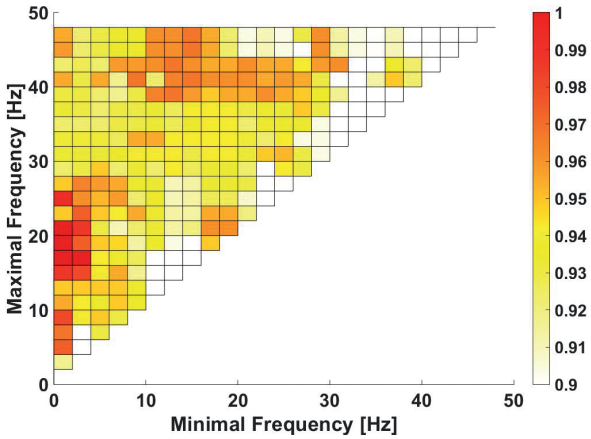

Fig. 6. *An example of a red frequency AUC-Drilling diagram. The envelopes of EMG signals in paired antagonist muscles in the right hands in two patient groups are compared. The patient groups are the same as in Fig. 2.*

(**Fig. 6**) and left (Fig. 4) hands of patients in the frequency range below 25 Hz have roughly the same shape. The difference in the red areas on the corresponding AUC diagrams (see Figs. 1 and 2) turned out to be only apparent. In particular, the large red area on the AUC diagram for the right hands of patients (Fig. 2, area B) stands out only because, in this frequency range, there are no blue solutions (see **Fig. 7,** area C).

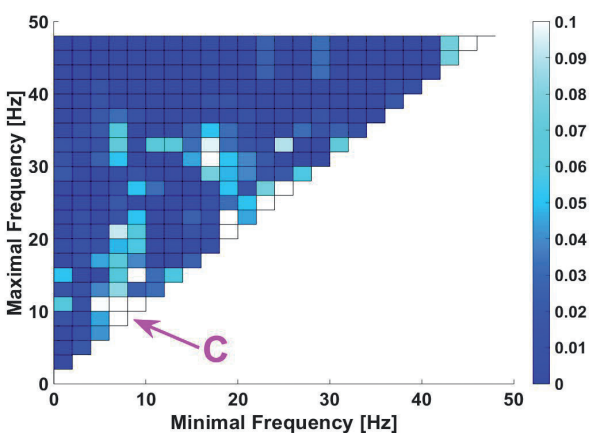

Fig. 7. *An example of a blue frequency AUC-Drilling diagram. The envelopes of EMG signals in paired antagonist muscles in the right hands in two patient groups are compared. The patient groups are the same as in Figs. 2 and 6. An area where blue solutions are absent is indicated by an arrow.*

The examples of AUC-Drilling diagrams discussed above allow us to hypothesize that the tremor in the left and right hands of patients with PD and ET is controlled by the same neurophysiological mechanisms, but the impact of these mechanisms occurs in different ratios, leading to different clinical presentations. This observation supports the conclusion that different algorithms need to be applied for diagnosing patients with PD with left-sided and right-sided onset [3].

3. ROBUSTNESS ASSESSMENT OF OPTIMIZATION PROBLEM SOLUTIONS

Robust solutions of an optimization problem are defined as points in the explored parameter space that possess a certain neighborhood in which the solution remains good in some sense [23-25]. As a quantitative assessment of the robustness of a solution, one can adopt the maximum radius R of a multidimensional ellipsoid (stability radius) surrounding the considered solution, inside which no "bad" solutions exist. In the context of this study, we consider "bad" solutions to be those in which the AUC value, compared to the AUC at the center of the ellipsoid, has approached the value of 0.5 by more than half. For instance, if a blue solution with an AUC value of 0.1 is considered, the quantitative assessment of the robustness of this solution would be the maximum radius of the ellipsoid within which AUC values do not exceed 0.1 + (0.5 - 0.1)/2 = 0.3. If a red solution with an AUC value of 0.9 is considered, the quantitative assessment of the robustness of this solution would be the maximum radius of the ellipsoid within which AUC values are not lower than 0.9 - (0.9 - 0.5)/2 = 0.7. Note that different coordinate axes in the wave train parameter space correspond to different units of measurement, so measuring the radius of the ellipsoid in absolute units does not make sense. We measure the radius of the ellipsoid in percentages of the ellipsoid's center coordinate values.

Unfortunately, the twelve-dimensional wave train parameter space does not have an analytical description, so the only tool available for assessing the robustness of blue and red solutions in the wave train parameter space is a computational experiment. As the neighborhood of the considered solution, models also must be applied.

Currently, we use the following model for the neighborhood of the optimization problem solution. The considered solution S is a point in the twelve-dimensional space and can be described by a vector of twelve coordinates $<S_1, ..., S_{12}>$. The model of the neighborhood (ellipsoid) with radius R of the solution S in the parameter space we call the set of all points P such that each coordinate P_i of the point differs from the corresponding coordinate S_i of the explored solution by a value of R or $-R$ (see **Fig. 8**).

It should be noted that the described ellipsoid model is only a crude approximation of the exact description of the set of points located in the neighborhood of the solution. However, the use of this simplified model allows for a significant reduction in the computational resources needed for conducting computational experiments while still providing a general understanding of the properties of the optimization problem solutions.

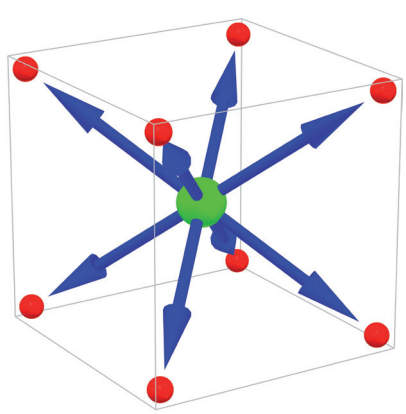

Fig. 8. *The model of the neighborhood (twelve-dimensional ellipsoid) of the optimization problem solution in the wave train parameter space. The figure shows only three dimensions of the ellipsoid.*

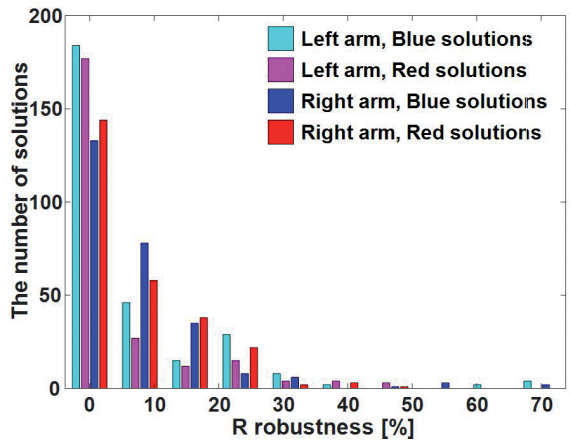

Fig. 9. *Histograms of quantitative R robustness assessments of optimization problem solutions during the construction of frequency AUC-Drilling diagrams comparing the EMG signal envelopes in paired antagonist muscles in patient groups with the first stage of PD and patients with ET.*

Fig. 9 presents histograms of the quantitative robustness assessments of the optimization problem solutions found during the construction of frequency AUC-Drilling diagrams, comparing the EMG signal envelopes in paired antagonist muscles in patient groups with the first stage of PD and patients with ET, as shown in Figs. 4-7. The histograms in Fig. 9 indicate that a significant number of solutions have robustness close to 0. This is even though the model of the multidimensional ellipsoid (Fig. 8) is inclined to overestimate the robustness assessments of solutions since it does not account for every point adjacent to the explored solution in the wave train parameter space. This means that the presence of "fragile" solutions, unfortunately, is one of the inherent properties of the wave train parameter space, and it must be taken into account when solving medical diagnostic problems.

One of the unique properties of the wave train parameter space is that each point in this space has a simple physical meaning, namely, the average number of Q_1 and Q_2 wave trains per second observed in the first and second signal samples respectively, whose parameters fall within

the ranges corresponding to the considered point in the space. This opens opportunities for the development of new methods for assessing the robustness of optimization problem solutions, which are not based on the concept of "stability radius" and other geometric analogies.

As a measure of solution robustness, the authors proposed using the maximum average number of wave trains observed in the considered signal samples, $Q = \max(Q_1, Q_2)$. The idea of the Q robustness assessment is based on an empirical observation made while studying the wave train parameter space. It turned out that fragile solutions often arise at points in the space imposing strong restrictions on certain wave train parameters. In such points of the space, the number of observed wave trains decreases to a few wave trains in tens or even hundreds of seconds. As a consequence, the probability increases sharply that at this point in space, the ratio of the number of wave trains observed in the two analyzed signal samples can substantially change due to random fluctuations in the number of wave trains. As a result, we obtain a solution with a very good AUC value, close to 0 or 1, which stops "working" with the slightest change in parameter boundaries.

The study of the correlation between the robustness estimates Q and R based on experimental data confirmed that both assessments yield similar results (see **Fig. 10**). In particular, it was found that the Spearman's rank correlation between the Q and R estimates is 0.6-0.8 with a high level of significance ($p < 0.001$) when comparing both the right and left hands of patients, for both red and blue solutions of the optimization problem. Interestingly, a significant number of the solutions do not fit this regularity and demonstrate high R robustness scores with Q metric values close to zero (points located near the ordinate axis in Fig. 10). This indicates the potential risk of using the stability radius and similar geometric estimates, as they may not always identify potentially fragile solutions.

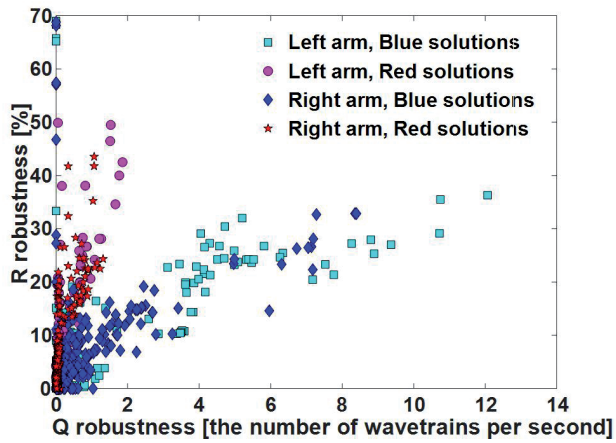

Fig. 10. *Correlation between robustness estimates Q and R for optimization problem solutions during the construction of frequency AUC-Drilling diagrams, comparing the EMG signal envelopes in paired antagonist muscles in patient groups with the first stage of PD and patients with ET.*

A significant advantage of the robustness estimate Q, compared to the R estimate, is its computational simplicity. Estimating the number of wave trains, whose parameter values fall within the considered intervals, is an intermediate step in calculating AUC, so any constraints on the Q value can be added to the optimization algorithm's objective function without additional computational costs. The situation with the robustness estimate R is quite different because an additional check of the solutions' neighborhood, assessed by the optimization algorithm, substantially increases the time to solve the optimization problem.

Currently, we apply a constraint on Q directly in the process of multidimensional drilling of the wave train parameter space, and then we perform an additional check of the robustness of the found solutions using the Q and R metrics. In particular, during the calculation of the AUC-Drilling diagrams presented in Figs. 4-7, an additional condition $Q \geq 0.5$ was applied. In the subsequent verification of the found solutions, restrictions on the AUC, Q, R, and other characteristics of the solutions can be established.

4. DISCUSSION

Experiments with clinical data have shown that using the method of multidimensional drilling of wave train parameter space, it is possible to compute several dozen or even hundreds of optimization solutions with high robustness suitable for clinical diagnostics of patients. A natural question arises: is there any reason to analyze such a large number of solutions? What benefit can be derived from them in studying the neurophysiological mechanisms of neurodegenerative diseases? Should all found solutions be used for clinical diagnostics, and what danger lies in the application of a large number of solutions? These questions are certainly subject to further research, but we can make some observations based on the experience of studying the clinical data of patients.

Typically, the set of solutions computed by the multidimensional drilling method is quite heterogeneous. Fig. 10 shows an example of a correlation matrix of 225 solutions, each characterized by a vector of 12 numbers representing the average number of wave trains per second observed in a patient with ET or a patient with the first stage of PD with onset in the left hand. In this example, only the red solutions are considered. As seen in **Fig. 11**, some solutions yield approximately similar results, while others yield completely different results. This means that combining some solutions can substantially increase the accuracy of patient diagnostics. However, combining solutions that are similar to each other can lead to overfitting of the diagnostic procedure, i.e., a very confident diagnosis of patients included in the training set and poor recognition of new patients.

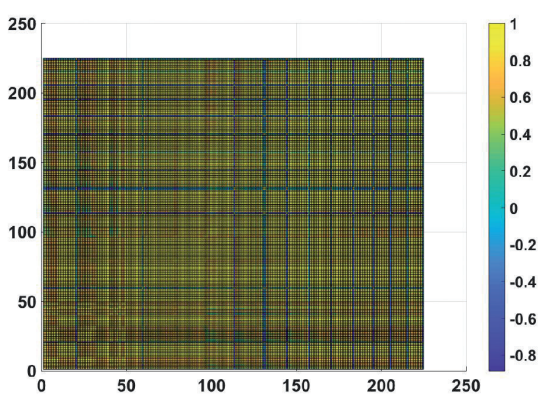

Fig. 11. *Correlation matrix of 225 optimization solutions obtained using the multidimensional drilling method in the wave train parameter space in patients with the first stage of PD with onset in the left hand (5 individuals) and patients with ET (7 individuals). Each solution is characterized by a vector of 12 values representing the average number of wave trains per second observed in the respective patient.*

Comparison of the number of wave trains satisfying different solutions allows researchers to assess the homogeneity of the patient sample, and clinicians to verify the diagnosis of individual patients. Let us consider an example of a correlation matrix of a patient group in **Fig. 12**. The correlation matrix vividly shows that patients diagnosed with PD differ from patients diagnosed with ET. However, in some cases, the EMG parameters of a patient may more closely resemble those of patients with a different diagnosis. Of course, this requires a careful reexamination of the patient's clinical data and possibly further analysis.

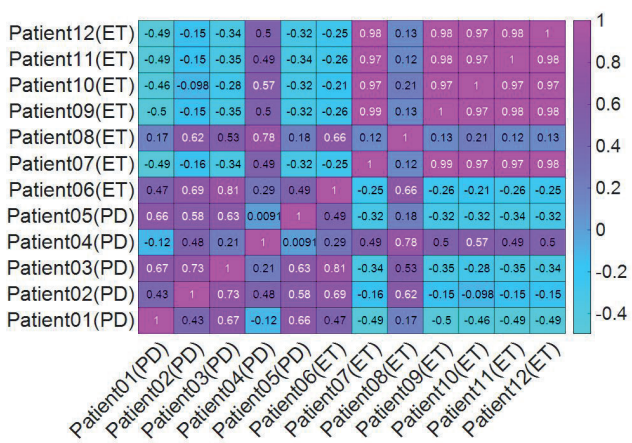

Fig. 12. *Correlation matrix of the patient group with PD and patients with ET, as considered in Figure 11. Each patient is characterized by a vector of 225 values of the average number of wave trains per second, satisfying certain 225 solutions of the optimization problem. The correlation matrix indicates, in particular, that the diagnosis of patient 6 needs to be reevaluated.*

5. CONCLUSIONS

The main idea of the method for analyzing wave train electrical activity lies in the statistical analysis and search for regularities in the parameters of local maxima (wave trains) identified in wavelet spectrograms of signals. The method is versatile and can be applied to investigate biomedical signals of various types, including EEG, EMG, and accelerometer signals.

AUC diagrams serve as the primary working tool of the wave train electrical activity analysis method. The new type of AUC diagrams described in the paper combines visualization tools for wave train parameters and automated search tools for regularities in the wave train parameter space. This statistical tool will be useful both for studying the neurophysiological mechanisms affecting the clinical condition of patients and for solving practical problems related to identifying diagnostic features of neurodegenerative disorders and developing diagnostic algorithms.

The issue of "fragile solutions" discovered during the investigation of clinical patient data has been addressed. Two fundamentally different approaches to assessing the robustness of solutions to the optimization problem, computed during the analysis of wave train parameter space, have been proposed. The first approach is based on calculating the stability radius of the investigated solution. The second approach is based on th physical meaning of the wave train parameter space. A comparison of robustness estimates of solutions to the optimization problem based on these two principles has been conducted.

REFERENCES

1. Sushkova OS, Morozov AA, Gabova AV, Karabanov AV. Application of brain electrical activity burst analysis method for detection of EEG characteristics in the early stage of Parkinson's disease. *Zhurnal Nevrologii i psikhiatrii im. SS Korsakova,* 2018, 118(7):45-48, (in Russ.).
2. Sushkova OS, Morozov AA, Gabova AV, Karabanov AV, Illarioshkin SN. A statistical method for exploratory data analysis based on 2D and 3D area under curve diagrams: Parkinson's disease investigation. *Sensors,* 2021, 21(14):4700. DOI: 10.3390/s21144700.
3. Sushkova OS, Morozov AA, Kershner IA, Khokhlova MN, Gabova AV, Karabanov AV, Chigaleichick LA, Illarioshkin SN. Investigation of phase shifts using AUC diagrams: application to differential diagnosis of Parkinson's disease and essential tremor. *Sensors,* 2023, 23(3):1531. DOI: 10.3390/s23031531.
4. Sushkova OS, Morozov AA, Gabova AV. A method of analysis of EEG wave trains in early stages of Parkinson's disease. *International Conference on Bioinformatics and Systems Biology* (BSB-2016). Allahabad, Indian Institute of Information Technology, 2016. DOI: 10.1109/BSB.2016.7552163.
5. Sushkova OS, Morozov AA, Gabova AV. Data mining in EEG wave trains in early stages of Parkinson's disease. *Advances in Soft Computing, MICAI 2016*. Springer, 2017, V. 10062 LNAI:403-412.
6. Sushkova OS, Morozov AA, Gabova AV. EEG beta wave trains are not the second harmonic of mu wave trains in Parkinson's disease patients. *International Conference on Information Technology and Nanotechnology* (ITNT 2017), Samara, CEUR, 2017, 1901:226-234.
7. Sushkova OS, Morozov AA, Gabova AV. Investigation of specificity of Parkinson's disease features obtained using the method of cerebral cortex electrical activity analysis based on wave trains. *13th International Conference on Signal-Image Technology and Internet-Based Systems,* India, Jaipur: MNIT, 2017, p. 168-172.
8. Sushkova OS, Morozov AA, Gabova AV, Karabanov AV. Investigation of surface EMG and acceleration signals of limbs' tremor in Parkinson's disease patients using the method of electrical activity analysis

based on wave trains. *Advances in Artificial Intelligence: IBERAMIA 2018*. Springer, 2018, V. 11238 LNAI:253-264.

9. Sushkova OS, Morozov AA, Gabova AV, Karabanov AV, Chigaleychik LA. Investigation of the 0.5-4 Hz low-frequency range in the wave train electrical activity of muscles in patients with Parkinson's disease and essential tremor. *RENSIT: Radioelectronics. Nanosystems. Information technologies*, 2019, 11(2):225-236. DOI: 10.17725/rensit.2019.11.225.
10. Sushkova OS, Morozov AA, Gabova AV, Karabanov AV. Investigation of the multiple comparisons problem in the analysis of the wave train electrical activity of muscles in Parkinson's disease patients. *Journal of Physics: Conference Series*, 2019, 1368(5):052004.
11. Sushkova OS, Morozov AA, Kershner IA, Petrova NG, Gabova AV, Chigaleichik LA, Karabanov AV. Investigation of distribution laws of the phase difference of the envelopes of electromyograms of antagonist muscles in Parkinson's disease and essential tremor patients. *RENSIT: Radioelectronics. Nanosystems. Information technologies*, 2020, 12(3):415-428. DOI: 10.17725/rensit.2020.12.415.
12. Sushkova OS, Morozov AA, Gabova AV, Karabanov AV, Chigaleychik LA. An investigation of accelerometer signals in the 0.5-4 Hz range in Parkinson's disease and essential tremor patients. Advances in Intelligent Systems and Computing. *International Conference on Frontiers in Computing and Systems* (COMSYS-2020), Jalpaiguri Government Engineering College, West Bengal, India, January 13-15, 2020. Springer, Singapore, 2021, 1255:455-462.
13. Sushkova OS, Morozov AA, Gabova AV, Karabanov AV. Development of a method for early and differential diagnosis of Parkinson's disease and essential tremor based on analysis of wave train electrical activity of muscles. *Information Technology and Nanotechnology* (ITNT-2020), Samara, Russia, 2020. Washington: IEEE Xplore Digital Library, 2020, p. 1-5. DOI: 10.1109/ITNT49337.2020.9253237.
14. Sushkova OS, Morozov AA, Gabova AV, Kershner IA, Chigaleychik LA, Karabanov AV. Investigation of phase analysis methods of antagonist muscles electromyograms in patients with neurodegenerative diseases. *Information Technology and Nanotechnology* (ITNT-2021), Samara, Russia, 2021. Washington: IEEE Xplore Digital Library, 2021, p. 1-5. DOI: 10.1109/ITNT52450.2021.9649193.
15. Sushkova OS, Morozov AA, Petrova NG, Khokhlova MN, Gabova AV, Karabanov AV, Chigaleychik LA, Sarkisova KY. Method of wave train electrical activity analysis – the theoretical basis and application. *RENSIT: Radioelectronics. Nanosystems. Information technologies,* 2022, 14(3):317-330. DOI: 10.17725/rensit.2022.14.317.
16. Sushkova OS, Morozov AA, Gabova AV, Karabanov AV. Method for differential diagnosis of essential tremor and early and first stages of Parkinson's disease using wave train activity analysis of muscles. *Patent number RU 2741233 C1*, 22 January 2021.
17. Sushkova OS, Morozov AA, Gabova AV, Karabanov AV, Chigaleychik LA, Illarioshkin SN. A method for differential diagnosis of essential tremor and the first stage of Parkinson's disease using the analysis of wave trains in the cross-wavelet spectrum of electromyographic signals of antagonist muscles. *Patent number RU 2797878 C1*, 9 July 2023.
18. Sushkova OS, Morozov AA, Gabova AV, Sarkisova KY. A method for detecting immature discharges in epilepsy in laboratory rats using the analysis of wave train electrical activity of the brain. *Patent number RU 2781622 C1*, 17 October 2022.
19. Audet C, Hare W. *Derivative-free and blackbox optimization*. Springer, 2017.
20. Ingber L. Adaptive simulated annealing (ASA): lessons learned. *Control and Cybernetics,* 1996, 25(1):33-54.

21. Audet C, Dennis JJ. Analysis of generalized pattern searches. *SIAM Journal on optimization*, 2002, 13(3):889-903.
22. Goldberg DE. *Genetic Algorithms in Search, Optimization, and Machine Learning*, Addison-Wesley, 1989.
23. Zlobec S. Characterizing optimality in mathematical programming models. *Acta Applicandae Mathematicae*, 1988, 12:113-180.
24. Sniedovich M. Fooled by local robustness. Risk Analysis. *An International Journal,* 2012, 32(10):1630-1637.
25. Ben-Tal A, El Ghaoui L, Nemirovski A. *Robust optimization.* Princeton University Press, 2021.

DOI: 10.17725/j.rensit.2024.16.079

Tracks of strange radiation. Their properties. An attempt at explanation

Alexander G. Parkhomov
KIT Experimental Design Laboratory
Moscow 121108, Russian Federation
E-mail: alexparh@mail.ru
Vladislav A. Zhigalov
Kazakh Satpayev National Research Technical University, https://satbayev.university/en/
Almaty 050013, Republic of Kazakhstan
E-mail: zhigalov@gmail.com
Vladimir K. Nevolin
Moscow Institute of Electronic Technology, https://eng.miet.ru/
Moscow, Zelenograd 124498, Russian Federation
E-mail: vkn@miee.ru

Received September 29, 2023, peer-reviewed October 06, 2023, accepted October 13, 2023, published March 15, 2024.

Abstract: **A brief description of the detected properties of tracks that occur near installations in which LENR processes occur is given. A hypothesis is presented explaining where the particles that "draw" tracks come from, why the drawings of tracks are unique, why the intensity of the appearance of tracks is not constant. Experiments confirming this hypothesis are described.**

Keywords: **LENR, strange radiation, tracks, drip tracks, microcraters, dust, electric charge, X-ray radiation, AUGER electrons, piezoelectrics**

UGC 53.043

Acknowledgments: The authors express gratitude to S.G. Chernook and L.A. Barsukov for SEM and AFM studies, A.I. Klimov, A.I. Nikitin, A.V. Chistolinov, V.F. Pevtsov, A.G. Sobolev for useful discussions.
For citation: Alexander G. Parkhomov, Vladislav A. Zhigalov, Vladimir K. Nevolin. Tracks of strange radiation. Their properties. An attempt at explanation. R*ENSIT: Radioelectronics. Nanosystems. Information Technologies,* 2024, 16(1):79-88e. DOI: 10.17725/j.rensit.2024.16.079.

Contents

1. INTRODUCTION

The phenomenon called "strange radiation tracks" (SRT) was first described in detail in an article on the effects detected during electric foil explosions [1], although LENR researchers (Low Energy Nuclear Reactions - nuclear reactions at low energies) had observed similar tracks before [2,3,4]. In the study [1], photoemulsions were used as detectors. The traces found were not similar to tracks formed by charged particles of high energy, since, first of all, they were very long (up to several millimeters). The shape of the detected tracks is different: continuous straight or curved tracks, tracks with kinks, tracks with a complex periodically repeating pattern. All tracks are located strictly along the surface. An estimate of the energy release in the tracks gave a value of ~1000 MeV (particles arising in nuclear reactions have an energy of ~ 1 MeV). Note that the effects of strange radiation are not only extended tracks, but also microcraters [5].

LENR reactors of various types (nickel-hydrogen, with incandescent lamps, with electrolysis and plasma electrolysis) were created in the KIT experimental design laboratory in 2015-2022 [6-13]. Some of them worked continuously for a long time (up to 7 months). The duration and stability of the operation of the reactors made it possible to conduct systematic studies of SRT, examining not only the type of specific tracks, but also the speed of their appearance on the surface of the detectors, dependence on distance and dynamics over time.

Initially, detectors used in nuclear physics experiments to register high-energy charged particles were used for the study of SRT: photographic films, X-ray films and nuclear photoemulsions. But it was soon discovered that SRT also appear on smooth surfaces of almost any substance. In addition to photoemulsion detectors, glass, mica, metals, plastics and a number of other materials were tested at KIT research laboratory. Most of the experiments were done using CD and DVD discs (polycarbonate) as detectors. Fresh discs have a very smooth surface without scratches and are easily accessible in large quantities, which makes it possible to increase the statistical reliability of the results obtained. Optical, scanning electron (SEM) and atomic force (AFM) microscopy methods were used to study the shape of the tracks.

This article does not aim at a detailed description of the research methodology and the array of data obtained, as they are set out in publications [14-19]. Here are only the most important results and the main conclusions arising from the various studies conducted. We will systematize the types of tracks, give an analysis of the results obtained, and on the basis of the revealed patterns we will formulate a hypothesis explaining the main experimentally discovered properties of SRT.

2. TACKS TYPES

2.1. Smooth tracks

Smooth tracks (**Fig. 1**) predominate in plastic fusible materials (plastics, gelatin in photoemulsion). Such tracks have the form of grooves with a depth of about 0.1 microns and a width of several microns. On the sides, protrusions are visible with a height approximately equal to the depth of the groove (probably squeezed out material).

2.2. Tracks with a periodically repeating complex pattern

Tracks with a period from 44 to 200 microns were detected. In each track of this type, the pattern is unique (**Fig. 2**). Occur both in plastic materials and moderately hard and heat-resistant (glass, metals). The cross-sectional profile of such tracks has a complex character (**Fig. 3**). Sometimes it is possible to observe the transition of a smooth track into a periodic one (**Fig. 4**).

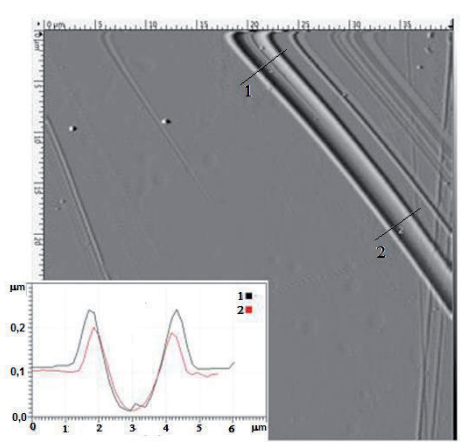

Fig. 1. *"Smooth" tracks on polycarbonate. The image obtained by atomic force (AFM) microscopy* [18,19].

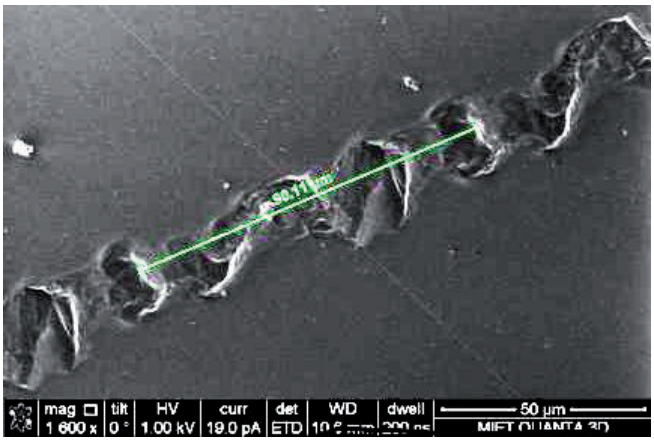

Fig. 2. *Fragment of a typical track with a periodic pattern on the surface of polycarbonate (SEM). The period is about 90 microns* [18,19].

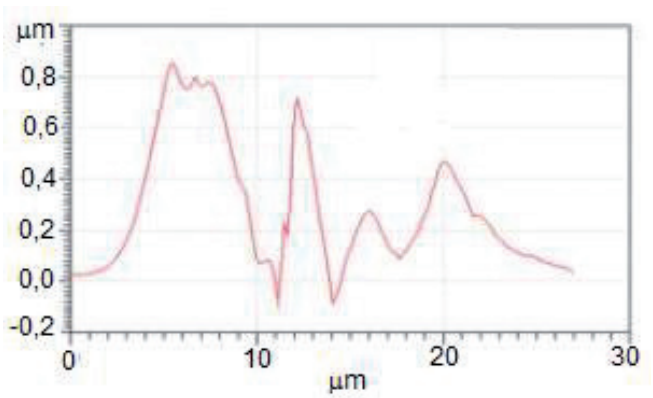

Fig. 3. *Example of AFM profilogram cross-sectional of one of the sections of a periodic track on polycarbonate* [18,19]

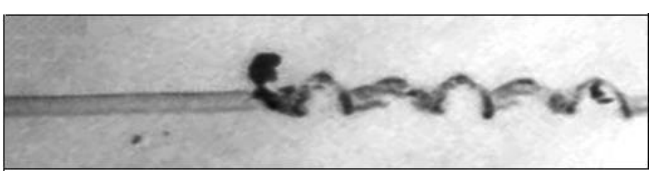

Fig. 4. *Transition of a periodic track (period 45 microns) to a smooth one (or vice versa). Polycarbonate. Optical microscope* [15]

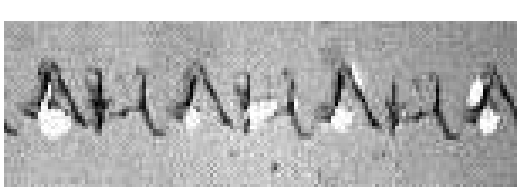

Fig. 5. *Fragment of the track on the glass. Optical microscope. The track pattern repeats with a period of about 70 microns. Bright areas, possibly cracks in the glass* [22].

2.3. Tracks along which cracking and scattering occurs

Occur in brittle heat-resistant materials (mica, glass, ceramics, etc.)

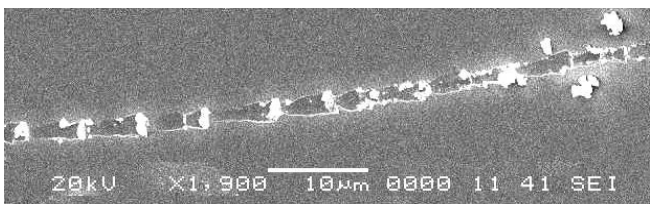

Fig. 6. *Example of a mica track (SEM) [15,17].Tracks on mica represent extended traces of surface destruction, as if the captured material is raked and then periodically left on the further path. Next to the tracks, small mica particles are visible on the mica surface, possibly ejected from the track.*

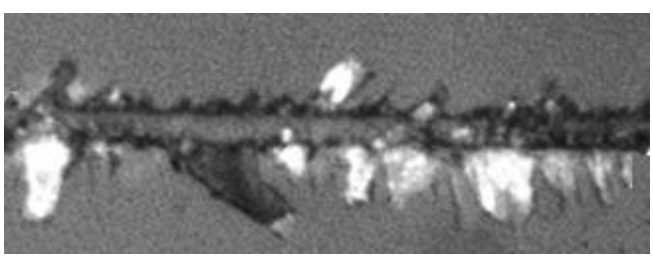

Fig. 7. *Tracks on the surface of lithium niobate $LiNbO_3$ are accompanied by numerous cracks. Optical microscope* [22].

2.4. Tracks in the form of chains of round spots ("drip tracks")

Found near electrolysis cells.

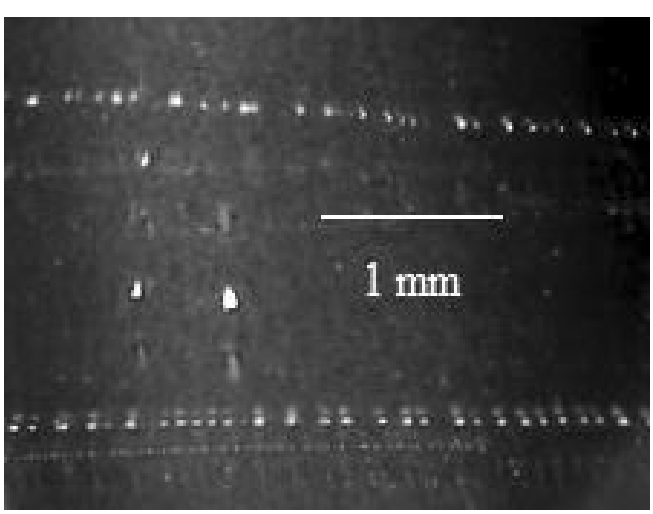

Fig. 8. *"Drip" tracks on DVDs near an H_2SO_4 electrolytic cell with nickel electrodes* [12].

2.5. Microcraters

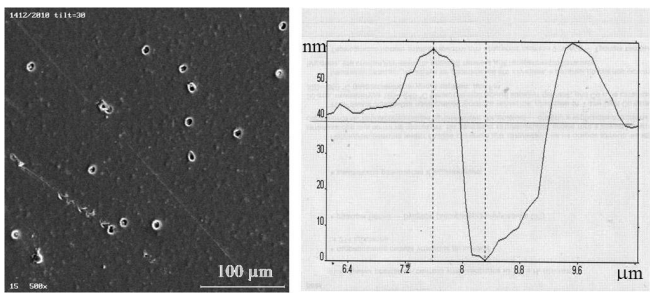

Fig. 9. *On the left: microcraters and tracks detected on the X-ray film located near the cavitation unit. On the right: AFM profilogram of one of the microcraters. This microcrater has a diameter of about 1.1 microns and a depth measured from the film plane of 38 nm* [5].

3. GENERAL PROPERTIES OF STRANGE RADIATION TRACKS

3.1. Intensity of the appearance of tracks depending on the distance to the LENR reactors. Variability

To numerically estimate the intensity of the appearance of tracks, the method of calculating the total length of tracks and comparing the obtained values of the experimental samples with the control was used [14-16]. The usual duration of each exposure is 1 week. Due to the fact that the size of the detectors is comparable to the size of the area in which the appearance of a sufficiently large number of tracks is observed, and, in addition, the intensity of the appearance of tracks is extremely unstable over time, the determination of the dependence on distance can only be estimated. Despite this, numerous long-term measurements allow us to draw an important conclusion about a sharp decrease in the intensity of the appearance of tracks at a distance of more than 20 cm from the reactors. Thus, the average for 5 exposures, the total length of tracks on mica for distances of 5 cm from the reactors (948 mm per sample) exceeds by more than an order of magnitude the average for 10 exposures, length of tracks for long distances (37 mm per sample). A large variation in the values of individual measurements is characteristic for this phenomena.

The results on the DVD are similar to those obtained for mica: on average, 980 mm per sample for a zone closer than 20 cm from the reactors (49 exposures) and 54 mm per sample for a zone further

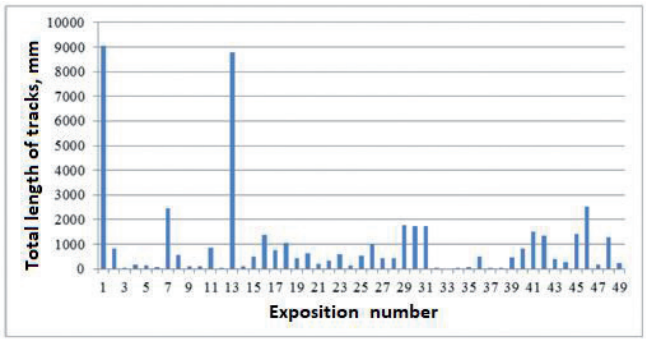

a

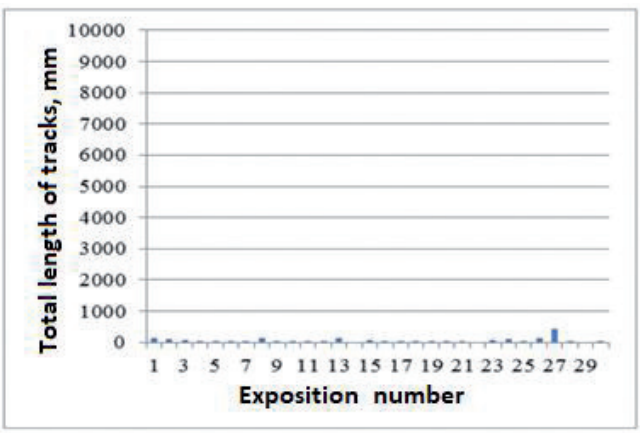

b

Fig. 10. *Total lengths of tracks on DVD by exposure: (a) for the near zone, (b) for the far zone* [14,15].

than 20 cm (30 exposures). There is also a large spread of values obtained both in the near and far zone (see **Fig. 10**).

Note that the appearance of tracks is a rather rare phenomenon. According to [14,15], the average rate of accumulation of tracks at a distance of 5-13 cm from the nickel-hydrogen reactor [7] is 0.027 mm per cm^2 per hour, i.e. the appearance of tracks with a total length of 1 mm on a square centimeter of the detector can be expected for a time of about 37 hours.

3.2. Intensity of the appearance of tracks depending on the shielding and orientation of the detectors

In the course of various experiments, the following was found out [16]. Discs tightly arranged in a stack protect each other (tracks appear mainly on the first disc). There are few tracks on discs located in a plastic box closed from all sides.

In part of the exposures from the nickel-hydrogen reactor, an aluminum foil curtain covered DVDs from thermal radiation. This curtain did not

form a solid shell around the disc, and was separated from the disc by a distance of several cm. At the same time, the discs gained a significant number of tracks, unlike the control discs located at a distance from the reactor. Protection against the appearance of tracks seems to work only in the case of a screen tightly covering the detector from all sides.

No regularity in the accumulation of tracks by discs depending on their orientation were observed in our experiments.

3.3. Investigation of the substance elemental composition in the tracks

One of the methods used to study the shape of tracks was scanning electron microscopy (SEM). This method, along with obtaining high-resolution images, makes it possible to analyze the elemental composition of a substance at specified points on the surface under study. Analyses made in the area of tracks and at a distance from them did not reveal significant differences.

4. HYPOTHESIZING THE NATURE OF STRANGE RADIATION TRACKS (SRT)

An overview of approaches to the explanation of SRT (the hypothesis of magnetic monopoles, the hypothesis of tachyons, the hypothesis of magneto-toro-electron radiation, the hypothesis of "dark" hydrogen, the hypothesis of multicharged clusters, etc.) can be found in the article [23]. None of these hypotheses can explain the complex of properties inherent in this amazing phenomenon. In particular, two important properties are ignored, without which it is impossible to do without an explanation: a very complex, diverse, non-repeating pattern of periodic tracks, and a strong unpredictable variability in the intensity of the appearance of tracks. The hypothesis outlined below makes it possible to approach the explanation of not only one side of this phenomenon, but the whole set of experimentally discovered properties.

4.1. Tracks with a periodically repeating complex pattern can be formed as a result of rolling objects ranging in size from 14 to 64 microns [18,19]. The irregularities of these objects are imprinted on the surface of the detector, which ensures the repeatability of the pattern with detected periods from 44 to 200 microns.

4.2. It is reasonable to assume that these objects are dust particles suspended in the air. The variety

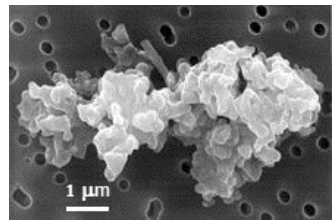

Fig. 11. *A dust particle under a microscope* [20].

of dust motes shapes explains the uniqueness of the drawings in various tracks (**Fig. 11**). The dustiness of the air, and, consequently, the intensity of the appearance of tracks, depends on many difficult-to-control circumstances. Dust particles driven by air currents can penetrate into any places that do not have reliable protection against air penetration.

4.3. In order for a dust particle to leave an imprint, it must be harder than the detector material and pressed hard enough against the detector surface. If we count the area of contact of a dust particle with the detector surface of 1 μm^2 and the tensile strength of 50 MPa (polycarbonate), a force of $f \sim 5 \cdot 10^{-5}$ N is needed for irreversible deformation.

4.4. Let's assume that the force is related to the electric charge of a dust particle. Suppose that a dust particle has the shape of a sphere with a diameter of $d = 20$ microns. To attract to a flat electrically conductive surface with a force of $f = 5 \cdot 10^{-5}$ N, a sphere with a diameter of 20 microns must have a charge $q = 2d(\pi\varepsilon_0 f)^{1/2} = 1.5 \cdot 10^{-12}$ C ($9.3 \cdot 10^6$ electron charges). The force of attraction to the dielectric surface has the same order of magnitude (depends on the permittivity). Electric capacity of a sphere with a diameter of 20 microns $C = 2\pi\varepsilon_0 d = 1.1 \cdot 10^{-15}$ F, potential $\varphi = q/C = 1350$ V, electric field energy $W = C\varphi^2/2 = 1.0 \cdot 10^{-9}$ J = 6300 MeV, the electric field strength on the surface of the sphere $E = q/\pi\varepsilon_0 d^2 = 1.3 \cdot 10^8$ V/m.

4.5. Such a charge may appear in a dust particle when it is located near the LENR reactor. Experiments show that the agent causing nuclear transmutations acts not only inside, but also outside the reactor [9-11]. Discussion of the nature of this agent is beyond the scope of this article. It is this agent, which has a high penetrating power, that is "strange radiation".

4.6. The electron shells of atoms resulting from nuclear transmutations are in a highly excited state (this is evidenced by soft X-ray radiation near LENR

reactors) [21]. The excitation of electron shells is removed not only by *X*-ray radiation, but also by the emission of Auger electrons with an energy of up to tens of keV. They are usually absorbed in close areas of the surrounding matter. But in the case of a small dust particle, they can come out. For example, the path length of an electron with an energy of 10 keV in a substance with a density of $2 \cdot 10^3$ kg/m^3 (silicon dioxide) is about 5 microns [24]. As a result, a dust particle acquires a positive charge. Assuming that each act of nuclear transmutation is accompanied by the loss of one electron, $9.3 \cdot 10^6$ transmutations (approximately one transmutation per 10^8 atoms of the dust particle substance) are required to acquire a charge of $1.5 \cdot 10^{-12}$ C.

4.7. The high intensity of the electric field near the charged dust particle (~10^8 V/m), it would seem, should lead to the ignition of the corona discharge and the rapid draining of the electric charge. However, the occurrence of electronic avalanches requires not only a high field strength, but also a sufficiently high potential difference [25]. A potential difference of about 1000 V is not enough for this. In addition, dielectric particles as a result of nuclear transmutations are charged volumetrically, which makes it difficult for charges to drain from the surface.

4.8. A dust particle attracted to the detector surface can either release the energy of an electric charge, forming a microcrater (6300 MeV energy is quite enough for this), or move if there is an electric field along the surface or the detector material is inhomogeneous (the relative permittivity is unstable). There may also be reasons unrelated to the electric field, for example, the movement of air along the surface of the detector. Moreover, the particle will predominantly not slide, but roll, since the coefficient of rolling friction is 2-4 orders of magnitude less than the coefficient of sliding friction.

4.9. "Smooth" tracks are formed by particles up to 10 microns in size [18,19]. During the movement, heat is released as a result of deformation and destruction of the detector material and dust particles. This can lead to melting of the material on which the tracks are formed, and to smoothing out possible irregularities [18,19]. It is clear why there are especially many "smooth" tracks on fusible materials (plastics).

4.10. Brittle materials with a high melting point (for example, mica, glass) are destroyed by a moving particle not only by pressure, but also by a sharp temperature drop. Particularly severe damage occurs in materials with piezoelectric properties (for example, lithium niobate) as a result of the action of a strong electric field. Approaching the surface of the dielectric detector of a positively charged body causes polarization of the dielectric, equivalent to the action of a negative charge of the same magnitude (in our example, $q = 1.5 \cdot 10^{-12}$ C). If a substance has piezoelectric properties with a typical piezo module $d \sim 10^{-11}$ C/N, it will contract with a force $f = q/d \sim 0.1$ *N*. This force acts on an area of about 10 μ^2 (10^{-11} m^2), causing a pressure of 10^{10} Pa, which significantly exceeds the strength limits of conventional materials.

4.11. "Drip" tracks. In the process of electrolysis, many droplets of electrolyte are formed in the form of an aerosol. Some of them, being in the field of action of the agent causing nuclear transmutation, acquire a positive electric charge. The properties of such droplets ("charged clusters") are studied in detail in [23]. They move, periodically approaching and moving away from the detector surface, dropping a cluster much smaller than the main one at the moment of approach. Chains of circular traces appear on the detector.

4.12. A sharp decrease in the probability of tracks appearing at a distance of 20-30 cm from LENR reactors is probably due not only to a geometric weakening of the intensity of the agent activating the dust particles, but also to the limited retention time of electric charges on the dust particles.

5. EXPERIMENTAL JUSTIFICATIONS

5.1. Modeling of the process of track formation as a result of dust particles rolling on the detector surface [22]

5.1.1. Tracks on DVD

a) For two days, a clean DVD disc without scratches lay on the windowsill near the open window with the working surface up, accumulating dust. Then the working surface of the dusty disc was rubbed against another disc with a very light pressure.

Tracks with periodic patterns appeared on the disc, as well as smooth single and double tracks, very similar to tracks of strange radiation (**Fig. 12**).

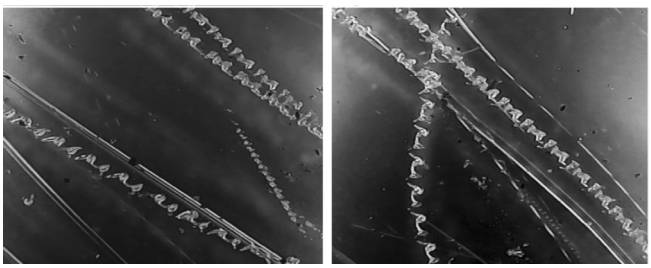

Fig. 12. *Tracks that appeared on the surface of a DVD disc when rolling dust particles (optical microscope).*

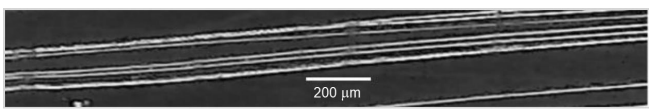

Fig. 13. *Tracks that appeared on the surface of a DVD disc during rolling of carbonyl nickel particles (optical microscope).*

b) Several carbonyl nickel particles with a shape close to spherical and a size from 5 to 20 microns were applied to a fragment of a clean DVD, covered with another fragment of a clean DVD and moved the upper disc by about 1 cm. Several parallel tracks with a width of ~ 10 microns appeared on the discs (**Fig. 13**).

5.1.2. Tracks on glass

Grains of quartz sand, corundum, and carbonyl nickel were placed between the microscope slides (**Fig. 14**). The compression force of the plates is ~ 1 *N* (light finger pressure), the movement of the upper glass relative to the lower one is about 1 cm.

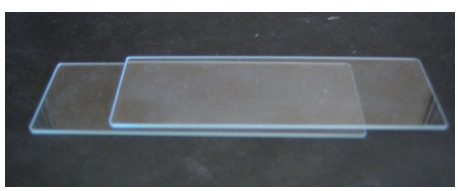

Fig. 14. *Location of the microscope slides.*

Fig. 15 shows one of the tracks that occurred when using corundum grains of ~ 50 microns in size. The randomness of the track pattern may be related to the randomness of the process of crack formation in the glass, as well as the gradual destruction of a grain of corundum.

When using grains of quartz sand and carbonyl nickel, tracks on the glass did not occur (the hardness of these substances is lower than the hardness of glass).

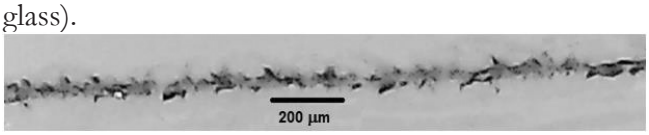

Fig. 15. *Slide glasses, corundum grains ~ 50 microns in size (optical microscope).*

Fig. 16. *Track on an X-ray film from a grain of quartz sand (optical microscope).*

5.1.3. Tracks on photoemulsions

Several grains of quartz sand 100-200 microns in size were applied to the RM-1 X-ray film with a size of 2x5 cm^2, covered with the same film and moved the upper film by about 1 cm with light pressure. Tracks with a distinct pattern periodicity appeared on the films (**Fig. 16**).

These experiments confirm the possibility of the appearance of traces similar to the tracks of strange radiation when rolling various particles on the surface of various materials.

5.2. High intensity of track formation at high concentration of dust-like particles

A halogen incandescent lamp with a rated power of 300 W at an increased supply voltage from 220 to 320 V is suspended inside a ceramic pipe. Experiments show that incandescent lamps operating in forced mode are sources of an agent that causes nuclear transmutations [9-12]. When turned on, the lamp and ceramic tube are heated to a high temperature, which contributes to the convection movement of air from the bottom up. If a powder, such as corundum, is poured at the bottom, rather small particles are carried away by the ascending air flow and pass near the lamp (**Fig. 17**). A detector (for example, a glass plate) is located on top of the pipe. The air coming out of the pipe with trapped particles washes the detector.

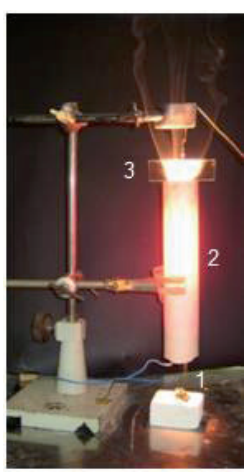

Fig. 17. *"Generator" of tracks. 1 – aerosol source, 2 – ceramic tube with an incandescent halogen lamp located inside, 3 – detector.*

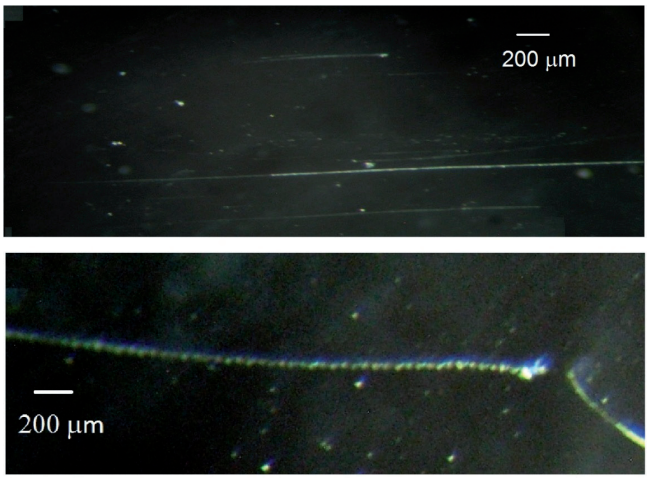

Fig. 18. *Some of the tracks that appeared on the slides during 1 minute of operation of the "track generator" (optical microscope).*

In order to avoid overheating, the installation can be turned on only for 1 minute. But even this time is enough for tracks to appear on the detectors (examples in **Fig. 18**). This is a very high intensity. Recall that under normal conditions, the appearance of tracks with a total length of 1 mm on a square centimeter detector can be expected in about 37 hours (see section 3.1)

6. CONCLUSION

The assumption that tracks of strange radiation form dust particles or liquid droplets suspended in the air, which have acquired an electric charge as a result of nuclear transmutations, allows us to explain many features of the phenomenon of tracks of strange radiation, indicated at the beginning of the article. The proposed hypothesis answers the questions:

- why tracks only appear on the surface;
- where do the particles forming the tracks come from;
- why does an electric charge appear in them and what does LENR have to do with it;
- how tracks with unique periodic patterns, smooth tracks, tracks with cracks and "drip" tracks arise;
- why the intensity of the appearance of tracks is unstable under seemingly identical conditions.

The possibility of the appearance of tracks similar to SRT when dust and dust-like particles are pressed against the surface of various detectors has been confirmed experimentally. Based on the hypothesis put forward, an experimental setup has been created in which the intensity of the appearance of tracks is significantly increased compared to the natural process.

Thus, the proposed hypothesis allows us to explain a number of characteristic features of the phenomenon of strange radiation tracks, which seemed mysterious. At the same time, there are still questions that require reflection and further research.

REFERENCES

1. Urutskoev LI, Liksonov VI, Tsinoev VG. Observation of transformation of chemical elements during electric discharge. *Ann. Fond. L.de Broglie,* 2002, 27(4):701-726.
2. Matsumoto T, Kurokawa K. Observation of Heavy Elements Produced During Explosive Cold Fusion. *Fusion Technology*, 1991, 20(3):323-329.
3. Solin MI. Eksperimental'nye fakty spontannogo zarozhdeniya kondensata solitonnyh zaryadov s obrazovaniem produktov yadernogo sinteza v zhidkom cirkonii [Experimental facts of spontaneous generation of a condensate of soliton charges with the formation of nuclear fusion products in liquid zirconium]. *Fizicheskaya mysl' Rossii,* 2001, 1:43-58 (in Russ.).
4. Rodionov BU, Savvatimova IB. O prirode strannyh trekov. Materialy 13 Rossijskoj konferencii Holodnaya transmutaciya yader himicheskih elementov i sharovaya molniya [About the nature of strange tracks]. *Proceedings of the 13th Russian Conference Cold Transmutation of Nuclei of Chemical Elements and Ball Lightning,* 2005, 187-205, (in Russ.).
5. Shishkin AL, Tatur VYu. Otsenka vozdejstviya strannogo izlucheniya na biologicheskie ob'ekty [Assessment of the impact of strange radiation on biological objects]. *Proceedings of the 25th Russian Conference Cold Transmutation of Nuclei of Chemical Elements and Ball Lightning*, 2018, 76-80 (in Russ.).
6. Parkhomov AG, Alabin KA, Andreev SN et al. Nickel-hydrogen reactors: heat release, isotopic and elemental composition of fuel. *RENSIT: Radioelectronics. Nanosystems. Information Technologies,* 2017, 9(1):74-93. DOI: 10.17725/rensit.2017.9.074.

7. Alabin KA, Andreev SN, et al. Isotopic and Elemental Composition of Substance in Nickel-Hydrogen Heat Generators. *J. Condensed Matter Nucl. Sci.,* 2018, 26:32. http://www.iscmns.org/CMNS/JCMNS-Vol 26.pdf.
8. Parkhomov AG, Zhigalov VA, Zabavin SN et al. Nikel-vodorodnyiy teplogenerator, nepreryivno prorabotavshiy 7 mesyatsev [Nickel-hydrogen heat generator, continuously worked for 7 months]. *Zhurnal formiruyushchikhsya napravleniy nauki* (ZHFNN), 2019, 23-24(7):57-63 (in Russ.), http://www.unconv-science. org/pdf/23/parkhomov2.pdf.
9. Parkhomov AG, Karabanov RV. Issledovanie elementnyh i izotopnyh izmenenij v veshchestve okolo lamp nakalivaniya. [Investigation of elemental and isotopic changes in matter near incandescent lamps]. *ZHFNN*, 2021, 27(8):116-119 (in Russ.), http://www.unconv-science.org/pdf/27/parkhomov2.pdf.
10. Parkhomov AG, Karabanov RV. LENR as a manifestation of weak nuclear interactions. New approach to creating LENR reactors. *RENSIT: Radioelectronics. Nanosystems. Information Technologies,* 2021, 13(1):45-58. DOI: 10.17725/rensit.2021.13.045.
11. Parkhomov AG, Karabanov RV, Belousova EO. Investigation of LENR Processes Near Incandescent Metals. *Proceedings of the 23rd International Conference on Condensed Matter Nuclear Science,* Xiamen, China, June 9-11, 2021. *J. Condensed Matter Nucl. Sc*i, 2022, 36:362-376. https://yadi.sk/d/sZOkktMQkxDjvg.
12. Zhigalov VA, Parkhomov AG, Nevolin VK. Investigation of strange radiation tracks near incandescent lamps and electrolytic cell. *RENSIT: Radioelectronics. Nanosystems. Information Technologies*, 2023, 15(1):95-105. DOI: 10.17725/rensit.2023.15.095.
13. Parkhomov AG. Issledovanie processov na ustanovke impul'snogo plazmennogo elektroliza. [Investigation of processes at a pulsed plasma electrolysis plant]. *Proceedings of the 20th Russian Conference Cold Transmutation of Nuclei of Chemical Elements and Ball Lightning,* 2013, 65-76. http://www.unconv-science.org/n25/ parkhomov.
14. Parkhomov AG, Zhigalov VA, Zabavin SN, Sobolev AG, Timerbulatov TR. Statistika trekov strannogo izlucheniya ot dvuh tipov reaktorov LENR [Statistics of strange radiation tracks from two types of LENR reactors]. *Proceedings of the 25th Russian Conference Cold Transmutation of Nuclei of Chemical Elements and Ball Lghtning*, 2018, 51-62 (in Russ.).
15. Zhigalov VA, Zabavin SN, Parkhomov AG, Sobolev AG, Timerbulatov TR. Statistika i struktura trekov strannogo izlucheniya ot dvuh tipov reaktorov LENR. [Statistics and structure of strange radiation tracks from two types of LENR reactors]. *ZHFNN*, 2018, 21-22(6):10-25 (in Russ.), http://www.unconv-science.org/pdf/21/zhigalov1.pdf.
16. Zhigalov VA. Strange radiation and LENR: what's the relation? *RENSIT: Radioelectronics. Nanosystems. Information Technologies*, 2021, 13(3):329-348. DOI: 10.17725/rensit.2021.13.329.
17. Parkhomov AG, Zhigalov VA, Zabavin SN, Sobolev AG., Timerbulatov TR. Struktura trekov strannogo izlucheniya ot dvuh tipov reaktorov LENR [The structure of strange radiation tracks from two types of LENR reactors]. *Proceedings of the 25th Russian Conference Cold Transmutation of Nuclei of Chemical Elements and Ball Lightning*, 2018, 63-75.
18. Zhigalov VA, Parkhomov AG. Treki strannogo izlucheniya – dvizhenie tverdyh chastic vdol' poverhnosti.[Tracks of strange radiation – the movement of solid particles along the surface]. *Proceedings of the 27th Russian Conference Cold Transmutation of Nuclei of Chemical Elements and Ball Lightning*, 2022, 51-64.
19. Zhigalov VA, Parkhomov AG. Strange radiation tracks - the movement of solid particles along the surface. *Preprint.* August 2023, https://www.researchgate.net/publication/373257344.
20. https://en.wikipedia.org/wiki/Dust.
21. Klimov AI, Belov NK, Tolkunov BN. Izmerenie potokov nejtronov, myagkogo rentgenovskogo izlucheniya v geterogennoj nano-klasternoj plazme [Measurement of neutron fluxes, soft X-rays in heterogeneous nano-cluster plasma].

Proceedings of the 26th Russian Conference Cold Transmutation of Nuclei of Chemical Elements and Ball Lightning, 2020, 29-36.

22. Parkhomov AG, Zhigalov VA. Novyj podhod k issledovaniyu trekov strannogo izlucheniya. [New approach to the study of strange radiation tracks]. Report at the Klimov-Zatelepin webinar on June 21, 2023, http://lenr.seplm.ru/seminary.
23. Anatoly I. Nikitin, Vadim A. Nikitin, Alexander M. Velichko, Tamara F. Nikitina. Strange traces of a "strange" radiation. *RENSIT: Radioelectronics. Nanosystems. Information Technologies*, 2022, 14(3):249-268. DOI: 10.17725/rensit.2022.14.249.
24. Grigoriev IS, Meilikhov EZ (eds) *Fizicheskie velichiny* [Physical quantity]. Moscow, Energoatomizdat Publ., 1991, 1170 p.
25. Rajzer YuP. *Fizika gazovogo razryada* [Physics of gas discharge]. Moscow, Nauka Publ., 1992.

DOI: 10.17725/j.rensit.2024.16.089

Analysis of the intrinsic spin-Hall effect in metals for spintronics problems

Vyacheslav K. Ignatjev, Sergey V. Perchenko, Dmitry A. Stankevich

Volgograd State University, https://volsu.ru/

Volgograd 400062, Russian Federation

E-mail: vkignatjev@yandex.ru, perchenko@volsu.ru, stankevich@volsu.ru

Received September 18, 2023, peer-reviewed September 25, 2023, accepted October 02, 2023, published March 15, 2024.

Abstract: **A method for estimating the transverse spin-Hall resistance for polycrystalline samples of pure metals has been proposed. The spin-Hall effect coefficients for various metals of 3-6 periods, including rare-earth lanthanides, have been calculated. It is shown that the sign of the calculated spin-Hall resistance always coincides with the experimental one. For most of the considered metals the calculation result agrees with the experimental data. It is shown that the agreement of the calculation results with experiment can be significantly improved if the used approximations of strong coupling and effective charge are supplemented by the assumption that the interaction of collectivized conduction electrons in the construction of the self-consistent field can be taken into account by the introduction of the effective mass of the conduction electron in the Hamiltonian of the spin-orbit interaction. The reasons for the deviation for aluminum, copper, dysprosium, holmium, and gadolinium are discussed.**

Keywords: **spintronics, spin-Hall effect, spin-orbit interaction, strong coupling approximation, nearest-neighbor approximation, ideal Fermi-gas approximation, self-consistent field, effective charge**

PACS: 67.57.Lm, 72.25.Ba, 75.76.+j

Acknowledgments: The research was carried out of the funds of the Russian Science Foundation grant № 22-22-20035 (https://rscf.ru/en/project/22-22-20035/), as well as the funds of the Volgograd region budget resources.

For citation: Vyacheslav K. Ignatjev, Sergey V. Perchenko, Dmitry A. Stankevich. Analysis of the intrinsic spin-Hall effect in metals for spintronics problems. *RENSIT: Radioelectronics. Nanosystems. Information Technologies,* 2024, 16(1):89-100e. DOI: 10.17725/j.rensit.2024.16.089.

Contents

1. INTRODUCTION

A promising direction for the development of a new generation of information technology and sensor devices [1] is non-magnetic spintronics based on the spin-Hall effect (SHE). It is accepted to distinguish between extrinsic and intrinsic SHE. The main role in the extrinsic SHE, predicted by M.I. Dyakonov and V.I. Perel in 1971 [2], the spin-dependent scattering of conduction electrons on impurity fields plays a major role. Such scattering provides a fraction of spin-polarized current of the order of fractions of a percent with a coherence length of the

order of tens of nanometers. This is sufficient for studies of spin effects in nanostructures, but not for information and biotechnology. The intrinsic SHE predicted by S. Murakami in 2003, J. Sinova in 2004 [3] and soon discovered experimentally [4] occurs due to the spin-orbit interaction of the Rashba-Dresselhaus type [5]. This interaction is caused by the field of atomic nuclei and can be induced by the non-zero orbital momentum of the conduction electron, or directly by its momentum [6].

The intrinsic SHE is that the charge current in pure nonmagnetic metals with strong spin-orbit interaction leads to a measurable transverse spin current [7]. There is also an opposite phenomenon, the inverse spin-Hall effect (ISHE), in that a spin current in a metal creates a transverse charge current [8]. Thus, the intrinsic SHE can be used in spintronics devices for both generation and detection of spin current. It has been experimentally found that in some cases polycrystalline samples exhibit an increase in the angle of the SHE, the fraction of spin-polarized current, and the coherence length compared to single-crystal samples [9].

At present, reliable experimental data on the spin-Hall effect in metals are available. Therefore, within the approximations used in [10], the spin-Hall effect coefficients of nonmagnetic metals of the 5th and 6th periods were calculated [11]. For platinum, tantalum, gold, alpha-tungsten, palladium, molybdenum, and niobium, the calculation of the transverse spin-Hall resistance gave results that agree with the published experimental ones within the measurement error. For beta-tungsten, the calculated values are about 2 times larger than the experimental values, reflecting the anomalously high SHE. The purposeful search for promising materials for spintronics devices, justification of methods for their design, calculation, and optimization of their signal characteristics implies expanding the basis for comparing calculated values with experimental ones. For this purpose, we calculated the constants of the spin-Hall effect for metals of the 4th and 3rd periods, as well as lanthanides.

2. SELF-CONSISTENT FIELD APPROXIMATION FOR COLLECTIVE ELECTRONS

The spin-orbit addition to the energy of a single electron located in a given electric field with potential $\Phi(\mathbf{r})$ has the form [12]

$$\hat{V} = -\frac{\hbar e}{2m^2c^2}\varepsilon_{\alpha\beta\gamma}\hat{s}_\alpha\frac{\partial\Phi}{\partial r_\beta}\hat{p}_\gamma. \quad (1)$$

Here m is the mass of an electron with charge $-e$, $\hbar$ is the reduced Planck constant, c is the speed of light in vacuum, $\varepsilon_{\alpha\beta\gamma}$ is the unit antisymmetric Levi-Civita tensor.

A pure metal crystal can be considered as a homonuclear molecule with metallic bonding. In the framework of the Hartree-Fock one-electron approximation, each collective electron is in a self-consistent field created by ion cores and other collective electrons [13]. The self-consistent field is usually obtained by the method of successive approximations. In the initial approximation, the wave function of a collective electron is considered as a molecular orbital and is represented as a linear combination of atomic orbitals (LCAO approximation).

For any spin state of an electron it is possible to choose such a direction of the z-axis that the projection of its spin on this axis has a certain value s_z, i.e. $\psi(\mathbf{r},\sigma) = \psi(\mathbf{r})\delta(\sigma, s_z)$. In the strong coupling approximation, such a combination for the coordinate part of the wave function can be the Wannier function [14]:

$$\psi(\mathbf{r}) = \frac{1}{\sqrt{N}}\sum_{n=1}^{N}\Psi(\mathbf{r}-\mathbf{R}_n)\exp(i\mathbf{k}\mathbf{R}_n), \quad (2)$$

Here $\Psi(\mathbf{r})$ is the atomic function of the outer electron, $\mathbf{R}_n$ is the translation vector, and N is the number of nodes in the crystallite.

As a model potential of the initial approximation we take the crystal field potential of ion cores with effective charge Ze and coordinates $\mathbf{R}_k$

$$\Phi(\mathbf{r}) = \frac{eZ}{4\pi\varepsilon_0}\sum_{k=1}^{N}\frac{1}{|\mathbf{r}-\mathbf{R}_k|}. \quad (3)$$

Here ε_0 is the electric constant.

If the atomic wave function $\Psi(\mathbf{r})$ in relation (2) is to be considered hydrogen-like as an initial approximation, the value of Z can be estimated by equating the coordinate of the maximum $\rho_{\max}$ of the radial component of this function to the atomic radius R_a.

$$Z = \frac{\rho_{\max} a_B}{R_a},$$

where $a_B = 5.3 \cdot 10^{-10}$ m is the Bohr radius. **Fig. 1** shows an example for estimating the value of Z for a metal of the fourth period, i.e., when the square of the modulus of the radial wave function R_{40} has four maxima.

The approximation of the effective charge in the model potential (3) together with the strong coupling approximation (2) means that, when constructing the self-consistent field for the collective electron, only its interaction with the nuclei and localized electrons of ion cores is taken into account. In the next approximation, the interaction, including exchange, of the collective electron with other conduction electrons should be taken into account. Such interaction is usually taken into account in the analysis of transport phenomena in the framework of the effective mass method. Formally, it is possible to replace in formula (1) the mass of the free electron by the effective mass. However, there is no reason to believe that this should be the effective mass determining the conductivity and thermal conductivity of the metal.

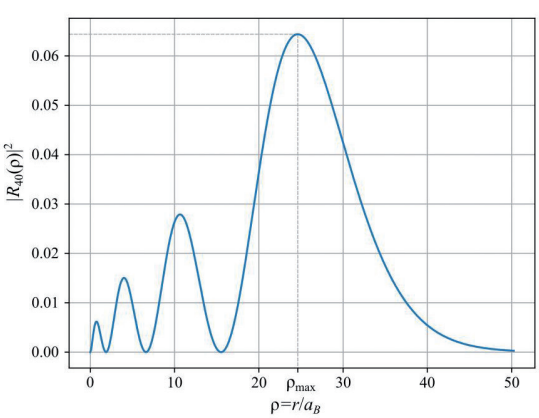

Fig. 1. *Dependence of the square of the absolute value of the radial wave function* $|R_{40}|^2$ *on the dimensionless coordinate* ρ. *Here the principal quantum number n = 4, orbital quantum number l = 0.*

3. DYNAMICS OF THE CONDUCTION ELECTRON MOMENTUM IN A CRYSTAL

Let us consider a mesoscopically homogeneous and isotropic metal. Individual crystallites exhibit anisotropic properties at the microscopic level, but a physically small volume containing a large number of randomly orientated crystallites will not have any distinguished direction. Under mesoscopic homogeneity and isotropy it is meant that there is no regular texture in the sample, i.e. the crystallites are oriented uniformly randomly. Regular texture may be formed during fabrication of the sample, such as mechanical rolling or other deformation of the sample, but not during sputtering. We will also assume that all crystallites have no intrinsic magnetic moment and there are no domain walls, so there is no significant spin perturbation during conduction electron transport across the boundary between crystallites.

The dynamics of the electron momentum created by the perturbation (1) is described by the equation for the mean [13]

$$\frac{dp_\delta}{dt} = \frac{i}{\hbar}\left\langle\left[\hat{V}, \hat{p}_\delta\right]\right\rangle = \\ = \frac{\hbar e \varepsilon_{\alpha\beta\gamma}}{2m^2c^2}\left\langle\psi\left|\hat{s}_\alpha \frac{\partial^2\Phi}{\partial r_\beta \partial r_\delta}\hat{p}_\gamma\right|\psi\right\rangle. \quad (4)$$

Integration over the coordinates and summation over the spin variables of the conduction electron are implied in the right-hand side of relation (4). For any spin state of the electron it is possible to choose such a direction of the z-axis that the projection of its spin on this axis has a certain value s_z, i.e. $\psi(\mathbf{r},\sigma) = \psi(\mathbf{r})\delta(\sigma,s_z)$. Then after summation in (4) on spin variables, putting $\langle\hat{\mathbf{s}}\rangle = \mathbf{s}$ and substituting variables $\mathbf{r} - \mathbf{R}_k \to \mathbf{r}$, we obtain

$$\frac{dp_\delta}{dt} = \frac{\hbar^2 e^2 Z s_\alpha}{8\pi\varepsilon_0 m^2 c^2 N}\sum_{n,m,k=1}^{N}\exp\left(i\mathbf{k}\left(\mathbf{R}_n - \mathbf{R}_m\right)\right)\times \\ \times\left\langle\Psi\left(\mathbf{r}+\mathbf{R}_k-\mathbf{R}_m\right)\left|3\frac{r_\delta}{r^5}\hat{l}_\alpha - \frac{\varepsilon_{\alpha\delta\gamma}}{\hbar r^3}\hat{p}_\gamma\right|\Psi\left(\mathbf{r}+\mathbf{R}_k-\mathbf{R}_n\right)\right\rangle. \quad (5)$$

The operator $3\frac{r_\delta}{r^5}\hat{l}_\alpha - \frac{\varepsilon_{\alpha\delta\gamma}}{\hbar r^3}\hat{p}_\gamma$, in the right-hand side of relation (5) is odd. Therefore, when $\mathbf{R}_n$

$-\mathbf{R}_k = 0$ and $\mathbf{R}_m - \mathbf{R}_k = 0$, its mean value is zero. The atomic functions are exponentially small at $r > R_a = na_B/Z$, n is the principal quantum number. At the same time, the distance between atoms in the crystal is significantly larger than R_a. Therefore, in relation (5) we can restrict ourselves to the nearest-neighbor approximation and leave in the right-hand side only the summands for which $\mathbf{R}_n - \mathbf{R}_k = \mathbf{a}_\nu$ and $\mathbf{R}_m - \mathbf{R}_k = 0$ or $\mathbf{R}_n - \mathbf{R}_k = 0$ and $\mathbf{R}_m - \mathbf{R}_k = \mathbf{a}_\nu$, where $\mathbf{a}_\nu$ is the vector drawn from the atom under consideration with the centre in the point $\mathbf{r} = 0$ to the nearest neighbor. Then, taking into account the Hermiticity of operator in relation (5), we obtain

$$\frac{dp_\delta}{dt} = -\frac{\hbar^2 e^2 Z s_\alpha}{4\pi\varepsilon_0 m^2 c^2}\sin(\mathbf{k}\mathbf{a}_\nu)\times \\ \times \mathrm{Im}\left\langle \Psi_\nu \left| 3\frac{r_\delta}{r^5}\hat{l}_\alpha - \frac{\varepsilon_{\alpha\delta\gamma}}{\hbar r^3}\hat{p}_\gamma \right| \Psi \right\rangle. \quad (6)$$

Here $\Psi_\nu(\mathbf{r}) = \Psi(\mathbf{r} + \mathbf{a}_\nu) - \Psi(\mathbf{r} - \mathbf{a}_\nu)$ is a function with parity opposite to the parity of the function $\Psi(\mathbf{r})$ and the summation by ν over pairs of symmetrically located with respect to the considered atom its nearest neighbors is implied.

The right part of relation (6) is equal to the force acting on the electron. It can be represented as the result of the action of the external electric field $\mathbf{E}_{SH}$ on the electron. In the first order of smallness by $\mathbf{k}\mathbf{a}_\nu$ we obtain:

$$E_{SH\alpha} = \frac{\hbar^2 Z e s_\beta k_\mu}{4\pi\varepsilon_0 m^2 c^2} a_{\nu\mu}\times \\ \times \mathrm{Im}\left\langle \Psi_\nu \left| 3\frac{r_\alpha}{r^5}\hat{l}_\beta - \frac{\varepsilon_{\alpha\beta\gamma}}{\hbar r^3}\hat{p}_\gamma \right| \Psi \right\rangle. \quad (7)$$

Note that the quantum mean in formula (7) splits into two summands, the first of which is proportional to the orbital momentum of the conduction electron and the second to its momentum, which agrees with the models [6].

4. INTRINSIC SPIN-HALL EFFECT IN POLYCRYSTALLINE METAL

Let us consider a macroscopic region of a polycrystalline metal. For any state of an electron it is possible to choose the direction of the quantization axis (z-axis) so that the projection of its orbital momentum on this axis has a certain value $l_z = l$. The energy of an electron in an atom in an electric field depends on the projection of its orbital momentum to the field direction [13]. Therefore, the orientation of the atomic orbitals is determined by the position of the crystallophysical axes of a crystallite and we can consider that the relation (7) is written in the coordinate system associated with the symmetry axes of the crystallite.

Let us introduce a laboratory coordinate system associated with the instruments that set the conduction current and measure the spin components. Therefore, the wave vector and spin vector of conduction electrons should be considered as given in the laboratory coordinate system. The components of the vectors and tensors in the laboratory system will be denoted by primed indices, and in the coordinate system associated with the crystal axes of the domain, not primed.

We transform the wave vector and spin vector of conduction electrons from the laboratory system into the system of crystal axes $k_\mu = p_{\mu\mu'}k_{\mu'}$, $s_\beta = p_{\beta\beta'}s_{\beta'}$, and the vector of the Hall electric field from the system of crystal axes into the laboratory system $E_{SH\alpha'} = p^{-1}_{\alpha'\alpha}E_{SH\alpha}$, where $p_{\alpha'\alpha}$ is a unitary rotation matrix. Substituting this transformation into equation (7), we average the $\mathbf{E}_{SH}$ vector in the macroscopic region over random orientations of crystallites. It is convenient to express the rotation matrix in terms of Euler angles:

$$p_{ij} = \begin{bmatrix} \cos(\alpha)\cos(\gamma) - \sin(\alpha)\cos(\beta)\sin(\gamma) & -\cos(\alpha)\sin(\gamma) - \sin(\alpha)\cos(\beta)\cos(\gamma) & \sin(\alpha)\sin(\beta) \\ \sin(\alpha)\cos(\gamma) + \cos(\alpha)\cos(\beta)\sin(\gamma) & -\sin(\alpha)\sin(\gamma) + \cos(\alpha)\cos(\beta)\cos(\gamma) & -\cos(\alpha)\sin(\beta) \\ \sin(\beta)\sin(\gamma) & \sin(\beta)\cos(\gamma) & \cos(\beta) \end{bmatrix},$$

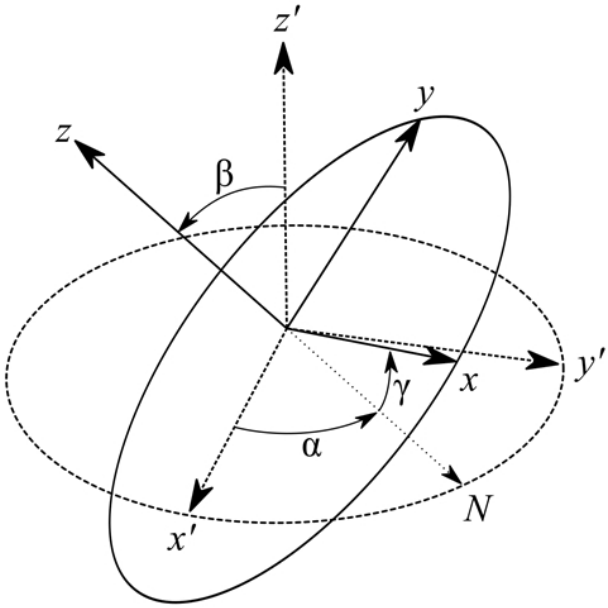

Fig. 2. *Transformation of vector components at transition from the laboratory coordinate system (primed indices) to the system of crystal axes. Here a, β and γ are Euler angles.*

Here $0 \le \alpha \le 2\pi$ is the precession angle, $0 \le \beta \le \pi$ is the nutation angle, $0 \le \gamma \le 2\pi$ is the angle of intrinsic rotation (**Fig. 2**). Then, for a mesoscopically isotropic metal, averaging over random crystallite orientations reduces to averaging over random uniformly distributed Euler angles.

$$E_{SH\alpha'} = \frac{\hbar^2 Zes_{\beta'} k_{\mu'} \overline{p^{-1}_{\alpha'\alpha} p_{\beta\beta'} p_{\mu\mu'}}}{4\pi\varepsilon_0 m^2 c^2} a_{\nu\mu} \times$$
$$\times \mathrm{Im}\left\langle \Psi_\nu \left| 3\frac{r_\alpha}{r^5}\hat{l}_\beta - \frac{\varepsilon_{\alpha\beta\gamma}}{\hbar r^3}\hat{p}_{\gamma\beta} \right| \Psi \right\rangle. \quad (8)$$

Here

$$\overline{p} = \frac{1}{8\pi^2}\int_0^{2\pi}\int_0^{\pi}\int_0^{2\pi} \sin(\beta) p(\alpha,\beta,\gamma)\, d\alpha\, d\beta\, d\gamma. \quad (9)$$

In the analytical averaging of equation (8), integrals of the form (9) were calculated in coordinate form, and then the result was converted to invariant form.

Considering the SHE only in metals, we will use the ideal Fermi-gas approximation for conduction electrons. The applicability of this model for conduction electrons in metals is justified by the fact that the thermodynamics of the Fermi system is determined by its microscopic structure only near the Fermi surface and does not depend at all on what is done beyond a blurring in an energy range of order $k_B T$, where k_B is the Boltzmann constant, T is the temperature.

As a result, the denser the Fermi-gas in a metal, the more ideal it is [15]. Experimental studies of the temperature dependence of the electron heat capacity in metals show that it corresponds well to the model of an ideal Fermi-gas with a scalar effective mass m^*. For many metals $m^* \approx m$. However, for gallium $m^* \approx 2.5m$ and for lanthanum $m^* \approx 0.23m$. Assuming within the effective mass method in (8) $\mathbf{k} = \mathbf{j}m^*/(\hbar e n_e)$, where j is the charge current density, n_e is the concentration of conduction electrons, we obtain

$$\mathbf{E}_{SH} = R_S\left[\mathbf{j}\times\frac{\mathbf{P}}{n_e}\right],$$
$$R_S = \frac{\hbar eZ}{48\pi\varepsilon_0 mc^2}\frac{m^*/m}{en_e}\times \quad (10)$$
$$\times \mathrm{Re}\left\langle \Psi_\nu \left| \frac{3\mathbf{r}(\mathbf{r}\mathbf{a}_\nu) - \mathbf{a}_\nu r^2}{r^5}\frac{\partial}{\partial\mathbf{r}} \right| \Psi \right\rangle.$$

Here $\mathbf{P} = 2\mathbf{s}n_e$ is the spin polarization density vector.

5. CALCULATION OF SPIN-HALL RESISTANCE

The first relation (10) coincides in form with the expression for the electronic Hall effect if we replace the vector $\mathbf{P}/n_e$ by the vector of magnetic induction $\mathbf{B}$. Therefore, it can be expected that the spin-Hall effect constant R_S depends as much on the effective mass of conduction electrons, including its sign, and their concentration as the electronic Hall effect constant $R_H = (m^*/m)/(en_e)$. Then the second part of formula (10) can be written as

$$R_S = \frac{\hbar eZR_H}{48\pi\varepsilon_0 mc^2}\mathrm{Re}\left\langle \Psi_\nu \left| \frac{3\mathbf{r}(\mathbf{r}\mathbf{a}_\nu) - \mathbf{a}_\nu r^2}{r^5}\frac{\partial}{\partial\mathbf{r}} \right| \Psi \right\rangle. \quad (11)$$

The crystal field potential of the form (3) is not centrally symmetric, and the orbital moment of the electron is not a "good" quantum number for it. Therefore, the wave function of an electron in the crystal is different from the wave function of an electron in an isolated atom. Accordingly, the wave function $\Psi(\mathbf{r})$ in relation (2) is not the wave function of an external electron, such as the *s*-electron, of an isolated atom. But it can always be represented as a linear combination of the wave functions of an isolated atom. As a result, in metals the conduction bands overlap, and part of the conduction electrons can be formed by collectivization of *p*-electrons.

Let us use in relation (9) the approximation of hydrogen-like atomic orbital for outer (valence) electrons

$$\Psi_{nlm}(x,\theta,\varphi) = R_{nl}(x)Y_{lm}(\theta,\varphi). \quad (12)$$

Here l is the orbital quantum number, m is the magnetic quantum number, θ is the polar angle, φ is the azimuthal angle, $R_{nl}(x)$ is the radial part of the wave function, $x = Zr/a_B$, $Y_{lm}(\theta, \varphi)$ is the angular wave function (spherical function). The radial hydrogen-like wave function (12) has the form [13]

$$R_{nl}(x) = -\frac{2}{n^2}\sqrt{\frac{(n-l-1)!}{\left[(n+l)!\right]^3}}\times$$

$$\times\exp\left(-\frac{x}{n}\right)\left(\frac{2x}{n}\right)^l L_{n+l}^{2l+1}\left(\frac{2x}{n}\right),$$

Here $L_{n+l}^{2l+1}(t)$ is a generalized Laguerre polynomial. For the *s*-electron, the normalized spherical function is $Y_{00}(\theta,\varphi) = 1/\sqrt{4\pi}$. The normalized spherical function of the p-electron oriented along the polar axis is $Y_{10}(\theta,\varphi) = i\sqrt{3/(4\pi)}\cos(\theta)$.

Let us divide the nearest neighbors of the considered atom into groups with equal distances from it $|\mathbf{a}_\nu| = a_l$, where l = 1, 2, ... is the number of the group of nearest neighbors.

For the *s*-electron of conduction, directing the polar axis along the vector $\mathbf{a}_\nu$, we obtain in each of the nearest neighbor groups

$$\left\langle\Psi_\nu\left|\frac{3\mathbf{r}(\mathbf{r}\mathbf{a}_\nu)-\mathbf{a}_\nu r^2}{r^5}\frac{\partial}{\partial\mathbf{r}}\right|\Psi\right\rangle =$$

$$= m_l\frac{4b_lZ^3}{a_B^3}\int_0^\infty\frac{dR_{n0}(x)/dx}{x}dx\times \quad (13)$$

$$\times\int_0^1 y\left\{R_{n0}(x_1)-R_{n0}(x_2)\right\}dy,$$

Here y = cosθ, $x_1 = \sqrt{x^2+b_l^2+2xb_ly}$, $x_2 = \sqrt{x^2+b_l^2-2xb_ly}$, $b_\nu = Z|a_l|/a_B$, m_1 is the number of pairs of symmetrically located nodes in the *l*-th group of nearest neighbors.

For the *p*-electron of conduction, let us direct the polar axis along the vector $\mathbf{a}_\nu$ and count the azimuthal angle φ from the plane $\mathbf{a}_\nu\mathbf{r}$. In spherical coordinates, $\frac{\partial}{\partial\mathbf{r}} = \frac{\partial}{\partial r}\mathbf{e}_r + \frac{1}{r}\frac{\partial}{\partial\theta}\mathbf{e}_\theta + \frac{1}{r\sin(\theta)}\frac{\partial}{\partial\varphi}\mathbf{e}_\varphi$, with the orth $\mathbf{e}_\varphi$ orthogonal to the plane $\mathbf{a}_\nu\mathbf{r}$ and the orth $\mathbf{e}_\theta$ forming an angle $\pi/2 + \theta$ with the polar axis. Then for the *l*-th group of nearest neighbors we obtain

$$\left\langle\Psi_\nu\left|\frac{3\mathbf{r}(\mathbf{r}\mathbf{a}_\nu)-\mathbf{a}_\nu r^2}{r^5}\frac{\partial}{\partial\mathbf{r}}\right|\Psi\right\rangle =$$

$$= \frac{3b_lZ^3}{2\pi a_B^3}m_l\int_0^\infty\left(\frac{2ydR_{n1}(x)/dx}{x}-\frac{1-y^2}{x^2}R_{n1}(x)\right)dx\times \quad (14)$$

$$\times\int_0^1 y\left\{R_{n1}(x_1)-R_{n1}(x_2)\right\}dy.$$

6. COMPARISON OF CALCULATION RESULTS WITH EXPERIMENTAL VALUES

Table 1 lists the properties of the atoms of the studied metals, the configurations of their electron shells, and the parameters of their crystal lattices.

The spin-Hall effect has been most thoroughly investigated in platinum [16]. For platinum, the atom radius is 139 pm, which for the 6s shell corresponds to $Z \approx 22.45$. The face-centered lattice constant is a = 392 pm, there are 4 atoms per unit cell, and each atom

Table 1

Lattice parameters and electronic configurations of metals

Metal	Lattice	Electronic configuration	r$_a$, pm	Z	a, pm	Pairs of nearest neighbors					
						a_1, пм	m_1	a_2, пм	m_2	a_3, пм	m_3
Au	f.c.c.	[Xe]4f^{14}5d^{10}6s^1	144	21.7	408	288	6	408	3	500	12
Pt	f.c.c.	[Xe]4f^{14}5d^{9}6s^1	139	22.45	392	277	6	392	3	480	12
α-W	b.c.c.	[Xe]4f^{14}5d^{4}6s^2	141	22.77	316	274	4	316	3	449	6
β-W	A15	[Xe]4f^{14}5d^{9}6s^2	141	22.77	504	281	6	436	4	454	6
						251	1	281	1	308	4
Ta	b.c.c.	[Xe]4f^{14}5d^{3}6s^2	147	21	331	286	4	331	3	468	6
Lu	h.c.p.	[Xe]4f^{11}5d^{1}6s^2	175	17.84	351	346	6	492	2	557	1
Ho	h.c.p.	[Xe]4f^{11}6s^2	179	17.44	358	350	6	499	2	562	1
Dy	h.c.p.	[Xe]4f^{10}6s^2	180	17.44	359	353	6	502	2	565	1
Cd	h.c.p.	[Xe]4f^{7}5d6s^{21}	179	17.44	363	359	6	510	2	579	1
Ag	f.c.c.	[Kr]4d105s1	144	14.66	409	289	6	409	3	500	12
Pd	f.c.c.	[Kr]4d105s1	137	15.4	389	275	6	389	3	476	12
Mo	b.c.c.	[Kr]4d105s1	140	15.22	315	273	4	315	3	445	6
Nb	b.c.c.	[Kr]4d105s1	147	14.4	331	287	4	331	3	468	6
Cu	f.c.c.	[Ar]3d104s1	128	10.1	362	256	6	361	3	442	12
α-Mn	A12	[Ar]3d104s1	137	10.25	889	277	8	451	12	460	8
Cr	b.c.c.	[Ar]3d104s1	129	10	289	250	4	289	3	408	6
V	b.c.c.	[Ar]3d104s1	135	9.72	302	262	4	302	3	428	6
Ti	h.c.p.	[Ar]3d104s1	147	8.86	295	291	6	412	2	468	1
Al	f.c.c.	[Ne]3s23p1	143	4.81	495	286	6	405	3	496	12

has 6 pairs of nearest neighbors at a distance of 277 pm, next 3 pairs at a distance of 392 pm and 12 pairs at a distance of 480 pm, $b_1 = 117$, $b_2 = 166$, $b_3 = 204$. At 80 K parameter $R_H = -2\cdot10^{-11}$ m^3/(A·s), for the *s*-electron by formulas (11) and (13) we obtain $R_S = 3.48\cdot10^{-9}$ Ω·m, for the *p*-electron by formulas (11) and (14) we obtain $R_S = -5.12\cdot10^{-10}$ Ω·m.

Table 2 lists the theoretical, calculated by formulas (11), (13) and (14), and experimental values of spin-Hall resistance R_S for different metals. The values of the Hall constant R_H are taken from the reference book [17]. The values of conductivity are taken from the works cited, if they are not given there – from the reference book [17].

In experiment, the spin-Hall angle $\theta_{SH} = \sigma R_S$ is usually determined [9,18,19]. Here σ usually denoted as σ_{xx} is the conductivity of the metal in the absence of spin-orbit interaction. For platinum at 10 K, $\sigma = 8.1\cdot10^6$ Ω^{-1}m^{-1}, $\theta_{SH} = 0.021 \pm 0.005$ [20]. Accordingly $R_S = (2.6 \pm 0.7)\cdot10^{-9}$ Ω·m. Agreement with experiment for *s*-electrons is obtained if in formula (1)

Table 2

Experimental values of spin-Hall effect constants R_S^e and calculated values according to formula (11) R_S^s and R_S^p together with (13) for *s*-electrons and (14) for *p*-electrons.

Metal	σ, 10^5 (Ω·m)$^{-1}$	θ_{SH}, %	R_H, 10^{-11}, m^3/(A·s)	R_S^e, 10^{-9}·Ω·m	R_S^s, 10^{-9}·Ω·m	R_S^p, 10^{-9}·Ω·m
Au	200	0.25±0.05	-7.3	12±3	7.1	-1.08
Pt	81	2.1±0.5	-2	2.6±0.7	3.48	-0.512
α-W	47.6	≈7	11.1	-14.7	-13.96	2.56
β-W	20.4	-35±4	-162	740±80	1660	-294
Ta	3	-0.37±0.1	9.75	-13±4	-15.38	-2.15
Lu	12	1.4±0.2	-12	11±2	9.17	-1.28
Ho	11	14±2	-32	122±17	25.6	-3.34
Dy	18	5±1	-25	28±6	18.0	-2.47
Gd	7	4±1	-12	56±14	6.98	-1.07
Ag	150	0.7±0.1	-8.98	0.47±0.07	-11.7	1.43
Pd	40	0.64±0.1	-8.45	1.6±0.3	-13.4	1.64
Mo	28	-0.8±0.18	18	-2.8±0.7	25.4	-4.41
Nb	11	-0.87±0.2	8.88	-7.9±2	10.1	-11.9
Cu	160	0.32±0.03	-5.36	0.2±0.02	8.32	-1.18
α-Mn	1.42	-0.19±0.01	8.44	-13.3±1	-11.1	1.85
V	55	-1±0.1	7.9	-1.8±0.3	-9.73	1.39
Cr	1.2	-5.1±0.5	36.3	-42±4	-59	8.12
Ti	3.33	-0.036±0.004	1.0	-1.2±0.1	-1.0	0.134
Al	160	0.02±0.01	-3.3	-0.012±0.006	-1.68	0.19

the mass of a free electron is replaced by the effective mass $m^* \approx (1.15 \pm 0.15)m$.

Gold is the second representative of the 6th period and a noble metal. The spin-Hall angle for gold is an order of magnitude smaller than for platinum [21]. The face-centered cubic lattice constant $a = 407.8$ pm, there are 4 atoms per unit cell, 6 pairs of nearest neighbors at a distance of 288 pm, next 3 pairs at a distance of 408 pm and 12 pairs at a distance of 500 pm. Agreement with experiment for *s*-electrons is obtained at $m^* \approx (0.77 \pm 0.1)m$.

Tantalum has a body-centered cubic lattice with constant $a = 331$ pm. There are 2 atoms per unit cell, 4 pairs of nearest neighbors at 286 pm, then 3 pairs at 331 pm and 6 pairs at 468 pm. Agreement with experiment for *s*-electrons will be obtained at $m^* \approx (1.1 \pm 0.1)m$.

Tungsten in the stable alpha-modification has a body-centered cubic lattice with constant $a = 316$ pm. There are 2 atoms per unit cell, 4 pairs of nearest neighbors at 274 pm, then 3 pairs at 316 pm and 6 pairs at 449 pm. In the experiment [22], a value of $|\theta_{SH}| < 0.07$ was obtained on a 15 nm thick film, which corresponds to $|R_S| < 1.47 \cdot 10^{-8}$ Ω·m. The error of the experimentally measured spin-Hall angle in [22] is not given, but the calculated value agrees with the experimental one for *s*-electrons at $m^* \approx (1.0 \pm 0.03)m$.

Tungsten in metastable beta-modification has a lattice of the form A15 for compound AB_3 with constant $a = 503.6$ pm, there are 8 atoms per unit cell. For atom A (in the center and at the corners) there are 6 pairs of nearest neighbors at a distance of 281 pm, then 4 pairs at a distance of 436 pm, 6 pairs at a distance of 454 pm, 3 pairs at a distance of 504 pm, 12 pairs at a distance of 577 pm. For atom B (on the face) 1 pair of nearest neighbors at a distance of 251 pm, then 1 pair at a distance of 281 pm, 4 pairs at a distance of 308 pm, 2 pairs at a distance of 454 pm, 8 pairs at a distance of 471 pm. The calculation shows that atoms A and B contribute equally to the spin-Hall effect. Agreement with the experiment [23, 24] for *s*-electrons is obtained at $m^* \approx (1.5 \pm 0.1)m$.

There are no reliable experimental data on the spin-Hall angle for rare-earth metals. In [25] the value $\xi_{SH} = T_{int}\theta_{SH}$ is given, where T_{int} is the spin transfer coefficient. For estimation we take it equal to 1.

For gadolinium, hexagonal close-packed lattice constants are $a = 363.4$ pm and $c = 578.5$ pm there are 2 atoms per unit cell, 6 pairs of nearest neighbors at 359 pm, then 2 pairs at 510 pm and 1 pair at 579 pm. Agreement with experiment for *s*-electrons will be obtained at $m^* \approx (0.35 \pm 0.05)m$.

For dysprosium, hexagonal close-packed lattice constants are $a = 359.3$ pm and $c = 565.4$ pm there are 2 atoms per unit cell, 6 pairs of nearest neighbors at 353 pm, then 2 pairs at 502 pm and 1 pair at 565 pm. Agreement with experiment for *s*-electrons will be obtained at $m^* \approx (0.8 \pm 0.1)m$.

For holmium, hexagonal close-packed lattice constants are $a = 357.7$ pm and $c = 561.6$ pm there are 2 atoms per unit cell, 6 pairs of nearest neighbors at 350 pm, then 2 pairs at 499 pm and 1 pair at 562 pm. Agreement with experiment for *s*-electrons is obtained at $m^* \approx (0.46 \pm 0.04)m$.

For lutetium, hexagonal close-packed lattice constants are $a = 351$ pm and $c = 556.7$ pm there are 2 atoms per unit cell, 6 pairs of nearest neighbors at 346 pm, then 2 pairs at 492 pm and 1 pair at 557 pm. Agreement with experiment for *s*-electrons will be obtained at $m^* \approx (1.1 \pm 0.1)m$.

Note that of the considered rare-earth metals only lutetium is paramagnetic at all temperatures. At low temperatures dysprosium and holmium are ferromagnets. The magnetic behavior of gadolinium is complex, various magnetic anomalies are

detected [26]. It can be hypothesized that at room temperature they lack only long-range spin ordering but, unlike lutetium, near-order remains. Formula (2) does not take into account the exchange interaction of collective conduction electron with localized magnetization electrons. Therefore, relation (11) applies only to paramagnets such as lutetium. In the presence of near spin ordering, in addition to the spin-Hall electric field of the form (7), there may be a Hall electric field due to the anomalous Hall effect [27]. This phenomenon probably takes place in dysprosium, holmium and gadolinium.

When analyzing the elements of the 5th period, the calculation by formulas (11) and (13) for the *s*-electrons of conduction gives values that do not agree with the experimental ones. This is especially true, apparently, for palladium, which has no 5*s*-electrons.

For silver, the face-centered cubic lattice constant is a = 408.6 pm, there are 4 atoms per unit cell, 6 pairs of nearest neighbors at 289 pm, then 3 pairs at 409 pm, and 12 pairs at 500 pm. Agreement with the experiment [28] for *p*-electrons will be obtained at $m^* \approx (1.75 \pm 0.07)m$.

For molybdenum, the body-centered cubic lattice constant is a = 315 pm, there are 2 atoms per unit cell, 4 pairs of nearest neighbors at 273 pm, then 3 pairs at 315 pm, and 6 pairs at 445 pm. Agreement with the experiment [20] for *p*-electrons will be obtained at $m^* \approx (1.25 \pm 0.15)m$.

For palladium, the face-centered cubic lattice constant is a = 389 pm, there are 4 atoms per unit cell, 6 pairs of nearest neighbors at 275 pm, then 3 pairs at 389 pm, and 12 pairs at 476 pm. Agreement with the experiment [25] for *p*-electrons will be obtained at $m^* \approx (1.0 \pm 0.1)m$.

For niobium, the body-centered cubic lattice constant is a = 331 pm, there are 2 atoms per unit cell, 4 pairs of nearest neighbors at 287 pm, then 3 pairs at 331 pm, and 6 pairs at 468 pm. Agreement with the experiment [20] for *p*-electrons will be obtained at $m^* \approx (1.25 \pm 0.15)m$.

For copper, the face-centered cubic lattice constant is a = 361.5 pm, there are 4 atoms per unit cell, 6 pairs of nearest neighbors at 256 pm, then 3 pairs at 362 pm, and 12 pairs at 442 pm. Agreement with the experiment [29] for *s*-electrons will be obtained at $m^* \approx (6.4 \pm 0.4)m$.

For titanium, hexagonal close-packed lattice constants are a = 295 pm, c = 469.7 pm, there are 2 atoms per unit cell, 6 pairs of nearest neighbors at a distance of 291 pm, then 2 pairs at a distance of 412 pm and 1 pair at a distance of 468 pm. Manganese in alpha modification has structure A12, cubic lattice constant is a = 889 pm, there are 58 atoms per unit cell, 8 pairs of nearest neighbors at a distance of 277 pm, then 12 pairs at a distance of 451 pm and 8 pairs at a distance of 460 pm. Agreement with the experiment [30] for *s*-electrons in titanium and manganese will be obtained at $m^* \approx (0.91 \pm 0.05)m$.

For vanadium, the cubic body-centered lattice constant is a = 302.4 pm, there are 2 atoms per unit cell, 4 pairs of nearest neighbors at a distance of 262 pm, then 3 pairs at a distance of 302.4 pm and 6 pairs at a distance of 427.7 pm. Agreement with the experiment [27] for *s*-electrons will be obtained at $m^* \approx (2.3 \pm 0.2)m$.

For chromium, the cubic body-centered lattice constant is a = 288.5 pm, there are 2 atoms per unit cell, 4 pairs of nearest neighbors at a distance of 249.8 pm, then 3 pairs at a distance of 288.5 pm, and 6 pairs at a distance of 408 pm. Agreement with the experiment

[27] for *s*-electrons will be obtained at $m^* \approx (1.18 \pm 0.05)m$.

For aluminum, the face-centered cubic lattice constant is $a = 405$ pm, there are 4 atoms per unit cell, 6 pairs of nearest neighbors at 286 pm, then 3 pairs at 405 pm, and 12 pairs at 496 pm. Agreement with the experiment [31] for *p*-electrons will be obtained at $m^* \approx (3.9 \pm 1)m$. Aluminum has no *d*- and *f*-electrons on the inner shells. These electrons have a good shielding ability, so for transition and rare-earth metals the use of a hydrogen-like orbital (12) with a corresponding effective charge for the conduction electrons is a justified approximation. For aluminum, such an approximation is apparently inapplicable. In addition, of all the metals considered, only aluminum has a filled *p*-shell. As a result, the contribution to the SHE from *s*- and *p*-electrons almost compensates each other, and the small experimental value of the spin-Hall effect constant R_S is obtained as a difference of two relatively large values, not because of the large effective mass of the charge carriers.

For copper, the experimental value of the spin-Hall effect constant is very small, and as in the case of aluminum, is probably obtained as the difference of two relatively large values. Good agreement with the experiment for copper is obtained if we assume that 90% of the conduction electrons are collective electrons *p*-electrons and 10% are *s*-electrons.

Comparative analysis of the data listed in Tables 1 and 2 shows that for elements of even periods (6th and 4th) the sign of the measured spin-Hall resistance always coincides with the sign calculated for the *s*-electron, and for elements of odd periods (5th and 3rd) – with the sign calculated for the *p*-electron.

7. CONCLUSION

The justification of methods for designing spintronics systems, calculating and optimizing their characteristics requires additional assumptions about the system. Such assumptions are the representation of the wave function of a collective conduction electron as a Wannier function, the effective charge approximation and the nearest-neighbor approximation in the Hamiltonian (5), and the ideal Fermi-gas model for conduction electrons. The applicability of these models for a particular problem should be substantiated experimentally. The intrinsic SHE coefficients calculated within the framework of these models agree with the measured ones. The question of the admissibility of introducing the effective mass of the conduction electron into the spin-orbit interaction Hamiltonian (1) to account for the interaction of collective conduction electrons when constructing the self-consistent field potential (3) in the framework of the one-electron approximation requires further study.

Spin polarization according to the mechanism described in this work does not require external magnetic fields and residual magnetization and therefore does not interfere with work in micro- and nano-sized spintronics structures. Of undoubted interest is the search for new promising materials for spintronics devices based on metal alloys and intermetallic compounds. The design of such spintronics systems, calculation and optimization of their characteristics is possible on the basis of the described methods and approaches, if we consider the crystallite of intermetallic compound as a heteronuclear macromolecule. The methods of constructing molecular orbitals for such structures, including those in the form of Wannier functions, are well studied [32,33].

REFERENCES

1. Bukharaev AA, Zvezdin AK, Pyatakov AP, Fetisov YK. Straintronics: a new trend in micro- and nanoelectronics and materials science. *Phys.-Usp.*, 2018, 61:1175-1212; doi: 10.3367/UFNe.2018.01.038279.
2. Dyakonov MI, Perel VI. Current-induced spin orientation of electrons in semiconductors. *Physics Letters A*, 1971, 35(6):459-460; doi: 10.1016/0375-9601(71)90196-4.
3. Sinova J, Culcer D, Niu Q, Sinitsyn NA, Jungwirth T, MacDonald AH. Universal Intrinsic Spin Hall Effect. *Phys. Rev. Lett.,* 2004, 92(12):126603-126606; doi: 10.1103/PhysRevLett.92.
4. Wunderlich J, Kaestner B, Sinova J, Jungwirth T. Experimental observation of the spin-Hall effect in a two dimensional spin-orbit coupled semiconductor system. *Phys. Rev. Lett.*, 2005, 94(4):047204-047216; doi: 10.1103/PhysRevLett. 94.047204.
5. Zhang S. Spin torques due to large Rashba fields. In book "*Spin Current*", Edited by Maekawa S, Valenzuela SO, Saitoh E, Kimura T. Oxford, University Press, 2012, pp 424–431.
6. Sinova J, Valenzuela SO, Wunderlich J, Back CH, Jungwirth T. Spin Hall effects. *Reviews of Modern Physics,* 2015, 87:1213-1259; doi: 10.1103/RevModPhys.87.1213.
7. Hoffmann A. Spin hall effects in metals. *IEEE Transactions on Magnetics,* 2013, 49(10):5172-5193; doi: 10.1109/TMAG.2013.2262947.
8. Saitoh E, Ueda M, Miyajima H, Tatara G. Conversion of spin current into charge current at room temperature: Inverse spin-Hall effect. *Applied Physics Letters*, 2006, 88:182509; doi: 10.1063/1.2199473.
9. Xiao Y, Wang H, Fullerton EE. Crystalline Orientation–Dependent Spin Hall Effect in Epitaxial Platinum. *Frontiers in Physics*, 2022, 9:791736; doi: 10.3389/fphy.2021.791736.
10. Ignatjev VK, Lebedev NG, Stankevich DA. The effect of the spin polarization control of conduction electrons through the deformation of a ferromagnet. *Technical Physics Letters,* 2022, 48(12):25-28; doi: 10.21883/TPL.2022.12.54941.19363,
11. Ignatjev VK, Lebedev NG, Stankevich DA. The spin Hall effect in polycrystalline samples of nonmagnetic fifth- and sixth-period metals. *Technical Physics Letters,* 2023, 49(3):60-62; doi: 10.21883/TPL.2023.03.55688.19437.
12. Berestetskii VB, Pitaevskii LP, Lifshitz EM. *Teoreticheskaya fizika. T. IV. Kvantovaya electrodinamika* [Course of Theoretical Physics, Vol. 4, Quantum Electrodynamics]. Moscow, Fizmatlit Publ., 2002, 720 p.
13. Landau LD, Lifshitz EM. *Teoreticheskaya fizika. T. III. Kvantovaya mehanika. Nerelyativ-istskaya teoriya* [Course of Theoretical Physics, Vol. 3, Quantum Mechanics. Non-relativistic Theory]. Moscow, Fizmatlit Publ., 2004, 800 p.
14. Madelung O. *Teoiriya tverdogo tela* [Theory of solid states]. Moscow, Nauka Publ., 1980, 416 p.
15. Kvasnikov IA. *Teoriya ravnovesnyh sistem: Statisticheskaya fizika* [Theory of equilibrium systems: Statistical physics]. Moscow, Editorial URSS, 2002, 240 p.
16. Sinova J, Valenzuela SO, Wunderlich J, Back CH, Jungwirth T. Spin Hall effects. *Reviews of Modern Physics,* 2015, 87:1213; doi: 10.1103/RevModPhys.87.1213.
17. Cardarelli F. *Materials Handbook*. Springer International Publishing AG. Switzerland. 2018.
18. Dyakonov MI, Khaetskii AV. Spin Hall effect. In book "*Spin Physics in Semiconductors*". Edited by Dyakonov MI. Chapter 8, Ser. in Solid-State Sciences. New

York, Springer, 2008, 157:211-243; doi: 10.1007/978-3-319-65436-2_8.
19. Dyakonov MI. Magnetoresistance due to edge spin accumulation. *Physical Review Letters,* 2007, 99(12):126601; doi: 10.1103/PhysRevLett.99.126601.
20. Morota M, Niimi Y, Ohnishi K, Wei DH, Tanaka T, Kontani H, Kimura T, Otani Y. Indication of intrinsic spin Hall effect in 4d and 5d transition metals. *Physical Review B*, 2011, 83:74405; doi: 10.1103/PhysRevB.83.174405.
21. Vlaminck V, Pearson JE, Bader SD, Hoffmann A. Dependence of spin pumping spin Hall effect measurements on layer thickness and stacking order. *Physical Review B*, 2013, 88(6):064414; doi: 10.1103/PhysRevB.88.064414.
22. Pai C-F, Liu L, Tseng HW, Ralph DC, Buhrman RA. Spin transfer torque devices utilizing the giant spin Hall effect of tungsten. *Applied Physics Letters*, 2012, 101(12):122404- 122412; doi: 10.1063/1.4753947.
23. Hao Q, Chen W, Xiao G. Beta (β) tungsten thin films: Structure, electron transport, and giant spin Hall effect. *Applied Physics Letters*, 2015, 106(18):182403; doi: 10.1063/1.4919867.
24. Hao Q, Xiao G. Giant Spin Hall Effect and Switching Induced by Spin-Transfer Torque in a W/Co40Fe40B20/MgO Structure with Perpendicular Magnetic Anisotropy. *Physical Review Applied,* 2015, 3:034009; doi: 10.1103/PhysRevApplied.3.034009.
25. Reynolds N, Jadaun P, Heron JT, Jermain CL, Gibbons J, Collette R, Buhrman RA. Schlom DG, Ralph DC. Spin-Hall Torques Generated by Rare-Earth (Lanthanide) Thin Films. *Physical Review B*, 2017, 95:064412; doi: 10.1103/PhysRevB.95.064412.
26. Belov KP, Belyanchikova MA, Levitin RZ, Nikitin SA. *Redkozemel'nye ferromagnetiki i antiferromagnetiki* [Rare-earth ferromagnets and antiferromagnets]. Moscow, Nauka Publ., 1965, 320 p.
27. Smejkal L, MacDonald AH, Sinova J, Nakatsuji S, Jungwirth T. Anomalous Hall antiferromagnets. *Nature Reviews Materials,* 2022, 7:482-496, doi: 10.1038/s41578-022-00430-3.
28. Wang HL, Du CH, Pu Y, Adur R, Hammel PC, Yang FY. Scaling of Spin Hall Angle in 3d, 4d, and 5d Metals from Y3Fe5O12. Metal Spin Pumping. *Physical Review Letters,* 2014, 112: 197201, doi: 10.1103/PhysRevLett.112.197201.
29. Mosendz O, Vlaminck V, Pearson JE, Fradin FY. Bauer GEW, Bader SD, Hoffmann A. Detection and quantification of inverse spin Hall effect from spin pumping in permalloy/normal metal bilayers. *Physical Review B*, 2010, 82(21):214403, doi: 10.1103/PhysRevB.82.214403.
30. Du C, Wang H, Yang F, Hammel C. Systematic variation of spin-orbit coupling with d-orbital filling: Large inverse spin hall effect in 3d transition metals. *Physical Review B*, 2014, 90:40407, doi: 10.1103/PhysRevB.90.140407.
31. Valenzuela S, Tinkham M. Direct electronic measurement of the spin Hall effect. *Nature,* 2006, 442:176-179; doi: 10.1038/nature04937.
32. Bazilevskij MV. *Metod molekulyarnyh orbit i reakcionnaya sposobnost' organicheskih molekul* [Molecular orbital method and reactivity of organic molecules]. Moscow, Himiya Publ., 1969, 304 p.
33. Gribov LA, Mushtakova SP. *Kvantovaya himiya* [Quantum chemistry]. Moscow, Gardariki Publ., 1999, 390 p.

DOI: 10.17725/j.rensit.2024.16.101

Optimization of optical absorption in spintronic terahertz emitters using Bragg reflectors

Anastasiya V. Gorbatova, Arseny M. Buryakov

MIREA - Russian technological university, https://www.mirea.ru/

Moscow 119454, Russian Federation

E-mail: gorbatova@mirea.ru, buryakov@mirea.ru

Received October 21, 2023, peer-reviewed October 25, 2023, accepted October 31, 2023, published March 15, 2024.

Abstract: **An optimized design of a spintronic terahertz emitter has been developed, based on a bilayer Co/Pt structure with an integrated distributed Bragg reflector. The incorporation of the Bragg mirror between the Co/Pt structure and the silicon substrate enhances optical absorption in the ferromagnetic layer, thereby amplifying spin current generation and, consequently, THz signal. A model was developed for calculating the optical absorption in the ferromagnetic layer of the spintronic emitter, taking into account the parameters of the Bragg mirror (layer thicknesses, period) based on the superlattice structure [TiO_2/SiO_2] N. This model is grounded on the solution of Maxwell's equations for electromagnetic waves using the COMSOL Multiphysics software. The effect of anti-reflective dielectric coatings on the level of optical absorption in the ferromagnetic layer was also analyzed. The study confirmed that using the optimized Bragg mirror is sufficient for achieving optimal absorption.**

Keywords: **terahertz radiation, spintronic emitter, Bragg mirror, anti-reflection coating, Fabry-Perot cavity, COMSOL Multiphysics**

UDC 535.34, 537.9

Acknowledgments: The study was supported by the Russian Science Foundation Grant No. 21-79-1035, https://rscf.ru/en/project/21-79-10353/

For citation: Anastasiya V. Gorbatova, Arseny M. Buryakov. Optimization of optical absorption in spintronic terahertz emitters using Bragg reflectors. *RENSIT: Radioelectronics. Nanosystems. Information Technologies,* 2024, 16(1):101-110e. DOI: 10.17725/j.rensit.2024.16.101.

Contents

1. INTRODUCTION

Terahertz (THz) radiation in the 0.1-30 THz range represents an effective means for spectroscopic analysis, opening new horizons in condensed matter physics research, including studies of phonon and magnon modes, as well as electronic and spin dynamics [1-4]. Consequently, there is a growing demand for high-power and broadband terahertz emitters capable of exciting a variety of physical processes in solids. Among THz emitters, the most well-known and utilized in THz spectrometers are nonlinear optical crystals, such as $LiNbO_3$, ZnTe, and GaP [5], organic crystals, photoconductive antennas (PCAs), and spintronic terahertz emitters (STEs) [5,6]. The first two types of sources operate on the basis of nonlinear optical rectification [5-7], while the latter two rely on ultrafast current generation [8,9]. Most

nonlinear optical crystals generate THz pulses with peak field strengths around 100 kV/cm [5,6]. An exception is $LiNbO_3$, which, when pumped with a tilted-front pulse for phase matching and at cryogenic temperatures, generates THz pulses with peak field strengths exceeding 4 MV/cm [10]. Organic crystals, such as BNA, also facilitate the generation of THz pulses with high electric field strengths, approximately 1-10 MV/cm, across spectral widths from 1 to 10 THz [5,6]. However, their stability depends on the optical pumping conditions, often requiring the use of IR lasers. For generating high field strengths in THz pulses, nonlinear optical and organic crystals are frequently used in combination with pumping lasers with powers of several tens of mJ. In contrast, PCAs do not require large energies, but their field strength rarely exceeds 100 kV/cm [5,6].

In recent years, special attention has been devoted to spintronic terahertz emitters, which operate on the principle of spin-charge conversion [8]. According to the 2023 roadmap, THz spintronics introduces new functional capabilities for THz photonics in the generation, modulation, and detection of THz radiation [11]. The classical design of STEs consists of a bilayer (or trilayer) structure based on ferromagnetic (FM) and non-magnetic metals (NM): FM/NM or NM($\pm\gamma$)/FM/NM($\mp\gamma$), where γ signifies the sign of the Spin Hall angle [12]. The film thickness within the structure does not exceed a few nanometers ($\sim 2-3$ nm) [12]. The operating principle of STEs includes four fundamental stages [13]:

1. Absorption of the optical pulse from laser pumping.
2. Generation of spin current in the magnetic layer and its transfer to the non-magnetic layer.
3. Conversion of spin current into a transverse charge current.
4. Operation of STE as a source of THz electromagnetic pulses.

STE devices are characterized by their simple architecture, high manufacturability, and the generation of THz pulses with significant amplitudes, spanning from 100 kV/cm to 1.5 MV/cm. Additionally, these devices operate across a broad frequency range of 0.1 to 30 THz [6]. Another key benefit is the capacity for fine-tuning parameters of THz radiation, such as polarization, ellipticity, amplitude, and frequency range [14-18].

Despite the many advantages of STEs, their low absorption of optical and near-infrared (IR) pump radiation leads to inefficient optical-THz conversion. This issue primarily stems from the minimal thickness of standard STEs. To date, considerable efforts have been directed toward enhancing these parameters, including modifying STEs' functional layers (material type, thickness, etc.) [12,19-21], adopting cascade amplification schemes for THz radiation [22], and amplifying THz radiation through the creation of hybrid structures. These structures combine spin-charge conversion approaches with the development of antennas on the surface of STE films [18,23]. Additionally, the application of plasmonic approaches and the creation of microstructured STEs [24-26], as well as the establishment of conditions for resonant absorption of optical radiation in STEs' functional structure via the integration of dielectric (Bragg) mirrors [27,28], have been explored. Among all these approaches, the last appears to be the simplest from a technological standpoint. Furthermore, alongside Bragg mirrors, the use of anti-reflection coatings (ARCs) operating in the IR range, which also serve a protective function, can reduce the loss of exciting radiation upon reflection from the air/STE interface.

This study focuses on optimizing STE with Co/Pt layers to enhance optical absorption in the ferromagnetic cobalt layer. Employing numerical simulations within the COMSOL Multiphysics

software package, two strategies were examined to maximize the absorption of pump radiation in the functional layer of STE: 1) the construction of Bragg mirrors, serving as analogues to optical resonators between the STE and the substrate; and 2) the application of anti-reflective coatings on the surface of STEs.

2. MODEL OF A THZ GENERATOR WITH A BRAGG MIRROR AND ANTI-REFLECTIVE COATING

The concept of developing a STE with a Bragg mirror hinges on the fundamental processes of THz radiation generation. Among these, a crucial step is the absorption of the optical pulse by the ferromagnetic layer within the STE heterostructure. According to formula (1), the amplitude of the generated THz wave is directly proportional to the energy absorbed from the optical excitation beam [13,29]:

$$E_{THz} \propto \frac{P_{abs}}{d_{Co}+d_{Pt}} \tanh\frac{d_{Co}+d_0}{2\lambda_{pol}} \tanh\frac{d_{Pt}}{2\lambda_{pol}} \times \times \frac{1}{n_{air}+n_{sub}+Z_0(\sigma_{Co}d_{Co}+\sigma_{Pt}d_{Pt})} e^{-\frac{d_{Co}+d_{Pt}}{S_{THz}}}, \quad (1)$$

where P_{abs} is the laser radiation power absorbed by the emitter, d_{Co} is the thickness of the ferromagnetic cobalt layer, d_{Pt} is the thickness of the non-magnetic platinum layer, d_0 is the critical value of the thickness of the ferromagnetic layer, below which the ferromagnetic layer loses its magnetic properties, λ_{pol} is the characteristic spin polarization constant that appears in case when $d > d_0$, n_{air}, n_{sub} and Z_0 – are the refractive index of air, the refractive index of the substrate at THz frequencies and the vacuum impedance, respectively, σ_{Co} and σ_{Pt} – denote the electrical conductivity of the two materials, respectively, S_{THz} is the effective inverse attenuation coefficient of THz radiation in both metal layers. Note that the simplified formula does not take into account the spin and charge components [13,29].

Addressing the issue of optimizing the absorption capacity of the Spintronic Terahertz Emitter (STE) structure, we delve into the operational principles and characteristics of the Bragg mirror. This mirror features a periodic structure composed of two materials with differing refractive indices. The optimal number of periods in a Bragg mirror for achieving maximum reflection is dictated by the difference in the refractive indices of two dielectric materials: $\Delta n/n = (n_H - n_L)/n_H$, where H and L denote the materials with high and low refractive indices, respectively. The Bragg mirror achieves 100% reflection of incident radiation at the central wavelength $\lambda_p = 2(n_H d_H + n_L d_L)$, with d representing the layer thickness. Optimal reflection efficiency occurs when the thicknesses of the individual layers are equal to a quarter wavelength, $n_H d_H = n_L d_L = \lambda_p/4$. The quality factor of the resonator is defined as $Q = f/\Delta f$, where f and Δf are the frequency and the frequency peak width, respectively [30]. In the STE context, an experimental deployment of a Bragg mirror is documented in [27]. In this study, a Bragg structure [TiO_2 (113 nm, n = 2.265)|SiO_2 (185 nm, n = 1.455)]$_5$ optimized for a pump wavelength of approximately 1030 nm was incorporated into a three-layer W/CoFeB/Pt spintronic emitter. This integration resulted in the electric field in the THz range being doubled and a fourfold increase in power. Another study [28] demonstrated a performance enhancement of SSCs optically pumped at 800 nm by up to sixfold, attributable to the [SiO_2 (165 nm) TiO_2 (94 nm)]$_5$ structure. Hence, the creation of an optical resonator can significantly boost the absorption within the STE structure, which, in turn, facilitates an increase in THz power output.

Optimizing the properties of the Bragg mirror is critical to improve optical pump absorption. However, to ensure optimal transmission of optical pumping through the STE, creating conditions for complete "anti-reflection" at the air/STE interface using ARCs is equally important. Two primary criteria must be satisfied to achieve this condition [31]. First, the waves

reflected from the structure's surface and from the interface should have a phase difference of $\delta = n\pi/2$, where n is the refractive index of the film. Second, the film thickness (d) must be an odd multiple of $i\lambda/4$, where λ is the wavelength of the incident beam and i is an odd positive integer. ARCs can be either homogeneous, consisting of one uniform layer with refractive index n, or inhomogeneous, comprising layers with a gradient of n in each layer.

To ensure total reflection conditions when using an ARC source, the refractive index must equal $n = \sqrt{n_{air} n_s}$, where n_s is the refractive index of the substrate, and the thickness of the ARC (h_{ARC}) should be a quarter of the wavelength. Single-layer homogeneous ARCs are utilized to suppress reflectance down to 2.5% across a broad spectral range (450–1100 nm) at normal incidence. Examples of single-layer ARCs for the visible and IR ranges include MgF_2, SiO_2, Si_3N_4, Al_2O_3, TiO_2, etc. To further reduce reflectance, two-layer ARCs can be employed. A necessary condition for achieving zero reflectance with a two-layer coating, where both layers have the same optical thickness ($n_1 d_1 = n_2 d_2 = \lambda/4$), is that the product of their refractive indices meets the relationship $n_1 n_2 = n_0 n_s$ [31].

This work introduces a model of a classical Spintronic Terahertz Emitter (STE), comprising a two-layer structure (**Fig. 1***a*). Both layers, made of Co and Pt, share the same thickness of 2 nm. The selection of these thickness values, $d_{Co} = d_{Pt}$, was determined by the optimal balance between the critical thickness of the ferromagnetic layer, d_0, and the effective attenuation coefficient for THz radiation, S_{THz}, in both metal layers. A consensus among most experimental and theoretical studies suggests that maximal THz generation is attained in a two-layer STE structure with an overall thickness of 4 nm [12,29]. Subsequently, a Bragg mirror, forming a superlattice of the $[SiO_2|TiO_2]_N$ type where N varies as 1, 3, 5, and 10, is inserted between the STE and the high-resistivity silicon substrate (illustrated in Fig. 1*b*). This high-resistivity silicon

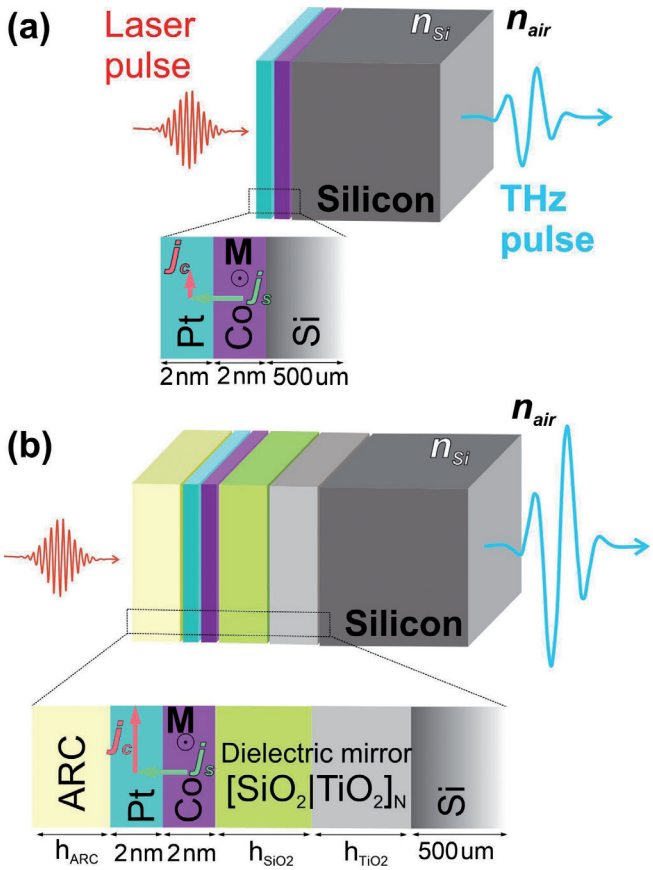

Fig. 1. *(a) STE structure fabricated on a silicon substrate. (b) STE design incorporating a Bragg mirror, constructed on a silicon substrate, and equipped with an anti-reflection coating.*

substrate was selected for its superior THz radiation transmission capability ($nSi_{THz} \approx 3.4$, significantly greater than $n_{air} \approx 1$). Fig. 1*a* depicts the configuration of the STE without a Bragg mirror, whereas Fig. 1*b* displays the schematic with a Bragg mirror. An anti-reflection coating (ARC) was applied to shield the surface of the STE from external factors and to enhance radiation transmission.

The COMSOL Multiphysics software platform was utilized for calculating the absorption in a STE based on a Co/Pt bilayer structure. Through the physical interface "Optics" > "Wave Optics" > "Electromagnetic Waves, Frequency Domain", it is possible to ascertain the distribution of the electromagnetic field within the medium by solving Maxwell's equation for an electromagnetic wave:

$$\nabla \times \mu_r^{-1}\left(\nabla \times \vec{E}\right) - k_0^2\left(\varepsilon_r - \frac{j\lambda\sigma}{2\pi c\varepsilon_0}\right)\vec{E} = 0, \qquad (2)$$

where μ_r and ε_r are the magnetic and dielectric constants of the material, respectively, σ is its conductivity, ε_0 is the vacuum permittivity, k_0 is the wave number, λ is the wavelength of the pump radiation, c is the speed of light in a vacuum, and $\vec{E}$ is the complex vector of the electric field.

The simulation of the electromagnetic wave was executed with the "Port" boundary condition, where the electric field strength vector is oriented along the *X*-axis, and its amplitude was set at 1 V/m. To the side boundaries of the model, the "Perfect Electric Conductor" boundary condition was applied, enforcing the condition $\vec{n} \times \vec{E} = 0$.

3. RESULTS AND DISCUSSION

In the initial stage, the most basic version of the structure depicted in Fig. 1*a* is examined, absent both a Bragg mirror and ARC. It is important to highlight that silicon substrates are invariably characterized by a thin layer of natural oxide, SiO_2, on their surface. The absorption of optical radiation at a wavelength of 800 nm in the SiO_2 layer is relatively low (extinction coefficient k_{SiO2} = 0.000687 [32]). However, considering that the refractive index of the oxide is n_{SiO2} = 1.4574 [32], and the SiO_2 layer is situated between the STE structure and the silicon substrate, which exhibits high refractive indices in the IR range (n_{Co} = 4.56, n_{Pt} = 6.57 [33], and n_{Si} = 3.6690) [34]), this configuration leads to multipath interference. This structure acts as the simplest form of an optical resonator and can circumvent the need for more complex designs to moderately suppress back reflection. By adjusting the thickness of the oxide layer, an enhancement in optical absorption can be achieved, which may also contribute to an increase in the THz signal.

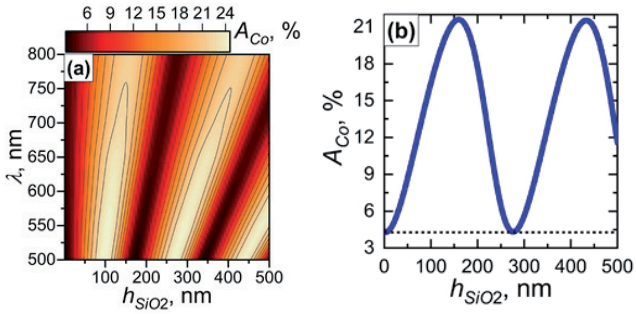

Fig. 2. *Impact of SiO_2 layer thickness on optical absorption in STE based on the Pt (2 nm)/Co (2 nm) structure. (a) Distribution map of absorption in STE across optical and near-IR pump wavelength ranges. (b) Relationship between absorption in the ferromagnetic layer and SiO_2 thickness at a wavelength of 800 nm.*

The results depicted in **Fig. 2***a* and *b* illustrate a map of optical absorption in the ferromagnetic cobalt layer (A_{Co}) as a function of the SiO_2 thickness and the wavelength of the exciting radiation (500-800 nm). As shown in the figures, for cases with a minimum natural oxide thickness of ~ 1-2 nm, the absorption at these wavelengths is approximately 4.3%. However, as the oxide thickness increases, the maximum absorption shifts towards the 500 nm region, potentially reaching up to 24% of the total exciting radiation. When considering a wavelength of 800 nm (Fig. 2*b*) – the operational range for most available femtosecond laser systems used to pump THz STEs – the absorption does not exceed 21.6% for an oxide thickness of ~ 160 nm. In this scenario, the resultant total absorption ratio for Co(2 nm)/Pt(2 nm) is approximately 52.5%, with the proportion of reflected light being around 7.6%. The remaining excitation radiation, 39.3%, passes through the STE and is absorbed by the SiO_2/Si substrate.

This example underscores the ineffectiveness of a SiO_2 film alone, situated between the STE's functional structure and the silicon substrate, in achieving maximum absorption. Consequently, in the subsequent stage, the focus shifted to an STE structure enhanced by a Bragg mirror, utilizing the $[SiO_2|TiO_2]_N$ superlattice configuration. The

pairing of SiO_2 layers with TiO_2 layers, which have markedly distinct refractive indices at a wavelength of 800 nm (n_{TiO2} = 2.0951, n_{SiO2} = 1.4608) [32,35], facilitates a reduction in the fraction of radiation transmitted into the substrate. The primary goal for achieving maximum absorption in STE involves determining the optimal period N for the $[SiO_2|TiO_2]_N$ structure, along with the optimal thicknesses for each dielectric layer. **Fig. 3***a-d* showcase the results from calculating the absorption efficiency in the cobalt layer for various N values (1, 3, 5, 10), considering SiO_2 layer thicknesses in the range of 1-300 nm and TiO_2 layer thicknesses also within 1-300 nm.

From the analysis of the data presented, it is clear that the structure with a single period $[SiO_2|TiO_2]$ does not offer a significant enhancement in absorption compared to the previously considered Pt/Co/SiO_2(160nm)/Si configuration. The maximum absorption in the Co layer is capped at 21.6% (Fig. 3*a*). However, as the periodicity of the Bragg mirror increases, so does the absorption in the STE. For N = 3 (Fig. 3*b*), the absorption maximum increases to 27.5%. Considering the structure $[SiO_2(145\ нм)|TiO_2(105\ нм)]_5$ (Fig. 3*c*), similar to the one studied in [28], the peak absorption in the ferromagnetic layer achieves approximately 35%. With an increment in the number of periods to 10 in the $[SiO_2(160\ нм)|TiO_2(95\ нм)]_{10}$ configuration, the absorption in the Co layer rises to approximately 39% (Fig. 3*d*). Further increases in the number of superlattice periods become impractical, as the total absorption in the STE (accounting for both the cobalt and platinum layers) at 10 superlattice periods approaches approximately 97%.

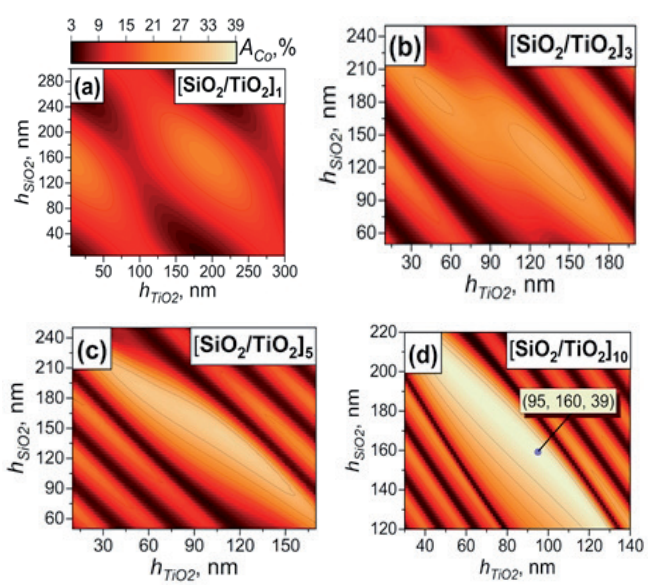

Fig. 3. *Dependence of absorption in the cobalt layer of an STE with a Bragg mirror $[SiO_2|TiO_2]N$ on the thicknesses of the dielectric layers h_{SiO2} and h_{TiO2} and the structure period N: N = 1 (a), N = 3 (b), N = 5 (c), N = 10 (d).*

To achieve maximum absorption efficiency in the cobalt A_{Co} layer, further calculations were conducted for the optimized structure $[SiO_2(160\ нм)|TiO_2(95\ нм)]_{10}$. These calculations incorporated the application of an anti-reflection coating to the STE structure, as depicted in Fig. 1*b*. The selection of a material for such a coating is pivotal, necessitating the right refractive index and optimal thickness for efficient performance at a wavelength of 800 nm. Our research evaluated a broad spectrum of materials commonly utilized as anti-reflection coatings in the near-infrared region. The materials considered, along with their characteristic refractive indices n at a wavelength of 800 nm and references to literature sources, are listed in **Table 1.**

Table 1

Materials for Anti-Reflection Coatings in the Visible and IR Wavelength Ranges

Material	*n*	Source
MgF_2	1.4194	[36]
SiO_2	1.4574	[32]
MgO	1.7276	[37]
Al_2O_3	1.6710 1.75	[38] [39]
HfO_2	1.9809	[40]
Si_3N_4	1.9962	[41]
Ta_2O_5	2.0719 2.1594	[32] [42]
TiO_2	2.0951	[35]

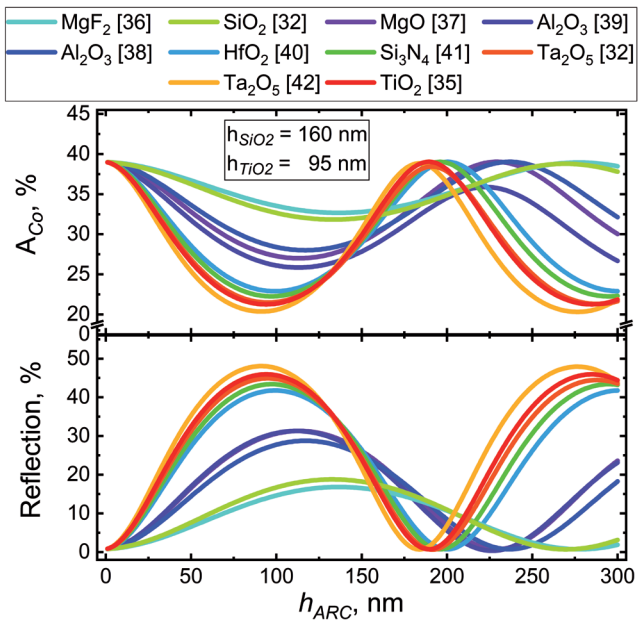

Fig. 4. *Absorption and reflection characteristics for an STE based on Pt(2 nm)/Co(2 nm) with a Bragg grating* $[SiO_2(160\ nm)|TiO_2(95\ nm)]_{10}$ *and with an anti-reflection coating.*

Fig. 4 presents the results of a comprehensive analysis of reflection and absorption of 800 nm wavelength radiation in the STE Pt(2 nm)/Co(2 nm), conducted based on the type of anti-reflection coating material (see Table 1) and the thickness of this coating.

Based on our calculations, we concluded that employing an anti-reflection coating does not result in a significant increase in absorption within the cobalt layer. This outcome aligns with previous findings indicating that the absorption efficiency in an STE, when using a Bragg mirror with $N = 10$, approaches 100%. At the minimum thickness of the ARC for all considered materials, a peak absorption in the cobalt layer is observed (see Fig. 4). This corroborates the efficiency of the optimized Bragg mirror design in effectively absorbing radiation traversing the structure.

Although various types of ARCs are ineffective in enhancing absorption and cannot fulfill their primary function in this context, their high resistance to external factors allows them to serve as conventional protective coatings. The thickness of the protective layer can be optimized so as not to detrimentally impact the optical properties or reduce the efficiency of pump laser radiation absorption. From the data presented in Fig. 4, three key groups of materials used in the simulations emerge: 1) TiO_2, Ta_2O_5, Si_3N_4, and HfO_2; 2) MgO and Al_2O_3; and 3) SiO_2 and MgF_2. Materials in the first group exhibit the most pronounced absorption minima at a characteristic thickness of 90 nm, achieving absorption up to ~ 20% and reflection ~ 50%. Conversely, materials in the second group display more gradual absorption minima, with absorption reaching ~ 25% at a characteristic layer thickness of ~ 115 nm. The third group's materials are the least sensitive to thickness changes, showing a minimum absorption of ~ 32% at a characteristic thickness of ~ 137 nm. Therefore, different ARC materials possess distinct characteristics that must be considered when selecting the most appropriate protective coating for a specific optical application.

4. CONCLUSION

The study developed a model of a spintronic terahertz emitter integrated with Bragg mirrors, structured as a $[SiO_2(160\ nm)|TiO_2(95\ nm)]_N$ superlattice, where N denotes the number of periods. The investigation revealed that with N equal to 10, the developed model achieves maximum optical absorption in the cobalt layer, reaching approximately 39%. Simultaneously, the total absorption in the STE structure approaches 100%. This marks a significant increase, over ninefold, compared to the absorption in the non-optimized Co(2 nm)/Pt(2 nm) structure on a high-resistivity silicon substrate, initially at only 4.3%. These findings are crucial as they underscore the potential of employing optical resonators, such as Bragg mirrors, to significantly enhance optical-terahertz conversion in STE structures and optimize laser pump powers. Additionally, it was discovered that even a relatively simple STE/SiO_2/Si system with an optimized oxide layer thickness of 160 nm can enhance absorption by approximately fivefold.

Further analysis indicated that the application of anti-reflection coatings does not result in an additional increase in absorption within the ferromagnetic layer of the optimized structure incorporating a Bragg mirror [SiO_2(160 nm)|TiO_2(95 nm)]. Nonetheless, it is essential to acknowledge that the inclusion of reflective coatings, such as MgF_2 and SiO_2, does not impair the absorption and reflectance characteristics of the structure, thereby allowing their consideration as protective layers based on specific requirements.

In conclusion, the significance of an integrated approach in designing STE structures is emphasized, encompassing not only the optimization of the ferromagnetic layer but also the incorporation of additional optical elements, such as dielectric superlattices and protective coatings. This comprehensive strategy enhances the understanding of light interaction processes with these structures and paves the way for the development of highly efficient devices in the realms of terahertz electronics and spintronics.

REFERENCES

1. Kubacka T, Johnson JA, Hoffmann MC, Vicario C, de Jong S, Beaud P, Grübel S, Huang S-W, Huber L, Patthey L, Chuang Y-D, Turner JJ, Dakovski GL, Lee W-S, Minitti MP, Schlotter W, Moore RG, Hauri CP, Koohpayeh SM, Scagnoli V, Ingold G, Johnson SL, Staub U. Large-Amplitude Spin Dynamics Driven by a THz Pulse in Resonance with an Electromagnon. *Science,* 2014, 343(6177):1333-1336.
2. Blank TGH, Grishunin KA, Mashkovich EA, Logunov MV, Zvezdin AK, Kimel AV. THz-Scale Field-Induced Spin Dynamics in Ferrimagnetic Iron Garnets. *Phys. Rev. Lett.,* 2021, 127(3):037203.
3. Mikhaylovskiy RV, Hendry E, Kruglyak VV, Pisarev RV, Rasing T, Kimel AV. Terahertz emission spectroscopy of laser-induced spin dynamics in $TmFeO_3$ and $ErFeO_3$ orthoferrites. *Phys. Rev. B.*, 2014, 90(18):184405.
4. Zhang W, Maldonado P, Jin Z, Seifert TS, Arabski J, Schmerber G, Beaurepaire E, Bonn M, Kampfrath T, Oppeneer PM, Turchinovich D. Ultrafast terahertz magnetometry. *Nat. Commun.*, 2020, 11(1):4247.
5. Fülöp JA, Tzortzakis S, Kampfrath T. Laser-Driven Strong-Field Terahertz Sources. *Adv. Opt. Mater.*, 2020, 8(3):1900681.
6. Bilyk VR, Brekhov KA, Agranat MB, Mishina ED. Dispersion of optical constants of Si:PbGeO crystal in the terahertz range. *Russian Technological Journal,* 2023, 11(3):38-45; doi: 10.32362/2500-316X-2023-11-3-38-45.
7. Blanchard F, Razzari L, Bandulet HC, Sharma G, Morandotti R, Kieffer JC, Ozaki T, Reid M, Tiedje HF, Haugen HK, Hegmann FA. Generation of 1.5 μJ single-cycle terahertz pulses by optical rectification from a large aperture ZnTe crystal. *Opt. Express*, 2007, 15(20):13212.
8. Feng Z, Qiu H, Wang D, Zhang C, Sun S, Jin B, Tan W. Spintronic terahertz emitter. *J. Appl. Phys.*, 2021, 129(1):010901.
9. Lepeshov S, Gorodetsky A, Krasnok A, Rafailov E, Belov P. Enhancement of terahertz photoconductive antenna operation by optical nanoantennas. *Laser Photon. Rev.*, 2017, 11(1):1600199.
10. Wu X, Ma J, Zhang B, Chai S, Fang Z, Xia C-Y, Kong D, Wang J, Liu H, Zhu C-Q, Wang X, Ruan C-J, Li Y-T. Highly efficient generation of 0.2 mJ terahertz pulses in lithium niobate at room temperature with sub-50 fs chirped Ti:sapphire laser pulses. *Opt. Express*, 2018 26(6):7107.
11. Leitenstorfer A, Moskalenko AS, Kampfrath T, Kono J, Castro-Camus E, Peng K, Qureshi N, Turchinovich D, Tanaka K, Markelz AG, Havenith M, Hough C, Joyce HJ, Padilla WJ, Zhou B, Kim K-Y, Zhang X-C, Jepsen PU, Dhillon S, Vitiello M, Linfield E, Davies AG, Hoffmann MC, Lewis R, Tonouchi M, Klarskov P, Seifert TS, Gerasimenko YA, Mihailovic D, Huber R, Boland JL, Mitrofanov O, Dean P, Ellison BN, Huggard PG, Rea SP, Walker C, Leisawitz DT, Gao JR, Li C, Chen Q, Valušis G, Wallace VP, Pickwell-MacPherson E, Shang X, Hesler J, Ridler N, Renaud CC, Kallfass I, Nagatsuma T, Zeitler JA, Arnone D, Johnston MB, Cunningham J. The 2023 terahertz science and technology roadmap. *J. Phys. D. Appl. Phys.*, 2023, 56(22):223001.

12. Seifert T, Jaiswal S, Martens U, Hannegan J, Braun L, Maldonado P, Freimuth F, Kronenberg A, Henrizi J, Radu I, Beaurepaire E, Mokrousov Y, Oppeneer PM, Jourdan M, Jakob G, Turchinovich D, Hayden LM, Wolf M, Münzenberg M, Kläui M, Kampfrath T. Efficient metallic spintronic emitters of ultrabroadband terahertz radiation. *Nat. Photonics,* 2016, 10(7):483-488.
13. Seifert TS, Cheng L, Wei Z, Kampfrath T, Qi J. Spintronic sources of ultrashort terahertz electromagnetic pulses. *Appl. Phys. Lett.*, 2022, 120(18):180401.
14. Khusyainov D, Ovcharenko S, Gaponov M, Buryakov A, Klimov A, Tiercelin N, Pernod P, Nozdrin V, Mishina E, Sigov A, Preobrazhensky V. Polarization control of THz emission using spin-reorientation transition in spintronic heterostructure. *Sci. Rep.*, 2021, 11(1):697.
15. Lezier G, Koleják P, Lampin J-F, Postava K, Vanwolleghem M, Tiercelin N. Fully reversible magnetoelectric voltage controlled THz polarization rotation in magnetostrictive spintronic emitters on PMN-PT. *Appl. Phys. Lett.*, 2022, 120(15):152404 .
16. Khusyainov D, Ovcharenko S, Buryakov A, Klimov A, Pernod P, Nozdrin V, Mishina E, Sigov A, Preobrazhensky V, Tiercelin N. Composite Multiferroic Terahertz Emitter: Polarization Control via an Electric Field. *Phys. Rev. Appl.,* 2022, 17(4):044025.
17. Buryakov AM, Gorbatova AV, Avdeev PY, Lebedeva ED, Brekhov KA, Ovchinnikov AV, Gusev NS, Karashtin EA, Sapozhnikov MV, Mishina ED, Tiercelin N, Preobrazhensky VL. Efficient Co/Pt THz spintronic emitter with tunable polarization. *Appl. Phys. Lett.*, 2023, 123(8):082404.
18. Chen M, Wu Y, Liu Y, Lee K, Qiu X, He P, Yu J, Yang H. Current-Enhanced Broadband THz Emission from Spintronic Devices. *Adv. Opt. Mater.*, 2019, 7(4):1801608.
19. Buryakov A, Avdeev P, Khusyainov D, Bezvikonnyy N, Coclet A, Klimov A, Tiercelin N, Lavrov S, Preobrazhensky V. The Role of Ferromagnetic Layer Thickness and Substrate Material in Spintronic Emitters. *Nanomaterials,* 2023, 13(11):1710.
20. Buryakov A, Gorbatova A, Avdeev P, Bezvikonnyi N, Abdulaev D, Klimov A, Ovcharenko S, Mishina E. Controlled Spintronic Emitter of THz Radiation on an Atomically Thin WS2/Silicon Substrate. *Metals,* 2022, 12(10):1676.
21. Khusyainov D, Guskov A, Ovcharenko S, Tiercelin N, Preobrazhensky V, Buryakov A, Sigov A, Mishina E. Increasing the Efficiency of a Spintronic THz Emitter Based on WSe2/FeCo. *Materials,* 2021, 14(21):6479.
22. Jin Z, Peng Y, Ni Y, Wu G, Ji B, Wu X, Zhang Z, Ma G, Zhang C, Chen L, Balakin AV, Shkurinov AP, Zhu Y, Zhuang S. Cascaded Amplification and Manipulation of Terahertz Emission by Flexible Spintronic Heterostructures. *Laser Photon. Rev.,* 2022, 16(9):2100688.
23. Nandi U, Abdelaziz MS, Jaiswal S, Jakob G, Gueckstock O, Rouzegar SM, Seifert TS, Kläui M, Kampfrath T, Preu S. Antenna-coupled spintronic terahertz emitters driven by a 1550 nm femtosecond laser oscillator. *Appl. Phys. Lett.*, 2019, 115(2):022405.
24. Rathje C, von Seggern R, Meyer N, Denker C, Munzenberg M, Schafer S. Emission Properties of Structured Spintronic Terahertz Emitters. *Proc. 44th International Conference on Infrared, Millimeter, and Terahertz Waves* (*IRMMW-THz*), IEEE, 2019, pp. 1-2.
25. Liu S, Guo F, Li P, Wei G, Wang C, Chen X, Wang B, Zhao W, Miao J, Wang L, Xu Y, Wu X. Nanoplasmonic-Enhanced Spintronic Terahertz Emission. *Adv. Mater. Interfaces,* 2022, 9(2):2101296.
26. Song B, Song Y, Zhang S, Jin K, Zhu W, Li Q, Zhang Z, Lin X, Dai Y, Yan X, Ma G, Jin Z, Yao J. Controlling terahertz radiation with subwavelength blocky patterned CoFeB/Pt heterostructures. *Appl. Phys. Express,* 2019, 12(12):122003.
27. Herapath RI, Hornett SM, Seifert TS, Jakob G, Kläui M, Bertolotti J, Kampfrath T, Hendry E. Impact of pump wavelength on terahertz emission of a cavity-enhanced spintronic trilayer. *Appl. Phys. Lett.*, 2019, 114(4):041107.
28. Rouzegar R, Chekhov AL, Behovits Y, Serrano BR, Syskaki MA, Lambert CH, Engel D, Martens U, Münzenberg M, Wolf M, Jakob G, Kläui M, Seifert TS, Kampfrath T. Broadband Spintronic Terahertz Source with Peak Electric Fields Exceeding 1.5 MV/cm. *Phys. Rev. Appl.,* 2023, 19(3):034018.

29. Torosyan G, Keller S, Scheuer L, Beigang R, Papaioannou ET. Optimized Spintronic Terahertz Emitters Based on Epitaxial Grown Fe/Pt Layer Structures. *Sci. Rep.*, 2018, 8(1):1311.
30. Yu Y, Cai J, Sun J, Zhang Z, Qin H. Fabrication and characterization of a wide-bandgap and high-Q terahertz distributed-Bragg-reflector micro cavities. *Opt. Commun.*, 2018, 426:84–88.
31. Raut HK, Ganesh VA, Nair AS, Ramakrishna S. Anti-reflective coatings: A critical, in-depth review. *Energy Environ. Sci.*, 2011, 4(10):3779.
32. Rodríguez-de Marcos LV, Larruquert JI, Méndez JA, Aznárez JA. Self-consistent optical constants of SiO_2 and Ta_2O_5 films. *Opt. Mater. Express,* 2016, 6(11):3622.
33. Carey R, Newman DM, Sandoval PAG, Thomas BWJ, Grundy PJ, Lacey ETM. Optical, magneto-optical and related properties for Pt and Co multi-layer structures. *J. Magn. Soc. Japan.*, 1991, 15(91):25-28.
34. Schinke C, Christian Peest P, Schmidt J, Brendel R, Bothe K, Vogt MR, Kröger I, Winter S, Schirmacher A, Lim S, Nguyen HT, MacDonald D. Uncertainty analysis for the coefficient of band-to-band absorption of crystalline silicon. *AIP Adv.*, 2015, 5(6):067168.
35. Sarkar S, Gupta V, Kumar M, Schubert J, Probst PT, Joseph J, König TAF. Hybridized Guided-Mode Resonances via Colloidal Plasmonic Self-Assembled Grating. *ACS Appl. Mater. Interfaces,* 2019, 11(14):13752-13760.
36. Rodríguez-de Marcos LV, Larruquert JI, Méndez JA, Aznárez JA. Self-consistent optical constants of MgF2, LaF3, and CeF3 films. *Opt. Mater. Express,* 2017, 7(3):989.
37. Stephens RE, Malitson IH. Index of refraction of magnesium oxide. *J. Res. Natl. Bur. Stand.*, 1952, 49(4):249.
38. Boidin R, Halenkovič T, Nazabal V, Beneš L, Němec P. Pulsed laser deposited alumina thin films. *Ceram. Int.,* 2016, 42(1):1177-1182.
39. Querry MR. *Optical constants*. MISSOURI UNIV-KANSAS CITY, 1985.
40. Bright TJ, Watjen JI, Zhang ZM, Muratore C, Voevodin AA. Optical properties of HfO2 thin films deposited by magnetron sputtering: From the visible to the far-infrared. *Thin Solid Films,* 2012, 520(22):6793-6802.
41. Luke K, Okawachi Y, Lamont MRE, Gaeta AL, Lipson M. Broadband mid-infrared frequency comb generation in a Si_3N_4 microresonator. *Opt. Lett.,* 2015, 40(21):4823.
42. Bright TJ, Watjen JI, Zhang ZM, Muratore C, Voevodin AA, Koukis DI, Tanner DB, Arenas DJ. Infrared optical properties of amorphous and nanocrystalline Ta_2O_5 thin films. *J. Appl. Phys.,* 2013, 114(8):083515.

DOI: 10.17725/j.rensit.2024.16.111

Sensor coating based on lipid Langmuir monolayer with the glucose oxidase enzyme molecules

Iliya A. Gorbachev, Vladimir V. Kolesov

Kotel'nikov Institute of Radioengineering and Electronics of RAS, http://www.cplire.ru/

Moscow 125009, Russian Federation

E-mail: iliyagor36@gmail.com, kvv@cplire.ru

Received December 01, 2023, peer-reviewed December 12, 2023, accepted December 13, 2023, published March 15, 2024.

Abstract: **The sensor coating was created based on a Langmuir monolayer of 1,2-dipalmitoyl-sn-glycero-3-phosphoethanolamine (DPPE) with immobilized molecules of the enzyme glucose oxidase and its sensor properties were studied. The process of incorporation of glucose oxidase enzyme molecules into a Langmuir monolayer of phospholipid DPPE molecules was studied using the compression isotherm method. Adsorption of glucose oxidase molecules has an expanding effect on the Langmuir monolayer of DPPE and leads to an increase in the area per molecule from 32.5 Å^2 to 49 Å^2 and a decrease in the compression modulus of the monolayer from 133 mN/m to 83 mN/m. Also, the adsorption of glucose oxidase leads to an increase in the desorption coefficient of the monolayer into the k_d subphase from $0.5 \cdot 10^{-3}$ to $1.2 \cdot 10^{-3}$. The morphology of films with immobilized enzyme molecules at different adsorption times was characterized by atomic force microscopy. Increasing the enzyme adsorption time leads to a decrease in the surface roughness of the formed film from 3.6 nm at 5 minutes to 2.4 nm at 60 minutes. The formed DPPE monolayers with immobilized enzyme molecules were transferred to graphite electrodes. Their sensory properties were studied using cyclic voltammetry and impedance measurements. The resulting coatings were sensitive to glucose in solutions with concentrations from 0 to 1 mg/ml. The presence of a linear concentration dependence of the maximum and minimum currents and resistances in the specified concentration range makes the created films promising for use as touch coatings.**

Keywords: **amperometric glucose sensor, enzymatic sensors, Langmuir-Blodgett films, biosensors**

UDC 539.23, 544.032.7

Acknowledgments: The study was carried out with financial support from the Russian Science Foundation, grant No. 22-29-20317.

For citation: Iliya A. Gorbachev, Vladimir V. Kolesov. Sensor coating based on a lipid Langmuir monolayer with the enzyme glucose oxidase molecules. *RENSIT: Radioelectronics. Nanosystems. Information Technologies,* 2024, 16(1):111-120e. DOI: 10.17725/j.rensit.2024.16.111.

Contents

1. INTRODUCTION.

Polysaccharides, and in particular glucose, are actively used in the food industry, so the creation of glucose sensors with increased sensitivity and selectivity is a fairly urgent task for monitoring its content in technological processes, in final products, as well as in production waste. A promising solution to this problem is the development of a touch coating for a biosensor based on molecules of the enzyme glucose oxidase (GO). The main task in this case is to fix the enzyme molecule in the sensor layer and maintain its activity over a long period of time. One of the approaches that allows, within one technological operation, to form a film with enzyme molecules included in it and ensure its protection from environmental influences is the Langmuir-Blodgett technology [1-4]. Its use makes it possible to form a bilayer membrane-like film with included enzyme molecules. In such a film, the enzyme molecules will be protected from external influences by a thin layer of lipid molecules. Therefore, the urgent task is to study the process of incorporation of enzyme molecules into Langmuir monolayers of various surfactants [5-8]. A similar approach can also be used to dope monolayers and Langmuir-Blodgett films with metal ions dissolved in the subphase [9]. Authors [10] The effect of the charge of the head group of surfactant molecules on the process of incorporation of enzyme molecules into a lipid monolayer was studied. At the same time, the authors did not take into account the influence of the acidity of the subphase on the charge of the enzyme molecule. The influence of the length of the hydrophobic part of the lipid molecule on the enzyme adsorption process was studied in [11]. The work also studied the time of adsorption of glucose oxidase molecules on the surface of water before the onset of compression to phase transitions in the monolayer and its surface properties. Studying the effect of adsorption time on the properties of Langmuir monolayers is an urgent task, since in order to produce reproducible samples of touch coatings it is necessary to precisely control the number of enzyme molecules adsorbed by the film. The stability of dipalmitoylphosphate acid monolayers was studied in [12]. The authors paid more attention to the surface properties of monolayers during enzyme adsorption and did not focus on changes in the morphology of the films. It is worth noting the works that studied the process of adsorption of glucose oxidase by mixed monolayers of phospholipid molecules and nanoparticles [13]. The work also studied the effect of the thickness of films with an immobilized enzyme on the sensitivity of sensors based on them. It has been shown that at film thicknesses up to 10-11 nm, the concentration dependence of the sensor parameters remains linear over large concentration ranges. At the same time, there is not enough information about the stability of monolayers on the surface of the aqueous subphase. This aspect becomes especially relevant when trying to mass produce touch coatings using the Langmuir-Blodgett technology.

Therefore, in this work, the sensory properties of a coating based on a lipid Langmuir monolayer with molecules of the enzyme glucose oxidase formed were studied. For this purpose, the stability of monolayers of 1,2-dipalmitoyl-sn-glycero-3-phosphoethanolamine during the adsorption of glucose oxidase molecules was studied using compression isotherms and the morphology of films obtained on their basis was studied.

2. EXPERIMENTAL PART

2.1. Formation of Langmuir monolayers

To prepare a solution of 1,2-dipalmitoyl-sn-glycero-3-phosphoethanolamine (DPPE, Sigma Aldrich, 99%), DPPE powder was dissolved in chloroform (Sigma Aldrich, 99%), resulting in a solution with a concentration of 10^{-3} M.

All experiments on the formation and study of the surface properties of Langmuir DPPE monolayers were carried out on a KSV Nima LB Trough KN2001 installation (Finland) with

a working area of 243 cm^2. The formation of Langmuir monolayers with immobilized molecules of the enzyme glucose oxidase was carried out according to the following procedure. A solution of DPPE in chloroform was applied to the surface of the aqueous subphase in an aliquot of 50 µl. Deionized water with a resistivity of 18 MOhm×cm and a glucose solution with a concentration of 0.015 mg/ml were used as a subphase. After 30 minutes, the monolayers were compressed by movable barriers at a constant rate of monolayer area loss equal to 0.7 cm^2/min. During the compression of the monolayer by movable barriers, the $\pi(A)$ isotherm was automatically recorded – the dependence of the change in surface pressure (π) on the area occupied by one molecule in the monolayer (A). Compression isotherms of DPPE monolayers formed in the absence and presence of dissolved GO molecules in the subphase are shown in **Fig. 1**.

By analyzing the compression isotherms, such monolayer parameters as the specific area per molecule in the non-tilting condensed phase (A_0) and the compression modulus (k) were obtained. The value of A_0 coincides with the abscissa of the intersection point of the tangent drawn to the condensed phase of the graph of the monolayer compression isotherm. To calculate the compression modulus we used the formula [14]:

$$k = -A_0 \frac{d\pi}{dA}, \quad (1)$$

where A_0 is the specific area per molecule in the non-obliquely condensed phase, k is the compression modulus of the monolayer, A is the area occupied by the monolayer. The values of k, A_0 are given in **Table** 1.

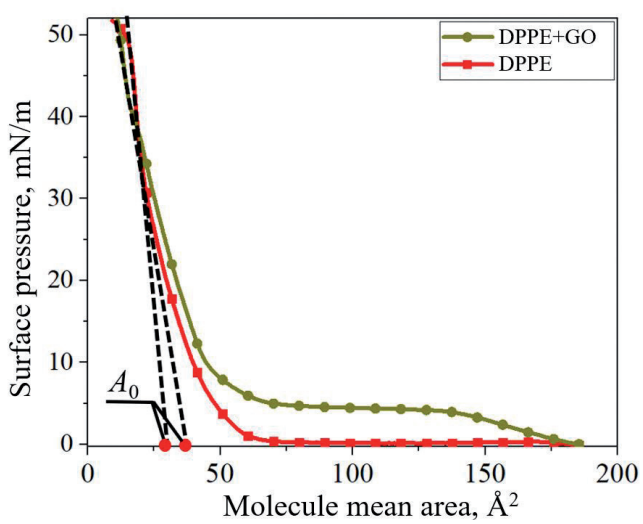

Fig. 1. *Compression isotherms of a DPPE monolayer formed on the subphase in the presence and absence of dissolved glucose oxidase enzyme molecules. Points A_0 – areas occupied by one molecule in a non-tilting-condensed phase.*

Table 1

Compression modulus (k) and area occupied by one molecule in the non-tilt-condensed phase of a DPPE monolayer (A_0), formed in the presence (DPPE+GO) and in the absence (DPPE) of enzyme molecules dissolved in the subphase, π_e – equilibrium pressure

Monolayer parameter	DPPE	DPPE+GO
k, (mN/m)	133	87
A_0, (Å^2)	32.5	49
π_e, (mN)	37.5	42

The transfer of monolayers to solid substrates was carried out using the Langmuir-Blodgett method at an equilibrium value of surface pressure (πe). Atomically smooth highly oriented pyrographite was used as a substrate.

2.2 Study of film surface morphology

The study of surface morphology was carried out using the atomic force microscopy method on an NT-MDT Ntegra installation in a hybrid mode with a single line scanning speed of 0.79 Hz. An NT-MDT NSG10 series cantilever with a tip radius not exceeding 10 nm was used. Image processing and calculation of the average roughness and film thickness were performed in the open source software Gwyddion 2.63.

2.3. Studying the sensory properties of Langmuir-Blodgett films with an immobilized enzyme using electrophysical methods

To measure the electrophysical parameters of the created films, a P-45X potentiostat was used. The sensory properties of the formed coatings were studied using the following method.

The formed Langmuir monolayers with the immobilized GO enzyme were compressed to a pressure of πe. Next, the monolayers were transferred by the Langmuir-Blodgett method onto graphite electrodes with a diameter of 2 mm at a speed of electrodes passing through the water surface of 1 mm/min. Thus, sensor coatings were formed, consisting of 2 Langmuir monolayers with an immobilized glucose oxidase enzyme. The electrodes were placed at a distance of 5 mm from each other in a reservoir with 2 ml of glucose solution of various concentrations. To eliminate the influence of electromagnetic interference, the measuring cell was placed in a steel box with a metal lid. Voltammograms of the measured solutions were obtained in the potential range from –1 V to +1 V with a voltage sweep rate of 0.2 mV/s. Impedance measurements were carried out in the frequency range from 50 KHz to 4 KHz with a bias voltage of 0.8 V.

3. RESULTS AND DISCUSSION

3.1. Study of the adsorption process of glucose oxidase molecules

An analysis of the compression isotherms presented in Fig. 1 shows that the adsorption of enzyme molecules leads to a change in the type of compression isotherm. The moment of phase transition between the liquid phase and the inclined-condensed phase is extended. Section II-III of the compression isotherm appears in cases where the contribution to the growth of surface pressure from the interaction of the head groups of surfactant molecules increases. Adsorption of GO molecules led to a decrease in the monolayer compressive modulus k from 133 mN/m to 87 mN/m and an increase in A_0 from 32.5 Å^2 to 49 Å^2. Thus, we can conclude that the adsorption of GO molecules by a DPPE monolayer has an expanding effect on the monolayer [15]. It is worth noting that after the collapse pressure was reached, a kink was observed in the compression isotherm, after which the value of the surface pressure remained constant. The presence of such a section is explained by the beginning of the formation of a multilayer membrane-like structure [16].

The study of the adsorption of GO molecules by DPPE film occurred in two stages. At the first stage, the value of the equilibrium pressure at which the monolayer was subsequently transferred to solid substrates, πe, was established. To do this, the monolayer was compressed to a surface pressure value corresponding to the middle of the non-obliquely condensed phase, after which the compression process stopped. A further change in the surface pressure is associated with the occurrence of relaxation processes in the monolayer. To analyze them, changes in surface pressure (π) versus time (t) were recorded automatically in automatic mode. The graph of the dependence $\pi(t)$ is shown in **Fig. 2.** The coordinate of the intersection point of the projection of the linear part of the graph $\pi(t)$ and the ordinate axis (π) corresponds to the value of the equilibrium pressure π_e, at which the rates of adsorption and desorption of the monolayer substance into the subphase are equalized [17]. The value of the tangent of the angle of inclination of the linear part of the graph $\pi(t)$ corresponds to the rate of decrease in surface pressure (k_d) due to the structural

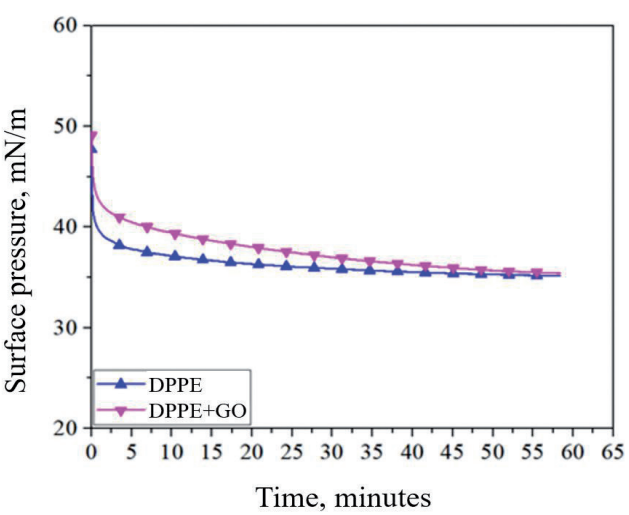

Fig. 2. *Graphs of the decrease in surface pressure of DPPE monolayers (a), obtained in the subphase in the presence and absence of dissolved enzyme molecules, at a constant monolayer area.*

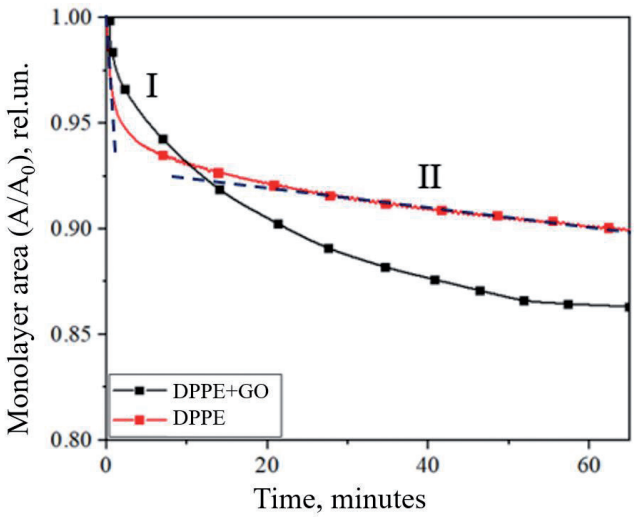

Fig. 3. *Graphs of the decrease in the area of DPPE monolayers, obtained in the subphase in the presence and absence of dissolved enzyme molecules, at a constant monolayer area.*

reorganization of molecules in the monolayer, as well as due to the possible loss of part of the substance of the monolayer under water [18,19]. It can be seen from Fig. 2 that the adsorption of GO molecules led to an increase in k_d and π_e from $0.5 \cdot 10^{-3}$ and 37.5 mN/m to $1.2 \cdot 10^{-3}$ and 42 mN/m, respectively.

To determine the mechanism of loss of the monolayer substance into the subphase, a method was used based on the analysis of desorption curves in the coordinates of the relative loss of area versus time. For this purpose, curves of the decrease in monolayer area were recorded at constant surface pressure near the point of phase transition of the monolayer two-dimensional liquid - condensed film. **Fig. 3** shows graphs of changes in the relative monolayer area over time for DPPE monolayers formed on the subphase in the presence and absence of dissolved GO molecules. In the presented desorption curves, two sections can be distinguished, approximated by a linear dependence. This is due to the presence of several mechanisms of desorption of the monolayer substance into the near-surface layer. In the literature, two types of desorption are distinguished. The first is desorption, controlled by the departure of the monolayer substance into a near-surface layer of finite thickness. And the second is the diffusion transition of monolayer molecules from a static near-surface layer deep into the subphase. In the desorption graph presented in Fig.3, areas with the first and second desorption mechanisms are marked with numbers (I) and (II), respectively. To describe the desorption processes (I) and (II), expressions (1) and (2) were used [20,21]:

$$ln\frac{A}{A_0} = -k_s t, \tag{2}$$

$$ln\frac{A}{A_0} = -k_v t, \tag{3}$$

where A/A_0 is the relative change in the monolayer area over time t, k_v and k_s are the desorption and diffusion coefficients, respectively.

The numerical values of the coefficients k_s and k_v correspond to the angle of inclination of the linear sections of the area loss curves presented in **Fig. 4**. The values of ks and kv are given in **Table 2**.

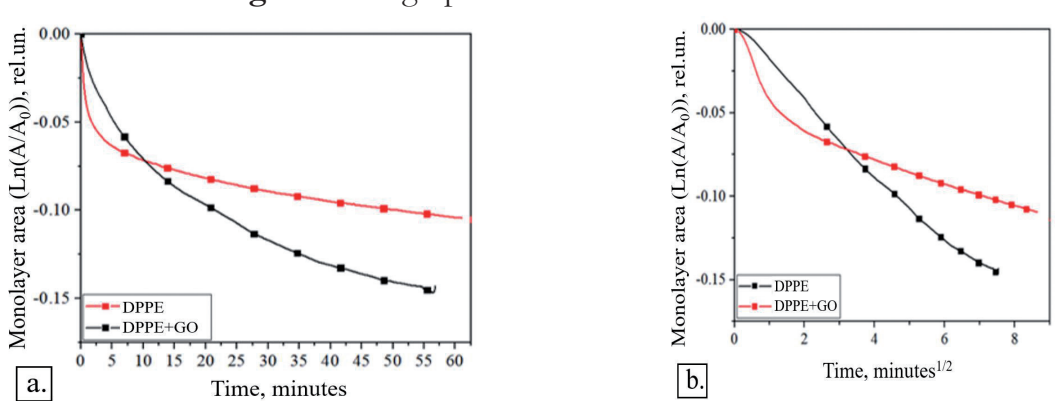

Fig. 4. *Curves of the decrease in the area of DPPE monolayers (a, b), formed in the presence and absence of enzyme molecules dissolved in the subphase.*

Table 2

Desorption coefficients of DPPE monolayers formed on the subphase in the presence and absence of dissolved GO molecules

	DPPE	DPPE+GO
T, min	3	12
k_s	$5 \cdot 10^{-4}$	$6 \cdot 10^{-4}$
k_v	$3.3 \cdot 10^{-2}$	$1.1 \cdot 10^{-2}$
k_d	$0.5 \cdot 10^{-3}$	$1.2 \cdot 10^{-3}$

Table 3

Average roughness (R_a), thickness (L) and surface area (S_q) of monolayer DPPE films transferred at different enzyme adsorption times.

GO adsorption time	5	30	60
R_a, nm	3.6	3.3	2.4
S_q, mkm^2	0.3	0.3	0.3
L, nm	10.7	10.4	8.7

From Table 2 it can be seen that the adsorption of GO molecules by a DPPE monolayer leads to a change in desorption coefficients, controlled by the transition of the monolayer substance to the surface layer and the transition of the substance from the surface layer deep into the subphase. The coefficient k_s increases from $5 \cdot 10^{-4}$ to $6 \cdot 10^{-4}$, and k_v decreases from $3.3 \cdot 10^{-2}$ to $1.1 \cdot 10^{-2}$ in the presence of enzyme molecules in the subphase. The presence of GO molecules in the subphase leads to a decrease in the rate of desorption, which is controlled by the transition of the monolayer substance to the near-surface layer, and an increase in the rate of transition of molecules of the substance from the near-surface layer deep into the subphase.

3.2. Effect of enzyme adsorption time on the surface morphology of the formed films

Fig. 5 shows images of the surface morphology of monolayer DPPE films with adsorbed aggregates to GO molecules transferred at different adsorption times. **Table 3** shows the values of the roughness of the formed films, the average thickness and the average surface area of the films.

Adsorption of GO by monolayers leads to a change in the morphology of films obtained on their basis. When GO is adsorbed by a DPPE monolayer for 5 minutes, regions with a height of 12 to 24 nm are formed on the film surface. The GO molecule has dimensions of 6×5.2×7 nm [22], while the DPPE monolayer has a thickness of about 3 nm. Thus, we can conclude that these areas are aggregates of GO molecules adsorbed by a monolayer of DPPE molecules. When the adsorption time increases to 30 minutes, the area occupied by GO islands increases. In this case, the thickness of individual sections increases to 25-30 nm. The average film roughness decreases from 3.6 nm to 3.3 nm, which can be explained by an increase in the area occupied by GO aggregates. A further increase in the adsorption time to 60 minutes leads to a decrease in surface roughness and average film thickness. This behavior can be associated

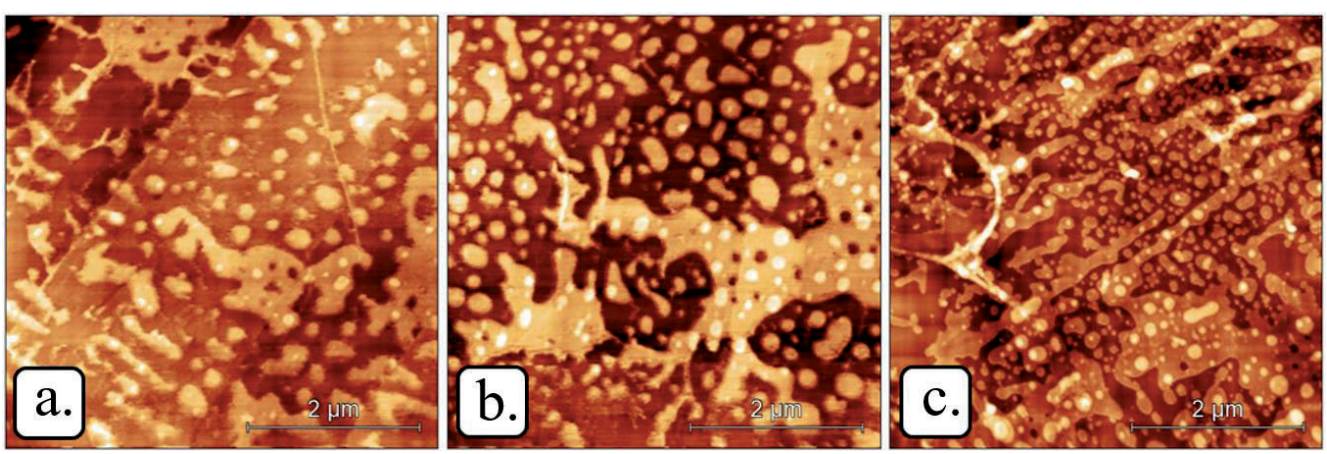

Fig. 5. *Images of the surface morphology of monolayer DPPE films formed on a subphase containing GO at GO adsorption times of 5 minutes (a), 30 minutes (b) and 60 minutes (c).*

with a decrease in the rate of transition of the monolayer substance into the diffusion layer. As a result, the area covered by aggregates of GO molecules increases. At the same time, the height of individual aggregates decreases to 22-25 nm.

An increase in the adsorption time of the GO enzyme on the film leads to a change in its morphology. The most developed morphology is observed in the film transferred 5 minutes after holding the monolayer at constant pressure (the total adsorption time, including the time of compression of the monolayer by movable barriers, is 125 minutes). Further adsorption leads to a decrease in the average surface roughness and average film thickness. Therefore, a monolayer with an adsorption time of 30 minutes was used to form the sensor coating.

3.3. Studying the sensory properties of the formed coatings using voltammetric and impedancemetric methods

The formed sensor coatings were studied by cyclic voltammetry. Cyclic voltammograms and graphs of changes in maximum currents between the electrodes at different concentrations of glucose in the solution are shown in **Fig. 6**. For a biofilm with the immobilized GO enzyme, a linear dependence of the current on the concentration of glucose in the solution is observed. The increase in current with increasing concentration to 0.9 mg/ml is 0.25 μA for forward bias and 0.35 μA for reverse bias. In the absence of biofilm on the electrodes, concentration changes in current are random. The large operating currents are explained by the absence of a film of lipid molecules, which is a dielectric, on the electrodes.

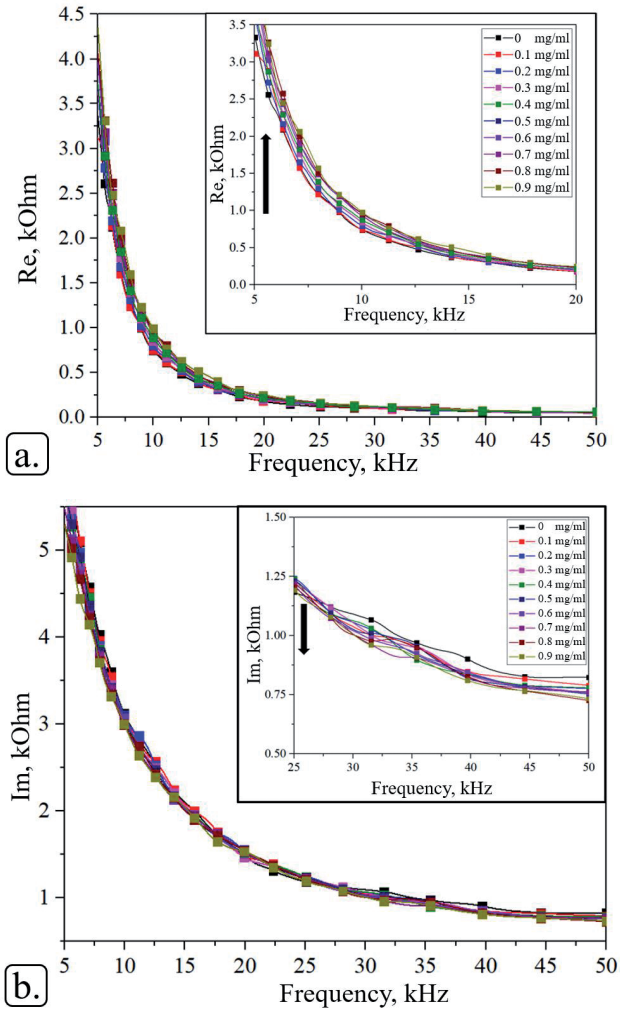

Fig. 7. *Frequency dependences of the real (a) and imaginary (b) parts of the total impedance of the system at different concentrations of glucose molecules in solution.*

Fig. 7 shows the frequency dependences of the real (a) and imaginary (b) parts of the total

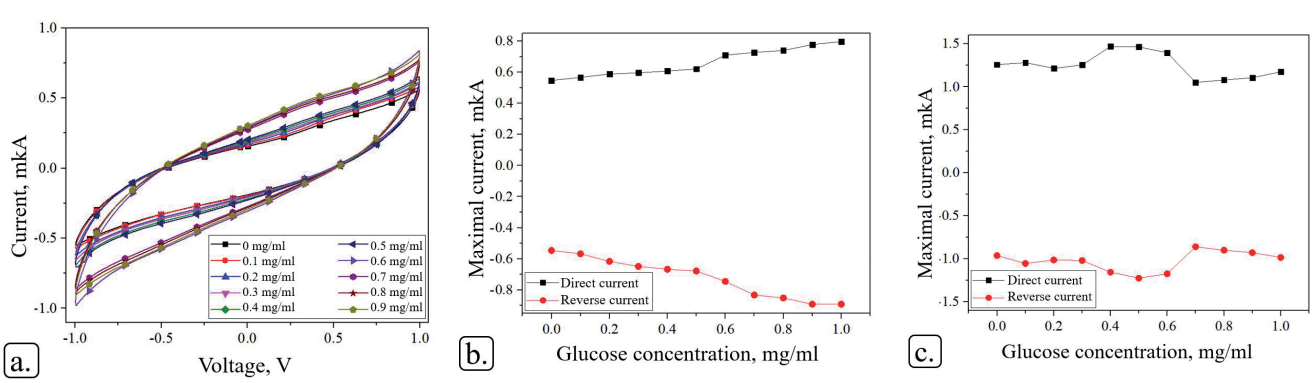

Fig. 6. *Cyclic voltammograms (a) and changes in the maximum values of forward and reverse currents in the presence (b) and in the absence of a sensor film (c) at different concentrations of glucose in the solution.*

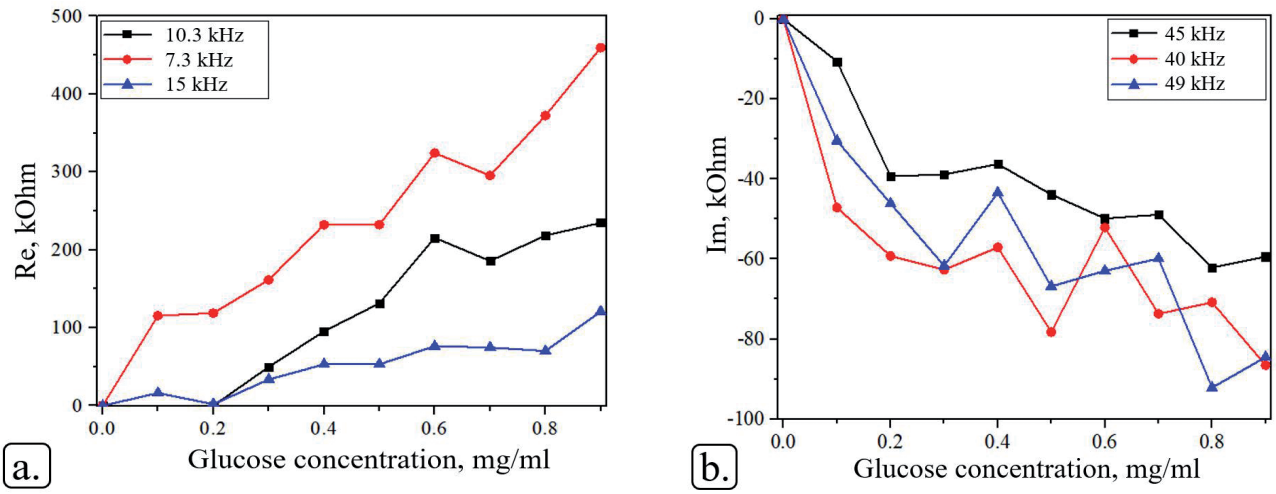

Fig. 8. *Concentration dependences of the real (a) and imaginary (b) parts of the total impedance of the system for the corresponding frequencies.*

impedance of the measured cell at different concentrations of glucose molecules in the solution. In the frequency range from 5 to 20 kHz and from 30 to 50 kHz, frequencies can be distinguished for which the concentration dependence of the real and imaginary parts of the impedance is monotonic.

Thus, the concentration dependence of the real part of the impedance at frequencies of 7.3 kHz, 10 kHz and 15 kHz has a sublinear form. The concentration dependence of the imaginary impedance particles at frequencies of 40 kHz, 45 kHz and 49 kHz can be approximated by an exponential function. The corresponding concentration dependences are shown in **Fig. 8**.

4. CONCLUSION

In this work, the influence of the adsorption time of glucose oxidase molecules on the surface properties of Langmuir DPPE monolayers and their morphology was studied. Based on the formed monolayers, sensor bilayer coatings were created. Differences in the adsorption time of the enzyme lead to differences in the morphology of the films. The process of incorporation of glucose oxidase enzyme molecules into a Langmuir monolayer of DPPE lipid molecules was studied. The adsorption of GO molecules has an expanding effect on the Langmuir DPPE monolayer. Adsorption of GO molecules leads to a structural restructuring of the monolayer, accompanied by an increase in the specific area of the monolayer, a decrease in the rate of decrease in surface pressure and an increase in pressure πe. When GO is adsorbed by a DPPE monolayer, the filling rate of the near-surface diffusion layer decreases, but at the same time the rate of transition of molecules from the diffusion layer into the bulk of the subphase increases. The increase in the specific area per molecule during the adsorption of an enzyme by a monolayer is associated with the floating of the enzyme and the formation of an adsorption Gibbs monolayer at the water-air interface, which is subsequently compressed by the emerging monolayer of lipid molecules. As a result, when the monolayer is compressed, the position of all formed phases shifts to a region of large areas. An increase in the adsorption time of GO molecules leads to a decrease in the average roughness of the film and its thickness.

Voltammetry and impedance measurements of the films showed the sensitivity of the sensor coating to glucose molecules in aqueous solutions. The presence of a linear concentration dependence of maximum and minimum currents and resistances in the glucose concentration range from 0 to 1 mg/ml makes such sensor coatings promising for use as sensor coatings.

Thus, the possibility of creating an enzymatic glucose biosensor based on a LB film from DPPE phospholipid molecules with immobilized glucose oxidase enzyme molecules has been demonstrated. The main advantage of such biosensors is their high selectivity and sensitivity with respect to the molecules being detected.

REFERENCES

1. Ariga K, Nakanishi T, Michinobu T. Immobilization of Biomaterials to Nano-Assembled Films (Self-Assembled Monolayers, Langmuir-Blodgett Films and Layer-by-Layer Assemblies) and Their Related Functions. *Journal of Nanoscience and Nanotechnology*, 2006, 6:2278-2301.
2. Caseli L. Enzymes immobilized in Langmuir-Blodgett films: Why determining the surface properties in Langmuir monolayer is important?. *An Acad Bras Cienc*, 2018, 90:631-644.
3. Rodrigues RT, Nordi CFS, Siqueira Junior JS, Caseli L. Effect of interfering agents for urease immobilized in Langmuir-Blodgett films of controlled molecular architecture. *Thin Solid Films,* 2020, 704:138043.
4. Gorbachev IA, Smirnov AV. Biosensor based on Langmuir-Blodgett film with alcohol oxidase enzyme. *RENSIT: Radioelectronics. Nanosystems. Information Technologies*, 2023, 15(3):307-316. DOI: 10.17725/rensit.2023.15.307.
5. Zaitsev SY. Functional Langmuir films with glucose oxidase. *Colloids and Surfaces A: Physicochemical and Engineering Aspects*, 1993, 75:211-216.
6. Wang K-H, Syu M-J, Chang C-H, Lee Y-L. Immobilization of glucose oxidase by Langmuir–Blodgett technique for fabrication of glucose biosensors: Headgroup effects of template monolayers. *Sensors and Actuators B*, 164:29-36.
7. Furtado FAS, Caseli L. Enzyme activity preservation for galactose oxidase immobilized in stearic acid Langmuir-Blodgett films. *Thin Solid Films,* 2020, 709:138253.
8. Saha S, Chowdhury J. Sustained and improved enzymatic activity of trypsin immobilized in the Langmuir Blodgett film of DPPC: A rapid enzyme sensor for the detection of Azocasein. *Materials Chemistry and Physics,* 2020, 243:122647.
9. Gorbachev IA, Smirnov AV, Kuznetsova IE, Kolesov VV. Temperature influence on the formation of Langmuir monolayers with Ni arachidic acid and Ni arachidate clusters. *RENSIT: Radioelectronics. Nanosystems. Information Technologies*, 2023, 15(3):295-306. DOI: 10.17725/rensit.2023.15.295.
10. Li J, Rosilio V, Boissonnade M-M, Baszkin A. Adsorption of glucose oxidase into lipid monolayers: effect of a lipid headgroup charge. *Colloids and Surfaces B: Biointerfaces*, 2003, 29:13/20.
11. Zhang J, Rosilio V, Goldmann M, Boissonnade M-M, Baszkin A. Adsorption of Glucose Oxidase into Lipid Monolayers. Effect of Lipid Chain Lengths on the Stability and Structure of Mixed Enzyme/Phospholipid Films. *Langmuir,* 2000, 16:1226-1232.
12. Lee Y-L, Lin J-Y, Lee S. Adsorption Behavior of Glucose Oxidase on a Dipalmitoylphosphatic Acid Monolayer and the Characteristics of the Mixed Monolayer at Air/Liquid Interfaces. *Langmuir*, 2007, 23:2042-2051.
13. Ohnuki H, Saiki T, Kusakari A, Endo H, Ichihara M, Izumi M. Incorporation of Glucose Oxidase into Langmuir-Blodgett Films Based on Prussian Blue Applied to Amperometric Glucose Biosensor. *Langmuir,* 2007, 23:4675-4681.
14. Vu TT, Kharitonova NV, Maiorova LA, Gromova OA, Torshin IY, Koifman OI, Compression Speed as a Parameter Changing the Dimensionality of Corrole Nanostructures in Layers at the

Air-Water Interface. *Macroheterocycles,* 2018, 11(3):286-292.

15. Yanklovich AI. Regular multimolecular structures of surfactants - Langmuir-Blodgett films. *Advances in colloidal chemistry.* Leningrad, Khimiya Publ., 1991, 262-291.
16. Gopal A, Lee KYC. Headgroup Percolation and Collapse of Condensed Langmuir Monolayers. *J. Phys. Chem. B,* 2006, 110:22079-22087.
17. Sanchez CC, Nino MRR, Patino JMR. Relaxation phenomena in monoglyceride films at the air–water interface. *Colloids and Surfaces B: Biointerfaces,* 1999, 12:175-192.
18. Rabinovitch W, Robertson RF, Mason AG. Relaxation of surface pressure and collapse of unimolecular films of stearic acid. *Can. J. Chem.*, 1960, 38:1881-1890.
19. Hac-Wydro K, Wydro P, Dynarowicz-Latka P. Metal ions binding to tri-n-octylphosphine oxide (TOPO) monolayer spread at the air/water interface. *Thin Solid Films,* 2008, 516:8839-8843.
20. Gorbachev IA, Shtykov SN, Brezesinski G, Glukhovskoy EG. Studying of Quantum Dots Langmuir Monolayers Stability at the Different Subphase Temperature. *BioNanoSci.,* 2017, 7:686-691.
21. Ter-Minassian-Saraga L. Recent work on spread monolayers, adsorption and desorption. *Journal of Colloid Science,* 1956, 11:398-418.
22. Hecht HJ, Kalisz HM, Hendle J, Schmid RD, Schomburg D. Crystal Structure of Glucose Oxidase from Aspergillus niger Refined at 2·3 Å Reslution. *Journal of molecular biology,* 1993, 229(1):153-172.

DOI: 10.17725/j.rensit.2024.16.121

Morphology and electrical properties of modified Langmuir graphene oxide films

Iliya A. Gorbachev, Vladimir V. Kolesov

Kotel'nikov Institute of Radioengineering and Electronics of RAS, http://www.cplire.ru/

Moscow 125009, Russian Federation

E-mail: iliyagor36@gmail.com, kvv@cplire.ru

Received December 01, 2023, peer-reviewed December 12, 2023, accepted December 13, 2023, published March 15, 2024.

Abstract: **The work devoted to study of the electrical properties and morphology of Langmuir-Blodgett films of modified graphene oxide (GO). The Langmuir-Blodgett method was used for studying of formation process of Langmuir monolayers formed on the subphase contained dissolved ions of tin chloride salt. The compression isotherms of monolayers formed in the presence of tin ions shifted towards larger occupied areas. Langmuir monolayers of graphene oxide formed under various conditions were transferred on solid substrates and studied by atomic force microscopy and voltammetry. It has been established that the presence of tin ions in the aqueous subphase leads to changes in the morphology of the formed films. Thus, the average roughness and surface area of such films increased from 0.2 nm and 0.04 μm^2 to 5.4 nm and 0.46 μm^2, respectively. The presence of tin ions dissolved in the aqueous subphase influenced the type of current-voltage characteristics of the films under study. The maximum reverse current increases from 0.75 nA to -0.3 nA and the resistance increases from 11 GOhm to 700 GOhm. Temperature annealing of the graphene oxide film at 300°C leads to a decrease in the maximum forward current and an increase in the reverse current from 0.0407 nA and -0.071 nA to 0.0065 nA and 0.0616 nA, respectively. For a film formed in the presence of ions in the subphase, annealing does not affect the maximum forward current, and the current of the reverse branch of the current-voltage characteristic increases from -0.1669 nA to 0.0468 nA.**

Keywords: **graphene oxide thin films, Langmuir graphene oxide monolayers, thin films conductivity, graphene oxide hybrid coatings**

UDC 539.23, 544.032.7

Acknowledgments: The study was carried out with financial support from the Russian Science Foundation, grant No. 22-29-20317

For citation: Iliya A. Gorbachev, Vladimir V. Kolesov. Morphology and electrical properties of modified Langmuir graphene oxide films. *RENSIT: Radioelectronics. Nanosystems. Information Technologies,* 2024, 16(1):121-128e. DOI: 10.17725/j.rensit.2024.16.121.

Contents

1. INTRODUCTION

Nowadays, ensuring environmental monitoring of the state of the atmosphere is an urgent task. This is due to the growing level of environmental pollution. This task is of particular relevance in large cities with a large number of road transport. One of the products of car exhaust is carbon monoxide and carbon dioxide. The development of sensor coatings capable of selectively

absorbing carbon monoxide or carbon dioxide is an urgent task in the development of gas sensors. Graphene oxide is a promising material for such sensor coatings. [1-3].

Despite the possibility of creating sensors with high sensitivity [4,5], their main disadvantage is low selectivity with respect to target gases. To solve this problem, films based on graphene oxide are modified with functional groups and nanoparticles [6,7]. In particular, to create coatings selective to carbon dioxide and carbon dioxide, films based on graphene oxide are modified with tin oxide nanoparticles [8], that allows to significantly increase the selectivity and sensitivity of sensors [9-11]. Also, the disadvantages of such sensors include low reproducibility of characteristics from device to device [12,13]. One of the approaches to reduce the number of defects in a graphene oxide film is the Langmuir-Blodgett technology, since it remains possible to orient graphene oxide particles in the film [14].

The Langmuir-Blodgett (LB) Technology is widely used for the formation of thin films of various surfactants, nanoparticles and polymer molecules [15-18]. There are also works devoted to the formation and study of the properties of Langmuir monolayers of graphene oxide [19]. The influence of subphase acidity on the morphology of Langmuir-Blodgett graphene oxide films was studied by authors [20]. It has been shown that changing the acidity makes possible to control the thickness of graphene oxide films. One of the promising tasks in this direction is doping a graphene oxide monolayer with ions of various metals. The study of adsorption process of heavy metal ions to colloidal graphene oxide was performed by authors [21-23]. The presence of similar works allows us to conclude that it is possible to embed charged particles into graphene films. The process of incorporation of Cs^{2+}, Sr^{2+} and Y^{3+} ions into a graphene film on the surface of water has been studied by authors [25,24]. The authors demonstrated that ion adsorption is determined not only by electrostatic interaction with graphene oxide, but is more complex in nature. In such works, the authors pay little attention to studying the possibility of incorporating metal ions into Langmuir monolayers of graphene oxide, which could lead to the creation of new types of ordered two-dimensional materials. Also, due attention is not paid to the electrical properties of graphene oxide films with adsorbed ions, as well as the influence of the thermal treatment process on their properties. This problem becomes particularly relevant when attempting to sensitize graphene oxide films with oxide particles.

Therefore, the main goal of the present work was to study the effect of metal ions dissolved in the aqueous subphase on the electrical properties and morphology of Langmuir-Blodgett graphene oxide films. And also, the effect of thermal treatment of films on them.

2. EXPERIMENTAL PART

2.1. Materials and methods

The graphene oxide powder with an average particle diameter of 10 to 100 μm (Rusgrafen LLC, Russia) was used for preparation a solution of graphene oxide. Graphene oxide powder was dissolved in a water:methanol mixture with a volume ratio of 1:5 to obtain a solution with a concentration of 0.5 mg/ml. The resulting solution was sonicated in an ultrasonic bath (Skymen JP-031S, China) with a power of 180 W for 30 minutes. The solution was centrifuged at a rotation speed of 4000 rpm for 30 minutes. After stratification of the solution and precipitation, the supernatant part of the solution was selected, which was sonicated for 40 minutes and precipitated into a centrifuge at a rotation speed of 13,000 rpm. The sediment part of the solution formed during centrifugation was collected. The precipitate was dried in a vacuum chamber at room temperature for 60 minutes and re-dissolved in a water:methanol mixture with a volume ratio of components of 1:5. In this way, a water-methanol solution of graphene

oxide particles with a concentration of 0.1 mg/ml was obtained. Before forming a Langmuir monolayer, the solutions were sonicated for 15 minutes in an ultrasonic bath.

To prepare the subphase with dissolved tin chloride ($SnCl_2$), dry tin chloride powder was taken and dissolved in deionized water to obtain a concentration of 1 Mol/L. The resulting solution was diluted with deionized water to obtain a concentration of 10^{-2} M, which was used as an aqueous subphase.

2.2. Formation of Langmuir monolayers and Langmuir-Blodgett films of graphene oxide

All experiments on the formation and transfer of Langmuir monolayers to solid substrates were carried out on a KSV Nima LB Trough KN2002 setup. The temperature of the subphase was maintained constant at 22°C using an A300 circulation cooler (Termex LLC, Russia, Tomsk). Deionized water with a resistivity of 18 MOhm×cm and an aqueous solution of tin chloride with a concentration of 10^{-2} M were used as a subphase. The formation of Langmuir monolayers of graphene oxide took place according to the following procedure. An aliquot of graphene oxide solution with a volume of 500 μL was applied to the surface of the aqueous subphase. After 20 minutes for deionized water, 40 minutes and 80 minutes for the subphase containing tin ions, the monolayer was compressed by movable barriers with a constant rate of area loss equal to 0.7 cm^2/min. During the compression process, a π-A diagram was recorded automatically – the dependence of the change in pressure on the area occupied by the monolayer. The compression isotherm of the formed monolayers is shown in **Fig. 1**. The monolayer was transferred to a solid substrate at a constant surface pressure of 40 mN/m using the Langmuir-Blodgett method – vertical lift. The speed of movement of the substrate through the monolayer was constant and amounted to 1 mm/min. In this way, 5-layer films were formed based on monolayers of graphene oxide (film

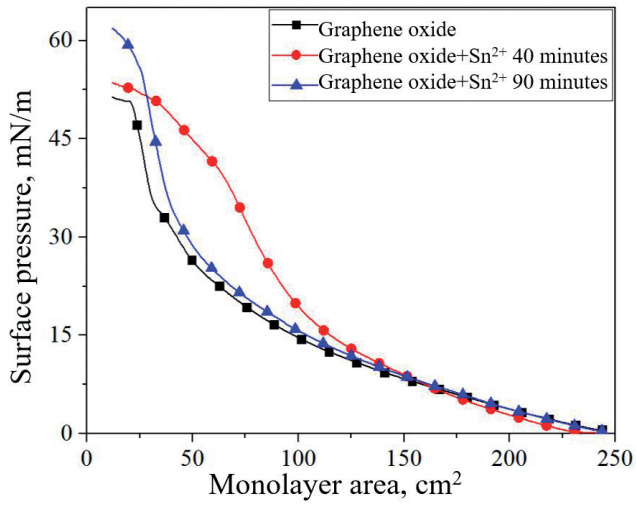

Fig. 1. *Compression isotherms of graphene oxide monolayers formed on deionized water and on deionized water containing dissolved tin ions at 40 minutes and 90 minutes of ion adsorption time by the monolayer.*

1), graphene oxide that adsorbed tin ions for 40 minutes (film 2) and adsorbed tin ions for 90 minutes (film 3). The surface properties of monolayers were studied using the compression isotherm method. The linear sections on the compression isotherm correspond to the phase state of the monolayer and are characterized by the compression modulus of the monolayer (k) and the specific area of the monolayer in the phase state (A_0). The value of A_0 can be obtained by extrapolating the linear portion of the phase state of the monolayer to the A axis at a value of π = 0 mN/m. To calculate the compression modulus of a monolayer, the formula is used:

$$k = -A_0 \frac{d\pi}{dA}, \quad (1)$$

where k, A and A_0 are the compression modulus of the monolayer, the area of the monolayer and the specific area of the monolayer in the phase state under study. Since the values of k and A_0 change during the interphase transition of the monolayer, analysis of the dependence $k(A_0)$ allows us to identify areas on the compression isotherm that correspond to the gaseous, inclined-condensed phase and non-inclined-condensed phase of the liquid and condensed phase of the monolayer [26-28].

Table 1

Values of the compression modulus (k) and specific area of monolayers in the non-obliquely condensed phase (A_0), formed under various conditions

Subphase	A_0, cm^{22}	k, mN/m
Deionized water	47.5	1.6
40 minutes adsorption	32.8	2.3
90 minutes adsorption	38.8	2

Compression isotherms of graphene oxide monolayers formed on an aqueous subphase in the absence and presence of dissolved tin ions at different times of their adsorption by the monolayer are shown in Fig. 1.

Table 1 shows the values of k and A_0 of graphene oxide monolayers formed under various conditions.

2.3. Studying the morphology of formed Langmuir-Blodgett films using atomic force microscopy

The formed Langmuir monolayers were transferred to solid substrates made of atomically smooth mica using the Langmuir-Blodgett technology. In this way, monolayer films were formed based on monolayers of graphene oxide, formed in the absence and presence of dissolved tin ions in the subphase. The morphology of the resulting film coatings was studied by atomic force microscopy using an NT-MDT Netgra installation in hybrid mode. **Fig. 2** shows typical images of the surface morphology of the resulting films.

Mathematical processing of the obtained images in the Gwyddion 2.63 program made it possible to determine the average surface area of the film (S) and the value of its average roughness (R_a). The surface area of the film was calculated by the triangulation method, the average roughness of the film surface was calculated using the formula [29,30]:

$$R_a = \frac{1}{N}\sum_{j=1}^{N}|r_j|, \qquad (2)$$

where R_a is the arithmetic mean deviation of the profile from the baseline (profile mean line), N is the number of points at which the roughness parameter R_a was measured, and rj is the absolute

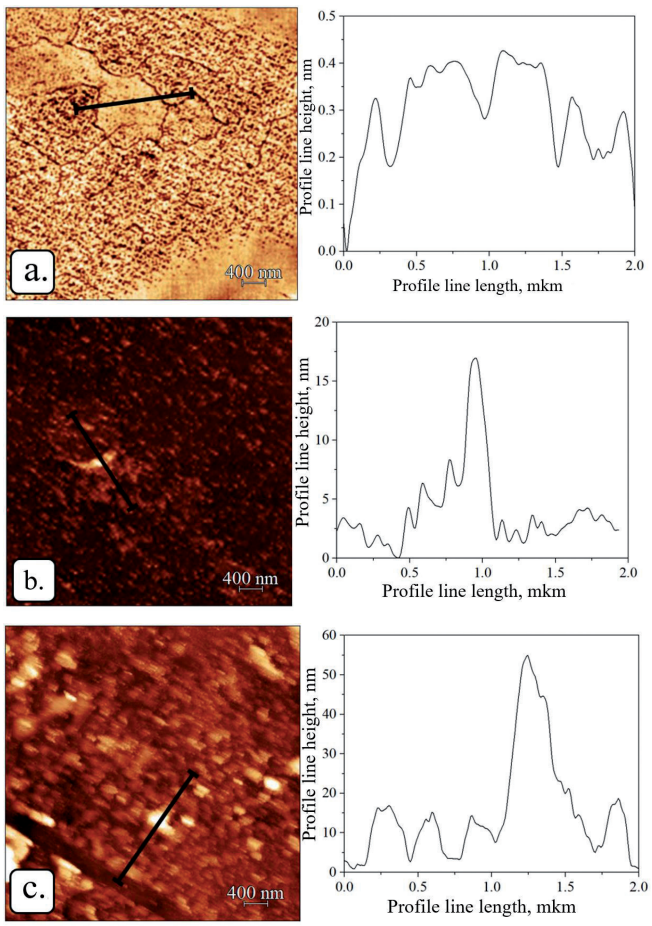

Fig. 2. *Images of the surface and its profile lines of a graphene oxide film (a), a film based on a monolayer that adsorbed tin ions for 40 minutes (b) and 90 minutes (c).*

Table 2

Values of the average surface roughness (R_a) of the film and its surface area (S)

Film	R_a, nm	S, mkm^2
Graphene oxide	0.2	0.04
Graphene oxide + $SnCl_2$ 40 minutes	1.4	0.42
Graphene oxide + $SnCl_2$ 90 minutes	5.4	0.46

deviation of the profile height value from the mean line at each roughness measurement point.

Table 2 shows the average roughness and surface area of films formed under various conditions.

2.4. Study of the electrical characteristics of the formed films

Langmuir graphene oxide monolayers formed under different conditions were transferred onto solid coverslip substrates with formed interdigitated electrode structures. The distance between the pins was 100 μm. The electrical

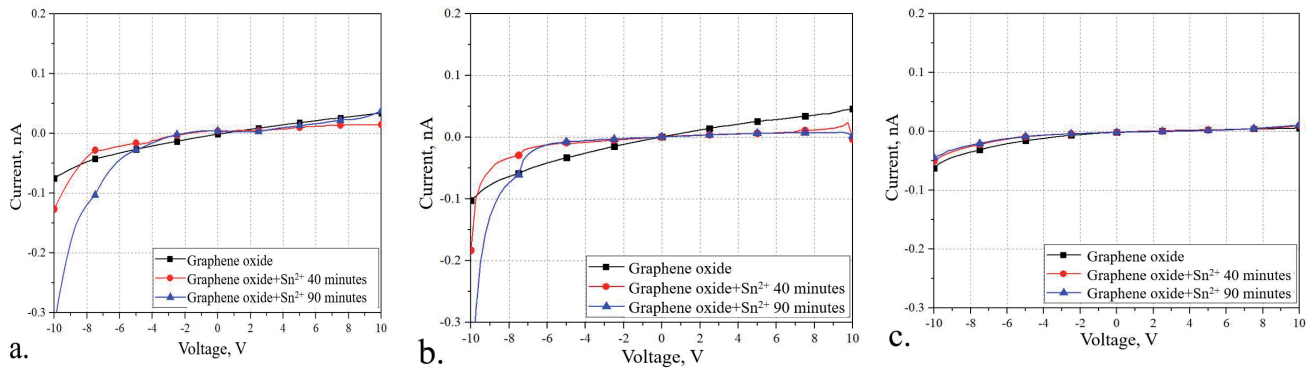

Fig. 3. *Current-voltage characteristics of the formed films before annealing (a), after annealing at a temperature of 150°C (b) and 300°C (c).*

characteristics of films 1, 2 and 3 were studied by voltammetry. The current-voltage characteristics were measured on a Keythley 6487 picoammeter in the voltage range of +10 V –10 V with a scan step of 0.2 V. The formed film coatings were annealed at temperatures of 150°C and 300°C for 30 minutes in an air atmosphere. The current-voltage characteristics of the films under study are shown in **Fig. 3**.

3. DISCUSSION AND CONCLUSIONS

The compression isotherm of graphene oxide monolayers formed under various conditions is shown in Fig. 1. In a graphene oxide monolayer, one can distinguish a gas phase corresponding to section I-II, an inclined condensed phase (section II-III) and a non-obliquely condensed phase (section III-IV). When the surface pressure exceeds 50 mN/m, monolayer collapse occurs, which characterizes a sharp change in the slope of the compression isotherm. The addition of tin ions to the subphase affects the type of compression isotherm depending on the time of interaction of tin ions with graphene oxide particles. With an interaction time of 40 minutes, the collapse pressure of the monolayer increases from 50 mN/m to 60 mN/m. The compression modulus of the monolayer also increases from 1.6 mN/m to 2.3 mN/m. The A_0 value increases from 49 cm^2 to 51 cm^2. The compression isotherm of the monolayer formed at a time of interaction of graphene oxide and tin ions of 90 minutes also shifted towards larger areas. It can be concluded that tin ions have an expanding effect on the graphene oxide monolayer.

Fig. 2 shows images of the surface of graphene oxide films formed in the presence and absence of tin ions in the subphase. The monolayer of used graphene oxide particles has a thickness of about 0.2 to 0.4 nm with individual particle diameters from 1 to 4 μm. Such a scatter in heights allows us to conclude that individual graphene particles are non-monolayer. The interaction of a monolayer of graphene oxide with tin ions leads to a change in the morphology of the film. The average film roughness increases from 0.2 to 1.4 nm, the average surface area increases by 0.38 μm^2. On the surface of the film, aggregates with heights from 3 to 20 nm and areas up to 0.8 μm^2 can be distinguished. An increase in the interaction time of tin ions with a monolayer of graphene oxide leads to an increase in the average roughness to 5.4 nm and the average surface area to 0.46 μm^2. The average heights of the formed aggregates increased and ranged from 15 nm to 55 nm. The interaction of tin ions and a Langmuir monolayer of graphene oxide leads to the formation of aggregates on the surface of the film. The sizes of the aggregates increased with increasing interaction time between the graphene oxide monolayer and tin ions.

Fig. 3 shows the current-voltage characteristics of multilayer films 1, 2 and 3. The current-voltage characteristic of film 1 has a linear form. Its conductivity was about 0.09 pS.

The presence of tin hydroxide aggregates in the film leads to a change in the type of current-voltage characteristic. The current-voltage characteristics of films 2 and 3 have a nonlinear shape; an increase in the adsorption time of tin ions leads to an increase in the maximum reverse current from 0.125 nA to 0.3 nA. The maximum current of the forward branch of the current-voltage characteristic decreases from 0.025 nA to 0.01 nA with increasing adsorption time of tin ions. Thermal treatment of the formed film 1 for 30 minutes at a temperature of 150°C leads to an increase in the current of the forward and reverse branches of the current-voltage characteristic to –0.1 nA and 0.05 nA, respectively. The maximum current of the reverse branch of the current-voltage characteristics of films 2 and 3 also increases to 0.18 nA and 0.4 nA, respectively. The increase in maximum currents may be associated with the beginning of the reduction process of graphene oxide and an increase in its conductivity. At the same time, the high defectiveness of the films and the loss of conductivity at the edges of reduced graphene oxide particles explain the low conductivity values in the films. Annealing films at a temperature of 300°C leads to an increase in film resistance to 700 GOhm. After annealing at a temperature of 300°C, the current-voltage curves of films 2 and 3 acquire a linear form. A similar effect may be associated with the reduction of graphene oxide and desorption of tin dioxide particles from the film surface.

4. CONCLUSION

Thus, the work studied the electrical properties and morphology of Langmuir-Blodgett films based on graphene oxide during their thermal reduction. The possibility of modifying Langmuir monolayers of graphene oxide with metal ions during the formation of monolayers has been established. The possibility of controlling the electrical conductivity of Langmuir-Blodgett graphene oxide films by thermal treatment has been demonstrated. The recovery temperature regime has been determined, at which the current-voltage characteristics retain their nonlinear form. The approach used in the work can be used to form sensor coatings sensitive to carbon monoxide and carbon monoxide, to develop gas sensors with greater sensitivity.

REFERENCES

1. Anju M, Renuka NK. Graphene–dye hybrid optical sensors. *Nano-Structures & Nano-Objects,* 2019, 17:194-217.
2. Tiwari SK, Sahoo S, Wang N, Huczko A. Graphene research and their outputs: Status and prospect. *Journal of Science: Advanced Materials and Devices*, 2020, 5(1):10-29.
3. Kornilov DY. Graphene oxide – a new electrode nanomaterial for chemical current sources. *RENSIT: Radioelectronics. Nanosystems. Information Technologies*, 2021, 13(1):105-108. DOI: 10.17725/rensit.2021.13.105.
4. Schedin F; Novoselov KS. Detection of Individual Gas Molecules by Graphene Sensors. *Nat. Mater.*, 2006, 6:652-655.
5. Yavari F, Castillo E, Gullapalli H, Ajayan PM, Koratkar N. High sensitivity detection of NO2 and NH3 in air using chemical vapor deposition grown graphene. *Appl. Phys. Lett.*, 2012, 100:203120.
6. Koteeswara RN, Devika M, Sungwon L. Functionalization of graphene layers and advancements in device applications. *Carbon,* 2019, 152:954-985.
7. Mehmood A, Mubarak NM, Khalid M, Walvekar R, Abdullah EC, Siddiqui MTH, Baloch HA, Nizamuddin S, Mazari S. Graphene based nanomaterials for Strain Sensor Application A-review. *Journal of Environmental Chemical Engineering*, 2020, 8(3):103743.
8. Lee ZY, Fahmi bin Hawari H, Witjaksono bin Djaswadi G, Kamarudin K. A Highly Sensitive Room Temperature CO_2 Gas Sensor Based on SnO_{2-r}GO Hybrid Composite. *Materials*, 2021, 14:522.
9. Tai H, Yuan Z, Zheng W, Ye Z, Liu C, Du X. ZnO Nanoparticles/Reduced Graphene

Oxide Bilayer Thin Films for Improved NH3-Sensing Performances at Room Temperature. *Nanoscale Research Letters,* 2016, 11:130.

10. Lee J-H, Kang W-S, Najeeb CK, Choi B-S, Choi S-W, Lee HJ, Lee SS, Kim J-H. A hydrogen gas sensor using single-walled carbon nanotube Langmuir–Blodgett films decorated with palladium nanoparticles. *Sensors and Actuators B,* 2013, 188:169-175.
11. Botcha VD, Sutar DS, Major SS. Study of GO-Cu2O and RGO-Cu nanocomposite monolayer sheets prepared by modified Langmuir Blodgett route. *Journal of Physics and Chemistry of Solids*, 2018, 118:158-165.
12. Massera E, Miglietta ML, Polichetti T, Ricciardella F, Girolamo A, Francia D. Reproducibility of the Performances of Graphene-Based Gas-Sensitive Chemiresistors. *Lecture Notes in Electrical Engineering,* 2013, 268, doi: 10.1007/978-3-319-00684-0-26.
13. Schedin F, Geim AK, Morozov SV, Hill EH, Blake P, Katsnelson MI, Novoselov KS. Detection of Individual Gas Molecules Adsorbed on Graphene. *Nat. Mater.*, 2007, 6:652-655.
14. Shi L-F, Liu J-Z, Yang J-H, Cai L-F, Shi L-Y, Qiu H-X. Langmuir-Blodgett assembly of transparent graphene oxide-silver microwire hybrid films with an antibacterial property. *New Carbon Materials,* 2017, 32(4):344-351.
15. Kondalkara VV, Yang SS, Patil PS, Choudhury S, Bhosale PN, Lee KK. Langmuir-Blodgett assembly of nanometric WO3 thin film for electrochromic performance: A new way. *Materials Letters,* 2017, 194:102-106.
16. Podolskaya EP, Serebryakova MV, Krasnov KA, Grachev SA, Gzgzyane AM, Sukhodolov NG. Application of Langmuir–Blodgett technology for the analysis of saturated fatty acids using the MALDI-TOF mass spectrometry. *Mendeleev Commun.,* 2018, 28:337-339.
17. Xu L, Tetreault AR, Khaligh HH, Goldthorpe IA, Wettig SD, Pope MA. Continuous Langmuir-Blodgett Deposition and Transfer by Controlled Edge-to-Edge Assembly of Floating 2D Materials. *Langmuir,* 2019, 35:51-59.
18. Ly TN, Park S. Highly sensitive ammonia sensor for diagnostic purpose using reduced graphene oxide andconductive polymer. Scientific Reports, 2018, 8:18030.
19. Zheng Q-B, Shi L-F, Yang J-H. Langmuir-Blodgett assembly of ultra-large graphene oxide films for transparent electrodes. *Trans. Nonferrous Met. Soc. China*, 2012, 22:25042511.
20. Botchaa VD, Narayanama PK, Singha G, Talwar SS, Srinivasa RS, Major SS. Effect of substrate and subphase conditions on the surface morphology of graphene oxide sheets prepared by Langmuir–Blodgett technique. *Colloids and Surfaces A: Physicochem. Eng. Aspects,* 2014, 452:65-72.
21. Park S, Lee K-S, Bozoklu G, Cai W, Nguyen SBT, Ruoff RS. Graphene Oxide Papers Modified by Divalent Ions–Enhancing Mechanical Properties via Chemical Cross-Linking. *ACS NANO*, 2008, 2(3):572-578.
22. Mokoena LS, Mofokeng JP. A Review on Graphene (GN) and Graphene Oxide (GO) Based Biodegradable Polymer Composites and Their Usage as Selective Adsorbents for Heavy Metals in Water. *Materials,* 2023, 16:2527.
23. GroshkovaYuA, Buslaeva EYu, Kraevskii SV, Gubin SP. Preparation of titanium oxide nanoparticles on the surface of reduced graphene oxide in supercritical isopropanol. *RENSIT: Radioelectronics. Nanosystems. Information Technologies*, 2023, 15(1):43-50. DOI: 10.17725/rensit.2023.15.043.
24. Monjezi R, Azadi R, Hamoule T. Design, synthesis, and characterization of thiol-decorated cross-linked graphene oxide framework for high-capacity Hg^{2+} ion adsorption. *Journal of Saudi Chemical Society,* 2024, 28:101786.

25. Carr AJ, Kumal RR, Bu W, Uysal A. Effects of ion adsorption on graphene oxide films and interfacial water structure: A molecular-scale description. *Carbon,* 2022, 195:131-140.
26. Vollhardt D, Fainerman VB. Progress in characterization of Langmuir monolayers by consideration of compressibility. *Advances in Colloid and Interface Science,* 2006, 127:83-97.
27. Khomutov GB, Gainutdinov RV, Gubin SP, Kislov VV, Rakhnyanskaya AA, Sergeev-Cherenkov AN, Tolstikhina AL. Formation and organization of planar polymeric and nanocomposite nanostructures on liquid and solid surfaces. *Surface Science,* 2004, 566(568):396-401.
28. Vu TT, Kharitonova NV, Maiorova LA, Gromova OA, Torshin IY, Koifman OI. Compression Speed as a Parameter Changing the Dimensionality of Corrole Nanostructures in Layers at the Air-Water Interface. *Macroheterocycles,* 2018, 11(3):286-292.
29. Necas D, Klapetek P, Valtr M. Estimation of roughness measurement bias originating from background subtraction. *Measurement Science and Technology,* 2020, 31:094010.
30. Necas D, Valtr M, Klapetek P. How levelling and scan line corrections ruin roughness measurement and how to prevent it. *Scientific Reports*, 2020, 10:15294.

DOI: 10.17725/j.rensit.2024.26.129

Maximum detection range of an underwater noise source using holographic processing

Venedikt M. Kuz'kin
A.M. Prokhorov Institute of General Physics of RAS, http://www.gpi.ru/
Moscow 119991, Russian Federation
E-mail: *kumiov@yandex.ru*

Sergey A. Pereselkov, Pavel V. Rybyanets, Sergey A. Tkachenko
Voronezh State University, http://www.vsu.ru/
Voronezh 394006, Russian Federation
E-mail: pereselkov@yandex.ru, rybyanets.edu@yandex.ru, sega-tk@mail.ru

Vladimir I. Grachev
V.A. Kotelnikov Institute of Radioengineering and Electronics of RAS, http://www.cplire.ru/
Moscow 125009, Russian Federation
E-mail: *grachev@cplire.ru*

Received January 29, 2024, peer-reviewed February 05, 2024, accepted February 12, 2024, published March 15, 2024.

Abstract: **The formation of a hologram of a noise signal from an underwater source against the background of distributed interference is described. An expression is obtained for the bandwidth of the angular distribution of the spectral density of the noise signal on the hologram. The minimum duration of the noise signal is estimated, which determines the maximum detection range of the noise sound source. An algorithm is presented for determining the parameters of holographic processing that realizes the maximum detection range. Holographic processing of noise signals is considered using a single vector-scalar receiver and linear antennas.**

Keywords: **holographic processing, underwater noise source, receiving system, signal duration, detection range**

UDC 004.052.34

Acknowledgments: The study was supported by the Russian Science Foundation grant No. 23-61-10024, https://rscf.ru/project/23-61-10024/.

For citation: Venedikt M Kuz'kin, Sergey A. Pereselkov, Vladimir I. Grachev., Pavel V. Rybyanets, Sergey A. Tkachenko. Maximum detection range of an underwater noise source using holographic processing. *RENSIT: Radioelectronics. Nanosystems. Information Technologies*, 2024, 16(1):129-136e. DOI: 10.17725/j.rensit.2024.16.129.

Contents

1. INTRODUCTION

Scenarios for the behavior of broadband acoustic signals in oceanic waveguides are extremely diverse and complex, but they obey one general pattern, first established in [1]. It manifests itself in the fact that the interference of the modes of such signals, due to waveguide dispersion, forms a stable interference pattern (interferogram) of the maxima of the energy parameters spectral density of the wave field in the variables of frequency-distance (time). The localized bands configuration is determined by the frequency range, waveguide parameters,

speed and source trajectory This pattern is applicable – which is one of its main advantages – also to noise source signals, the description of which is statistical in nature. This allows us to consider the interferogram as a universal deterministic mathematical model of the noise signal and propagation medium. The model is quite simple and at the same time contains a wide variety of forms of behavior. In addition, it has predictive power, but does not require strict causal constraints. In essence, the role of models in physical constructions is determined by how well they convey the real processes essential features.

Based on the interferogram model, a holographic method for detecting and localizing a noise source is proposed and implemented, based on recording a two-dimensional time-frequency interferogram using a two-dimensional Fourier transform [2,3]. The state of the issue of noise signals holographic processing in hydroacoustics is reflected in [4].

This article describes the formation of a hologram of a noise signal from a single source against the background of distributed noise interference in an oceanic waveguide. The conditions for the formation of an undistorted interferogram are given. The angular distribution of the hologram spectral density is discussed. A heuristic criterion for the noise source detection range is formulated. The minimum duration of recording a noise signal, which determines the maximum detection range of the source, has been estimated. Holographic processing of noise signals using a single vector-scalar receiver and linear antennas is considered.

2. HOLOGRAPHIC PROCESSING

We will consider holographic processing of a noise signal $s(t)$ against the background of interference $n(t)$ using the example of sound pressure $p(t)$ recorded by a single receiver. For the vector components of a vector-scalar receiver, the consideration is similar. During the observation time Δt in the frequency band Δf, J independent time noise realizations $p(t) = s(t) + n(t)$ with duration T and with a time interval δT between them are accumulated

$$J = \Delta t/(T + \delta T). \quad (1))$$

Realizations are independent if $\delta T \geq 1/\Delta f$. The Fourier transform restores the time-frequency representation of noise implementations $p(f,t) = s(f,t) + n(f,t)$ and generates a sound pressure interferogram

$$\begin{aligned} I(f,t) &= p(f,t)\,p^*(f,t) = \\ &= |s(f,t)|^2 + n(f,t)s^*(f,t) + \\ &+ s(f,t)n^*(f,t) + |n(f,t)|^2, \end{aligned} \quad (2)$$

where the superscript "*" denotes the complex conjugate quantity. The first and fourth terms (2) give the spectral density of the signal and noise in the (f,t) plane, and the second and third terms give the mutual spectral densities of the signal and noise. Since the signal and noise are uncorrelated, the mutual spectral densities will have the form of a low-contrast smeared background and its weight in the interferogram $I(f,t)$ can be neglected. Consequently, interferogram (2) can be approximately represented as a linear combination of signal and noise interferograms

$$\begin{aligned} I(f,t) &\approx |s(f,t)|^2 + |n(f,t)|^2 = \\ &= I_s(f,t) + I_n(f,t). \end{aligned} \quad (3)$$

The sound pressure hologram taking into account relation (3) takes the form

$$\begin{aligned} F(\tau,\nu) &\approx \int_0^{\Delta t}\int_{f_1}^{f_2} \left[I_s(f,t) + I_n(f,t)\right] \exp\left[i2\pi(\nu t - f\tau)\right] df dt = \\ &= F_s(\tau,\nu) + F_n(\tau,\nu). \end{aligned} \quad (4)$$

Here ν and τ are the frequency and time of the hologram; $f_{1,2} = f_0 \mp (\Delta f/2)$ – average frequency of the spectrum. In the hologram, the spectral density of the signal $F_s(\tau,\nu)$ of a moving source is concentrated in two narrow bands, mirror-inverted relative to the origin, in the form of focal spots caused by the interference of modes of different numbers. They are located in the first and third quadrants of the hologram if the radial velocity of the source is $w < 0$ (the source

approaches the receiver), and in the second and fourth quadrants ($w > 0$) when the source moves away from the receiver. Radial velocity refers to the projection of the source velocity in the direction of the receiver. When the source is stationary and moves along a circular arc, the coordinates of the peaks of the focal spots are located on the time axis τ. The concentration region contains $(M - 1)$ main maxima with coordinates (τ_μ,ν_μ) located on the straight line $\nu = \varepsilon\tau$ with the angular coefficient $\varepsilon = \nu_\mu/\tau_\mu$ where M is the number of modes forming the field and is the number of the focal spot. The maximum of the first focal spot closest to the origin of coordinates is due to the interference of neighboring modes and falls on the values (τ_1,ν_1). The coordinates of the neighboring peak caused by the interference of mode numbers $(m, m + 2)$ are located at the point (τ_2,ν_2), etc. And finally, the coordinates of the most distant peak, dictated by the interference of the first and last modes – $(\tau(M - 1), \nu(M - 1))$. At points with coordinates (τ_μ,ν_μ), the $(M - \mu)$ main maxima are summed up. The spectral noise density $F_n(\tau,\nu)$ is distributed over the entire plane (τ,ν) of the hologram.

Under the condition $r_0 \gg |w|\Delta t$, where r_0 is the distance of the source from the receiver at the initial time $t = 0$, the radial speed and distance are equal

$$\dot{w} = -2\pi\kappa_{w\mu}\nu_\mu,\ \dot{r}_0 = \kappa_{r\mu}\tau_\mu, \tag{5}$$

$$\kappa_{w\mu} = \left[\overline{h_{m(m+\mu)}(f_0)}\right]^{-1},\quad \kappa_{r\mu} = 2\pi\left[\overline{dh_{m(m+\mu)}(f_0)/df}\right]^{-1} \tag{6}$$

– coefficients that determine the spatial and frequency scales of variability of the waveguide transfer function [5]. Here $h_{mn} = h_m - h_n$, h_m is the horizontal wave number of the m-th mode. The restored source parameters, in contrast to their true values, are marked with a dot at the top. The bar above means averaging over mode numbers. For the first ($\mu = 1$) and last ($\mu = M - 1$) focal spots limiting the localization region of the signal spectral density, relation (6) is simplified

$$\kappa_{w1} = (M-1)\left[h_{1M}(f_0)\right]^{-1},$$
$$\kappa_{r1} = 2\pi(M-1)\left[dh_{1M}(f_0)/df\right]^{-1}, \tag{7}$$
$$\kappa_{w(M-1)} = \kappa_{w1}/(M-1),\ \kappa_{r(M-1)} = \kappa_{r1}/(M-1).$$

The spectral density of the signal is concentrated in a band limited by straight lines

$$\nu_1 = \varepsilon\tau + \delta\nu,\ \ \nu_2 = \varepsilon\tau - \delta\nu, \tag{8}$$

where $\delta\nu = 1/\Delta t$ is the half-width of focal spots in the direction of the ν axis. Outside this band, the spectral density of the signal is practically suppressed. Along the τ axis, the half-width of focal spots is $\delta\tau = 1/\Delta f$. The angular coefficients of the direct location of the maxima of focal spots ε and interference fringes $\delta f/\delta t$ are related by the relation

$$\varepsilon = -\delta f/\delta t, \tag{9}$$

where δf is the frequency shift of the wave field maximum over time δt.

3. UNDISTORTED INTERFEROGRAM

The interference pattern formed by a noise source is characterized by frequency and time scales of variability caused by the interference of the mth and nth modes [5]:

$$\Lambda_f^{(mn)} = \frac{2\pi}{r\left|dh_{mn}(f_0)/df\right|},\quad \Lambda_t^{(mn)} = \frac{1}{\left|wh_{mn}(f_0)\right|}. \tag{10}$$

The recorded interferogram and hologram are not distorted if the band Δf and observation time Δt for any pair (m,n) of modes satisfy the conditions

$$\Delta f > \Lambda_f^{(mn)},\quad \Delta t > \Lambda_t^{(mn)}. \tag{11}$$

Inequalities (11) impose lower restrictions on the reception bandwidth and observation time depending on the distance, radial velocity and time-frequency scales of variability of the waveguide transfer function during the formation of the interferogram. An increase in the bandwidth and a decrease in the average frequency of the spectrum causes a decrease in the distance at which the observed interferogram and hologram are not distorted. Increasing the observation time reduces the permissible values of the radial velocity. Violation of condition (11)

leads to a change in configuration and blurring of focal spots, accompanied by an increase in the error in reconstructing source parameters (5). Inequalities (11) are most critical with respect to neighboring modes that form the first focal spot. If the first (left) condition is not met, localization of bands of interfering (*m,n*) modes is not observed. A different pattern appears when the second (right) condition is not met, when the observation time is not enough for the source to cross the spatial scales of the interferogram variability. In this case, the position of the peak of the focal spot of such interfering modes is shifted to the time axis of the hologram, so that in relation to them the interferogram is formed as if by a stationary source. If the interferogram is distorted, the source parameters (5) are restored with respect to the undistorted configuration of the focal spots.

4. ANGULAR DISTRIBUTION OF THE SPECTRAL DENSITY OF THE HOLOGRAM

The angular distribution of the signal spectral density $F_s(\tau,\nu)$ on the hologram (detection function) is described by the expression

$$G_s(\chi) = \int_0^{\Delta\tau} \left|F_s(\tau, \chi\tau)\right| d\tau, \qquad (12)$$

where $\Delta\tau$ is the linear size of the concentration area along the time axis τ; χ – variable value of the angular coefficient when integrating along straight lines $\nu = \chi\tau$. When the source approaches the receiver, $0 \le \chi < \infty$, in the case of distance – $-\infty < \chi \le 0$. The maximum signal detection function is achieved at the value $\chi = \varepsilon$. For illustration in **Fig. 1** shows the experimental results of holographic processing of a pneumatic source signal when approaching a single vector-scalar receiver. Accumulation time Δt = 10 min. Input signal-to-noise ratio (*s*/*n*) q_0 = 25.5 (14.1 dB). In Fig. 1*b*, the dotted line and squares respectively show the straight line $\nu = \varepsilon\tau$, on which the peaks of the focal spots are located, and the straight lines $\nu_{1,2}$ (8), limiting the spectral

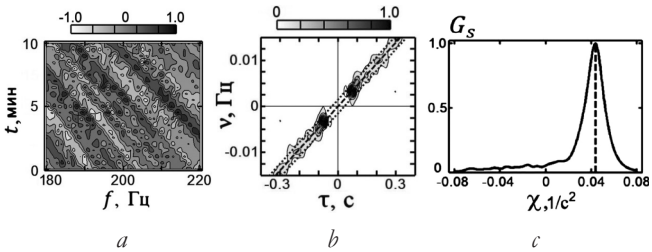

a *b* *c*

Fig. 1. *Normalized interferogram (a), hologram (b) and detection function (c)*[2].

density. In Fig. 1*c*, the vertical dotted line marks the value $\chi = \varepsilon$.

Bandwidth of the detection function, according to Fig. 1*c*, at the level of 0.1 and 0.5 from the maximum is $\Delta\chi_{0.1}$ = 0.048 s^{-2} and $\Delta\chi_{0.5}$ = 0.018 s^{-2}. The width of the band $\Delta\chi_{0.1}$ can be estimated from the condition as the difference in the angular coefficients of the straight lines $\nu = \chi\tau$ passing through the points (τ_1, $\varepsilon\tau_1 + \delta\nu$), ($\tau_1$, $\varepsilon\tau_1 - \delta\nu$), and the width of the band $\Delta\chi_{0.5}$ – through the points ($\tau_{(M-1)}$, $\varepsilon\tau_{(M-1)} + \delta\nu$), ($\tau_{(M-1)}$, $\varepsilon\tau_{(M-1)} - \delta\nu$). As a result we get

$$\Delta\chi_{0.1} = 2/\Delta t\tau_1,\ \Delta\chi_{0.5} = 2/\Delta t\tau_{(M-1)}. \qquad (13)$$

From Fig. 1*b* it follows that τ_1 = 0.066 s^{-2}, $\tau_{(M-1)}$ = 0.22 s^{-2}. According to (13), the bandwidth is $\Delta\chi_{0.1}$ = 0.050 s^{-2} and $\Delta\chi_{0.5}$ = 0.015 s^{-2}, which is close to the experimental values. The bandwidth $\Delta\chi$ of the detection function, according to (5) and (13), is determined by the accumulation time, distance, frequency scales of variability of the waveguide transfer function and does not depend on the width of the signal spectrum and the radial velocity of the source. It decreases with increasing observation time Δt, distance r_0 and decreasing average frequency of the spectrum f_0. The smaller the bandwidth, the more accurate and reliable the estimate of the slope ε.

5. HEURISTIC CRITERION FOR SOURCE DETECTION RANGE

As a heuristic criterion for the detection range of a noise source, the condition is accepted that the maximum of the detection function of the noise implementation of the signal against the background of interference

$$G(\chi,q_0)=\int_0^{\Delta\tau}\left|F(\tau,\chi\tau,q_0)\right|d\tau \qquad (14)$$

in the direction $\chi = \varepsilon$ the location of the peaks of the focal spots of the signal is two or more times higher than the interference level in the directions $\chi \neq \varepsilon$ at the input ratio s/n q_0

$$q = G(\varepsilon,q_0)/G(\chi,q_0). \qquad (15)$$

The position of the maximum peak is taken as the estimate of ε, $maxG(\chi) = G(\varepsilon)$. In this case, the reconstructed estimates of the source parameters (bearing, distance, radial velocity and depth) are close to real values [2,3]. If condition (15) is not met, then interference peaks appear in the detection function, which increase as the input s/n ratio q_0 decreases and mask the peak of the noise signal. The ambiguity in determining the angular coefficient ε corresponding to the noise signal increases, and the reliability of source detection decreases.

For given processing parameters (accumulation time Δt, frequency range Δf, duration of noise realizations T and the interval between them δT) and the input ratio s/p q_0, the maximum detection range rmax is realized when equality (15) is satisfied. As an example in **Fig. 2, 3** show the results of holographic processing obtained by numerical simulation in the transition region of maximum detection distances of a moving noise source against the background of interference. Processing parameters: Δf = 900-950 Hz, Δt = 30.60 s, T = 1.5 s, δT = 0.5 s, J = 15.30.

With the number of time intervals J = 15.30, according to criterion (15), the maximum detection ranges are estimated as r_{max} = 6 km (Fig. 2) and r_{max} = 9 km (Fig. 3), which correspond to the input ratios s/n q_0 = –8.99, –12.07 dB. Fig. 2*c* and 3*c* show that doubling the number of time samples entails a halving of the bandwidth $\Delta\chi_{0.5}$. With a further decrease in the input s/n ratio, the signal is masked by interference, and ambiguity arises in determining the position ε of the maxima of the detection functions (Fig. 2*i*, 3*i*). Detection of the source at distances r = 7, 10 km becomes impossible. Distances r = 7, 10 km correspond to input s/p ratios q_0 = –10.14, –12.84 dB. At the same time, from Fig. 2*b,e*, 3*b,e* it follows that the configuration of the first focal spots is distorted, since the time coordinate of the position of their peak is located on the time axis, i.e. for neighboring interfering modes, the right-hand condition (11) is violated.

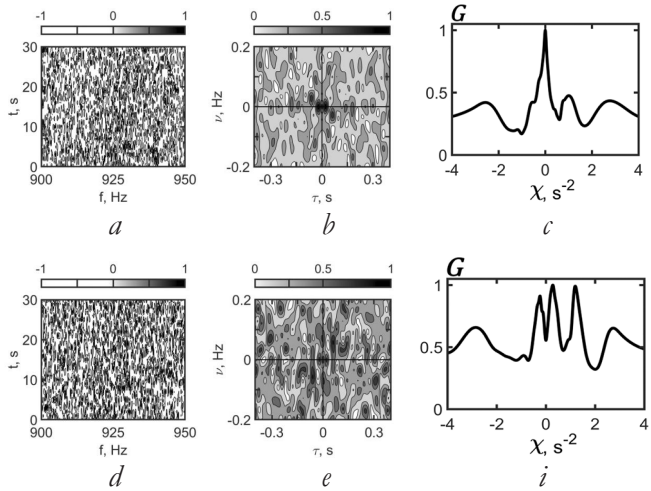

Fig. 2. *Normalized interferograms (a, d), holograms (b, d) and detection functions (b, i). Distances: (a – c) – r = 6 km, (d – i) – r = 7 km. Accumulation time Δt = 30 s, number of noise realizations J = 15* [6].

By the ratio s/p q at the output of holographic processing, taking into account criterion (15), we agree to understand the quantity

$$q = G(\varepsilon,q_0)/G(\chi,q_0). \qquad (16)$$

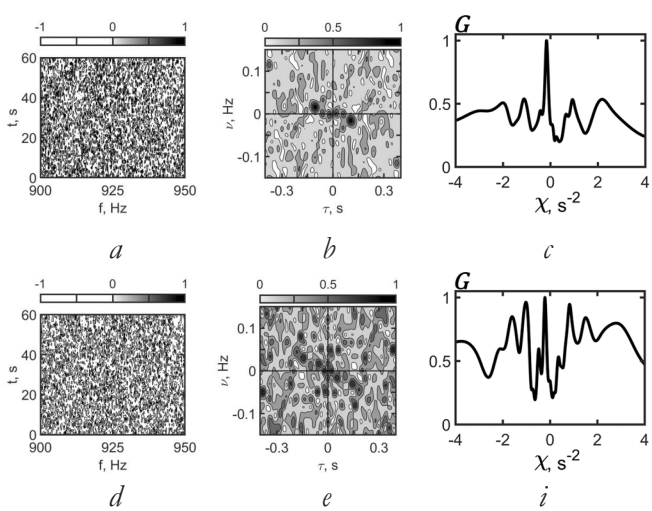

Fig. 3. *Normalized interferograms (a, d), holograms (b, d) and detection functions (c, i). Distances: (a – c) – r = 9 km, (d – i) – r = 10 km. Accumulation time Δt = 60 s, number of noise realizations J = 30* [6].

Then, assuming that the frequency shifts of the interference maxima of the wave field accumulate coherently, and the interference incoherently, expression (16) takes the form

$$q = Jq_0. \quad (17)$$

For a fixed value of temporary noise realizations J, the maximum detection range rmax of a noise source, according to (15), (16), is determined by the implicit expression

$$2 = Jq_0(r_{\max}), \quad (18)$$

where the value $q_0(r_{\max})$ is determined by the law of decay of the average noise emission power of the source with distance and interference level. Thus, for a fixed accumulation time Δt, the maximum detection range rlim is achieved with a minimum duration $T_{\min}$ of the noise signal, i.e. at maximum J value.

6. MAXIMUM DETECTION RANGE

We will estimate the minimum duration of the noise signal from the representation of the signal using frequency samples of the waveguide transfer function. In this case, it is sufficient to limit ourselves to considering the smallest frequency scale of field variability caused by interference between extreme modes.

In accordance with (10), the smallest frequency scale in the vicinity of the frequency f_0 at a distance r between the source and receiver

$$\min\Lambda_f = \frac{2\pi}{r\left|dh_{1M}(f_0)/df\right|}. \quad (19)$$

The period of signal variability is determined by independent values of the transfer function at five points. The frequency interval δf between two samples should not exceed the value $1/T$, $\delta f \le 1/T$, where T is the duration of the noise signal, therefore value (19) is also equal to

$$\min\Lambda_f = 5\delta f = 5/T. \quad (20)$$

From (19), (20) it follows that the duration of the noise implementation must satisfy the inequality

$$T \ge T_{\min} = \frac{5}{2\pi} r\left|dh_{1M}(f_0)/df\right|, \quad (21)$$

so that with increasing distance r and decreasing average frequency f_0 of the spectrum, the minimum time for recording a noise signal increases.

As a result, the admissible number of independent time noise realizations (1) is estimated from above as

$$J \le J_{\max} = \frac{\Delta t}{(5/2\pi) r\left|dh_{1M}(f_0)/df\right| + (1/\Delta f)}. \quad (22)$$

By choosing the spectrum width Δf it is almost always possible to ensure that the condition is satisfied

$$J_{\max} \approx \frac{2\pi}{5}\frac{\Delta t}{r\left|dh_{1M}(f_0)/df\right|}. \quad (23)$$

If the registration duration T is less than $T_{\min}$ (21), this leads to distortions in the reconstruction of the signal spectrum, which entails an increase in the error in determining the position of the focal spot maxima and, as a consequence, an increase in the error in estimating the distance and radial velocity of the source. For the input ratio s/n q_0 ($r_{\lim}$) for the maximum detection range of a noise source, according to (18) and (23), we obtain an implicit estimate.

$$r_{\lim} = \frac{2\pi}{10}\frac{\Delta t}{\left|dh_{1M}(f_0)/df\right|} q_0(r_{\lim}), \quad (24)$$

A characteristic feature of relation (24) for the maximum range rlim of a noise source is the fact that it includes parameters of the waveguide transfer function, the physical content of which varies depending on the water area. Recall that expression (24) relates the maximum detection range to the input ratio of a single receiver.

Let us generalize estimate (24) to linear antennas. Let us assume that the interference at the input of the antenna elements is not correlated. To satisfy this condition, it is sufficient to require the inequality $d \ge \lambda/2$, where d and λ are the interelement distance and wavelength. Then expression (24) takes the form

$$r_{\lim(an)} = \frac{2\pi}{10}\frac{\eta}{b}\frac{\Delta t}{\left|dh_{1M}(f_0)/df\right|} q_{0(an)}(r_{\lim}), \quad (25)$$

where η and b are the gain and the number of antenna elements, $q_{0(an)}$ is the s/n ratio at the input of a single antenna element [7]. In the case of a horizontal linear antenna, the maximum noise immunity of holographic processing is achieved at a bearing equal to the compensation angle, with $\eta = b^2$. For a vertical antenna $\eta \approx b^2$. If we set $b = 1$, then formula (25) becomes the corresponding formula for a single receiver.

An algorithm for implementing holographic processing parameters at the maximum detection range using the example of a single receiver is presented below.

1. An a priori model of the waveguide is introduced. The maximum detection range rlim is set and the processing parameters are selected: accumulation time Δt, bandwidth Δf and average spectrum frequency f_0. The level of interference is fixed. The dependence of the power of the noise source on the distance r is modeled.

2. Based on the dependence (r) for the maximum detection range r_{lim}, the input ratio s/n is calculated.

3. From expression (24) the value $|(dh_1M(f_0))/df|$ is found, which determines the minimum duration of the noise implementation $T_{\min}$.

4. According to (21), assuming $r = r_{\text{lim}}$, the minimum duration $T_{\min}$ of the noise signal is determined.

The described algorithm does not require prior knowledge of the number of energy-carrying modes that form the field at the maximum distance. Therefore, it is applicable to both model and real waveguides. Let us consider the fruitfulness of the algorithm using the example of a numerical experiment [6]. Initial data: $\Delta f = 50$ Hz, $f_0 = 925$ Hz, $\Delta t = 30$ s, $= -61.01$ dB, $r_{\text{lim}} = 15$ km. Dependence (r) is shown in Fig. 2 [6], from which it follows that $q_0(r_{\text{lim}}) = 2.87 \cdot 10^{-2}$ (–15.42) dB. According to (24) we have $|(dh_1M(f_0))/df| = 3.61 \cdot 10^{-5}$ s/m. Using (21), we obtain the estimate $T_{\min} = 4.31 \cdot 10^{-1}$ s. Note that expression (23) is justified, since the inequality $T_{\min} \gg (1/\Delta f)$ is satisfied.

7. CONCLUSION

The fruitfulness of the holographic method for detecting and localizing underwater noise sources stems from the extreme ease with which the two-dimensional Fourier transform performs the rather complex and intricate linear transformation required to image the source. This simplicity is determined mainly by the fact that the interferogram of a noise signal against the background of interference is represented as a linear combination of interferograms of the signal and interference, on the one hand, and the preservation of amplitude and phase information, on the other.

In this case, a very important role is played by the detection function, which determines the time-frequency focusing of the noise signal, which makes it possible to explicitly determine the maximum detection range of the source depending on the processing parameters and the input signal-to-noise ratio. The expression for the maximum detection range is obtained in relation to a single receiver and linear antennas. The algorithm for determining the maximum detection range was tested in a numerical experiment using a single receiver as an example.

REFERENCES

1. Chuprov SD. Interference structure of sound in a layered ocean. In: *Ocean acoustics. Current state*. Moscow, Nauka Publ., 1982, pp. 71-91.
2. Kuznetsov GN, Kuz'kin VM, Pereselkov SA. Spectrogram and localization of a sound source in shallow water. *Acoust. Phys.*, 2017, 63(4):449-461.
3. Kaznacheev IV, Kuznetsov GN, Kuz'kin VM, Pereselkov SA. An interferometric method for detecting a moving sound source with a vector-scalar receiver. *Acoust. Phys.*, 2018, 64(1):37-48.
4. Pereselkov SA, Kuzkin VM. *Holographic Processing of Broadband Hydroacoustic Signals.*

Voronezh, Publishing House of VSU, 2023, 183 p.

5. Brekhovskikh LM, Lysanov YuP. *Fundamentals of ocean acoustics*. Berlin, New York, Springer Verlag, 1982, 250 p.
6. Kuz'kin VM, Pereselkov SA, Tkachenko SA, Matvienko YuV, Khvorostov YuA. Range of detection of underwater sound source. *Phys. Wave Phenom.*, 2023, 31(5):339-345.
7. Kuz'kin VM., Pereselkov SA, Tkachenko SA, Kaznacheev IV. Interferometric processing of acoustic information by using extended antennas in dispersing media. *RENSIT: Radioelectronics. Nanosystems. Information Technologies*, 2020, 12(4):483-494. DOI: 10.17725/rensit.2020.12.483.

DOI: 10.17725/j.rensit.2024.16.137

The grid-characteristic method on chimeric meshes application to study the keel morphometric characteristics of ice ridges

Evgeniy A. Pesnya, Maxim V. Muratov, Alena V. Favorskaya, Anton A. Kozhemyachenko

Moscow Institute of Physics and Technology, https://mipt.ru/

Dolgoprudny 141700, Moscow region, Russian Federation

E-mail: pesnya.ea@phystech.edu, max.muratov@gmail.com, aleanera@yandex.ru, kozhemyachenko@yandex.ru

Received November 24, 2023, peer-reviewed November 30, 2023, accepted December 07, 2023, published March 15, 2024.

Abstract: **Designing engineering structures in the Arctic zone requires to consider the loads transmitted to the structure construction in connection with collisions with various ice formations: icebergs, ice ridges, stamukhs. The paper considers the use of the grid-characteristic method for modeling the passage of elastic waves in a cross-section of the ice ridge together with its porosity in the consolidated layer and in the lower part of the keel. We propose to use chimeric (overlapped) computational meshes for the describing curvilinear shape of pores filled with air or water. As a result of computer simulation, the direct problem of ultrasound investigation of the ice ridge has solved, velocity vector fields have obtained at various moments in time, including a system of reflections from pores.**

Keywords: **computer simulation, grid-characteristic method, ice ridges morphometry, ultrasound investigation**

UDC 519.63

Acknowledgments: This work was carried out with the financial support of the Russian Science Foundation, project no. 21-71-10015.

For citation: Engeniy A. Pesnya, Maxim V. Muratov, Alena V. Favorskaya, Anton A. Kozhemyachenko. The grid-characteristic method on chimeric meshes application to study the keel morphometric characteristics of ice ridges. *RENSIT: Radioelectronics. Nanosystems. Information Technologies,* 2024, 16(2):137-142e. DOI: 10.17725/j.rensit.2024.16.137.

Contents

1. INTRODUCTION

The safety of the operation of oil-producing facilities and shipping in the Arctic regions is affected by loads when interacting with hummocks. To obtain design estimates of ice loads on engineering structures, it is necessary to conduct a morphometric analysis of the characteristics of such ice formations. Ice ridges formed as a result of compression of the ice sheet are called a hummock, while the surface part of the hummock is called a sail, and the underwater part is called a keel. For example, [1-2] provide information on the morphometry and internal structure of the hummock of the first year of formation using electrothermal drilling in the Barneo ice camp. At the same time, it is customary to use sonar approaches to study the lower part of the hummocks [3]. A large set of statistical data on ice sediment and keel depth collected by upward-pointing sonars is given in [4] for five locations in the Barents Sea. Another morphometric analysis of the keel of hummocks of the first year of formation using sonar has performed in [5], where it has assumed that the best generalization of

the shape of the ridges of the first year is the trapezoidal shape of the keel. In [6] the keels of hummocks have been monitored using sonar located on the bridge in the Northumberland Strait. The shape of the keels has been classified as one of four shapes: triangular, trapezoidal, w-shaped and keels with multiple peaks. The observed distributions of keel depth values have been compared with the calculated ones. In [7] the ice sheet and the ice ridge are modeled as thin elastic plates to consider the interaction of waves with the round body trapped by a thin layer of sea ice, an analytical analysis of the impact of waves on a circular ice ridge embedded in the ice sheet is conducted. In [8-9] the probabilistic method based on the search for the relationship between the levels of ice precipitation, the sediment of the keel of the hummock and the frequency of ridge formation is proposed to assess the loads transmitted to offshore structures. The analysis of seasonal data obtained with the help of sonar in the Beaufort Sea on the levels of ice precipitation, the keel of the ice ridge, the frequency of ridge formation allowed us to obtain probabilistic analytical approaches for modeling the age of the ridge, determining the formula for the growth of the consolidated layer and studying its thickness. Based on a field experiment on strengthening the artificial ice ridge in [10] analytical and two-dimensional discrete numerical modeling approaches have been obtained to predict the thickness of the consolidated layer in the probabilistic analysis of the impact of ice on structures that require information about meteorological conditions and general physical and mechanical properties of ice as input data. At the same time, numerical modeling of the ice level and ridge consolidation has been performed using the finite element method, and the position of the ice-water boundary has been determined from the Stefan energy balance condition.

In [11] to study the structure of ice ridges of various configurations, the grid-characteristic method is used on structured regular computational meshes and the comparative analysis of the seismograms obtained using full-wave modeling is conducted. To solve the equations of mathematical physics, chimeric or overlapping computational meshes have recently been used, which are previously used to solve hydrodynamic problems [12-13]. The grid-characteristic method using chimeric meshes makes it possible to describe the boundaries of a complex shape [14-15], including contact [16] or non-aligned with coordinate axes [17-19]. In this paper to describe curved cavities filled with air or water, the grid-characteristic method is used with chimeric regular computational meshes.

2. MODELS AND METHODS

For numerical simulation of the problem of wave signal propagation in the hummock systems of equations for an isotropic linear elastic medium and for an acoustic medium are jointly considered, which in general can be reduced to the following system of equations:

$$\frac{\partial \mathbf{u}}{\partial t} + \mathbf{A}_1 \frac{\partial \mathbf{u}}{\partial x} + \mathbf{A}_2 \frac{\partial \mathbf{u}}{\partial y} = 0, \quad (1)$$

where in (1) $\mathbf{u}$ – vector of the unknown functions.

In the case of the linear elastic medium, the vector of the unknown functions are considered $\mathbf{u} = (v_x, v_y, \sigma_{xx}, \sigma_{yy}, \sigma_{xy})^T$, that is the components of the perturbation propagation velocity $\mathbf{v}$ and the components of the symmetric Cauchy stress tensor $\boldsymbol{\sigma}$. Matrices $\mathbf{A}_1$, $\mathbf{A}_2$ have the set of eigenvalues $\{c_P, -c_P, c_s, -c_s, 0\}$, where c_p – the velocity of propagation of longitudinal waves, c_s – the velocity of propagation of transverse waves.

In the case of the acoustic medium the unknown functions are $\mathbf{u} = (v_x, v_y, p)^T$, that is the components of the perturbation propagation velocity $\mathbf{v}$ and pressure p. Matrices have the set of eigenvalues $\{c_P, -c_P, 0\}$.

Thus, the systems of equations (1), describing a linearly elastic body and an acoustic medium are hyperbolic, which means that in both cases the matrices $\mathbf{A}_1$, $\mathbf{A}_2$ can be represented as

$$\mathbf{A} = \mathbf{\Omega}\mathbf{\Lambda}\mathbf{\Omega}^{-1},$$

where the matrix $\mathbf{\Omega}$ consists of columns that are the right eigenvectors of the original matrix, which, in turn, correspond to the eigenvalues, which are elements of the diagonal matrix $\mathbf{\Lambda}$. Splitting the system (1) in spatial directions, we proceed to the Riemann invariants $\boldsymbol{\omega}\mathbf{\Omega}^{-1}\mathbf{u}$, which are transferred according to the characteristics of the hyperbolic system, we obtain the hyperbolic system from linear transfer equations with constant coefficients in Riemann invariants

$$\frac{\partial \boldsymbol{\omega}}{\partial t} + \mathbf{\Lambda}\frac{\partial \boldsymbol{\omega}}{\partial x} = 0. \qquad (2)$$

The system in Riemann invariants (2) on the upper layer in time can be numerically integrated using finite-difference schemes, for example, using the Rusanov scheme of the third order in time and space [16], used in calculations in this paper. To move to the components $\mathbf{v}$ and $\boldsymbol{\sigma}$ or $\mathbf{v}$ and p respectively on the upper layer in time after calculating the Riemann invariants, the inverse transformation is used $\mathbf{u} = \mathbf{\Omega}\boldsymbol{\omega}$.

The basic model of the ice ridge is shown in **Fig. 1**, where the red cross section schematically shows the calculated area when considering the lower part of the keel of the hummock. **Fig. 2***a* and Fig. 2*b* show the calculated areas of 16 by 16 meters, in which seismic responses from cavities and pores filled with air or water are studied for the case of specifying the source in the consolidated layer of the hummock and in the seawater, when considering the lower part of the keel, respectively. The characteristics of the media are given in **Table 1**. It is worth noting that by changing the corresponding parameters of the medium (velocity, density), ice formations with different salinity and temperature conditions can be considered.

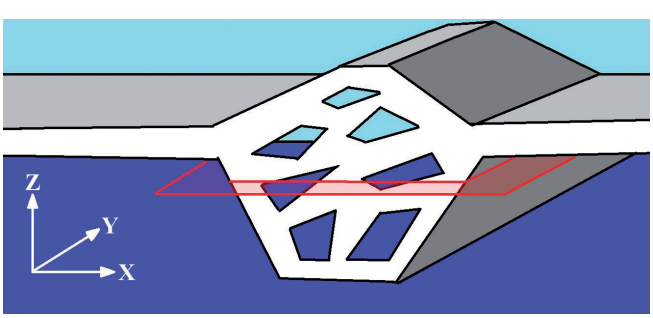

Fig. 1. *The basic model of the ice ridge (hummock).*

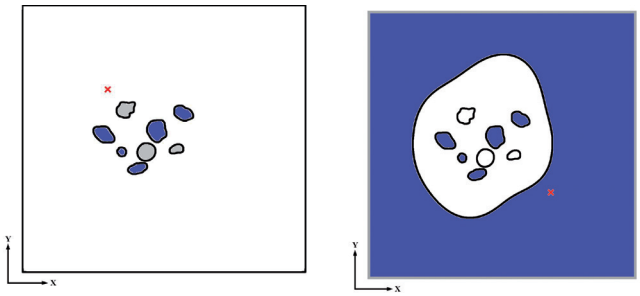

a *b*

Fig. 2. *The cross section of the ice ridge with cavities filled with air (gray areas) or water (blue areas): a – in the consolidated layer, b – in the lower part of the keel.*

Table 1

Parameters of simulated media

medium	Velocity P-wave, m/s	Velocity S-wave, m/s	Density, kg/m^3
Ice	3940	2493	917
Water	1500	–	1000

At the boundaries of the ice-air interface the conditions of the free border were set

$$\boldsymbol{\sigma}\cdot\mathbf{n} = 0,$$

where $\mathbf{n}$ – normal to the corresponding boundary.

At the interface of the ice-water media (1 and 2 media respectively) the following contact condition was set:

$$\mathbf{v}_1\cdot\mathbf{n} = \mathbf{v}_2\cdot\mathbf{n},$$
$$\boldsymbol{\sigma}_1\cdot\mathbf{n} + p\cdot\mathbf{n} = 0,$$

here $\mathbf{n}$ – normal to the boundary of the contacting medium 1.

Non-reflecting boundary conditions are used at the boundaries of the computational domain in Fig. 2. The Riker impulse with the frequency of 25 kHz was used as the initial perturbation, the source location is marked in Fig. 2 with a red cross.

In the calculation the integration areas in Fig. 2 were covered with background rectangular computational grids and curved chimeric meshes with the characteristic spatial step of 10^{-2} m, the integration step in time was $2.54\cdot10^{-7}$ s. The

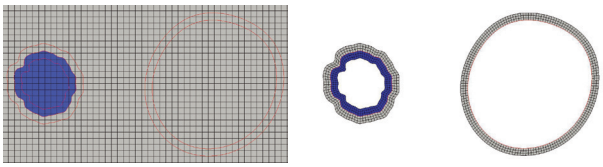

a *b*

Fig. 3. *The example of the configuration of computational meshes: a – background mesh, b – chimeric meshes.*

example of the location of the background and overlapped meshes for cavities filled with air and water is shown in **Fig. 3.** The nodes of the background mesh contain information about the parameters of the medium, so in Fig. 3*a* ice is highlighted in gray, water is highlighted in blue. At the same time, to describe the cavities in the boundary region, the calculation was performed using overlapped meshes according to Fig. 3*b*, which, considering the boundary conditions and the mutual interpolation algorithm [18], allows correctly calculate the wave signal propagation through water pores and does not consider the areas filled with air in the calculation.

3. RESULTS AND DISCUSSION

Fig. 4 and **Fig. 5** show the results of full-wave modeling of the propagation of perturbation and wave responses from the cavities under

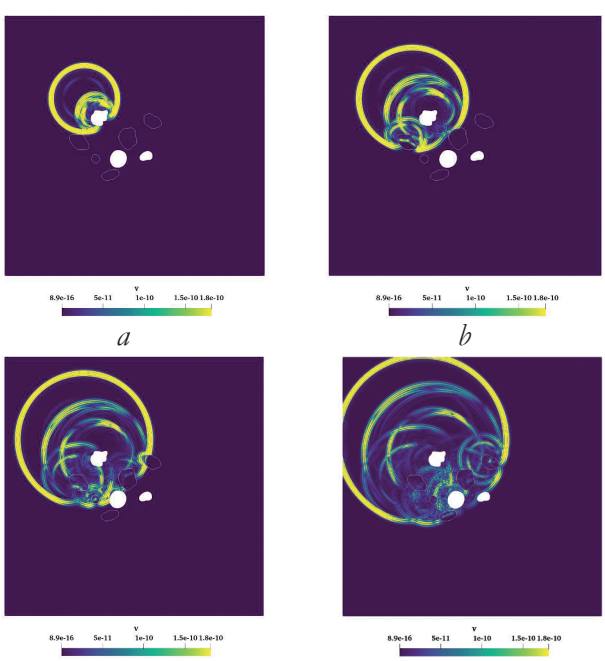

a *b* *c* *d*

Fig. 4. *Propagation of wave responses from the system of cavities in a slice located in the consolidated layer: a – 0.014 s, b – 0.021 s, c – 0.027 s, d – 0.034 s.*

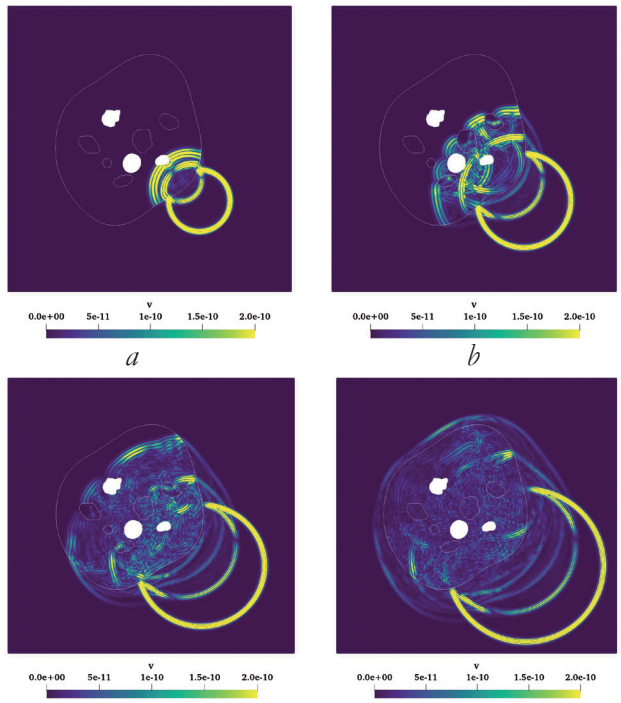

a *b* *c* *d*

Fig. 5. *Propagation of wave responses from a system of cavities in the slice located in the lower part of the keel: a – 0.030 s, b – 0.045 s, c – 0.060 s, d –0.075 s.*

consideration at various points in time when considering the computational domain in the consolidated layer of the hummock and the lower part of its keel, respectively.

In Fig. 4*a* the first response is formed from a cavity filled with air, in Fig. 4*b* the initial impulse is reflected from the pore filled with water, while part of the wavefront passes through the pore. Fig. 4*c* and Fig. 4*d* show the complex system of reflections from all remaining pores and cavities.

In Fig. 5*a* the first reflections occur from the keel of the hummock itself and the first cavity in the future, new reflected signals from other cavities are formed, incoming from the ice surface of the keel into the water in Fig. 5*b* and Fig. 5*c*, and in Fig. 5*d* the original signal completely passes the thickness of the keel.

4. CONCLUSION

Using the grid-characteristic method on structured rectangular and chimeric regular computational meshes, the direct problem of the passage of the ultrasonic signal along

the hummock is solved and the results of full-wave modeling of the velocity vector at various points in time are obtained. The proposed approach allows consider the complex geometry and structure, porosity of the ice ridge. The obtained algorithms and models can be used to obtain and analyse synthetic seismograms, which can be used to determine a number of morphometric parameters of the hummock, when solving the inverse problem.

REFERENCES

1. Kharitonov VV. Morphometry and unusual internal structure of ice ridge investigated at Barneo ice camp in April 2013. Polar Science, 2022, 31:100736.
2. Kharitonov VV, Borodkin VA. On the results of studying ice ridges in the Shoka-l'skogo Strait, part I: Morphology and physical parameters in-situ. Cold Regions Science and Technology, 2020, 174:103041.
3. Mironov YU, Guzenko RB, Porubaev VS, Kharitonov VV, Khotchenkov SV and Nesterov AV. Morphometric Parameters of Stamukhas in the Laptev Sea. International Journal of Offshore and Polar Engineering, 2019, 29(4):383-390.
4. Hansen E, Ervik Å, Eik K, Olsson A, Teigen SH. Long-term observations (2014–2020) of level ice draft, keel depth and ridge frequency in the Barents Sea. Cold Regions Science and Technology, 2023, 216:103988.
5. Ekeberg O, Høyland K, Hansen E. Ice ridge keel geometry and shape derived from one year of upward looking sonar data in the Fram Strait. Cold Regions Science and Technology, 2015, 109:78-86.
6. Obert KM, Brown TG. Ice ridge keel characteristics and distribution in the Northumberland Strait. Cold Regions Science and Technology, 2011, 66(2-3):53-64.
7. Mandal S, Law AW, Shen HH. Wave interactions with circular ice ridge embedded in level ice. Cold Regions Science and Technology, 2018, 155:90-99.
8. Samardžija I, Høyland K, Leira BJ, Naess A. Consolidated layer thickness in probabilistic simulation of first-year ice ridges. Cold Regions Science and Technology, 2023, 216:104021.
9. Samardžija I, Høyland K. Analysis of the relationship between level ice draft, ridge frequency and ridge keel draft for use in the probabilistic assessment of ice ridge loads on offshore structures. Ocean Engineering, 2023, 270:113593.
10. Salganik E, Høyland K, Shestov A. Medium-scale experiment in consolidation of an artificial sea ice ridge in Van Mijenfjorden, Svalbard. Cold Regions Science and Technology, 2021, 181:103194.
11. Favorskaya AV, Muratov MV. Ultrasonic Study of Sea Ice Ridges. In: Czarnowski, I., Howlett, R.J., Jain, L.C. (eds) Intelligent Decision Technologies. Smart Innovation, Systems and Technologies, 2022, 309, Springer, Singapore.
12. Henshaw WD, Schwendeman DW. Parallel computation of three-dimensional flows using overlapping grids with adaptive mesh refinement. Journal of Computational Physics, 2008, 227(16):7469-7502.
13. Chang XH, Ma R, Wang NH, Zhao Z, Zhang LP. A Parallel Implicit Hole-cutting Method Based on Background Mesh for Unstructured Chimera Grid. Computers & Fluids, 2020, 198:104403.
14. Favorskaya AV, Khokhlov NI, Petrov IB. Grid-Characteristic Method on Joint Structured Regular and Curved Grids for Modeling Coupled Elastic and Acoustic Wave Phenomena in Objects of Complex Shape. Lobachevskii Journal of Mathematics, 2020. 41(4):512-525.
15. Kozhemyachenko A, Favorskaya A, Pesnya E, Stetsyuk V. Modification of the Grid-Characteristic Method on Chimera

Meshes for 3D Problems of Railway Non-Destructive Testing. Lobachevskii Journal of Mathematics, 2023. 44(1):376-386.

16. Favorskaya A, Khokhlov N. Accounting for curved boundaries in rocks by using curvilinear and Chimera grids. Procedia Computer Science, 2021, 192:3787-3794.
17. Khokhlov N, Favorskaya A, Stetsyuk V, Mitskovets I. Grid-characteristic method using Chimera meshes for simulation of elastic waves scattering on geological fractured zones. Journal of Computational Physics, 2021, 446(1):110637.
18. Ivan A. Mitskovets. Application of Chimeric Meshes for Explicit Accounting for Inhomogeneities in Modeling the Propagation of Elastic Waves. *RENSIT: Radioelectronics. Nanosystems. Information Technologies,* 2023, 15(2): 185-192e. DOI: 10.17725/rensit.2023.15.185.
19. Favorskaya AV, Khokhlov N. Using Chimera Grids to Describe Boundaries of Complex Shape. In: Czarnowski, I., Howlett, R.J., Jain, L.C. (eds) Intelligent Decision Technologies. Smart Innovation, Systems and Technologies, 2022, 309. Springer, Singapore.

DOI: 10.17725/j.rensit.2024.16.143

Application of the 5G NR Physical Layer in Space Communications, Performance Evaluation

Evgeniy V. Rogozhnikov, Edgar M. Dmitriev, Danila A. Kondrashov, Yakov V. Krukov, Artem V. Konovalchikov, Semyon M. Mukhamadiev

Tomsk State University of Control Systems and Radio Electronics, http://tusur.ru/

Tomsk 634050, Russian Federation

E-mail: evgenii.v.rogozhnikov@tusur.ru, edegor1993@mail.ru, danila.a.kondrashov@tusur.ru, iakov.v.kriukov@tusur.ru, artem.konovalchikov@tusur.ru, sema.fandmc3@mail.ru

Received September 02, 2023, peer-reviewed September 09, 2023, accepted September 16, 2023, published March 15, 2024.

Abstract: **The propagation channel is significantly modified in the case of 5th Generation New Radio radio access technology (5G NR) in space communication systems. In particular, large delays occur with respect to the terrestrial propagation channel, and signal attenuation increases, resulting in a lower signal-to-noise ratio (SNR). The Doppler shift of the carrier frequency is also significantly increased due to the high velocity of the spacecraft (SC) relative to the user equipment (UE). The aim of the work is to investigate the decoding capability of the physical channels and signals of the 5G NR system in case of its application in satellite communication systems (SCS), as well as to calculate the performance of such a system to assess the applicability of 5G NR in SCS. The ability to correctly decode signals and channels depending on SNR is evaluated using mathematical modelling of 5G NR signal and channel shaping in conjunction with the Quasi Deterministic Radio Channel Generator (QuaDRiGa) model. The research within the paper draws conclusions on the applicability of 5G NR radio access technology in a space communications environment.**

Keywords: **5G NR, satellite communication systems, performance evaluation, radio access technology, QuaDRiGa, decoding of 5G NR signals and channels**

УДК 621.396.41

For citation: Evgeniy V. Rogozhnikov, Edgar M. Dmitriev, Danila A. Kondrashov, Yakov V. Kryukov, Artem V. Konovalchikov, Semyon M. Mukhamadiev. Application of the 5G NR Physical Layer in Space Communications, Performance Evaluation. *RENSIT: Radioelectronics. Nanosystems. Information Technologies,* 2024, 16(1):143-156e. DOI: 10.17725/j.rensit.2024.16.143.

Contents

1. INTRODUCTION

The integration of satellite communications and wireless terrestrial networks is actively discussed in the context of systems using 5G NR. In fact, the benefits of including spacecraft in 5G networks is to provide ubiquitous coverage. Compatibility between different radio access interfaces has been studied in 3GPP since the release of 3GPP TS 38.300 version 16.

A number of considered works (Cassiau N., 2018; Völk F., 2021; Saarnisaari H., 2021; Dahlman E., 2020; Saarnisaari, 2020) are devoted to reviewing the latest developments in the field of random access methods and the physical layer to support satellite communications in 5G networks, as well as testing some solutions.

The main problems for 5 GR in the space communication channel are a large signal propagation delay, greater signal attenuation and Doppler shift in satellite channels relative to ground channels. The distance between the subscriber device and the base station located on the spacecraft in the SCS can range from 500 km for satellites in Low Earth Orbit (LEO) to 36000 km in Geostationary Earth Orbit (GEO) [6 (Saarnisaari H., 2019)]. These values exceed the maximum distance in 5G NR of 300 km. This leads to the fact that the round-trip time (RTT), i.e. the signal propagation time from the UE to the SC and back, ranges from 4 ms for LEO satellites and up to several hundred ms for GEO satellites [7 (Saarnisaari H., 2019)]. The satellites move at a speed of 7200 km/s, which leads to a carrier frequency shift of more than 720 kHz at a frequency of 30 GHz [8 (2017)]. In this regard, 3GPP presented the concept of non-terrestrial networks (NTN), in which it is planned to use air or spacecraft for data transmission.

Also, 3GPP has investigated implementation features and possible network architecture options [8 (2017)]. Until now, terrestrial and satellite systems have been developed independently of each other, and their interaction has only been possible through gateway solutions. For example, satellite systems are already supported in 4G systems, but with limited compatibility. However, as of 2018, the integration of these systems has begun and must be done at all levels. Currently, the key technologies introduced in 5G NR are still in the process of being integrated. One of the integration goals is to enable 5G NR to be used in satellite systems. This article considers the following channels and signals in the 5G NR downlink: Physical Downlink Shared Channel (PDSCH) is designed to transfer user data from the gNB to the UE; Physical Downlink Control Channel (PDCCH) is designed to transmit control and service information, including DCI; Synchronisation Signal Block (SSB) includes Primary Synchronization Signal (PSS), Secondary Synchronization Signal (SSS) and Physical Broadcast Channel (PBCH); Channel Status Information Reference Signals (CSI-RS). This article considers the following channels and signals in the downlink: Physical Uplink Shared Channel (PUSCH), Physical Uplink Control Channel (PUCCH) and Physical Random-Access Channel (PRACH). Evaluation of system throughput and spectral efficiency is necessary to determine the capabilities of 5G NR in a satellite transmission channel.

2. MATHEMATICAL MODELING

To assess the applicability of 5G NR, it is necessary to implement downlink and uplink simulation models for satellite networks using the 5G NR physical layer protocol. The satellite link must be implemented using the QuaDRiGa model, which considers: signal propagation delay, attenuation, Doppler frequency shift, multipath signal propagation. models for the formation and processing of the above-described 5G NR channels and signals.

Evaluation of the performance of the radio interface for downlink and uplink data transmission lines should consider different values of the radio interface parameters: channel bandwidth, signal carrier frequency, numerology, transmission power, signal-code design index (QAM modulation index and error-correcting coding speed), etc.

As a result of simulation modeling, the noise immunity characteristics of signals generated according to the 5G NR radio communication standard in terms of the physical layer and used in satellite networks of broadband multi-user access Ku and Ka bands should be obtained. The developed model should be divided into 3 functional parts: the data transmission model in the downlink, the data transmission model in the uplink and the satellite link model. For all models, the overall execution structure must follow the sequence of the following steps:

1. Entering input parameters by the user;
2. Signal shaping and distribution in the frequency-time resource (FVR);
3. Calculation of the parameters of the satellite communication line according to the trajectory of the satellite in orbit in the QuaDRiGa model;
4. Performing a given number of iterations;
   4.1. Modeling the passage of a signal through a channel:
   4.1.1. Formation of a vector with noise;
   4.1.2. Convolution of the transmitted signal with the impulse response (IR) of the channel;
   4.1.3. Doppler shift of the frequency of the transmitted signal;

4.1.4. AWGN overlay on the signal in the transmission channel;
4.2. Calculation of SNR at the input of the receiver;
4.3. Reception and decoding of the signal. Estimation of the required parameters;
4.4. Calculation of BLER;
4.5. Return to point 4.

2.1. Mathematical models of physical channels and signals

Fig. 1 shows the structure diagram of the function block of the synchronisation signal transmission simulation model. The task of the model is to estimate the probability of correct decoding of the physical identifier of the cell (Cell ID), which is contained in PSS and SSS, as well as the estimation of Block Error Rate (BLER) in the PBCH channel. Formation and processing of signals is carried out with the help of scripts from MATLAB library, the internal parameters of which are pre-set for the used system configuration.

The model provides for time and frequency synchronization by PSS and SSS, along with an estimate of the synchronization error. **Tables 1** and **2** show the input and output parameters of the SSB transmission and processing model.

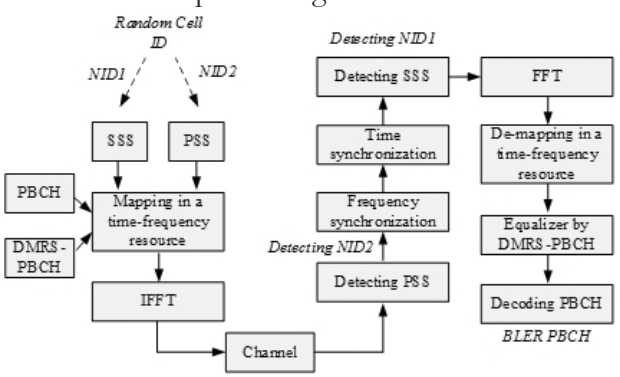

Fig. 1. *Structure diagram of the SSB transmission and processing model.*

Table 1

Input parameters of SSB transmission and processing model

Input parameters	Description
F_c	Carrier frequency, Hz
H	Orbital altitude, km
G	Gain of the receiving antenna, dB
T_{sat}	Index of a point on the satellite trajectory
ItN	Number of simulation iterations
SSC	Distance between subcarriers, Hz
T_n	Noise temperature, K

Table 2

Output parameters of SSB transmission and processing model

Output parameters	Description
freqOffset	Frequency offset estimation, Hz
FreqEstimateError	Error of frequency offset estimation, Hz
pbchErrorProb	Probability of PBCH decoding error
CellIDDecodeProb	Probability of correct detection of PSS and SSS
SNR	Signal-to-noise ratio, dB

Fig. 2 shows the structure diagram of the functional block of the CSI-RS transmission and processing simulation model. The task of the model is to estimate the probability of correct detection of the NID identifier, which is transmitted to CSI-RS. Formation and processing of signals is carried out with the help of scripts from MATLAB library, the internal parameters of which are pre-set for the used system configuration.

Tables 3 and **4** show the input and output parameters of the CSI-RS transmission and processing model.

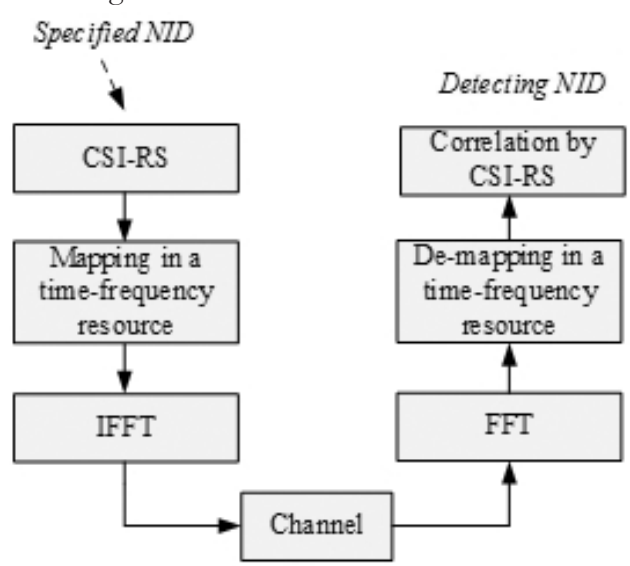

Fig. 2. *Structure diagram of the SSB transmission and processing model.*

Table 3

Input parameters of CSI-RS transmission and processing model

Input parameters	Description
F_c	Carrier frequency, Hz
H	Orbital altitude, km
G	Gain of the receiving antenna, dB
T_{sat}	Index of a point on the satellite trajectory
ItN	Number of simulation iterations
N_{rb}	Number of resource blocks
T_n	Noise temperature, K

Table 4

Output parameters of CSI-RS transmission and processing model

Output parameters	Description
DetectProbt	Probability of correct detection of CSI-RS parameters
SNR	Signal-to-noise ratio, dB

In 5G NR, the PDCCH carries the downlink control information. DCI messages are transmitted on the PDCCH channel for each subscriber device. The user receives the information needed to decode the broadcast channel and mapping useful information into the PUSCH. PDCCH has two key features when forming: 1) a resource range is used for transmitting DCI (CORESET control resource set); 2) blind decoding of PDCCH on the subscriber side. The subscriber should detect the DCI by tracking the CORESET at the designated time for monitoring (Monitoring Occasion). This process is realised by performing blind decoding. **Fig. 3** shows the structural diagram of the PDCCH transmission and processing model. **Tables 5** and **6** show the input and output parameters of the PDCCH transmission and processing model.

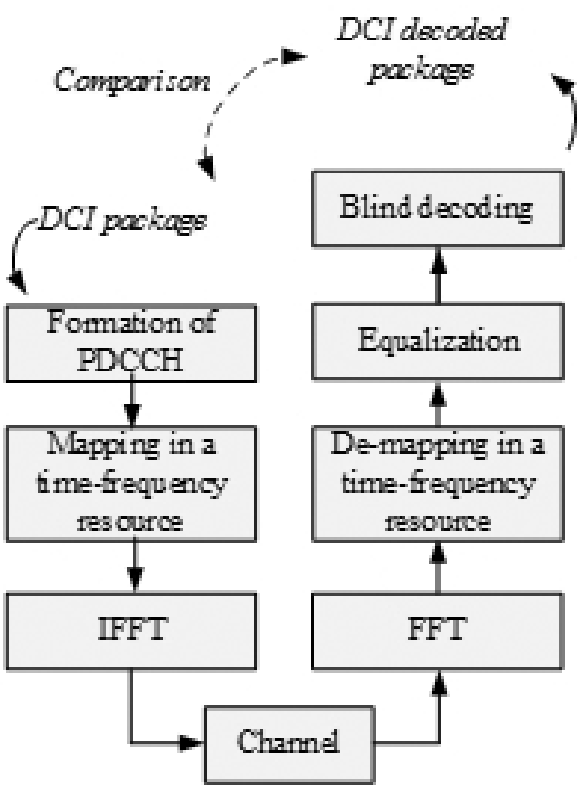

Fig. 3. *Structural diagram of PDCCH transmission and processing.*

Table 5

Input parameters of PDCCH transmission and processing model

Input parameters	Description
F_c	Carrier frequency, Hz
H	Orbital altitude, km
G	Gain of the receiving antenna, dB
T_{sat}	Index of a point on the satellite trajectory
ItN	Number of simulation iterations
N_{rb}	Number of resource blocks
T_n	Noise temperature, K
CodeRate	Speed of noise-resistant coding
dModulation	Type of modulation

Table 6

Output parameters of PDCCH transmission and processing model

Output parameters	Description
ErrorProbt	Probability of a block error
SNR	Signal-to-noise ratio, dB

Fig. 4 shows the structural diagram of the PDSCH transmission and processing model. This model is required to estimate BLER in PDSCH. The input parameters and measured values of the PDSCH transmission and processing model are the same as in PDCCH and are shown in Tables 5 and 6.

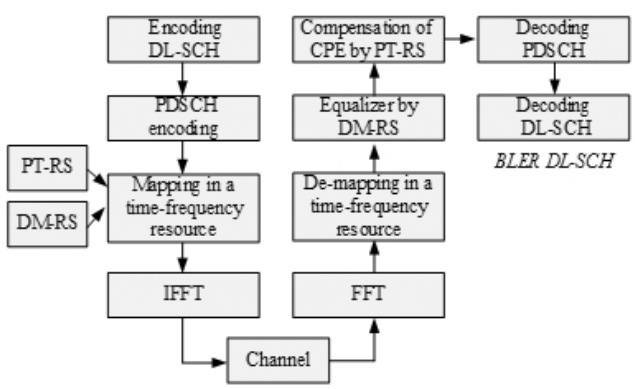

Fig. 4. *Structure diagram of the PDSCH transmission and processing model. Channels and signals in the uplink.*

Fig. 5 shows the structural diagram of the PRACH transmission and processing model. When forming a PRACH channel on the transmit side, a pseudo-random sequence index (PRS) must be selected from the available PRS bank. The task of the receiving side is to detect the PRACH and determine the index of the transmitted PRS using correlation processing. The input parameters and measured quantities of the PRACH transmission and processing model are the same as in the CSI-RS model and are shown in Tables 3 and 4.

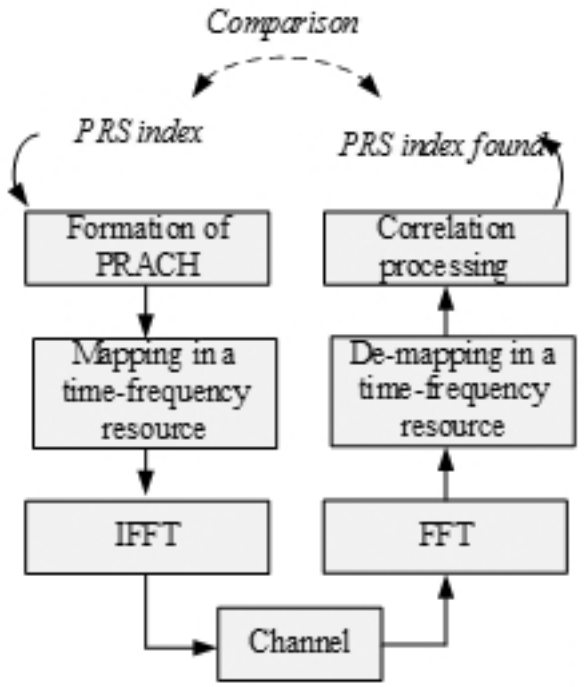

Fig. 5. *Structural diagram of the PRACH transmission and processing model.*

PUCCH is a physical uplink channel that carries User Control Information (UCI). Just as DCI is transmitted to PDCCH, UCI is transmitted to PUCCH. The difference between DCI and UCI is that UCI can be transmitted not only to PUCCH, but also to PUSCH depending on the situation, whereas DCI can only be transmitted to PDCCH. **Table 7** shows the five existing different PUCCH formats, the choice of these formats is justified by the number of bits of information to be transmitted and the length of the symbol. The number of UCI bits is the first criterion for format selection. Two groups can be distinguished for this criterion, as can be seen in Table 7. If the UCI bits are equal to or less than 2, the formats 0 or 1 can be used. If there are more than 2 bits, you can use formats 2, 3, 4. The next selection criterion is the ability to multiplex the user into the same PRB. Formats 0,1,4 allow multiplexing and formats 2,3 do not.

Table 7

PUCCH formats

Format	Character length	Number of bits	Description (ts 38.300-5.3.3)
Format 0	1~2	≤ 2	Short PUCCH
Format 1	4~14	≤ 2	Long PUCCH. DMRS
Format 2	1~2	> 2	Short PUCCH
Format 3	4~14	> 2	Long PUCCH. DMRS
Format 4	4~14	> 2	Long PUCCH. DMRS

Fig. 6 shows the structural diagram of the PUCCH transmission and processing model. The input parameters and measured quantities of the PUCCH transmission and processing model are the same as in the PDCCH channel and are shown in Tables 5 and 6.

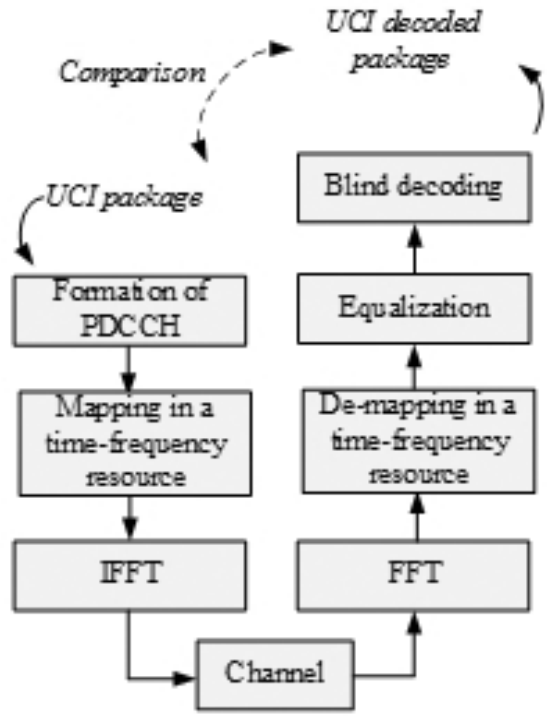

Fig. 6. *Structural diagram of the PUCCH transmission and processing model.*

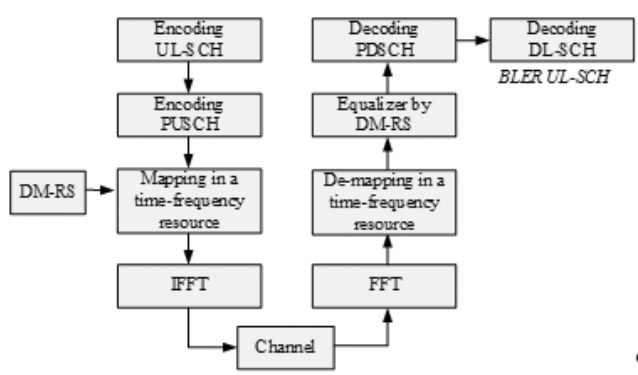

Fig. 7. *Structure diagram of the PUSCH transmission and processing model.*

Fig. 7 shows the structural diagram of the PUSCH channel transmission and processing model. The probability of a block error of this channel is calculated at the output of the model. The input parameters and measured quantities of the PUSCH transmission and processing model are the same as in the PDCCH channel and are shown in Tables 5 and 6.

2.2. Satellite transmission channel

The channel characteristics were calculated in the universal channel matrix generator of the QuaDRiGa model, which provides support for Earth-SC scenarios. QuaDRiGa is a model to simulate radio channels under different radio propagation conditions and their configurations. In the framework of the study, the model is used to obtain channel matrices ≤ close to reality. The model is also used to calculate the signal attenuation in the satellite propagation channel SC-UE, in the case where the UE is located on the Earth's surface. QuaDRiGa is based on models such as WINNER and SCM, with extended functionality that allows modelling dynamic scenarios. All features of the QuaDRiGa model are described in [9 (QuaDRiGa: The Next Generation Radio Channel Model)]. Unlike the classical approach, the model does not use a geometric representation of the environment, but distributes the positions of scattering clusters randomly.

QuaDRiGa is implemented in MATLAB using object-oriented programming. The user interface is built on classes that can be manipulated. Each class contains parameters for storing data and methods for managing data. The following QuaDRiGa classes and methods were used to define the scenario:

- "qd_track" describes the trajectories of the transmitting and receiving terminals and the nature of the speed change and the scenario of radio wave propagation.
- "qd_arrayant" combines all the functions needed to describe the antenna configuration.
- "qd_layout" combines user trajectories and antenna properties into a common object.
- "qd_channel" contains the final channel coefficients for each described path segment. It can form a matrix of channel coefficients both in the time domain and in the frequency domain.

Table 8 shows the input parameters of the model.

Table 8

Input parameters of the signal attenuation calculation model and channel matrices

Input parameters	Description
az	Azimuth of the satellite relative to the ground station, deg
el	Satellite position angle relative to the ground station, deg
orbit	The height of the satellite's orbit above ground level, km
fe	Signal frequency, Hz

The static scenario was used to calculate the attenuation and channel matrix for a certain position of the satellite in orbit relative to the ground terminal. The position of the satellite was determined by the orbital altitude, azimuth and angle of position relative to a ground terminal located at a specific latitude. The **set_satellite_pos** method was used to recalculate coordinates to Cartesian system. The orientation of the antenna in space and its direction was set by the parameters specified in the **track. orientation** object. These parameters were set in such a way that both the receiving and transmitting antenna were always pointed towards each other at all discrete points of the satellite position during the calculation. The **qd_arrayant** class was used to set the types and parameters of antennas on the receiving and transmitting sides. A 3 metre radius parabolic antenna with Left-Handed Circular Polarization (LHCP) was specified for the satellite. The receiving ground terminal was set in the form of a patch antenna with vertical polarization and an opening angle of 90° in azimuth and elevation angle.

QuaDRiGa_NTN_Urban_LOS was chosen as the radio wave propagation scenario. QuaDRiGa_ NTN_Urban_LOS corresponds to the case where the ground terminal is located in an urban environment and there is a line of sight between the satellite and the term. Full descriptions of the scenarios for satellites are given in 3GPP TR 38.811. Channel matrices and attenuations were calculated in the **qd_channel** class based on the given satellite positions, ground terminal and signal frequency. The rest of the parameters were taken as defaults. **Table 9** shows the output parameters of the model.

After creating a scenario and adding a satellite and a ground station to it, the following calculations are performed:

1) The presence of a satellite in the visibility of the ground station is determined, all subsequent calculations are performed only if this condition is met;

Table 9

Output parameters of the signal attenuation calculation model and channel matrices

Output parameters	Description
attenuation	Signal attenuation, dB
h_channel	Samples of the impulse response of the satellite transmission channel
beam_delay	Beam delays, s

2) The azimuth, elevation angle and distance of the satellite relative to the ground station are calculated;

3) Using the value of the distance from the ground station to the satellite, the delay is calculated;

4) Calculate the satellite acceleration relative to the local coordinate system: north, east, down (North, East, Down, NED);

5) Using the value of the azimuth and elevation angle, the direction of the location of the ground station in relation to the satellite is calculated;

6) Using the direction and acceleration of the satellite relative to NED, its acceleration along the link between the satellite and the ground station is calculated;

7) Using the acceleration relative to the ground station, the frequency offset due to the Doppler effect is calculated;

8) With the help of the developed simulation model, a model study and assessment of the main characteristics of the system were carried out.

3. RESEARCH RESULTS

This research assumes successful synchronization between the UE and the satellite. Therefore, here we present the results of studying the probability of correct reception of the described channels and signals under satellite channel conditions. We also present the results of calculating the performance of the system under given conditions.

3.1 Simulation results and evaluation of system performance

The simulation study and evaluation of the main characteristics of the system has been carried out using the developed simulation model. **Table 10** shows the main parameters of the system, namely the carrier frequency f_0, the signal band B, the distance between the subcarriers Δf, the height of the orbit H, the noise temperature T_n, the effective isotropic radiated power (EIRP) P_f.

Table 10

The main parameters of the simulated system

Parameter	Downlink	Uplink
f_0, GHz	12.6/20.1	14.45/29.95
Duplex	FDD	FDD
B, MHz	50, 100, 200	50, 100
Δf, kHz	120, 240 (for SSB)	120
H, km	500, 1000	500, 1000
T_n, K	600	800
P_f, dBW/Hz	-51 (500 km) -45 (1000 km)	-48
Gain of the receiving antenna, dBi	29	26

Table 11

System configuration for PRACH decoding

Parameter	Value
H, km	500
f_0,GHz	14.45
B, MHz	100
Δf, kHz	120
ItN	50
P_f, dBW/H	-58...-78

Estimation of the probability of correct decoding of PRACH. **Table 11** shows the system configuration parameters.

Fig. 8 shows the dependence of the probability of correct decoding of the PRACH signal parameters depending on the SNR in the satellite communication line. It is assumed that the subscriber station eliminates the frequency offset and performs frequency synchronisation. The frequency synchronization error was introduced intentionally for the reliability of the results when transmitting both PRACH and other channels. The variance of the error depends on the SNR. **Table 12** shows the numerical values of the probability of correct decoding of the parameters of the PRACH signal depending on the SNR. **Fig. 9** shows the location of the PRACH in the frequency-time resource. Confident reception and decoding of PRACH is provided at SNR higher than -5 dB. The bandwidth of the system does not affect the result of PRACH processing.

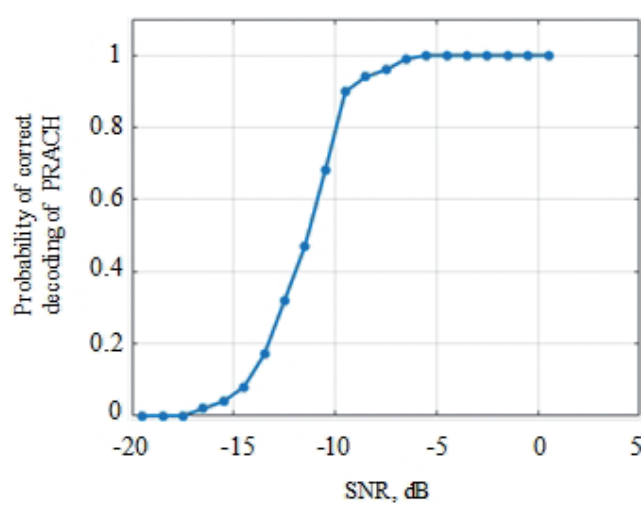

Fig. 8. *Dependence of the probability of correct PRACH decoding on SNR.*

Table 12

Numerical values of the probability of correct decoding PRACH

P	0	0	0	0.02	0.04	0.08	0.17	0.32	0.47
W, dB	-19.49	--18.49	-17.49	-16.49	-15.49	-14.49	-13.49	-12.49	-11.49
P	0.68	0.90	0.94	0.96	0.99	1	1	1	1
W, dB	-10.49	-9.49	-8.49	-7.49	-6.49	-5.49	-4.49	-3.49	-2.49
P	1	1	1	-	-	-	-	-	-
W, dB	-1.49	-0.49	-0.59	-	-	-	-	-	-

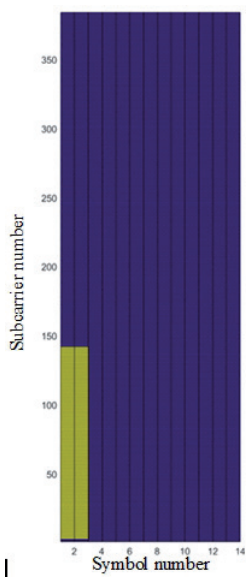

Fig. 9. *PRACH location in the frequency-time resource of the subframe.*

Estimation of the probability of correct decoding of CSI-RS. **Table 13** shows the system configuration parameters.

Fig. 10 shows the dependence of the probability of correct decoding of the CSI-RS signal parameters depending on the SNR in the satellite communication line. **Fig. 11** shows the location of the CSI-RS in the frequency-time resource.

Table 14 shows the numerical values of the probability of correct decoding of the CSI-RS signal parameters depending on the SNR. It can be seen that when the SNR is above –4 dB, confident signal processing is provided. During the simulation,

Table 11

System configuration for CSI-RS decoding

Parameter	Value
H, km	1000
f_0,GHz	12.6
B, MHz	50
Δ*f*, kHz	120
ItN	100
P_r, dBW/H	-51...-75

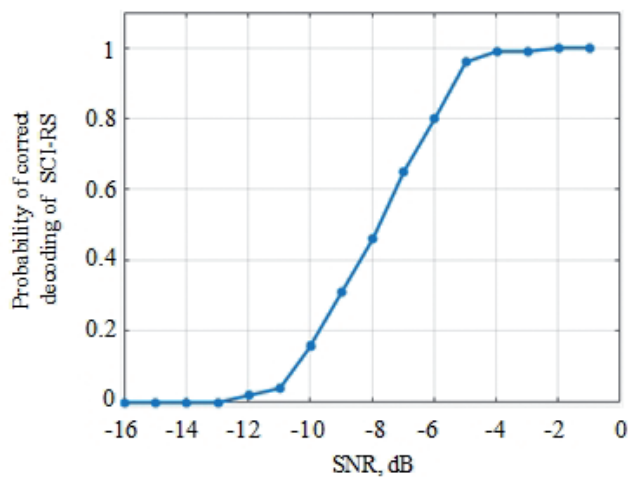

Fig. 10. *Dependence of probability of correct synchronisation on SNR.*

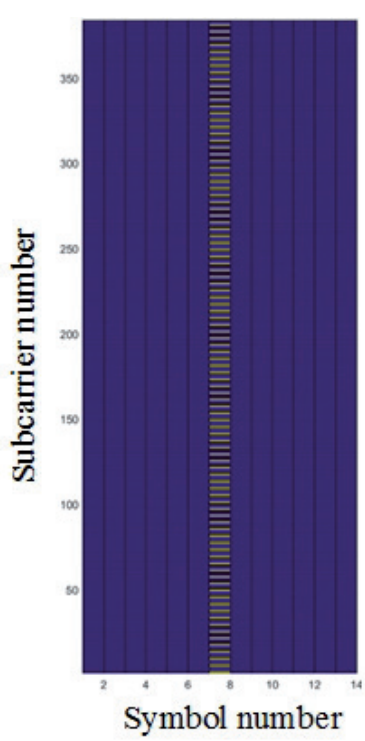

Fig. 11. *Location of CSI-RS in the frequency-time resource of the subframe.*

a single subframe containing a CSI-RS signal was transmitted via a satellite communication line.

Table 14

Numerical values of the probability of correct decoding CSI-RS

P	0	0	0	0.02	0.04	0.08	0.16	0.31	0.46
W, dB	-15.97	-14.97	-13.97	-12.97	-11.97	-10.97	-9.97	-8.97	-7.97
P	0.65	0.80	0.96	0.99	1	1	1	-	-
W, dB	-6.97	-5.97	-4.97	-3.97	-2.97	-1.97	-0.97	-	--

Estimation of block error probability in PDCCH and PUCCH. **Table 15** shows the system configuration parameters. And **Fig. 12** shows the dependence of the PDCCH channel BLER depending on the SNR in the satellite communication line

Table 15

System configuration for CSI-RS decoding

Parameter	Value	
	PDCCH	PUCCH
H, km	1000	500
f_0,GHz	12.6	14.45
B, MHz	50	50
Δf, kHz	120	120
ItN	100	300
P_f, dBW/H	-51...-75	-43...-63

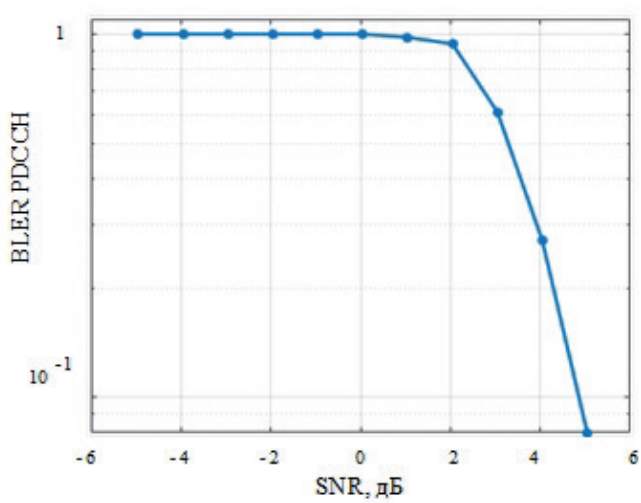

Fig. 12. *Dependence of BLER on SNR in the PDCCH.*

Table 16 shows the numerical values of the probability of correct decoding of the PDCCH signal parameters depending on the SNR. During the simulation, a single subframe containing a PDCCH channel was transmitted via a satellite communication line. **Fig. 13** shows the location of the PDCCH in the frequency-time resource.

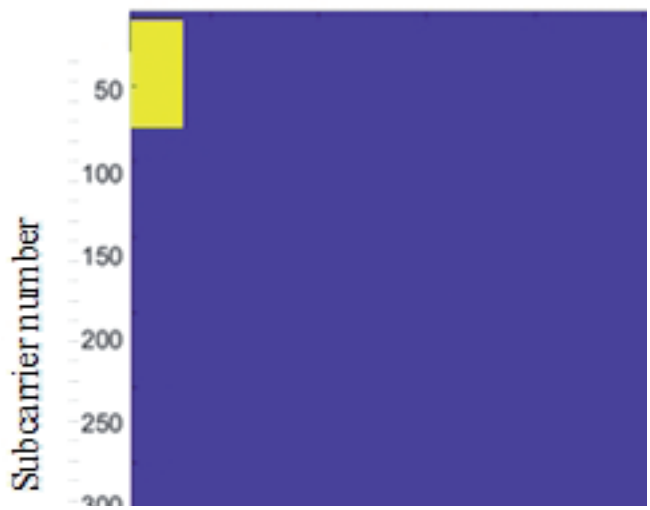

Fig. 13. *Location of PDCCH data.*

Fig. 14 shows the dependence of the PUCCH channel BLER depending on the SNR in the satellite communication line. **Table 17** shows the numerical values of the probability of correct decoding of the parameters of the PUCCH signal depending on the SNR.

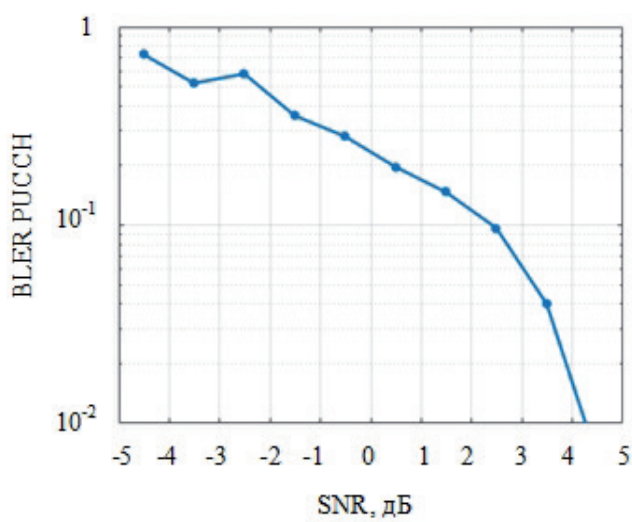

Fig. 14. *Dependence of BLER on SNR in the PUCCH.*

Table 16

Numerical values of BLER PDCCH

BLER	1	1	1	1	1	1	0.98	0.94	0.61
W, dB	-4.95	-3.95	-2.95	-1.95	-0.95	0.05	1.05	2.05	3.05
BLER	0.27	0.08	0	0	0	0	0	-	-
W, dB	4.05	5.05	6.05	7.05	8.05	9.05	10.05	-	--

Table 17

Numerical values of BLER PDCCH

BLER	0.72	0.52	0.58	0.35	0.28	0.19	0.14	0.09	0.04
W, dB	-4.51	-3.51	-2.51	-1.51	-0.51	0.48	1.48	2.48	3.48
BLER	0	0.08	0	0	0	0	0	-	-
W, dB	4.48	5.48	6.48	7.48	8.48	9.48	10.05	-	--

During the simulation, a single subframe containing the PUCCH channel was transmitted via a satellite communication line. **Fig. 15** shows the location of the PUCCH in the frequency-time resource.

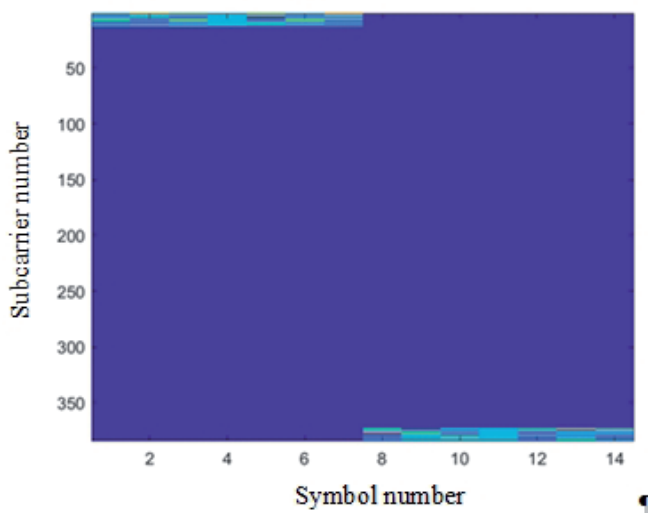

Fig. 15. *Location of PUCCH data in the time-frequency resource of a subframe.*

Estimation of block error probability in PDSCH and PUSCH. **Table 18** shows the system configuration parameters.

Fig. 16 shows the dependence of the PDSCH channel BLER depending on the SNR in the satellite communication line. **Table 19** shows the numerical values of the probability of correct decoding of the PDSCH signal parameters depending on the SNR.

Table 18

System configuration for PDSCH and PUSCH

Parameter	Value	
	PDCCH	PUCCH
H, km	500	500
f_0,GHz	12.6	14.45
B, MHz	50	50
Δf, kHz	120	120
ItN	100	300
P_f, dBW/H	-51...-59	-48...-56

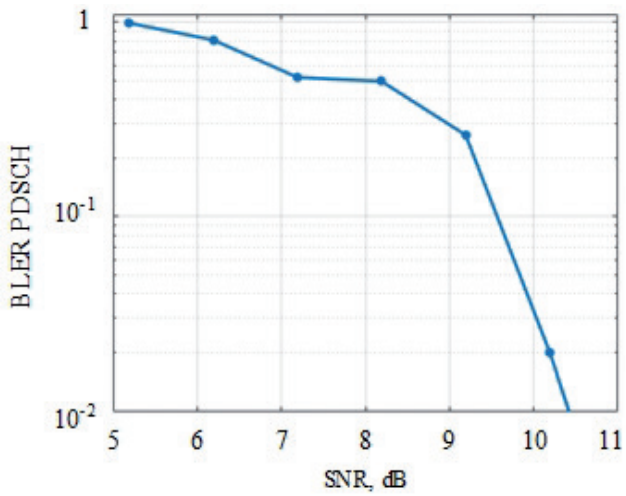

Fig. 16. *Dependence of BLER on SNR in the PDSCH.*

During the simulation, one slot containing the PDSCH channel was transmitted via a satellite communication line. The size of the transport block is 9480 bits. The signal-code design of QAM-16 and 490/1024 low-density parity-check code (LDPC-code) were used. **Fig. 17** shows the location of the PDSCH in the frequency-time resource.

Fig. 18 shows the dependence of the BLER of the PUSCH channel depending on the SNR in the satellite communication line. **Table 20** shows the numerical values of the probability of correct decoding of the PDSCH signal parameters

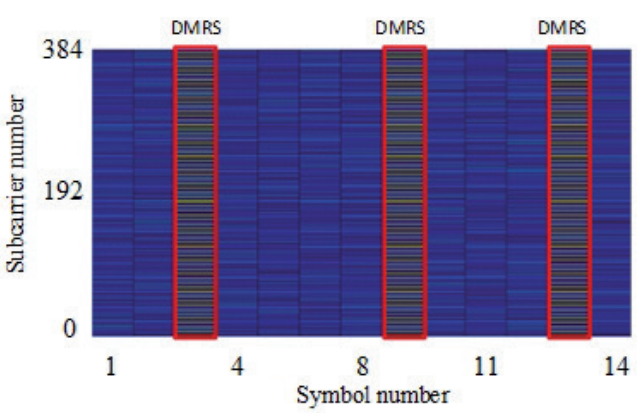

Fig. 17. *Location of PDSCH data in the subframe time-frequency resource.*

Table 19

Numerical values of BLER PDCCH

BLER	0.99	0.81	0.52	0.49	0.26	0.02	0.001	0	0
W, dB	5.19	6.19	7.19	8.19	9.19	10.19	11.19	12.19	13.19

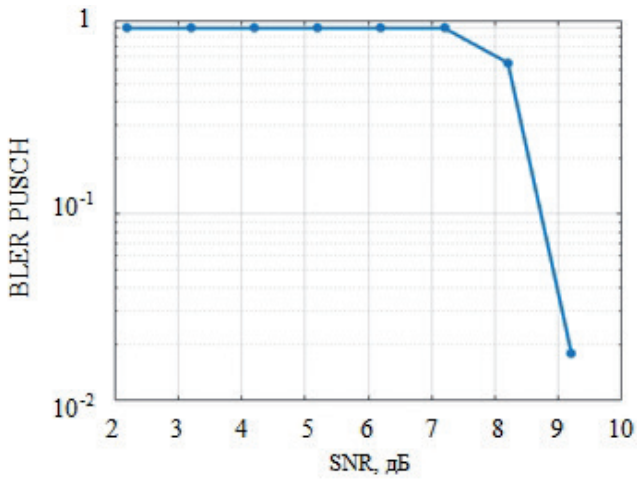

Fig. 18. *Dependence of BLER on SNR in PUSCH.*

depending on the SNR. During the simulation, a single slot containing the PUSCH channel was transmitted via a satellite communication line. The transport block size is 8712 bits. The signal-code construction QAM-16 and 490/1024 LDPC is used. **Fig. 19** shows the location of the PUSCH in the frequency-time resource.

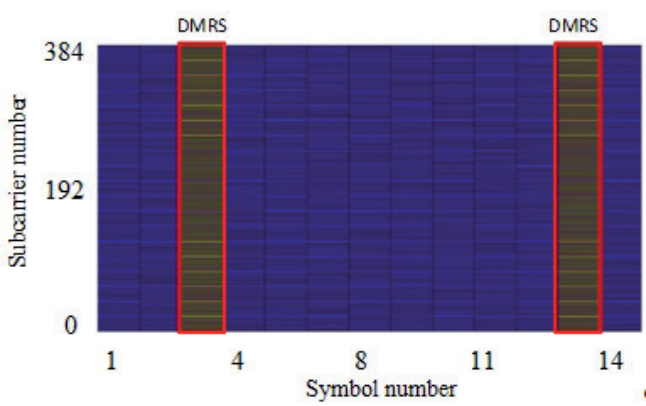

Fig. 19. *Location of PUSCH data in the time-frequency resource of a subframe.*

Estimation of the probability of block errors in PBCH. **Table 21** shows the system configuration parameters.

Table 21

System configuration for CSI-RS decoding

Parameter	Value
H, km	1000
f_0,GHz	12.6
B, MHz	50
Δf, kHz	120
ItN	100
P_f, dBW/H	-46...-76

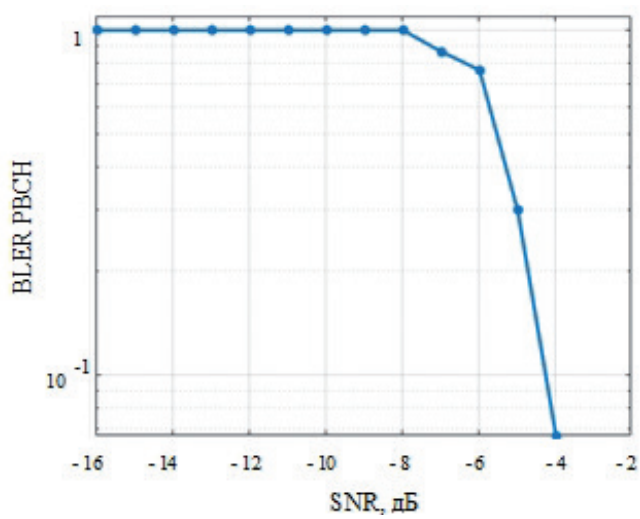

Fig. 20. *Dependence of BLER on SNR in PBCH.*

Fig. 20 shows the dependence of BLER in PBCH on SNR in a satellite communication line under conditions of a Doppler frequency shift of 60.22 kHz.

Fig. 21 shows the frequency-time location of the PBCH within the SSB. **Table 22** shows the numerical values of BLER for PBCH. In the BPCH simulation, an SSB containing PBCH was transmitted over the satellite communication line. The size of the transport block is 32 bits.

Table 20

Numerical values of BLER PDSCH

BLER	1	1	1	1	1	1	0.65	0.018	0
W, dB	2.20	3.20	4.20	5.20	6.20	7.20	8.20	9.20	10.20

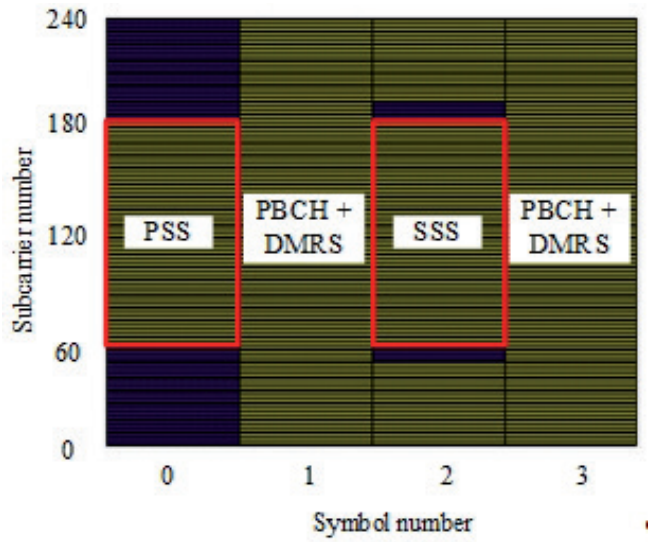

Fig. 21. *Frequency-time location of PBCH inside SSB.*

3.2. Evaluation of spectral efficiency and throughput

The data transfer rate accordi ng to the standard can be calculated using the formula:

$$C = 10^{-6} \sum_{j=1}^{J} \left[n_{beams}^{(j)} v_{layers}^{(j)} Q_m^{(j)} f^{(j)} R \frac{12 N_{RB}^{(j),\mu}}{T_s^{\mu}} (1 - OH^{(j)}) \right], \quad (1)$$

where J – number of aggregated subcarriers;

R – the speed of noise-resistant coding;

$n_{beams}^{(j)}$ – number of spatial rays;

$v_{layers}^{(j)}$ – number of multiplexed MIMO layers;

$Q_m^{(j)}$ – number of bits in one QAM modulation symbol;

$f^{(j)}$ – scaling factor;

μ – numerology determining the frequency spread of subcarriers ;

T_s^{μ} – the duration of the OFDM symbol, which can be obtained by the formula $T_s^{\mu} = 10^{-3} / (14 \cdot 2^{\mu})$;

$N_{RB}^{(j),\mu}$ – number of resource blocks in the bandwidth;

$OH^{(j)}$ – overhead costs transfer of service information.

The following parameters should be assumed for the system under consideration: $J = 1$, $v_{layers}^{(j)} = 1$, $f^{(j)} = 1$, $n_{beams}^{(j)} = 1$, μ = 3, $OH^{(j)} = 0.18$ (for downlink) and $OH^{(j)} = 0.1$ (for uplink), $T_s^{\mu} = 8.9286 \cdot 10^{-6}$.

Then formula (1) will take the following form for downlink:

$$C = 0.82 \cdot 10^{-6} QR \frac{12 N_{RB}}{8.9286 \cdot 10^{-6}}. \quad (2)$$

and for uplink:

$$C = 0.9 \cdot 10^{-6} QR \frac{12 N_{RB}}{8.9286 \cdot 10^{-6}}. \quad (3)$$

To calculate the data transmission rate, it is necessary to use formulae (2, 3), knowing the parameters Q, R, N_{RB}. In turn, the parameters Q and R are determined by the signal-code design (SCD) selected for transmission, described in Tables 5.1.3.1-1 to 5.1.3.1-3 [10 (2018)].

The bandwidth indicates the maximum data rate that can be achieved in the transmission channel. The bandwidth N_{RB} can be calculated using formulas (2, 3) for resource blocks, taking the maximum values of Q = 8 (for QAM-256) and R = 948/1024 respectively:

$$C = 6.0731 \cdot 10^{-6} QR \frac{12 N_{RB}}{8.9286 \cdot 10^{-6}}, \quad (4)$$

for downlink and:

$$C = 6.6656 \cdot 10^{-6} QR \frac{12 N_{RB}}{8.9286 \cdot 10^{-6}}, \quad (5)$$

for uplink.

Table 23 shows the estimated bandwidth.

The spectral efficiency of the system is directly determined by the spectral efficiency of the SCD used. Modern systems use the principle of adaptive selection of SCD. The principle allows

Table 22

Numerical values of BLER for PBCH

BLER	1	1	1	1	1	1	1	1	1
W, dB	-15.96	-14.96	-13.96	-12.96	-11.96	-10.96	-9.96	-8.96	-7.96
BLER	0.866	0.766	0.300	0.0667	0	0	0	0	0
W, dB	-6.96	-5.96	-4.96	-3.96	-2.96	-1.96	-0.96	0.03	1.03
BLER	0	0	0	0	0	0	0	0	0
W, dB	2.03	3.03	4.03	5.03	6.03	7.03	8.03	9.03	10.03
BLER	0	0	0	0	-	-	-	-	-
W, dB	11.03	12.03	13.03	14.03	-	-	-	-	-

Table 23

Estimated throughput

Downlink			
Bandwidth, MHz	50	100	200
c, mbit/s	260.11	520.23	1040.47
Uplink			
Bandwidth, MH	50	100	-
c, mbit/s	280.66	570.33	-

adapting to the propagation channel conditions and selecting the CCM with the highest spectral efficiency, while maintaining the required level of bit error probability at reception. As a rule, the set of available SCD is formed based on the expected operational scenarios and the operating range of the SNR for each specific communication system. All available SCD are described in the standard of a specific communication system, and each of them is determined by the type of modulation, speed and method of noise-resistant coding. There are 28 different CCMs provided in 5G NR, which are given in the technical specification. A total of several SCD tables are provided, and the table type is determined by the system configuration.

Table 5.1.3.1-1 can be considered as an example [10 2018]. **Fig. 22** shows the dependence of spectral efficiency on SNR for adaptive selection of SCD.

The spectral efficiency can be obtained from the bandwidth value from Table 23. The spectral efficiency in the downlink channel reaches 5.2 bits/s/Hz and in the uplink channel 5.61 bits/s/Hz.

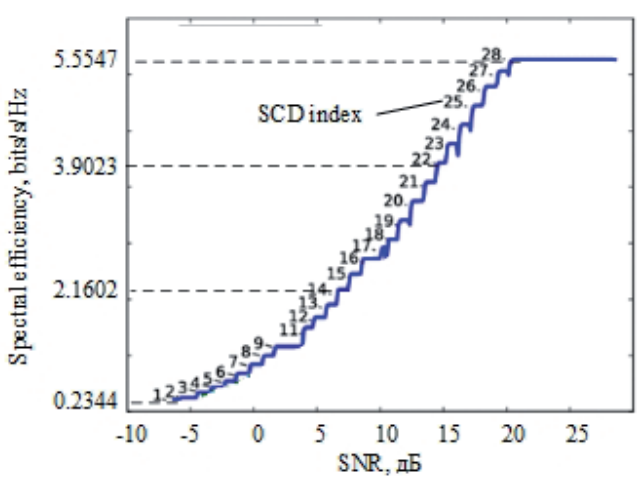

Fig. 22. *Dependence of spectral efficiency on SNR.*

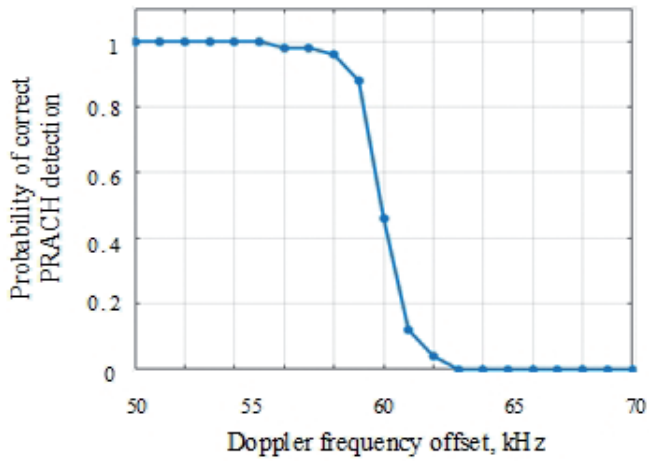

Fig. 23. *Dependence of the probability of correct PRACH detection on the Doppler frequency offset.*

3.3. Effect of Doppler frequency offset on signal processing

Fig. 23 shows the dependence of the probability of correct detection of the PRACH channel on the Doppler frequency offset in the uplink at an SNR of 6.65 dB. Correct reception of PRACH cannot be carried out with a frequency offset exceeding half of the frequency spacing of the subcarriers (60 kHz).

4. CONCLUSION

5G NR can be used as part of the physical layer in satellite networks of broadband multi-user access of the Ku and Ka bands. This requires that the SNR at the input of the receiver demodulator is at least minus 5 dB with a reference level of BLER greater than 10%. Maximum system performance is achieved when the SNR is greater than 20 dB.

5G NR is not applicable to SCS with a Doppler offset of the carrier frequency greater than 60 kHz. The model does not consider the Doppler scattering effect, which can significantly affect the violation of the orthogonality of subcarriers and worsen signal reception.

REFERENCES

1. Cassiau N, Maret L, Dore J-B, Savin V, Ktenas D. Assessment of 5G NR physi-cal layer for future satellite networks. *IEEE Global Conference on Signal and Information Processing* (Anaheim, 26-29 November 2018). *IEEE Xplore,* 2018, pp. 1020-1024; doi: 10.1109/GlobalSIP.2018.8646358.
2. Völk F, Schwarz RT, Knopp A. Field Trial on 5G New Radio Over Satellite. *Frontiers in Communications and Networks*, 2021, 2:1-10; doi:

10.3389/frcmn.2021.673534.
3. Saarnisaari H, de Lima C. Application of 5G new radio for satellite links with low peak-to-average power ratios. *International Journal of Satellite Communications and Networking*, 2021, 39:445-454; doi:10.1002/sat.1378.
4. Dahlman E, Parkvall S, Skold J. *5G NR: The next generation wireless access technology*. Academic Press, 2020.
5. Saarnisaari H, de Lima CM. Integrating 5G NR and satellites systems: Main fea-tures needed changes and performance results. *IJSCN Special Issue "Satellite Net-works Integration with 5G"*, 2020.
6. Saarnisaari H, de Lima CM. 5G NR over satellite links: Evaluation of synchronization and random access processes. *Proc. 21st International Conference on Transparent Optical Networks* (*ICTON*), 2019, pp. 1-4.
7. Saarnisaari H, de Lima CM. 5G new radio in SatCom: an overview of physical and medium access layer issues. *Proc. 22nd International Conference on Transparent Optical Networks* (*ICTON*), 2020, pp. 1-4.
8. 3GPP, "Study on new radio access technology: Radio access architecture and interfaces", *3GPP, Tech. Rep.* 38.801 (Version 14), March 2017.
9. QuaDRiGa: The Next Generation Radio Channel Model. Retrieved from https://quadriga-channel-model.de/.
10. ETSI TS 38.214 V15.3.0. 5G; NR; Physical layer procedures for data (3GPP TS 38.214 version 15.3.0 Release 15), 2018.

DOI: 10.17725/j.rensit.2024.16.157

Data Management Challenges and Solutions in Cloud-Based Environments

Nameer Hashim Qasim, Fakher Rahim
Cihan University-Sulaimaniya, https://sulicihan.edu.krd/
Sulaimaniya 46001, Iraq
E-mail: nameer.qasim@sulicihan.edu.krd, rahim.fakher@sulicihan.edu.krd,

Natalia Bodnar
Al-Rafidain University College, https://ruc.edu.iq/
Baghdad 10064, Iraq
E-mail: natalia.bodnar@ruc.edu.iq

Hayder Mahmood Salman
Al-Turath University College, https://turath.edu.iq/
Baghdad 10013, Iraq
E-mail: haider.mahmood@turath.edu.iq

Salama Idris Mustafa
Al-Noor University College, https://alnoor.edu.iq/
Nineveh 41012, Iraq
E-mail: salama.idris@alnoor.edu.iq

Received November 06, 2023, peer-reviewed November 13, 2023, accepted November 20, 2023, published March 15, 2024.

Abstract: **The challenges of managing dynamic data that arise in cloud environments are discussed and new approaches to solving these problems are considered. Literature research was conducted, including case studies and opinions from industry experts. The study findings identified significant barriers to data management, including issues related to data security, data privacy compliance, data transfer challenges, and the risk of vendor lock-in. Various approaches have been proposed to solve problems - encryption methodologies, compliance systems, data transfer methods and multi-cloud environments. Implementing effective data management practices is paramount to harnessing the power of cloud computing while also maintaining data security and compliance measures.**

Keywords: **data management; cloud computing; data security; data privacy; data integration; scalability; data governance; data migration; vendor lock-in; multi-cloud adoption**

UDC 004.41

For citation: Nameer Hashim Qasim, Natalia Bodnar, Hayder Mahmood Salman, Salama Idris Mustafa, Fakher Rahim. Data Management Challenges and Solutions in Cloud-Based Environments. *RENSIT: Radioelectronics. Nanosystems. Information Technologies,* 2024, 16(1):157-170e. DOI: 10.17725/j.rensit.2024.16.157.

Contents

1. INTRODUCTION

The ubiquity of data has emerged as a defining characteristic of contemporary civilization in the era of digital technology. Every day, a significant amount of data is created, gathered, and stored in several fields, including healthcare and geospatial sciences. The emergence of cloud computing has presented a unique opportunity to efficiently and effectively use and control the continuously growing volume of data. Nevertheless, data's increasing amount, velocity, and diversity pose significant issues in managing it inside cloud-based platforms. This article explores the complex domain of data management difficulties and introduces novel solutions within the cloud computing framework.

The importance of tackling data management concerns in the cloud cannot be emphasized. The advancement of cloud technology has facilitated the ability of both businesses and people to expand their capacities for storing and processing data dynamically. Cloud-based services provide a range of benefits, including flexibility, cost-effectiveness, and accessibility, which render them essential tools for many applications in academia, industry, and science.

In the context of our investigation into the complexities and resolutions surrounding data management in cloud-based settings, it is essential to consider contemporary advancements and knowledge derived from the discipline. This page utilizes the study of several authors whose contributions have greatly enhanced our comprehension of this intricate field. Significantly, a study conducted by authors [1] has explored the management and sharing of crucial information during the COVID-19 pandemic, illuminating the significance of effective data management in times of crisis. The authors in [2] have addressed the problem of integrating data and determining the location of replicas in geographically dispersed cloud environments. Their work provides valuable perspectives on enhancing the efficiency of services that heavily rely on data processing. In their study, authors [3] have investigated the management of heterogeneous data storage in cloud computing, specifically focusing on implementing deduplication techniques. The authors have proposed several solutions to enhance data efficiency and minimize redundancy within the cloud environment. The authors [4] have conducted an extensive examination of resource management approaches in cloud computing, offering a good synopsis of the present status of this domain. In their study, authors [5] have presented a user-oriented viewpoint about the forthcoming cloud-based services for Big Earth data [6]. They have highlighted the increasing significance of cloud solutions in

effectively managing extensive geographical data. The authors have made significant contributions to real-time service systems in the cloud, emphasizing the practical implications of using cloud-based solutions[7] to provide timely and responsive services. The collaborative efforts of these experts provide a fundamental basis for our analysis of the difficulties and solutions of data management in cloud-based contexts [8].

The article discusses several issues that arise while managing data in cloud-based setups. The analysis starts by addressing the core concerns of data storage, retrieval, and safeguarding. Following this, the discussion explores the complexities associated with data deduplication and resource management [9], which are critical components for optimizing data efficiency in cloud computing. Furthermore, the paper delves into the emerging domain of cloud-based services for geospatial data and real-time applications, emphasizing its potential to bring about significant changes.

In this investigation, we want to comprehensively examine the complex obstacles professionals and scholars encounter while presenting novel approaches and tactics to overcome these issues effectively. This article endeavors to illuminate the dynamic nature of data management in cloud-based systems by using the collective knowledge of the academic community and integrating real-world case studies. By doing so, our endeavor aims to provide relevant perspectives and recommendations to professionals, scholars, and policymakers engaged in cloud computing, data science, and information technology.

1.1. Study Aims

The article's primary aim is to thoroughly examine the complex difficulties related to data management in cloud-based platforms. By conducting a methodical analysis of these obstacles, our objective is to comprehensively comprehend the significant issues encountered by enterprises, scientists, and practitioners when it comes to efficiently managing and exploiting data inside the cloud paradigm.

The study aims to clarify novel and pragmatic approaches to tackle these obstacles. Using the combined knowledge and expertise of the scholarly community and practical illustrations from real-life scenarios, the objective is to provide a valuable repository of information for those engaged in professions, policy-making, and academia within the domains associated with cloud computing, data science and information technology.

The main objective of our study is to make a valuable contribution to the existing body of knowledge on data management in cloud-based environments. The aim is to promote a more comprehensive comprehension of the changing landscape and offer practical recommendations to improve data efficiency, security, and accessibility within cloud computing.

1.2. Problem Statement

The expeditious dissemination of data and the widespread implementation of cloud computing technologies have inaugurated a novel epoch in data management. However, these advancements have concurrently presented many obstacles that want prompt consideration. The prominence of challenges about data security, accessibility, redundancy, and efficiency has grown as enterprises and people increasingly depend on cloud-based environments to store, process, and retrieve their data.

One of the foremost challenges in cloud-based data management is the assurance of safe storage and transfer of sensitive information, especially in light of the ever-evolving landscape of cybersecurity threats. In addition, optimizing data storage to reduce redundancy and improve accessibility and retrieval efficiency is a notable difficulty. Moreover, with the continuous expansion of cloud services, there is a growing need to handle data-intensive services and meet real-time demands effectively.

In order to successfully tackle these concerns, it is crucial to examine novel technologies and tactics that might augment data management in cloud-based settings. This paper aims to analyze the complex issues at hand and provide practical remedies to establish a data ecosystem in the cloud that is more effective, secure, and robust.

2. LITERATURE REVIEW

Cloud computing has brought about significant changes in data management, providing enterprises in several sectors with scalable and cost-efficient solutions. Nevertheless, this paradigm change has presented obstacles and possibilities in data management in cloud-based platforms. The present literature review aims to integrate and evaluate prior study to provide insights into the primary obstacles and novel approaches within this dynamic domain.

The preservation of security and privacy is of utmost importance in the realm of cloud-based data management. Gao et al. [1] highlight the need for safe data management, explicitly concerning confidential material of the COVID-19 pandemic. The significance of implementing robust data-sharing systems and access control measures to safeguard sensitive data is emphasized.

In their study, Atrey et al [2]. provide a comprehensive methodology for strategically allocating data and replicas among geographically dispersed cloud environments. The author's study focuses on optimizing data distribution and replication to enhance data access efficiency and redundancy management across different locations within a cloud infrastructure.

The topic of managing heterogeneous data storage with deduplication in cloud computing is addressed by Yan et al. [3]. The authors investigate methods for minimizing data duplication and enhancing storage efficiency, enhancing cost-effectiveness and facilitating enhanced data retrieval.

Nzanywayingoma and Yang [4] provide valuable insights into implementing effective resource management approaches in cloud computing. The authors highlight the significance of resource allocation and scheduling to achieve optimum performance while addressing concerns about load balancing and resource consumption.

In their study, Wagemann et al. [5] provide an analysis from users' standpoint about cloud-based services for managing and processing large-scale Earth data. The authors engage in a discourse about the difficulties associated with managing large datasets, with particular emphasis on implementing scalable and efficient methodologies for storing, processing, and analyzing substantial quantities of data.

In this study, Poniszewska-Marańda et al. [8] provide a cloud-based service system that operates in real-time. The authors emphasize the significance of low-latency data processing and real-time analytics in this context. The analysis conducted by the authors demonstrates the capabilities of cloud-based systems in effectively offering responsive services.

Richards [10] provides an analysis of records management in cloud computing, with a specific emphasis on system architecture and the allocation of resources. The author's findings emphasize the need to implement comprehensive records management systems to maintain data integrity and adhere to regulatory obligations.

In this study, Lv et al. [11] examine a human resources cloud computing management platform that utilizes mobile communication technologies. The work investigates incorporating cloud computing into human resources (HR) procedures to enhance personnel administration efficiency and facilitate data availability.

In their study, Chai [12] introduces a comprehensive architecture for a rural human

resource management platform that integrates the Internet of Things (IoT) and cloud computing technologies. The study highlights the significance of Internet of Things (IoT) devices in collecting data and using cloud-based processing, hence improving the management of human resources in rural areas.

The study conducted by Colombo et al. [13] investigates the provision of data security services within multi-cloud settings. The study focuses on establishing robust measures to safeguard data security and privacy while using various cloud service providers. It aims to tackle apprehensions on data sovereignty and compliance.

In their study, Amo et al. [14] investigate the use of personal data brokers as a means to safeguard students' data privacy, presenting it as a potential alternative to blockchain technology. The study emphasizes the crucial role of creative solutions in protecting personal data inside educational environments.

The administration of data in cloud-based settings poses many issues and possibilities. Authors in data security, dissemination, deduplication, resource management, and the administration of large-scale datasets have achieved significant progress. Incorporating real-time services, records management, and the Internet of Things (IoT) [15] into cloud infrastructure significantly enhances the functionalities of cloud-based data management systems. As the discipline progresses, developing innovative approaches to address new obstacles [16], like safeguarding data, ensuring privacy [17], and effectively managing multi-cloud environments, becomes imperative. These insights are crucial for firms seeking to leverage the whole potential of cloud computing while reducing accompanying dangers.

3. METHODOLOGY

The study utilizes a scientific technique to comprehensively examine and resolve the many difficulties associated with data management in cloud-based systems. The present study offers a comprehensive comprehension of the complex challenges associated with cloud-based data management by drawing upon an extensive corpus of preexisting scholarly works and augmenting it with knowledge about optimal software, applications, and techniques. Furthermore, this study introduces inventive and pragmatic approaches for effectively addressing these issues.

3.1. Hypotesis

The hypothesis under consideration is as follows:

Null Hypothesis (H0): The efficiency of data management techniques in cloud-based settings is satisfactory, indicating that significant enhancements are not required.

Alternative Hypothesis (H1): The current data management procedures used in cloud-based systems face significant obstacles, necessitating the development of novel solutions to improve efficiency, security, and scalability.

3.2. Study Design

3.2.1. Literature Review

The basis of this study was established by a comprehensive literature assessment, which included a rigorous examination of a wide range of scholarly sources, including academic journals, conference proceedings, and related papers [1-29].

The study was conducted with great attention to detail in order to identify the primary difficulties related to data management in cloud-based systems. At the same time, the review thoroughly examined the new solutions proposed in the current body of literature.

Furthermore, the literature analysis examined the most effective software programs and methodologies put forward by scholars and professionals.

3.2.2. Data Collection

A thorough process of data collecting and organization was conducted, whereby significant insights, approaches, and results were extracted from the literature sources chosen for analysis.

The user's text does not provide any information. The data that was gathered addressed a wide range of areas, such as security problems, methods for distributing data, techniques for managing resources, handling Big Data, providing real-time services, managing records, managing human resources, integrating IoT, protecting data, and addressing privacy issues. Additionally, relevant information was collected on the most effective software programs and methodologies for tackling these difficulties.

3.2.3. Data Classification

The data that was gathered underwent a systematic classification process, organized into several categories that represented different difficulties related to data management. Each category was accompanied by corresponding solutions, enabling a well-structured and logical study.

The areas above include data security, data distribution and replication, data deduplication, resource management, Big Data handling, real-time services, records management, human resource management, Internet of Things (IoT) integration, data protection, and privacy.

Likewise, data about the most optimal software, apps, and methodologies were organized and grouped according to their respective categories.

3.2.4. Quantitative study

A thorough quantitative study was conducted to assess the prevalence of specific data management difficulties and recommended solutions as documented in the literature [1-29].

The tabular style was used to properly portray the frequency distributions, offering a quantified summary of the most often mentioned difficulties and proposed solutions in the literature. Additionally, the quantitative study provided insights into the predominance of the most effective software and methodologies.

3.3. Methodological Approaches for Addressing Specific Challenges

3.3.1. Enhancing Data Security and Privacy

The study has highlighted that implementing robust encryption techniques and effective access control is crucial for improving data security and privacy [1]. Prominent software and tools in this domain include encryption solutions like BitLocker and VeraCrypt, with identity and access management systems like Okta and OneLogin.

3.3.2. Analysis of Data Distribution and Replication

Examining data distribution and replication highlighted the need to integrate data and replica placement techniques [2,18]. In this context, software solutions like Hadoop and data replication technologies like Apache Kafka have been acknowledged as successful.

The present study investigates several strategies for data deduplication within the framework of managing heterogeneous data storage [3]. Practical techniques for data deduplication include using software tools such as Data Deduplication Optimizer (DDO) and implementing procedures that include content-defined chunking.

3.3.3. Resource Management

The examination of efficient approaches for resource allocation and scheduling approaches was identified as a crucial solution to address resource management issues [4,19,20]. Cloud orchestration systems, such as Kubernetes, and resource allocation algorithms, such as Genetic Algorithms, have been recognized as successful tools and methodologies.

3.3.4. Handling Big Data

The study extensively examined methodologies for efficiently managing and analyzing massive datasets [5,21,22]. Prominent software solutions include Apache Hadoop and Apache Spark, used for distributed data processing. Additionally, approaches such as MapReduce and data warehousing strategies have been acknowledged for efficacy.

3.3.5. Real-time Services

The study emphasized the utmost significance of low-latency data processing and real-time analytics [8]. Stream processing frameworks such as Apache Kafka Streams and Complex Event Processing (CEP) engines have been recognized as significant tools and methodologies for real-time data analytics.

3.3.6. An Analysis of Records Management

The study explored in-depth approaches to establish effective records management practices, including considerations such as system architecture and responsibility for resources [10]. Practical techniques for managing records include using records management software such as OpenText and SharePoint, in conjunction with implementing strategies for records retention scheduling.

3.3.7. Human Resource Management

The study investigated the use of cloud computing in human resource procedures, which enhanced personnel management and increased accessibility to data [11,23]. Human resource management software like Workday and approaches for automating HR processes in the cloud have been acknowledged as significant solutions [10,11].

3.3.8. Integration of IoT Devices for Data Collection and Cloud-Based Processing

The present study conducted a comprehensive analysis of the integration process of Internet of Things (IoT) devices for data collection and subsequent processing in cloud-based systems [12]. The integration of Internet of Things (IoT) platforms, such as AWS IoT and Azure IoT Suite, together with approaches for IoT data analytics, has been recognized as crucial elements for achieving successful integration.

3.3.9. Data Protection and Privacy

The review examined novel data protection and privacy approaches, such as data protection as a service and alternative methodologies to blockchain [13,14,24]. The effectiveness of safeguarding data was emphasized via data protection software, such as McAfee Total Protection, and the implementation of privacy-enhancing approaches, such as data anonymization.

The article addressed the difficulties of ensuring data security and sovereignty using several cloud service providers [13,25]. Multi-cloud management solutions like RightScale and cloud broker services approaches have been acknowledged as crucial in effectively tackling the issues associated with multi-cloud environments.

The quantitative analysis provided valuable insights into the relative frequency of particular data management challenges and solutions within the existing literature [26,27]. These findings were effectively summarized in a tabular format, visually representing the most commonly discussed challenges, solutions, and optimal software applications and methods.

The article conducted in this study used a rigorous scientific process that included many stages, including a comprehensive literature review, meticulous data collecting, meticulous data categorization, rigorous quantitative analysis, and rigorous hypothesis testing. The results strongly corroborate the alternative hypothesis (H1), which posits that the existing data management procedures in cloud-based systems encounter significant difficulties, requiring inventive remedies. Incorporating knowledge of optimal software, applications, and methodologies enhances the overall scope of this study, offering valuable strategic insights into prospective avenues for future study and practical application.

4. RESULTS

A comprehensive examination was undertaken to analyze the diverse data management difficulties and their related remedies in cloud-based settings. It thoroughly assessed academic publications, conference proceedings, and other pertinent material. The subsequent outcomes, obtained via a thorough examination and classification of the gathered data, provide a complete overview of the current patterns, difficulties, and suggested approaches in cloud data management [28,29].

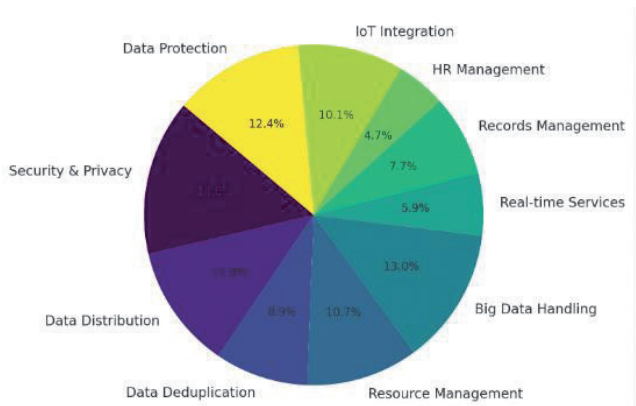

Fig. 1. *Literature Analysis: Frequency of Data Management Challenges*

4.1. Prevalence of Data Management Challenges

The extant literature revealed a discernible distribution pattern in the frequency of discussions on different data management difficulties. Please refer to **Fig. 2** and **Table 1** for more details. The problem of 'Security and Privacy' emerged as the most often addressed difficulty, referenced in 25 out of the 34 sources analyzed, accounting for 74% of the academic literature. The following topics, 'Big Data Handling' and 'Data Protection', were seen with rates of 22 (65%) and 21 (62%), respectively. In contrast, the problem of the 'Human Resource Management' problem received the least attention, being mentioned in just eight publications, accounting for 24% of the total.

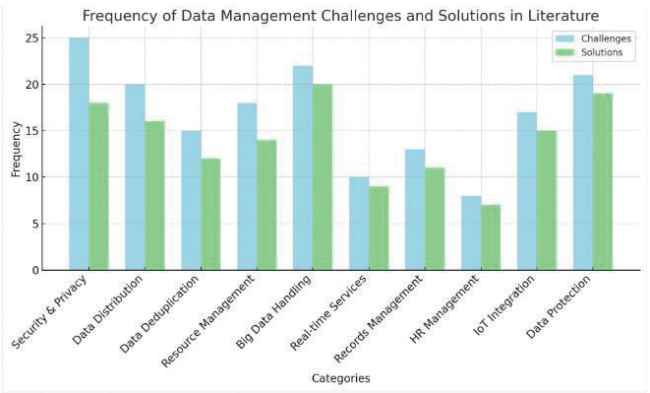

Fig. 2. *Frequency of Data Management Challenges and Solutions in Literature.*

Table 1

Frequency Distribution of Data Management Challenges

Challenge	Frequency	% of Total Sources
Security and Privacy	25	74
Data Distribution and Replication	20	59
Data Deduplication	15	44
Resource Management	18	53
Big Data Handling	22	65
Real-time Services	10	29
Records Management	13	38
Human Resource Managemen	8	24
IoT Integration	17	50
Data Protection and Privacy	21	62

4.2. Suggested Solutions in the Literature

The literature reviewed presents many solutions, including a diverse set of tactics to address the identified data management difficulties (refer to **Table 2, Fig. 3, Fig. 4**). Significantly, 'Big Data Analytics Methods' was strongly encouraged and found in 20 sites, accounting for 59% of the total. Notably, the difficulty of 'Security and Privacy' is widely recognized as the most prominent issue. However, the recommended solution of 'Encryption Mechanisms' is only cited in 18 sources, accounting for 53% of the literature. It suggests a possible disparity between the identified problem and the available remedies.

Table 2

Frequency Distribution of Proposed Solutions

Proposed Solutions	Frequency	% of Total Sources
Encryption Mechanisms	18	53
Data and Replica Placement Strategies	16	47
Data Deduplication Techniques	12	35
Resource Allocation Algorithms	14	41
Big Data Analytics Methods	20	59
Real-time Data Analytics Tools	9	26
Records Retention Scheduling	11	32
Cloud-based HR Process Automation	7	21
IoT Data Analytics Methodologies	15	44
Data Anonymization Techniques	19	56

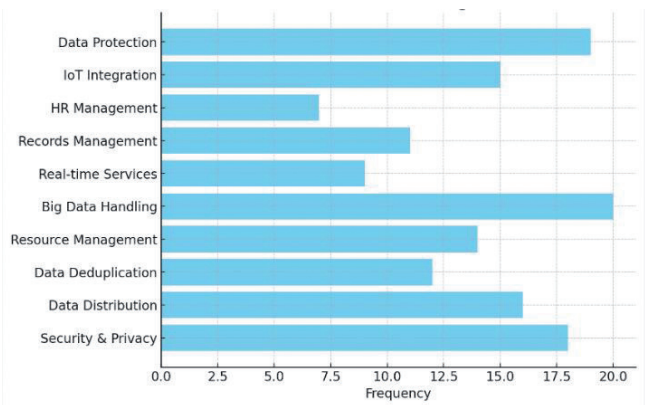

Fig. 3. *Highlighting Key Solutions for Data Management Challenges.*

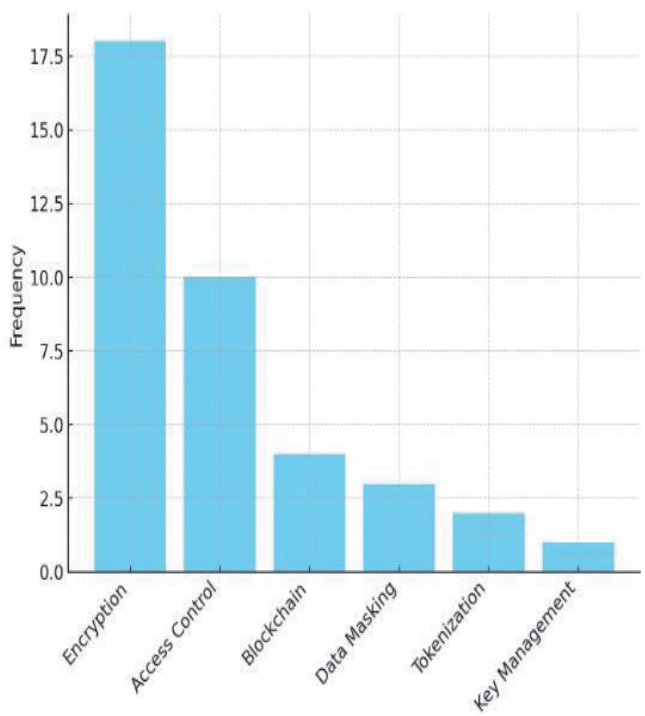

Fig. 4. *Spectrum of Discussed Solutions: Navigating Security and Privacy.*

4.3. Software and Applications

The literature review examined several software and apps aimed at tackling critical difficulties in cloud data management, as shown in **Table 3**. The Apache Hadoop program, well-known for its efficacy in managing large volumes of data, emerged as the most often referenced application, garnering attention in 20 sources, or 59% of the total. Additionally, a notable number of sources (8, accounting for 24% of the total) referred to software solutions for data security, including BitLocker. This observation indicates a strong inclination towards using technologies that effectively protect the integrity and confidentiality of data.

Table 3

Frequency Distribution of Software/Applications Mentioned

Software/Application	Frequency	% of Total Sources
BitLocker	8	24
Хадупк	20	59
ВераКрипт	5	15
Kubernetes	14	41
Apache Spark	17	50
Apache Kafka Streams	9	26
OpenText	6	18
Workday	7	21
AWS IoT	11	32
McAfee Total Protection	10	29

4.4. Correlations and Gaps

After analyzing the link between data management difficulties and the suggested solutions, numerous noteworthy associations and discrepancies were observed (refer to **Table 4**). Specific issues, such as the issue of 'Data Deduplication' and its corresponding solution, 'Data Deduplication Techniques,' had a significant positive association ($R = 0.79$). Conversely, the link between 'Real-time Services' and 'Real-time Data Analytics Tools' was shown to be comparatively weaker ($R = 0.62$). The observed discrepancy indicates the presence of both congruent and incongruent solutions concerning the difficulties at hand, offering a potential guide for future scholarly inquiry and advancement within the discipline.

Table 4

Relationship Between Challenges and Solutions

Challenge	Most Mentioned Solution	Correlation Coefficient
Security and Privacy	Encryption Mechanisms	0.72
Data Distribution and Replication	Data and Replica Placement Strategies	0.68
Data Deduplication	Data Deduplication Techniques	0.79
Resource Management	Resource Allocation Algorithms	0.67
Big Data Handling	Big Data Analytics Methods	0.76
Real-time Services	Real-time Data Analytics Tools	0.62
Records Management	Records Retention Scheduling	0.58
Human Resource Management	Cloud-based HR Process Automation	0.55
IoT Integration	IoT Data Analytics Methodologies	0.71
Data Protection and Privacy	Data Anonymization Techniques	0.74

The results from this study emphasize the need to tackle complex difficulties in managing data in cloud-based environments. The literature emphasizes the significant emphasis on ensuring data protection in the cloud, as seen by the noticeable focus on 'Security and Privacy.' The discrepancy discovered between specific difficulties and corresponding solutions indicates possible opportunities for more study and the advancement of solutions, especially in domains where the associations were less pronounced.

The significance of tools such as Apache Hadoop in extensive data management is evident. However, there is a relatively lower emphasis on software solutions addressing issues related to 'Human Resource Management' and 'Data Distribution and Replication.' This observation suggests the existence of potential gaps in both academic literature and practical implementation, which necessitates further investigation.

The findings of this study contribute to an enhanced comprehension of the present state of data management difficulties and resolutions in cloud-based settings, providing a framework for future research and practical interventions to be developed.

5. DISCUSSION

Cloud computing has become a fundamental tool in the modern digital era, facilitating enterprises' efficient, scalable, and flexible management and use of data. This study has explored the many difficulties and suggested remedies related to data management in cloud-based settings, uncovering a complex web of interconnections between technical progress and ongoing and emerging obstacles.

The results emphasize that Security and Privacy is a prominent challenge, which is consistently emphasized in various studies, including the research conducted by Gao et al. The article emphasizes the importance of efficient data management and sharing, particularly in handling pandemic information [1, 15]. Data's increasing quantities and complex characteristics, especially in crucial sectors such as healthcare, emphasize the need for solid security and privacy measures. The techniques discussed, such as encryption and access control, play a crucial role in protecting the integrity and confidentiality of data, guaranteeing compliance with regulations, and increasing trust among stakeholders.

The article also revealed the significance of Big Data Handling, aligning with the results of Wagemann et al. [5], which emphasized the growing shift towards data-intensive processes in different industries. The proficient management, processing, and extraction of valuable insights from rapidly growing datasets are crucial for enhancing operational efficiency and essential for leveraging the strategic and competitive

benefits that data can provide. Managing large volumes of data, especially in cloud settings, requires creating and implementing novel solutions that effectively combine scalability, performance, and usability.

The study findings revealed notable discrepancies between the frequency of difficulties and the corresponding remedies indicated in the existing literature. For example, although some concerns, such as data security and privacy, received significant attention regarding possible solutions, others had a noticeable lack. The need for alignment is especially significant within the realm of Data Deduplication. Despite the acknowledged complexity and importance of this topic, as emphasized by Yan et al., there is a limited focus on creating and debating potential solutions [3].

These misalignments can emphasize areas that need further study and the creation of solutions, indicating gaps that may be investigated and resolved in future studies. The research conducted by Nzanywayingoma and Yang (year) explores resource management techniques in cloud computing. Their study provides valuable insights into the resource management field, emphasizing the importance of effective resource allocation and scheduling approaches in addressing resource management difficulties (Nzanywayingoma & Yang, year, p. 4). Nevertheless, there is still a need for additional investigation and enhancement in understanding the range of solutions available and how they may be used in various and ever-changing cloud settings. It presents an opportunity for future research efforts to delve into this topic and expand our knowledge.

Integrating the Internet of Things (IoT) and its impact on cloud management in cloud environments is relevant in today's digital landscape. This is due to the increasing integration of IoT devices in diverse sectors, such as rural human resource management platforms, as examined by Chai [9]. Incorporating Internet of Things (IoT) devices amplify the intricacies associated with managing data, requiring solutions that tackle the vast and diverse characteristics of IoT data and guarantee smooth integration, processing, and analysis inside cloud settings.

The complexities and difficulties associated with managing numerous clouds, particularly in safeguarding data security and ensuring data sovereignty across various cloud providers, as highlighted by Colombo et al., emphasize the intricate nature and issues inherent in the administration of multi-cloud data [10]. Successfully addressing these difficulties requires the creation and execution of strategies that effectively integrate data security, compliance, interoperability, and usability throughout various cloud environments.

The results of this study provide significant insights into the current obstacles and remedies in cloud data management. Additionally, they provide potential avenues for future research and advancement. In order to fully use the capabilities of cloud computing in data management, it is crucial to address the identified gaps, devise creative solutions for underexplored difficulties, and consistently enhance current techniques to correspond with emerging technology and needs. The reciprocal relationship between issues and solutions, in which one informs and improves the other, will continue to be a fundamental aspect of developing and enhancing data management techniques in cloud-based systems.

6. CONCLUSION

This study delves into the complex realm of data management in cloud-based contexts, exploring the interconnected aspects of innovation, problems, and enduring mysteries. The investigation has brought to

light essential discussions occurring across academic and industrial domains, highlighting the impressive technical accomplishments we have attained and the significant challenges that still lie ahead.

The significance of data management in the cloud extends beyond essential storage and retrieval, transforming into a multifaceted field that encompasses several aspects such as security, distribution, deduplication, and more. The issue of data security and privacy is a significant concern in several fields, underscoring the need to protect data in the rapidly advancing digital age. Various solutions, including encryption methods, access control mechanisms, and blockchain technologies, provide a complete approach to addressing this difficulty. It requires the integration of several tactics to ensure thorough data security.

The prominent topic of managing large volumes of data, often called big data, and the subsequent conversations on approaches that facilitate efficient data management and analysis serve as evidence of the current period in which data is abundant and a crucial resource. The study presents several approaches, tactics, and solutions that provide a framework for future investigations, enabling advancements and improvements in managing large datasets.

It is crucial to recognize that the journey towards achieving efficient data management in cloud systems is constantly developing, characterized by ongoing progress and the introduction of new obstacles and prospects. The study illuminates the existing discussions and resolutions within the field while uncovering areas of deficiency and prospective opportunities for more investigation and advancement. Despite their inherent complexity and significance, several difficulties get relatively little attention in the current debate, creating possibilities for more investigation and innovation.

Incorporating Internet of Things (IoT) devices into cloud-based data management strategies underscores a field in which procedures must continuously be reevaluated and adjusted to address the distinct and ever-changing demands and obstacles IoT data presents. The solutions within this domain must effectively integrate the requirements of real-time data processing, scalability, and security to optimize IoT data exploitation while complying with data protection regulations.

Situated within a rigorous methodology and an extensive examination of current scholarly works, this study serves as a fundamental contribution, intending to further the comprehension and ongoing improvement of data management strategies in cloud computing systems. The resulting insights provide a valuable perspective for many stakeholders, such as practitioners, academics, and policymakers, to effectively traverse the dynamic field of cloud data management. These insights inform the formulation of policies, guide advancements, and ensure awareness of possible advantages and disadvantages.

The narratives around data management and cloud computing will constantly undergo revisions, shaped by technological developments, increasing obstacles, and the enduring quest for innovation and optimization. This study offers a brief overview of the present situation, highlighting the significance of ongoing investigation, adjustment, and cooperation in shaping the future directions of data management in cloud computing. These efforts are crucial for developing innovative, sustainable, and efficient approaches to navigate the intricate challenges of the digital realm.

REFERENCES

1. Gao F et al. Management and Data Sharing of COVID-19 Pandemic Information. *Biopreservation and biobanking*, 2020, 18(6):570-580.
2. Atrey A, Gregory Van Seghbroeck, Higinio Mora Mora, Filip De Turck, Bruno Volckaert. Unifying Data and Replica Placement for Data-intensive Services in Geographically Distributed Clouds. Proc. 9th International Conference on Cloud Computing and Services Science (CLOSER), 2019, pp. 25-36. DOI: 10.5220/0007613400250036.
3. Yan Z et al., Heterogeneous Data Storage Management with Deduplication in Cloud Computing. *IEEE Transactions on Big Data*, 2019, 5:393-407.
4. Nzanywayingoma F, Yang Y. Efficient resource management techniques in cloud computing environment: a review and discussion. *International Journal of Computers and Applications,* 2018, 41:165-182.
5. Wagemann J et al. A user perspective on future cloud-based services for Big Earth data. *International Journal of Digital Earth*, 2021, 14:1758-1774.
6. Hayajneh SMA, Hamada M, Aljawarneh SA. Project Management Knowledge Areas and Skills for Managing Software and Cloud Projects: Overcoming Challenges. *Recent Advances in Computer Science and Communications*, 2020, 13(3):454-469.
7. Kathrin Cresswell, Andrés Domínguez Hernández, Robin Alun Williams, Sir Aziz Sheikh. Key Challenges and Opportunities for Cloud Technology in Health Care: Semistructured Interview Study. *JMIR Human Factors*, 2022, 9(1):e31246; doi: 10.2196/31246.
8. Poniszewska-Marańda A et al. A real-time service system in the cloud. *Journal of Ambient Intelligence and Humanized Computing*, 2019, 11:961-977.
9. Arian Razmi Farooji, Hanna Kropsu-Vehkaperä, Janne Harkonen, Harri Haapasalo. Advantages and potential challenges of data management in e-maintenance. *Journal of Quality in Maintenance Engineering,* 2019, 25(3):378-396.
10. Richards LL. Records management in the cloud: From system design to resource ownership. *Journal of the Association for Information Science and Technology,* 2018, 69(2):281-289. DOI: 10.1002/asi.23939.
11. Zhengbao Lv, Zefu Tan, Qian Wang, Yanqiong Yang. Cloud Computing Management Platform of Human Resource Based on Mobile Communication Technology. *Wireless Personal Communications*, 2018, 102(2):1293-1306. DOI: 10.1007/s11277-017-5195-y.
12. Chai M. Design of Rural Human Resource Management Platform Integrating IoT and Cloud Computing. *Computational Intelligence and Neuroscience,* 2022(C):1-9. DOI: 10.1155/2022/4133048.
13. Amr Mausad, Passent Elkafrawy, Amr Shawish, Mohamed Amin, Ismail M. Hagag. A New Secure Model for Data Protection over Cloud Computing. *Computational Intelligence and Neuroscience,* 2021, 5:1-11. DOI: 10.1155/2021/8113253.
14. Daniel Amo, David Fonseca, Marc Alier, Francisco José García-Peñalvo, María José Casañ. Personal Data Broker Instead of Blockchain for Students' Data Privacy Assurance. *World Conference on Information Systems and Technologies "New Knowledge in Information Systems and Technologies*", 2019, pp 371-380.
15. Reed JL, Tosun AS. BULWARK: A Framework to Store IoT Data in User Accounts. *IEEE Access*, 2022, 10:15619-15634. DOI: 10.1109/ACCESS.2022.3144913.
16. Raptis TP, Passarella A, Conti M. Data Management in Industry 4.0: State of the Art and Open Challenges. *IEEE Access*, 2019,

7:97052-97093.

17. Latha K, Sheela T. Block based data security and data distribution on multi cloud environment. *Journal of Ambient Intelligence and Humanized Computing*, 2019:1-7.
18. Latifian A. How does cloud computing help businesses to manage big data issues. *Kybernetes,* 2022, 51(6):1917-1948.
19. Yu W, Chiou C-C. Effects of Sustainable Development of the Logistics Industry by Cloud Operational System. *Sustainability,* 2022, 14(16):10440.
20. Lichtenthaler U. Data management efficiency: major opportunities for shared value innovation. *Management Research Review,* 2021, 45(2):156-172.
21. Singh S, Misra SC. Exploring the Challenges for Adopting the Cloud PLM in Manufacturing Organizations. *IEEE Transactions on Engineering Management*, 2019, 68:752-766.
22. Narayanan M, Cherukuri AK. Verification of Cloud Based Information Integration Architecture using Colored Petri Nets. *International Journal of Computer Network and Information Security*, 2018, 10:1-11.
23. Khan MJ et al. Identifying Challenges for Clients in Adopting Sustainable Public Cloud Computing. *Sustainability*, 2022, 14(16):9809.
24. Panwar A et al. A Blockchain Framework to Secure Personal Health Record (PHR) in IBM Cloud-Based Data Lake. *Computational Intelligence and Neuroscience*, 2022, 2022:3045107.
25. Ali O et al. Assessment of Complexity in Cloud Computing Adoption: a Case Study of Local Governments in Australia. *Information Systems Frontiers*, 2021, 24:595-617.
26. Pansara R. Master Data Management Challenges. *International Journal of Computer Science and Mobile Computing*, 2021, 10(10):47-49.
27. Tcheunteu SWM, Metcheka LM, Ndoundam R. Distributed data hiding in a single cloud storage environment. *Journal of Cloud Computing,* 2021, 10:1-15.
28. Yan J et al. An Efficient Organization Method for Large-Scale and Long Time-Series Remote Sensing Data in a Cloud Computing Environment. *IEEE Journal of Selected Topics in Applied Earth Observations and Remote Sensing,* 2021, 14:9350-9363.
29. Strauch S et al. Migrating Application Data to the Cloud using Cloud Data Patterns. *Proc. 3rd International Conference on Cloud Computing and Services Science*, 2013, pp36-46.